The Photophysics of Fluorescent Protein Chromophores

Kiri Addison

School of Chemistry

University of East Anglia

Norwich

UK

2014

A thesis submitted in partial fulfilment of the requirements for the degree of Doctor of Philosophy at the University of East Anglia.

Declaration

I declare that the work contained in this thesis submitted by me for the degree of Doctor of Philosophy is my work, except where due reference is made to other authors, and has not previously been submitted by me for a degree at this or any other university.

Kiri Addison

Acknowledgements

Firstly I would like to thank my supervisor Prof. Steve Meech, not only for giving me this opportunity, but also for his constant support and advice throughout my PhD. I am hugely appreciative of his encouragement and thank him for everything he has enabled me to learn during the course of my studies. I would also like to thank Dr. Ismael Heisler and Dr. Jamie Conyard for teaching me how to use the experimental setups and the data analysis procedures, as well as for their constant help, support and friendship throughout my studies.

I thank all other members of the Meech research group; Andras, Francesca, Leo, Kamila, Sergey, Roberta and Franco for their help and friendship.

I would also like to thank my second supervisor Prof. Phil Page and his research group, in particular Tara and Yohan for the synthesis of many chromophores. I thank our collaborators Dr. Kryil Solntsev and his research group for the synthesis of the HBDI analogues. I also thank our collaborators at the Central Laser Facility and Prof. Peter Tonge and his research group.

Finally, I would like to thank my family for their support. In particular, my nan for her constant encouragement, my dad for his help during the last year and Suzi for making sure I didn't give up.

Abstract

Fluorescent proteins of the Green Fluorescent Protein (GFP) family are important and versatile scientific tools used in a range of applications including the labelling of proteins, cells and tissue, high resolution imaging and studying protein-protein interactions. They exhibit a very diverse range of photochemical behaviour. Surprisingly this diversity originates from chromophores which have very similar structures. Accordingly, minor changes to the chromophore structure or to its surroundings in the protein can produce dramatic changes in optical behaviour.

In this work the photophysics of the chromophores of the green fluorescent protein, the Kaede fluorescent protein and some related analogues are investigated using ultrafast methods; predominantly the excited state is probed using ultrafast fluorescence up-conversion with a time resolution of better than 50 fs. The excited states of chromophores decay on the ultrafast timescale. The decay will be probed for both isomers of the GFP chromophore, and the mechanism of decay will be modelled, leading to conclusions on the nature of the radiationless coordinate. The derivative of the chromophore generated in the Kaede protein will be studied, and marked differences with the GFP chromophore found.

The importance of protein-chromophore interactions in influencing fluorescent protein behaviour will be demonstrated. The effects of chromophore modifications will be revealed through comparison of the analogues and the sensitivity of chromophore photophysics to the hydrogen bonding nature of the solvent will be demonstrated. It will also be shown that the Kaede chromophore undergoes aggregation enhanced fluorescence at relatively low concentrations.

Contents

Abstract

Abbreviations

FP	fluorescent protein
GFP	green fluorescent protein
RFP	red fluorescent protein
KFP	kindling fluorescent protein
FRET	Forster resonance energy transfer
PALM	photoactivated localization microscopy
STORM	stochastic optical reconstruction microscopy
PAFP	photoactivatable fluorescent protein
ICS	intersystem crossing
OPA	one photon absorption
TPA	two-photon absorption
PES	potential energy surface
TICT	twisted intramolecular charge transfer
TRIR	time-resolved infrared
BBO	β-barium borate
SFG	sum frequency generation
SHG	second harmonic generation
GVD	group velocity dispersion
GDD	group delay dispersion
IRF	instrument response function

ESPT	excited state proton transfer
AIE	aggregation-induced emission
DAS	decay associated spectrum
IC	internal conversion
MeOH	methanol
EtOH	ethanol
PrOH	propanol
BuOH	butanol
OcOH	octanol
PnOH	pentanol
EG	ethylene glycol
Gly	glycerol
F	formamide
NMF	n-methylformamide
CY	cyclohexane
MeCN	acetonitrile
D_2O	deuterium
H_2O	water

Chapter 1 – Introduction

In this thesis the photophysics of several chromophores from the family of fluorescent proteins will be investigated using ultrafast spectroscopy. The aim of this work is to better understand how different substitutions change chromophore photophysics and how the protein influences chromophore behaviour.

1.1.   Fluorescent Proteins

In the early 1960s Shimomura discovered and extracted the first fluorescent protein (FP), green fluorescent protein (GFP), from the jellyfish Aequorea Victoria[1]. However, the value of GFP was not realised until several decades later when Chalfie demonstrated that it could be expressed in living cells, resulting in strong fluorescence with no toxic effects[2]. This finding sparked a revolution in bioimaging, eventually leading to the award of the 2008 Nobel prize in chemistry to Shimomura, Chalfie and Tsien 'for the discovery and development of the green fluorescent protein, GFP'[3].

Since Chalfie first demonstrated some of the remarkable properties of GFP, prolific research has generated a substantial palette of FPs with colours covering the visible spectrum[3]. These discoveries enabled the development and improvement of many scientific applications and techniques. Most notably, the ability of many FPs to be expressed in living cells, allows *in vivo* imaging and cell labelling and tracking[4]. FPs are also commonly used for measuring protein-protein interactions by utilising the Förster resonance energy transfer (FRET) mechanism[5]. This technique involves the non-radiative transfer of energy from an excited donor FP to a nearby acceptor FP. Thus by attaching the donor and acceptor FPs to proteins of interest, their interactions may be studied by monitoring the emission spectrum[6]. The

efficiency of the transfer depends on the inverse of the distance between the FPs to the

power of six, making this process sensitive to very small changes in distance.

FPs have also permitted the realisation of super-resolution imaging, in which the classical

diffraction limit is surpassed. Techniques such as photoactivated localization microscopy

(PALM) and stochastic optical reconstruction microscopy (STORM) allow imaging with a

spatial resolution on the scale of a few nanometers[7,8]. These methods rely on second

generation FPs (Section 1.3) and are based on the principle of repeatedly exciting and

bleaching small subsets of fluorophores within a sample. If the separation of the excited

fluorophores is sufficiently large, such that there is no spatial overlap of the emission, it is

possible to precisely locate individual molecules with a resolution better than the classical

diffraction limit. The positions of all individual fluorophores can then be determined by

repeatedly exciting and bleaching different subsets of the population. These data can then

be compiled to form a super resolution image.

1.2.   Chromophore Photophysics

All fluorescent proteins contain a chromophore which is surrounded by a beta-barrel

structure. This structure protects the chromophore, to some extent, from the outside

environment. In addition, the covalent bonds anchoring the chromophore to the protein

produce highly stable fluorescence. These advantageous properties result in reliable cell

labelling and tracking. GFP is made of 238 amino acid residues and contains the 4-

hydroxybenzylidene-1,2-dimethylimidazoline (HBDI) chromophore, which is common to

many FPs. The chromophore is formed in autocatalytic reaction involving the three residues

Ser65-Tyr66-Gly67[9]. As Figure 1.1 shows, internal cyclization of the protein backbone forms the imidazolinone ring, with subsequent dehydration and oxidation completing the formation of the extended delocalization which gives rise to visible absorption and emission[10,11].
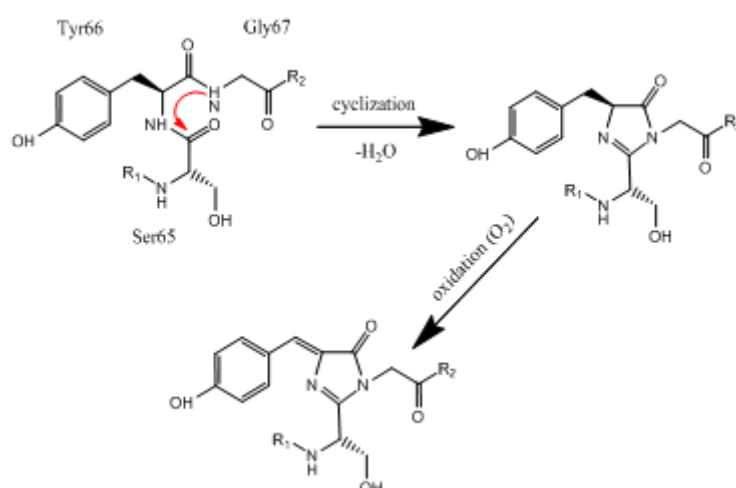
Figure 1.1. Formation of the GFP chromophore from residues Ser65-Tyr66-Gly67 through autocatalytic internal cyclization, dehydration and oxidation [10].

One intriguing aspect of the photophysics of HBDI is the dramatic reduction in the quantum yield when removed from the protein. Whilst GFP has a high quantum yield of 0.8, that of the isolated chromophore drops to 0.0002[9,12]. Studies have revealed that nonradiative decay via ultrafast internal conversion dominates the photophysics of HBDI. Time-resolved experiments have shown the internal conversion process to be almost barrierless and volume-conserving with a weak dependence on viscosity[13-16]. It is believed that the radiationless decay involves torsion or pyrimidalisation of the ring bridging bonds. Several mechanisms have been proposed, however the experimental findings place constraints on the nature of the mechanism i.e. the process must be consistent with ultrafast, barrierless,

volume conserving decay. Furthermore, the motion must be restricted within the protein cavity to restore the strong fluorescence. The 'hula-twist' mechanism, which involves torsion around both bridge bonds, was originally proposed to satisfy the volume conserving condition[17]. However, calculations predict that this mechanism would create an energetically uphill path to the ground-state[18]. This is not consistent with the ultrafast, almost barrierless decay of the excited state of HBDI. An alternative volume-conserving motion is pyramidalisation around the central bridging carbon atom[18-20]. This has been shown to be an important process in the photophysics of stilbene, ethylene and some molecular motors[21-23].

1.3. Second Generation Fluorescent Proteins

Some FPs known as second generation FPs or photoactivatable FPs (PAFPs) have properties which can be optically controlled[4]. In these PAFPs, irradiation may cause a change of the emission colour or even switching between bright and dark states. These changes can be reversible (photochromic proteins) or irreversible, depending on the switching mechanism involved.

Reversible PAFPs are valuable tools for applications such as ultra-resolution imaging, cell labelling and protein tracking, dual colour imaging, optical storage and molecular switches[24-29]. One such irreversible PAFP is Dronpa, which will be discussed in Chapter 3. Dronpa is a monomeric PAFP, containing the HBDI chromophore. In the fluorescent 'on' state Dronpa has a very high quantum yield and the dark 'off' state is stable for hours[30-32]. It has been shown that photoswitching results in different isomeric forms and charge states of the

chromophore in its 'on' and 'off' states[33-35]. Furthermore, the off and on states of the chromophore have very different protein environments, with the off chromophore possessing a more flexible attachment to the protein[33,36]. This increases the rate of radiationless decay, thus explaining the lack of emission in the off state[37]. Whilst the final geometric state and surrounding environment of the chromophore after photoswitching is relatively well understood, the exact mechanism and pathway of photoswitching is still the subject of debate[33,36,38-40].

The permanent nature of the photoswitching of irreversible PAFPs makes them highly reliable and efficient tools for protein tagging and tracking and imaging[30,41-45]. KaedeFP is an irreversible PAFP which can be permanently switched from a green to a red fluorescing state upon UV irradiation[30]. In the green state, the chromophore has the same structure as the HBDI chromophore. The photoconversion mechanism involves the irreversible backbone cleavage of the protein and a subsequent reaction with the chromophore. This extends the conjugation, thus red shifting the emission[46]. The photophysics of the red-shifted chromophore (Kaede) will be the subject of Chapter 4. More recently, the FPs IrisFp and NijiFP have been developed. These FPs exhibit both irreversible colour switching and reversible on-off photoswitching[47,48]. This dual property has led to the development of a technique called super-resolution pulse chase imaging[49]. This technique is based on the PALM technique described in Section 1.1. Firstly a super-resolution image is attained using the repeated photobleaching method, utilising the reversible properties. Next the irreversible switching is exploited by photoconverting a subset of the FPs whose motion can then be tracked using the PALM technique.

1.4. Theory of Absorption and Fluorescence

When a molecule absorbs electromagnetic radiation, it is excited to a higher electronic state. It can then return to the ground-state through radiative decay or by a form of radiationless decay. There are two forms of radiative decay, fluorescence and phosphorescence. Fluorescence occurs between singlet excited states (typically S_1 and S_0) and is therefore spin-allowed with typical lifetimes on the nanosecond timescale[50]. However, phosphorescence occurs from triplet excited states to the singlet ground-state, which are spin-forbidden transitions. This results in a much longer relaxation time in the millisecond to second range.

Absorption and emission processes can be illustrated using the Jablonski diagram[51]. Figure 1.2 shows an example Jablonski diagram where the ground, first and second electronic singlet states are indicated by S_0, S_1 and S_2 respectively and the first triplet excited state is shown by T_1. For each electronic level there exist multiple vibrational levels, shown by the labels 0, 1 and 2. The transitions between energy levels are illustrated by vertical lines. This indicates the Franck-Condon principle, the transition occurs on such a fast timescale, 10^{-15} s, that there can be no significant movement of the nuclei.
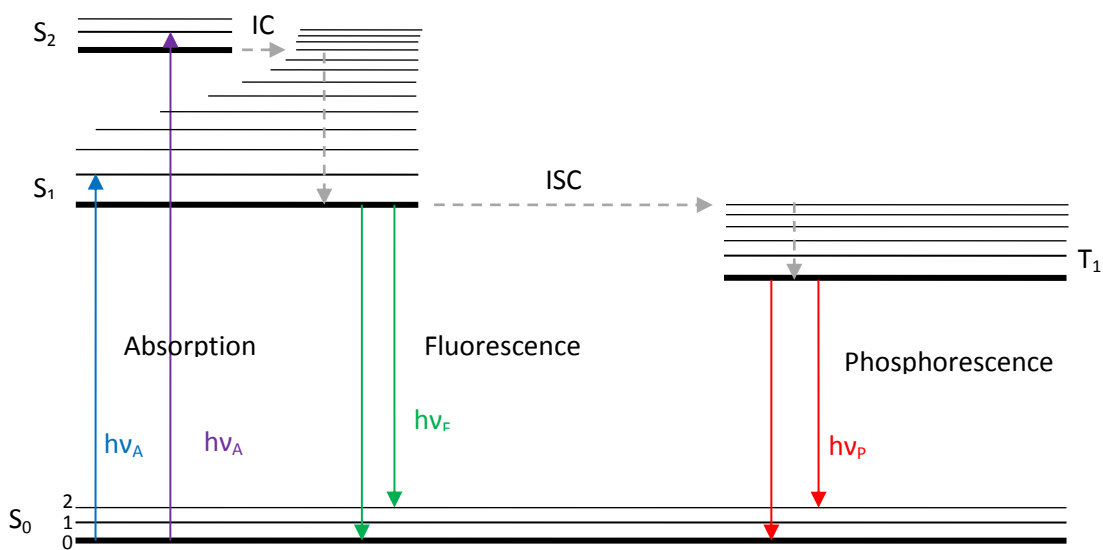
Figure 1.2. An example Jablonski diagram illustrating the processes involved in absorption and emission.

Upon absorption, a fluorophore will be excited to a higher energy electronic state (S_1 or S_2) often with excess vibrational energy. It will then usually relax to the lowest vibrational level of S_1. This is a rapid internal conversion (IC) process from S_2 typically occurring within 10^{-12} seconds. As this is much faster than a typical fluorescence lifetime, emission is generally from the lowest vibrational level of S_1. The fluorophore will then relax back to the ground-state, where vibrational relaxation to the lowest level will again happen on the 10^{-12} s timescale. A consequence of this is that the energy gap for S_1-S_0 decay is smaller than that of the original S_0-S_1 excitation. This results in a difference between the maxima of the absorption and emission spectra, known as the Stokes shift (Figure 1.3). The Stokes shift can

be enhanced by solvent effects, excited state reactions, complex formation and energy transfer[52].
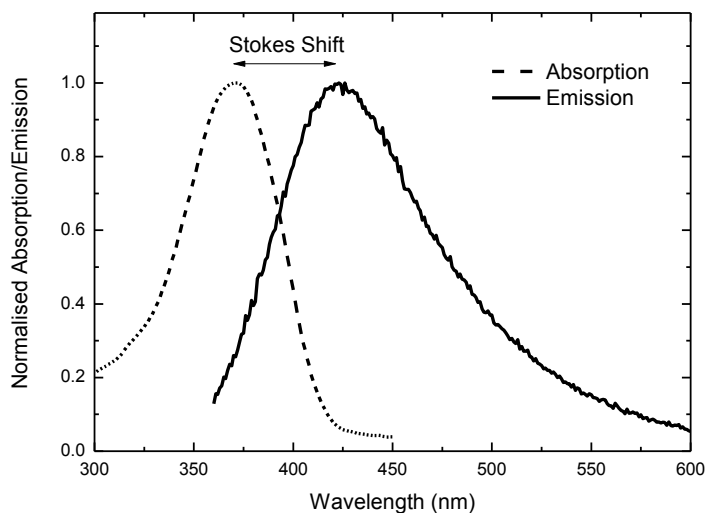
Figure 1.3. The absorption (dashed) and emission (solid) of HBDI in methanol. The Stokes shift is the difference between the absorption and emission maxima.

Phosphorescence can also occur via intersystem crossing (ISC). As shown in the Figure 1.2, a molecule in the S_1 state can be spin converted to the T_1 state. This results in longer lifetimes as transitions from T_1 to S_0 are forbidden. Also the emission wavelength is redshifted as the energy of the T_1 is lower than the singlet state[50].

The efficiency of light absorption at a particular wavelength can be described by the Beer-Lambert Law,

$$A(\lambda) = \varepsilon(\lambda)cl, \tag{1.1}$$

where $\varepsilon(\lambda)$ is the molar absorption coefficient, c is the concentration of the absorbing species and l is the path length. Clearly this predicts that the absorbance of a species will depend linearly on its concentration. The breakdown of this linearity can indicate the presence of other absorbing species or aggregation within the sample.

If a single photon is not sufficiently energetic to promote a fluorophore, excitation to a higher energy level can occur via the absorption of multiple photons. For two-photon absorption (TPA), as the name suggests, a molecule is excited by the simultaneous absorption of two-photons. TPA has been exploited for applications such as deep tissue imaging and photodynamic therapy[53-56]. For these applications the longer excitation wavelength allows greater tissue depth penetration and decreased photo-damage compared to one photon absorption (OPA). As TPA is a non-linear optical process, its probability depends on the intensity of the excitation light and the TPA cross section is different from the OPA cross section. Hence for TPA applications molecules with high TPA cross sections are desirable, otherwise very high sample concentrations or high intensity excitation light are required[53].

The fluorescence quantum yield is defined as the ratio of the number of photons emitted to those absorbed. The excited state can decay via radiative and nonradiative processes where each type of process has its own rate. The rate of emission is given by κ_F and that of nonradiative decay by κ_{nr}. Hence the quantum yield (Q) is given by,

$$Q = \frac{\kappa_f}{\kappa_f + \kappa_{nr}}. \tag{1.2}$$

The lifetime of the excited state (τ) is the average time spent in the excited state. Therefore this will also depend on the two rates κ_F and κ_{nr} as follows,

$$\tau = \frac{1}{\kappa_f + \kappa_{nr}}. \qquad (1.3)$$

The fluorescence intensity can be reduced by quenching reactions. There are various methods of quenching and this effect can be used to provide dynamic information about the excited molecule's environment[50].

Generally fluorescence obeys Kasha's rule, which states that the emission spectrum is independent of the excitation wavelength[57]. This is because, as mentioned previously, emission tends to occur from the lowest level of S_1. Hence any excess energy is lost as heat before emission occurs. However there are deviations from the rule, for example if emission occurs from the S_2 state or for aggregated samples[50,58].

1.5. Reactive Systems

Excited state photoisomerisation is a naturally occurring process which has been widely studied. For example, isomerisation of the pigments rhodopsin and iodopsin is an integral process in vision[59-61]. *Cis-trans* isomerisation is also now being exploited in order to control a variety of process by creating photochemical molecular switches[62].

Figure 1.4 illustrates the basic concept of excited state isomerisation, where the ground and excited state energies are described by potential energy surfaces (PESs). These PESs illustrate the variation of the energy of the states as a function of a particular reaction coordinate, e.g. isomerization. In the ground-state the barrier between the *cis* and *trans* states is sufficiently high that isomer exchange does not occur. However in the excited state, this barrier can be reduced or removed entirely[63]. After promotion to the higher energy

level, the excited state population evolves along the excited state PES. Eventually reaching a minimum, where relaxation to the ground-state via ultrafast internal conversion through a conical intersection can occur. This can result in decay to the ground-state *cis* or *trans* form[64].
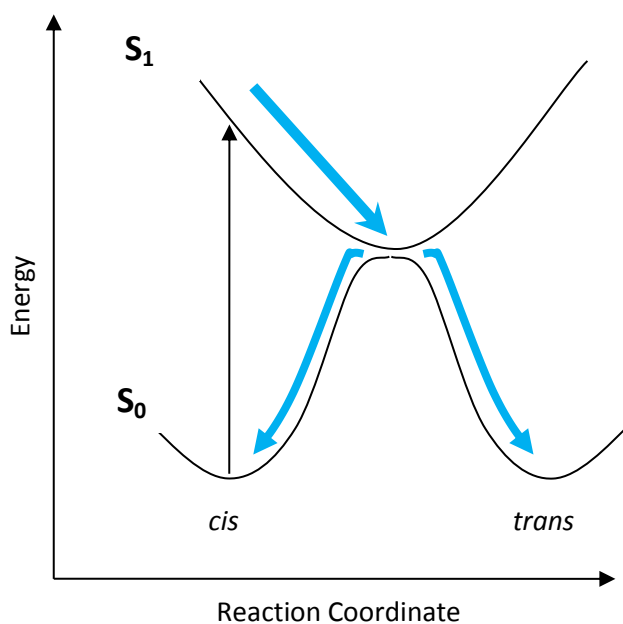
Figure 1.4. A schematic representation of an excited state isomerisation reaction.

Conical intersections (or seams in multi-dimensional space) occur when PESs are degenerate. Hence transition from a higher to a lower lying state occurs without the emission of radiation[65-67]. Conical intersections are necessary to explain the very fast nonradiative transitions between states which is crucial to our understanding of many excited state processes[68].

Many systems which experience ultrafast decay of the excited state, do so via barrierless excited state *cis – trans* isomerisation reactions. One such molecule which has been

thoroughly studied is stilbene[69]. The ground-state isomerisation barrier is approximately 50 kcal mol^{-1} but is reduced in the excited state[70]. It has been shown that *cis-trans* isomerisation occurs within 1 ps via a barrierless decay[70]. After excitation, the molecule moves along the barrierless S_1 PES to a twisted geometry, at which a conical intersection allows ultrafast internal conversion to the ground-state. In contrast, *trans-cis* isomerisation occurs with a non-negligible barrier between the Franck-Condon region and the twisted geometry. Thus extending the lifetime of the excited state. When isomerisation involves structural motion, such as that involved in the geometrical rearrangement of stilbene, solvent frictional effects can strongly influence the excited state dynamics. This is because the viscous medium will oppose the structural motions which occur as the molecule traverses the PES[69,70]. Hence the effects of solvent viscosity on excited state dynamics can indicate the degree of structural reorganisation involved in the decay of a molecule.

Activated barrier reactions, such as the excited state *trans-cis* isomerisation of stilbene, can be described theoretically using the Kramers equation[71]. At very low viscosity, the reaction rate increases with solvent viscosity due to solvent-solute energy transfer[72,73]. Whereas in the high viscosity regime, frequent solvent – solute collisions hinder the barrier crossing, hence the reaction rate decreases with increasing medium viscosity[73]. This leads to the observation of the 'Kramers turnover', where the two regimes meet. Whilst Kramers theory has been used successfully to describe frictional effects on activated reactions, it does not adequately reproduce barrierless reactions. For reactions such as the excited state isomerisation of *cis* stilbene, other models have been employed.

While there is no uniform scheme for modelling solvent frictional effects in barrierless reactions, one of the most widely used theories for describing an ultrafast, barrierless

excited state isomerisation reaction is the Bagchi – Fleming – Oxtoby (BFO) model[74,75]. This model uses a generalised Smoluchowski equation (Chapter 2) to describe the diffusion of an excited state population along a PES. Sink functions can be used to enable decay to the excited state, where pinhole sinks represent conical intersections[74,75]. When no barrier is present, the only force opposing the motion of the excited state population is the friction induced by the solvent. Thus as the motion of the population is increasingly hindered by a greater solvent viscosity, an extension of the lifetime of the excited state may be observed.

The effects of solvent viscosity on fluorescence intensity may be exploited for the use of environment sensitive fluorescent probes such as rotor molecules[76]. Molecular rotors an electron donor unit conjugated to an electron acceptor unit. Upon excitation, electron transfer induces the formation of twisted intramolecular charge transfer (TICT) complexes. Decay to the ground-state can then occur via fluorescence or internal conversion through rotation of the rotor group. These molecules can be used as viscosity sensors because excited state decay involves structural reorganisation which is affected by medium viscosity. Hence, increased viscosity hinders the rotation of the rotor part of the molecule, thus enhancing the fluorescence quantum yield[77]. One such molecule is 9-dicyanovinyljulolidine (DCVJ) (Figure 1.5) which will be used as an example in the experimental section (Chapter 2). The excited state decays rapidly in solution via rotation around the dicyanovinyl double bond. It has been shown that the rate of rotation has a weak dependence upon viscosity. This has been explained by the small size of the rotor, which will therefore displace only a small volume of solvent[78,79].
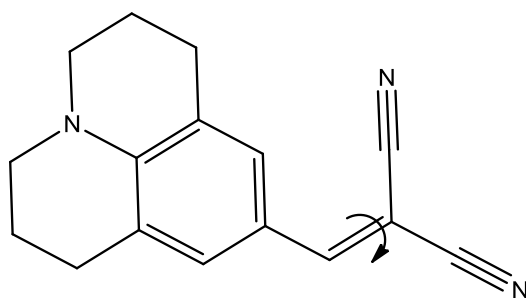
Figure 1.5. Molecular structure of the DCVJ molecular rotor.

As well as solvent viscosity, the polarity of a solvent can also strongly influence the excited state dynamics. This is of particular importance when the charge distribution of the solute differs greatly in the ground and excited states. As Figure 1.6 illustrates, when the molecule is excited the surrounding polar solvent molecules will reorientate in response to the changing electrostatic interactions with the solute until equilibrium is restored[80]. The timescale of this process can range from femtoseconds (fs) to picoseconds (ps) and the reorientation of the solvent molecules leads to closer approach of the ground and excited state. Thus leading to a red shifting of the fluorescence band and a rise time on the red edge[81].
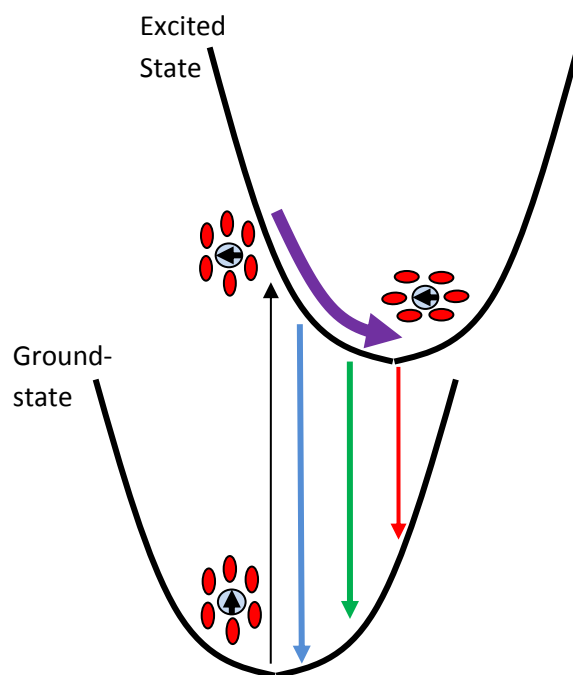
Figure 1.6. An illustration representing excited state solvent dynamics. When a molecule is promoted to the excited state, its charge distribution may change significantly. In such cases the surrounding solvent molecules reorientate to establish a new equilibrium, leading to closer approach of the ground and excited states.

The polarity of the solvent can have a large effect on the emission of a chromophore. Thus the sensitivity of the fluorescence properties to solvent polarity can give an indication of the molecule's own polarity, as a larger effect generally indicates a more polar chromophore[50]. In this work the measure of solvent polarity used will be the solvent polarity function,

$$F(\varepsilon_0, n) = \frac{\varepsilon_0 - 1}{\varepsilon_0 + 2} - \frac{n^2 - 1}{n^2 + 2}, \qquad (1.4)$$

Where ε_0 is the static dielectric constant and n is the refractive index of the solvent[82]. As depicted in Figure 1.6, the solvation process gives rise to a gradual red shift of the emission.

15

Consequently a time-dependent Stokes shift is observed[83]. This can be quantified using the Stokes shift response function *S(t)*,

$$S(t) = \frac{\upsilon(t) - \upsilon(\infty)}{\upsilon(0) - \upsilon(\infty)},$$ (1.5)

where $\upsilon(t)$ is the frequency of the emission maximum at time *t*. The dynamic Stokes shift gives insight into the solvent polarity sensitivity of the chromophore. It should be noted that excess vibrational energy and the subsequent relaxation to the lowest vibrational level of the excited state also leads to a time-dependent Stokes shift.

1.6.   References

(1)Shimomura, O.; Johnson, F. H.; Saiga, Y. *J Cell Comp Physiol* **1962**, *59*, 223.
(2)Chalfie, M.; Tu, Y.; Euskirchen, G.; Ward, W. W.; Prasher, D. C. *Sci* **1994**, *263*, 802.
(3)Tsien, R. Y. *Angew. Chem. Int. Ed. Engl.* **2009**, *48*, 5612.
(4)Chudakov, D. M.; Matz, M. V.; Lukyanov, S.; Lukyanov, K. A. *Physiol. Rev.* **2010**, *90*, 1103.
(5)Förster, T. *AnP* **1948**, *437*, 55.
(6)Siegel, R. M.; Chan, F. K.-M.; Zacharias, D. A.; Swofford, R.; Holmes, K. L.; Tsien, R. Y.; Lenardo, M. J. *Science Signaling* **2000**, *2000*, pl1.
(7)Betzig, E.; Patterson, G. H.; Sougrat, R.; Lindwasser, O. W.; Olenych, S.; Bonifacino, J. S.; Davidson, M. W.; Lippincott-Schwartz, J.; Hess, H. F. *Sci* **2006**, *313*, 1642.
(8)Rust, M. J.; Bates, M.; Zhuang, X. *Nat. Methods* **2006**, *3*, 793.
(9)Tsien, R. Y. *Annu. Rev. Biochem.* **1998**, *67*, 509.
(10)Lemay, N. P.; Morgan, A. L.; Archer, E. J.; Dickson, L. A.; Megley, C. M.; Zimmer, M. *Chem. Phys.* **2008**, *348*, 152.
(11)Heim, R.; Prasher, D. C.; Tsien, R. Y. *Proc. Natl. Acad. Sci. U. S. A.* **1994**, *91*, 12501.
(12)Kojima, S.; Ohkawa, H.; Hirano, T.; Maki, S.; Niwa, H.; Ohashi, M.; Inouye, S.; Tsuji, F. I. *Tetrahedron Lett.* **1998**, *39*, 5239.
(13)Litvinenko, K. L.; Webber, N. M.; Meech, S. R. *The Journal of Physical Chemistry A* **2003**, *107*, 2616.
(14)Litvinenko, K. L.; Webber, N. M.; Meech, S. R. *Chem. Phys. Lett.* **2001**, *346*, 47.
(15)Webber, N. M.; Litvinenko, K. L.; Meech, S. R. *The Journal of Physical Chemistry B* **2001**, *105*, 8036.
(16)Mandal, D.; Tahara, T.; Meech, S. R. *The Journal of Physical Chemistry B* **2003**, *108*, 1102.
(17)Liu, R. S. *Pure Appl. Chem.* **2002**, *74*, 1391.
(18)Martin, M. E.; Negri, F.; Olivucci, M. *J Am Chem Soc* **2004**, *126*, 5452.
(19)Toniolo, A.; Olsen, S.; Manohar, L.; Martinez, T. *Faraday Discuss.* **2004**, *127*, 149.
(20)Toniolo, A.; Granucci, G.; Martínez, T. J. *The Journal of Physical Chemistry A* **2003**, *107*, 3822.

(21)Conyard, J.; Addison, K.; Heisler, I. A.; Cnossen, A.; Browne, W. R.; Feringa, B. L.; Meech, S. R. *Nat Chem* **2012**, *advance online publication*.

(22)Kazaryan, A.; Kistemaker, J. C.; Schäfer, L. V.; Browne, W. R.; Feringa, B. L.; Filatov, M. *The Journal of Physical Chemistry A* **2010**, *114*, 5058.

(23)Quenneville, J.; Martínez, T. J. *The Journal of Physical Chemistry A* **2003**, *107*, 829.

(24)Brown, T. A.; Tkachuk, A. N.; Shtengel, G.; Kopek, B. G.; Bogenhagen, D. F.; Hess, H. F.; Clayton, D. A. *Mol. Cell. Biol.* **2011**, *31*, 4994.

(25)Marriott, G.; Mao, S.; Sakata, T.; Ran, J.; Jackson, D. K.; Petchprayoon, C.; Gomez, T. J.; Warp, E.; Tulyathan, O.; Aaron, H. L.; Isacoff, E. Y.; Yan, Y. *Proc. Natl. Acad. Sci. U. S. A.* **2008**, *105*, 17789.

(26)Hofmann, M.; Eggeling, C.; Jakobs, S.; Hell, S. W. *Proc. Natl. Acad. Sci. U. S. A.* **2005**, *102*, 17565.

(27)Lukyanov, K. A.; Chudakov, D. M.; Lukyanov, S.; Verkhusha, V. V. *Nat Rev Mol Cell Biol* **2005**, *6*, 885.

(28)Sauer, M. *Proc. Natl. Acad. Sci. U. S. A.* **2005**, *102*, 9433.

(29)Korpany, K. V.; Langat, P.; Kim, D. M.; Edelman, N.; Cooper, D. R.; Nadeau, J.; Blum, A. S. *J. Am. Chem. Soc.* **2012**, *134*, 16119.

(30)Ando, R.; Hama, H.; Yamamoto-Hino, M.; Mizuno, H.; Miyawaki, A. *Proc. Natl. Acad. Sci. U. S. A.* **2002**, *99*, 12651.

(31)Ando, R.; Mizuno, H.; Miyawaki, A. *Sci* **2004**, *306*, 1370.

(32)Stiel, A. C.; Trowitzsch, S.; Weber, G.; Andresen, M.; Eggeling, C.; Hell, S. W.; Jakobs, S.; Wahl, M. C. *Biochem. J.* **2007**, *402*, 35.

(33)Habuchi, S.; Dedecker, P.; Hotta, J.-i.; Flors, C.; Ando, R.; Mizuno, H.; Miyawaki, A.; Hofkens, J. *Photochemical & Photobiological Sciences* **2006**, *5*, 567.

(34)Habuchi, S.; Ando, R.; Dedecker, P.; Verheijen, W.; Mizuno, H.; Miyawaki, A.; Hofkens, J. *Proc. Natl. Acad. Sci. U. S. A.* **2005**, *102*, 9511.

(35)Andresen, M.; Stiel, A. C.; Trowitzsch, S.; Weber, G.; Eggeling, C.; Wahl, M. C.; Hell, S. W.; Jakobs, S. **2007**, *104*, 13005.

(36)Mizuno, H.; Kumar Mal, T.; Wälchli, M.; Kikuchi, A.; Fukano, T.; Ando, R.; Jeyakanthan, J.; Taka, J.; Shiro, Y.; Ikura, M.; Miyawaki, A. *Proceedings of the National Academy of Sciences*.

(37)Li, X.; Chung, L. W.; Mizuno, H.; Miyawaki, A.; Morokuma, K. *The Journal of Physical Chemistry Letters* **2010**, *1*, 3328.

(38)Nam, K.-H.; Kwon, O. Y.; Sugiyama, K.; Lee, W.-H.; Kim, Y. K.; Song, H. K.; Kim, E. E.; Park, S.-Y.; Jeon, H.; Hwang, K. Y. *Biochem. Biophys. Res. Commun.* **2007**, *354*, 962.

(39)Wilmann, P. G.; Turcic, K.; Battad, J. M.; Wilce, M. C. J.; Devenish, R. J.; Prescott, M.; Rossjohn, J. *J. Mol. Biol.* **2006**, *364*, 213.

(40)Schäfer, L. V.; Groenhof, G.; Boggio-Pasqua, M.; Robb, M. A.; Grubmüller, H. *PLoS Comput Biol* **2008**, *4*, e1000034.

(41)Sato, T.; Takahoko, M.; Okamoto, H. *Genesis* **2006**, *44*, 136.

(42)Tomura, M.; Yoshida, N.; Tanaka, J.; Karasawa, S.; Miwa, Y.; Miyawaki, A.; Kanagawa, O. *Proceedings of the National Academy of Sciences* **2008**, *105*, 10871.

(43)Fernández-Suárez, M.; Ting, A. Y. *Nature Reviews Molecular Cell Biology* **2008**, *9*, 929.

(44)Gould, T. J.; Gunewardene, M. S.; Gudheti, M. V.; Verkhusha, V. V.; Yin, S.-R.; Gosse, J. A.; Hess, S. T. *Nat. Methods* **2008**, *5*, 1027.

(45)McKinney, S. A.; Murphy, C. S.; Hazelwood, K. L.; Davidson, M. W.; Looger, L. L. *Nat. Methods* **2009**, *6*, 131.

(46)Mizuno, H.; Mal, T. K.; Tong, K. I.; Ando, R.; Furuta, T.; Ikura, M.; Miyawaki, A. *Mol. Cell* **2003**, *12*, 1051.

(47)Adam, V.; Lelimousin, M.; Boehme, S.; Desfonds, G.; Nienhaus, K.; Field, M. J.; Wiedenmann, J.; McSweeney, S.; Nienhaus, G. U.; Bourgeois, D. *Proceedings of the National Academy of Sciences* **2008**, *105*, 18343.

(48)Adam, V.; Moeyaert, B.; David, Charlotte C.; Mizuno, H.; Lelimousin, M.; Dedecker, P.; Ando, R.; Miyawaki, A.; Michiels, J.; Engelborghs, Y.; Hofkens, J. *Chem. Biol.* **2011**, *18*, 1241.

(49)Fuchs, J.; Böhme, S.; Oswald, F.; Hedde, P. N.; Krause, M.; Wiedenmann, J.; Nienhaus, G. U. *Nat. Methods* **2010**, *7*, 627.

(50)Lakowicz, J. R. *Principles of Fluorescence Spectroscopy*; Third edition ed.; Springer, 2006.

(51)Jabłoński, A. *ZPhy* **1935**, *94*, 38.

(52)Valeur, B.; Berberan-Santos, M. N. *Molecular fluorescence: principles and applications*; John Wiley & Sons, 2012.

(53)Mongin, O.; Porrès, L.; Moreaux, L.; Mertz, J.; Blanchard-Desce, M. *Org. Lett.* **2002**, *4*, 719.

(54)Parthenopoulos, D. A.; Rentzepis, P. M. *Science (New York, N.Y.)* **1989**, *245*, 843.

(55)Cumpston, B. H.; Ananthavel, S. P.; Barlow, S.; Dyer, D. L.; Ehrlich, J. E.; Erskine, L. L.; Heikal, A. A.; Kuebler, S. M.; Lee, I.-Y. S.; McCord-Maughon, D. *Natur* **1999**, *398*, 51.

(56)Bhawalkar, J.; Kumar, N.; Zhao, C.-F.; Prasad, P. *J. Clin. Laser Med. Surg.* **1997**, *15*, 201.

(57)Kasha, M. *Discuss. Faraday Soc.* **1950**, *9*, 14.

(58)Paul, A.; Mandal, P. K.; Samanta, A. *Chem. Phys. Lett.* **2005**, *402*, 375.

(59)Yoshizawa, T.; Wald, G. **1967**.

(60)Polli, D.; Altoè, P.; Weingart, O.; Spillane, K. M.; Manzoni, C.; Brida, D.; Tomasello, G.; Orlandi, G.; Kukura, P.; Mathies, R. A. *Natur* **2010**, *467*, 440.

(61)Yoshizawa, T.; Wald, G. **1963**.

(62)Garcia-Iriepa, C.; Marazzi, M.; Frutos, L. M.; Sampedro, D. *RSC Advances* **2013**, *3*, 6241.

(63)Levine, B. G.; Martínez, T. J. *Annu. Rev. Phys. Chem.* **2007**, *58*, 613.

(64)Levine, B. G.; Martínez, T. J. *Annu. Rev. Phys. Chem.* **2007**, *58*, 613.

(65)Domcke, W.; Yarkony, D. R. *Annu. Rev. Phys. Chem.* **2012**, *63*, 325.

(66)Yarkony, D. R. *Acc. Chem. Res.* **1998**, *31*, 511.

(67)Yarkony, D. R. *The Journal of Physical Chemistry A* **2001**, *105*, 6277.

(68)Robb, M. A.; Garavelli, M.; Olivucci, M.; Bernardi, F. *Rev. Comput. Chem.* **2000**, *15*, 87.

(69)Waldeck, D. H. *Chem. Rev.* **1991**, *91*, 415.

(70)Todd, D. C.; Jean, J. M.; Rosenthal, S. J.; Ruggiero, A. J.; Yang, D.; Fleming, G. R. *The Journal of Chemical Physics* **1990**, *93*, 8658.

(71)Kramers, H. A. *Phy* **1940**, *7*, 284.

(72)Meech, S. R. *Annual Reports Section "C" (Physical Chemistry)* **1990**, *87*, 199.

(73)Hynes, J. T. *Annu. Rev. Phys. Chem.* **1985**, *36*, 573.

(74)Bagchi, B.; Fleming, G. R.; Oxtoby, D. W. *The Journal of Chemical Physics* **1983**, *78*, 7375.

(75)Bagchi, B.; Fleming, G. R. *The Journal of Physical Chemistry* **1990**, *94*, 9.

(76)Haidekker, M. A.; Theodorakis, E. A. *Organic & biomolecular chemistry* **2007**, *5*, 1669.

(77)Sutharsan, J.; Lichlyter, D.; Wright, N. E.; Dakanali, M.; Haidekker, M. A.; Theodorakis, E. A. *Tetrahedron* **2010**, *66*, 2582.

(78)Allen, B. D.; Benniston, A. C.; Harriman, A.; Rostron, S. A.; Yu, C. *PCCP* **2005**, *7*, 3035.

(79)Jin, H.; Liang, M.; Arzhantsev, S.; Li, X.; Maroncelli, M. *The Journal of Physical Chemistry B* **2010**, *114*, 7565.

(80)Glasbeek, M.; Zhang, H. *Chem. Rev.* **2004**, *104*, 1929.

(81)Maroncelli, M.; Kumar, V. P.; Papazyan, A. *The Journal of Physical Chemistry* **1993**, *97*, 13.

(82)Horng, M. L.; Gardecki, J. A.; Papazyan, A.; Maroncelli, M. *The Journal of Physical Chemistry* **1995**, *99*, 17311.

(83)Hsu, C.-P.; Song, X.; Marcus, R. *The Journal of Physical Chemistry B* **1997**, *101*, 2546.

Chapter 2 - Experimental Methods, Analysis and Modelling

This chapter will describe the experimental methods used throughout this work. Firstly, a detailed description of the ultrafast fluorescence up-conversion experiment will be given (Section 2.1.). This will include a description of some of the main theoretical principles behind the experiment. Details of the extension of the up-conversion setup to two-photon excitation are described (Section 2.2.). A brief description of the transient absorption (Section 2.3.) and transient IR (TRIR) experiments is given (Section 2.4.). Data analysis procedures for the time-resolved fluorescence are also described (Section 2.5.). Finally, the theory underlying the model for simulating the excited state dynamics used in Chapter 7 is given (Section 2.6).

2.1. Ultrafast Fluorescence Up-conversion

Time-resolved fluorescence is used for studying the excited state dynamics of fluorophores, solvation dynamics, relaxation processes and vibrational cooling[1-10]. Fluorescence up-conversion is a powerful technique for studying dynamics which occur on the ultrafast timescale. This method involves the laser excitation of a sample and the subsequent time-resolved measurement of the fluorescence emission as the sample returns to the ground-state. Hence, only changes associated with the excited state are measured and the results are not complicated by ground-state contributions.

In order to measure the ultrafast dynamics of fluorescent excited states, the time gated frequency mixing technique is used. This method has been used since 1975, where picosecond time resolution was achieved[11]. Since then, the technique has been refined,

improving the time resolution, spectral range and width[10,12-14]. By using the laser pulse as a

gate, a time resolution comparable to the temporal width of the laser can be achieved[12,13].

The experimental setup used in this work is depicted in Figure 2.1. A Kerr lens mode locked

Ti:Sapphire laser (Coherent 10) driven by a continuous wave Nd:YLF laser operating at 532

nm produces a pulsed output centred around 800 nm with a bandwidth of 75 nm and a

temporal width of 20 fs, with a repetition rate of 76 MHz and a power of up to 1W. After the

laser, a prism compressor is used to compensate for dispersion of the pulse in order to

minimise its temporal width (Section2.1.2). The output is then focused onto a 50 μm thick

type 1 β-barium borate (BBO) crystal using a 150 mm focal length concave mirror, producing

the second harmonic with a power of up to 16 mW (Section 2.1.3.). A dichroic mirror

separates the fundamental (gate) beam and the second harmonic (pump) beam. Pairs of

chirped mirrors are used to further compensate for dispersive pulse broadening effects

(Section 2.1.2.). The pump is focused onto a 1mm cell with a 150 mm focal concave mirror,

exciting the sample. The fluorescence is then collected using a reflective microscope

objective with 15x magnification and focused onto a 100 μm type 1 BBO crystal (Section

2.1.4.). The gate is also focused onto the crystal and overlapped with the fluorescence spot.

Sum frequency generation (SFG) within the crystal produces a signal which is the sum of

both fluorescence and the gate frequencies (Section 2.1.3.). The sum frequency signal is

measured using a low-noise photon-counting PMT, where a monochromator and filters

(UG11 Schott and GG455 Schott) are used to minimise the background and scattered light

collected by the PMT (Section 2.1.4.). To minimise the scattering from the pump beam, a

GG455 Schott filter is placed directly after the microscope objective and a UG11 Schott filter

is placed over the entrance of the monochromator to ensure that only the upconverted

signal is detected.
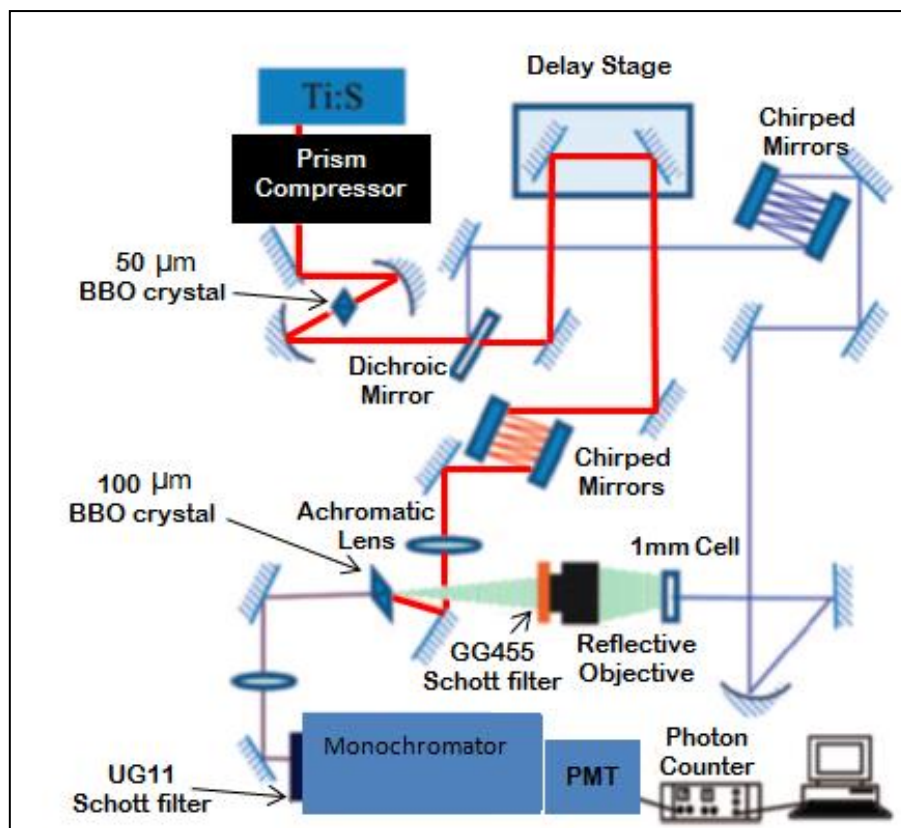
Figure 2.1. Schematic of the fluorescence up-conversion setup.

A delay stage with 0.1 µm resolution was used to introduce a pathlength difference

between the pump and gate pulses. The accuracy of the delay stage allows the pathlength

to be changed with sub-fs accuracy. The time resolution of the experiment is limited by the

widths of the pump and gate pulses. By measuring the cross correlation of the Raman

scattering of heptane (assumed to be instantaneous) at 475 nm the time resolution was

determined to be better than 50 fs (Figure 2.2).
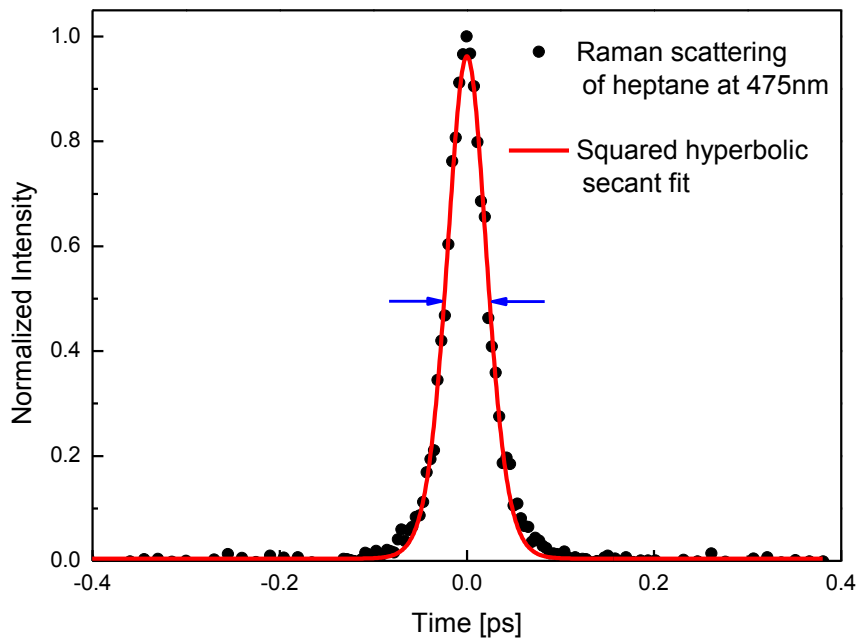
Figure 2.2. Cross correlation of the Raman scattering of heptane fitted with a hyperbolic

section function, giving a time resolution of better than 50 fs.

2.1.1. Laser and Mode locking

In a continuous wave laser, multiple longitudinal modes oscillate with random phases[15]. In

order to generate high intensity, short pulses a relationship between the phases of the

longitudinal modes must be created, this is known as mode locking (Figure 2.3). The more

modes that are locked, the higher the intensity of the pulse and the shorter the pulse

duration [16].
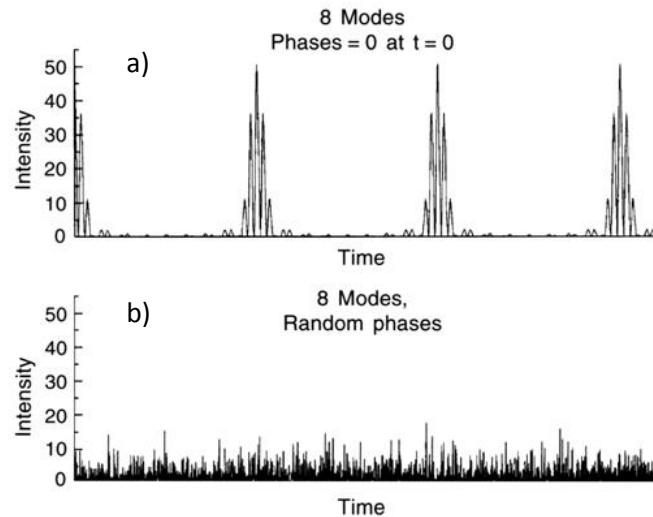
Figure 2.3. In continuous wave operation the longitudinal modes oscillate with random phases (b). In a mode locked laser the modes have a fixed phase relationship, generating a train of pulses (a)[17].

There are two types of mode locking, active and passive. The method used in the Ti:sapphire laser is Kerr-lens mode locking, a passive method[15]. The nonlinear refractive index of the Ti:sapphire crystal means that higher intensity light is focused more tightly. Therefore the centre of the beam will be more tightly focused than the periphery. As illustrated in Figure 2.4, additional optics can create better overlap between the returning high intensity beam and the Ti:sapphire crystal whilst removing the low intensity pulses. The higher intensity thus causes increased gain in the crystal. To initiate this self-focusing process, a high intensity noise spike is created by disturbing one of the mirrors in the laser cavity. This high intensity spike is amplified and produces a train of short stable pulses [15].
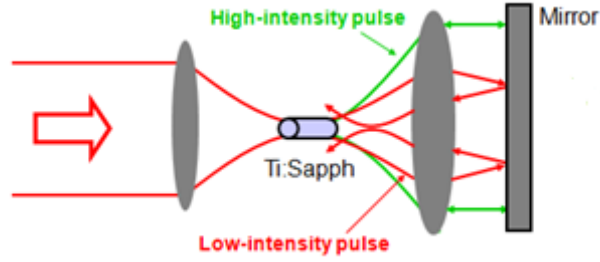
Figure 2.4. Self-focusing with a Ti:sapphire laser[17]. The high intensity pulses are focused back into the Kerr-medium, whilst the low-intensity pulses are filtered out.

2.1.2. Dispersion and Compression

The electric field of a plane, linearly polarized, monochromatic wave propagating in the z direction of a transparent medium can be written as

$$E(t,z) = A_0 e^{j(\omega t - k(\omega)z)} + \text{c.c} \tag{2.1}$$

where A_0 is a constant, and $k(\omega)$ is the phase constant (or wave vector) which describes the change in phase per meter along the path travelled by the wave and the phase is described by $\phi = (\omega t - k(\omega)z)$.

The phase velocity of the wave can be described in terms of the phase constant as follows,

$$v_{ph} = \frac{dz}{dt} = \frac{\omega}{k}. \tag{2.2}$$

For a pulse of light with centre frequency ω_c, width $\Delta\omega_c$, propagation constant k_c and using a linear dispersion law (which describes the variation of k with frequency), Equation 2.1 can be expanded and the electric field written as

$$E(t,z) = A\left(t - \frac{z}{v_g}\right)e^{j(\omega_c t - k_c z)} + c.c,$$ (2.3)

where v_g is the group velocity of the pulse [15]. Equation 2.3 implies that the pulse travels through a medium of length z at a speed v_g without changing its shape and experiences a group delay (τ_g),

$$\tau_g = \frac{l}{v_g}.$$ (2.4)

However two pulses with different centre frequencies will experience different group velocities, providing the gradient of their respective dispersion laws *(t – z/v_g)* from Equation 2.3 are different. Similarly, for a pulse with a large bandwidth, where the linear dispersion relationship breaks down, the different component frequencies of the pulse will have different group velocities. Hence the pulse broadens as it propagates and the pulse broadening due to dispersion ($\Delta\tau_d$) is given by,

$$\Delta\tau_d \cong l\left|\left(\frac{d^2 k}{d\omega^2}\right)_{\omega_c}\right|\Delta\omega_c,$$ (2.5)

where $\left(\frac{d^2 k}{d\omega^2}\right)_{\omega_c}$ is the group velocity dispersion (GVD) which is the pulse broadening per unit length of the medium per unit bandwidth. The group delay dispersion (GDD) is defined as the GVD multiplied by the length of dispersive material the beam traverses.

Thus, dispersion limits the minimum pulse width that can be achieved and in order to generate ultrashort pulses, which necessarily have a broad spectrum, this effect has to be carefully controlled. To balance dispersion in the up-conversion set up, prism compressors and chirped mirrors are used to introduce negative GDD and glass may be introduced to the beam for positive GDD.

As illustrated in Figure 2.5, negative GDD can be introduced using a four prism sequence. The lower frequency components of the input pulse propagate through more glass than the higher frequency components. Meaning that the lower frequency components are retarded whilst the higher frequency components are advanced with respect to the input pulse [18]. By controlling this effect through balancing positive and negative dispersion, pulses can be compressed.

Chirped mirrors have a coating composed of multiple dielectric layers (Figure 2.6), negative dispersion is introduced as the red components of the light are delayed because they travel deeper into the coating [19]. A major drawback of chirped mirrors is that they are wavelength specific. However they are much more compact than a prism compressor, which is convenient when trying to minimise the physical size of an experiment.
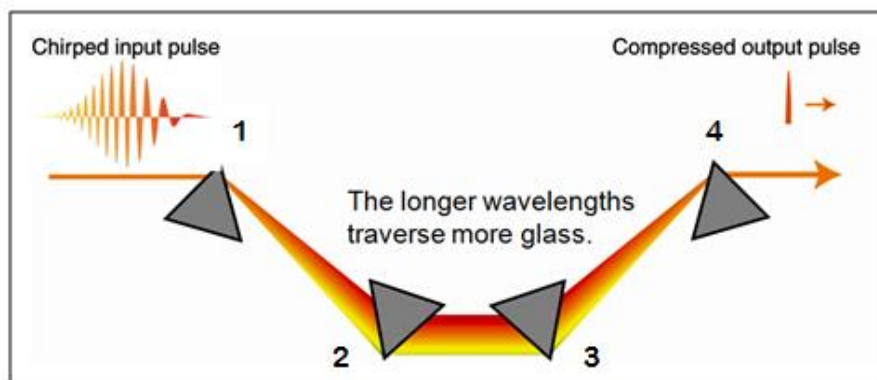
Figure 2.5. A four prism sequence introduces negative group delay dispersion. In the up-conversion set up a mirror is inserted between prisms 2 and 3 so only two prisms are needed[20].
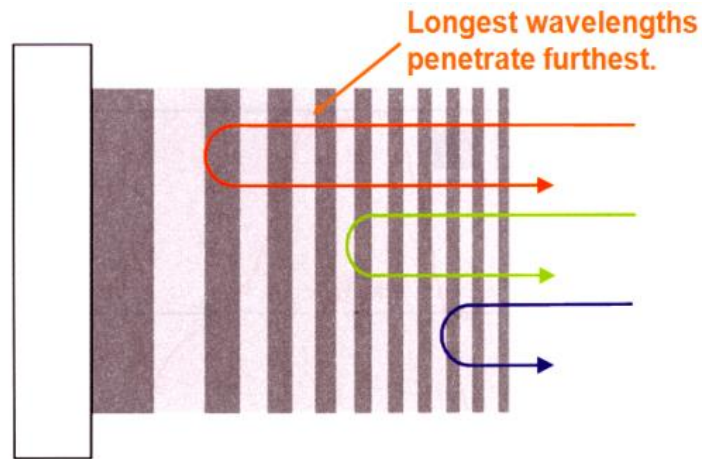
Figure 2.6. An illustration of a dielectric mirror used to introduce negative dispersion. The dielectric coating on chirped mirrors means that lower frequencies penetrate deeper[21].

2.1.3. Non-linear Optics

A material is optically non-linear if it has a non-linear response to the strength of an applied electric field. In linear optics the polarization (*P(t)*) of a material is given by

$$P(t) = \epsilon_0 \chi^{(1)} E(t), \tag{2.6}$$

where ϵ_0 is the permittivity of free space and $\chi^{(1)}$ is the linear susceptibility[17]. To describe non-linear optics equation 2.6 is expanded and written as the series,

$$P(t) = \epsilon_0 [\chi^{(1)} E(t) + \chi^{(2)} E^2(t) + \chi^{(3)} E^3(t) + \cdots], \tag{2.7}$$

where $\chi^{(2)}$ and $\chi^{(3)}$ are the second and third $-$ order non-linear susceptibilities respectively.

In the up-conversion setup a non-linear crystal which has a non-zero second order susceptibility is used to generate a second harmonic pulse. Such crystals are non-

centrosymmetric, and the absence of inversion symmetry is essential for a non-zero $\chi^{(2)}$.

The thickness of the crystal is minimised to reduce pulse broadening by dispersion (Section

2.1.2). If the incident laser beam is described as

$$E(t) = Ee^{-i\omega t} + E^* e^{i\omega t}, \qquad\qquad (2.8)$$

(a simplified expression of Equation 2.1) then the second order polarization will be

$$P^{(2)}(t) = 2\epsilon_0 \chi^{(2)} EE^* + \epsilon_0 \chi^{(2)}(E^2 e^{-2i\omega t} + E^{*2} e^{2i\omega t}). \qquad (2.9)$$

Equation 2.9 contains a zero frequency component and a doubled frequency component.

This double frequency component (second harmonic) becomes the excitation pulse in the

up-conversion experiment.

The second BBO crystal in the up-conversion setup is used for sum frequency generation.

The fluorescence and gate are overlapped on the crystal and the incoming beam can be

described as

$$E(t) = E_1 e^{-i\omega_1 t} + E_2 e^{-i\omega_2 t} + c.c, \qquad\qquad (2.10)$$

where ω_1 and ω_2 are the frequencies of the two pulses. The nonlinear polarization can be

expressed in the form

$$P^{(2)}(t) = \sum_n P(\omega_n) e^{-i\omega_n t}, \qquad\qquad (2.11)$$

where the components of the nonlinear polarization (which can describe second harmonic

generation (SHG),sum frequency generation (SFG), difference frequency generation (DFG)

or optical rectification (OR)) are given by [17],

$$P(2\omega_1) = \epsilon_0 \chi^{(2)} E_1^2 \qquad\qquad \text{(SHG)}, \qquad\qquad (2.12)$$

$$P(2\omega_2) = \epsilon_0 \chi^{(2)} E_2^2 \qquad \text{(SHG),} \qquad (2.13)$$

$$P(\omega_1 + \omega_2) = 2\epsilon_0 \chi^{(2)} E_1 E_2 \qquad \text{(SFG),} \qquad (2.14)$$

$$P(\omega_1 - \omega_2) = 2\epsilon_0 \chi^{(2)} E_1 E_2^* \qquad \text{(DFG),} \qquad (2.15)$$

$$P(0) = 2\epsilon_0 \chi^{(2)} (E_1 E_1^* + E_2 E_2^*) \qquad \text{(OR).} \qquad (2.16)$$

There are also corresponding negative frequency components arising from the complex conjugate. Generally one can choose which component to generate as there is a different phase matching condition for each [17]. For SHG, the wavevector mismatch is given by

$$\Delta k = k_2 - 2k_1 , \qquad (2.17)$$

where for perfect phase matching Δk = 0 and as Δk deviates from 0 the intensity of the second harmonic rapidly decreases. k is dependent on the refractive index (n) of the material [17],

$$k = \frac{n\omega}{2\pi c}. \qquad (2.18)$$

So for SHG the perfect phase matching condition $\Delta k = 0$ is,

$$n\omega_1 = n(2\omega_1). \qquad (2.19)$$

As shown in Figure 2.7 (left), this condition cannot be met under linear optical conditions, where n increases linearly with the frequency of incident light, due to normal dispersion[19]. However, this problem can be solved with the use of a birefringent crystal where the polarisation of the incident light determines the refractive index experienced. There are two refractive indices, ordinary (n_o) where the incident light is polarised perpendicular to the optical axis of the crystal and extraordinary (n_e) where the incident light is polarised parallel

to this axis. The BBO crystal used for SHG in this set up is a type 1 phase matching crystal. This means both photons have ordinary polarization. The phase matching condition can be satisfied (Figure 2.7 right) by tuning n_e which depends on the propagation angle through the crystal,

$$n_e\omega_1 = n_o(2\omega_1). \tag{2.20}$$

In the up-conversion setup the input polarization and crystal orientation are selected to enhance the intensity of the SHG and SFG components[17,22].
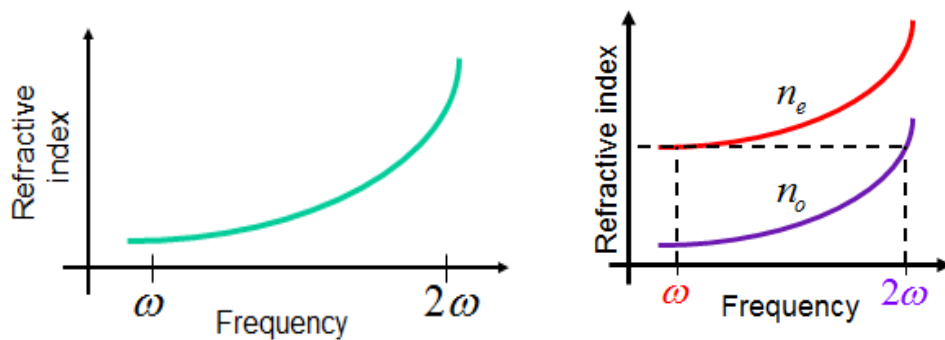
Figure 2.7. Left: The variation of refractive index with frequency for linear optics. Right: The variation of refractive index with frequency in a birefringent crystal[21].

2.1.4. Collection and Detection

The fluorescence is focused onto a 100 μm type 1 BBO crystal using a reflective microscope objective with 15x magnification. This method is ideal for up-conversion as it utilises a wide angle for collection of fluorescence and is completely reflective so does not introduce dispersion in the fluorescence before SHG.

The combination of a monochromator (Photon Technology International Model 101 resolution 2nm/mm spectral range 0-500nm), a Hamamatsu R585 PMT with a response range of 160-650nm and a photon counter (SR400 from Stanford Research Systems) are used to detect the up-converted signal. The monochromator is manually tuned to the desired up-conversion wavelength and the photon counter and delay stage are both controlled with LabVIEW software. As described in Section 2.1.1, filters are used to minimise the background noise.

2.2. Two-photon Up-conversion

A limitation of the single photon fluorescence up-conversion set up is that the lowest emission wavelength detectable is limited by the wavelength of the pump beam. Due to the broad spectral width of the 400 nm pump causing unwanted background signals due to up-converted scattered light, the bluest wavelength measureable is approximately 455 nm. However, using two-photon excitation it is possible to measure shorter wavelength emission. The single photon up-conversion apparatus can be modified by removing the second harmonic generating BBO crystal. The beam is split and one 800 nm pulse is used for sample excitation. Hence, the GG455 filter used to remove unwanted 400 nm excitation light is not required. A sample which is promoted to the first excited state through absorption of a single 400 nm photon can sometimes be excited via the absorption of two 800 nm photons. This is a non-linear optical process, which depends on the square of the intensity of the 800 nm excitation light (Section 2.1.3). The probability of this process, and hence the signal intensity, is dependent upon the two-photon absorption cross section of the sample.

It has been shown that the theoretical time resolution which can be attained using this set up is better by a factor of $\sqrt{2}$ for 2 photon excitation compared to 1 photon excitation as the SHG crystal can be removed[23,24]. Kim and Joo achieved a time resolution of 33 fs with a 100 µm BBO crystal for SFG and 40 fs with a 580 µm crystal[24]. Using the set up shown in Figure 2.8, a time resolution of 32 fs was achieved using a 100 µm BBO crystal. The cross correlation from the scattering of 800 nm light from paper and an example measurement of HBDI in methanol is shown in Figure 2.9.
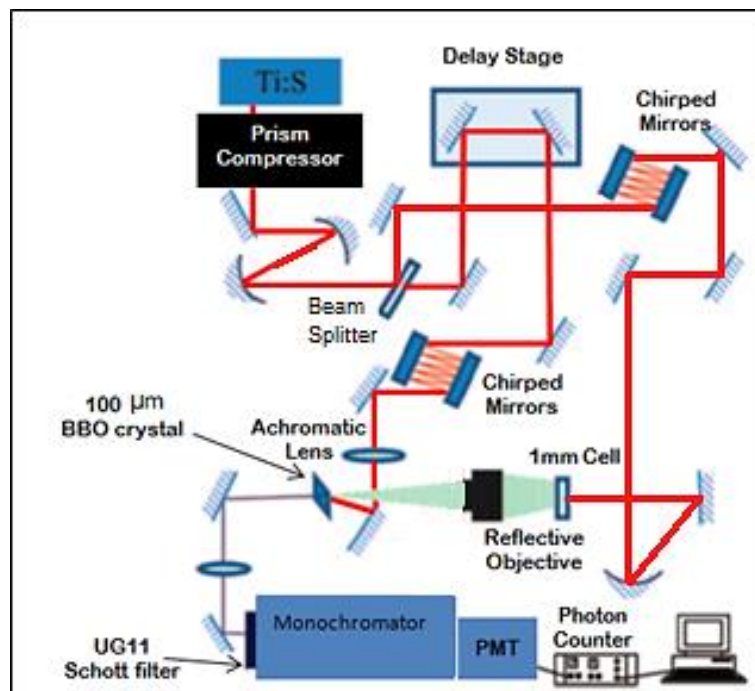
Figure 2.8. Schematic of the 2 photon up-conversion set up.
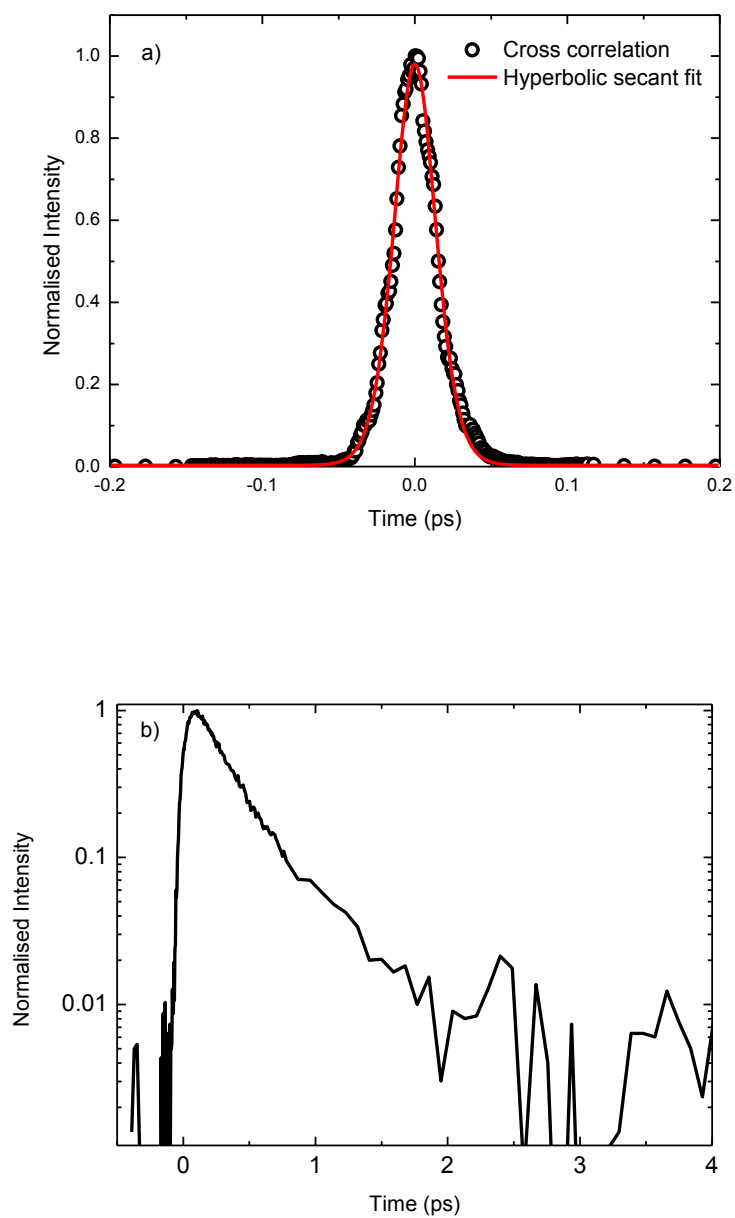
Figure 2.9. (a) Cross correlation from the Raman scattering of heptane. (b) An example fluorescence decay of HBDI in methanol measured by two-photon up-conversion.

2.3. Transient Absorption

Figure 2.10 shows the experimental set up for ultrafast transient absorption. A Clark MXR NJA-5 titanium sapphire laser produces a 300 mW 50 fs pulsed output at 100 MHz. This seeds a Clark- MXR ORC-1000 regenerative amplifier with a repetition rate of 1 KHz, producing 350 μJ pulses centred around 800 nm. This passes through a 90:10 beam splitter. The 10% beam passes through a half wave plate which sets the polarization of the pump beam to the magic angle relative to the pump. Thus removing the contribution due to molecular reorientation[25]. The 10% beam is then focused onto a CaF_2 window which generates a white light continuum stretching over the range 420 nm – 700 nm. The 90% beam is focused onto a 50 μm type I BBO crystal to generate the second harmonic pump beam at 400 nm. After the SHG crystal, a Schott BG400 filter removes the residual fundamental (800 nm) light. The pump beam then passes through a delay stage which is used to vary the path length of the pump relative to the probe, thus enabling time-resolved measurements. Both beams are then focused onto a 1mm quartz cell containing the sample. A chopper set at half the repetition rate of the amplifier (500 Hz) is used to block every other pump pulse. This allows the measurement of the sample transmission with and without a pump beam. Typically data are presented as pump-on minus pump-off difference spectra. The transmitted probe passes through a Jobin Yvon 270M spectrometer and is then detected by a CCD camera. A synchronised shutter is used to block the amplifier output after each cycle to determine the background noise.
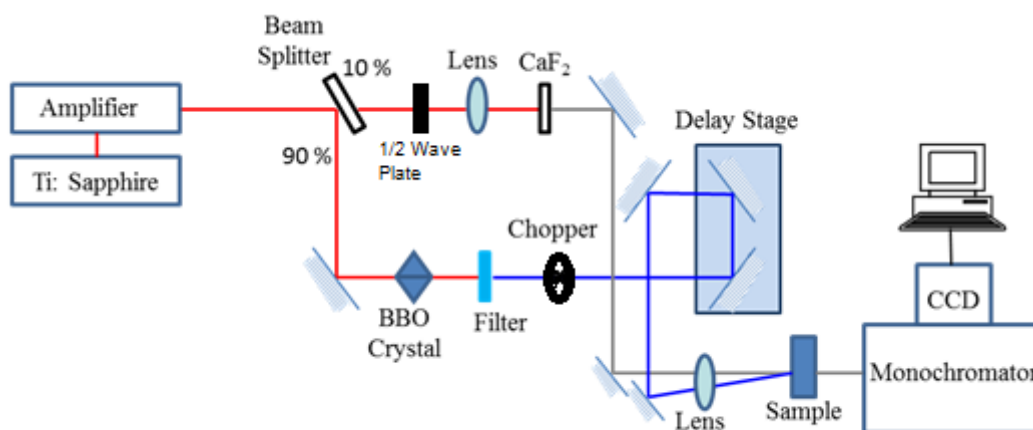
Figure 2.10. Schematic of the transient absorption setup[26].

Transient absorption spectroscopy provides information on both the ground and excited states of molecules. Furthermore, unlike fluorescence spectroscopy, it can also reveal the presence of dark (non-emissive) excited states. The negative peaks in Figure 2.11 (bleaches) indicate ground-state depletion or stimulated emission, while the positive peaks (transients) indicate the population of excited states. The example measurement is shown in Figure 2.11 for the Kaede chromophore in methanol from 8 to 344 ps. The ground-state bleach is located around 450 nm and the excited state at 620 nm.
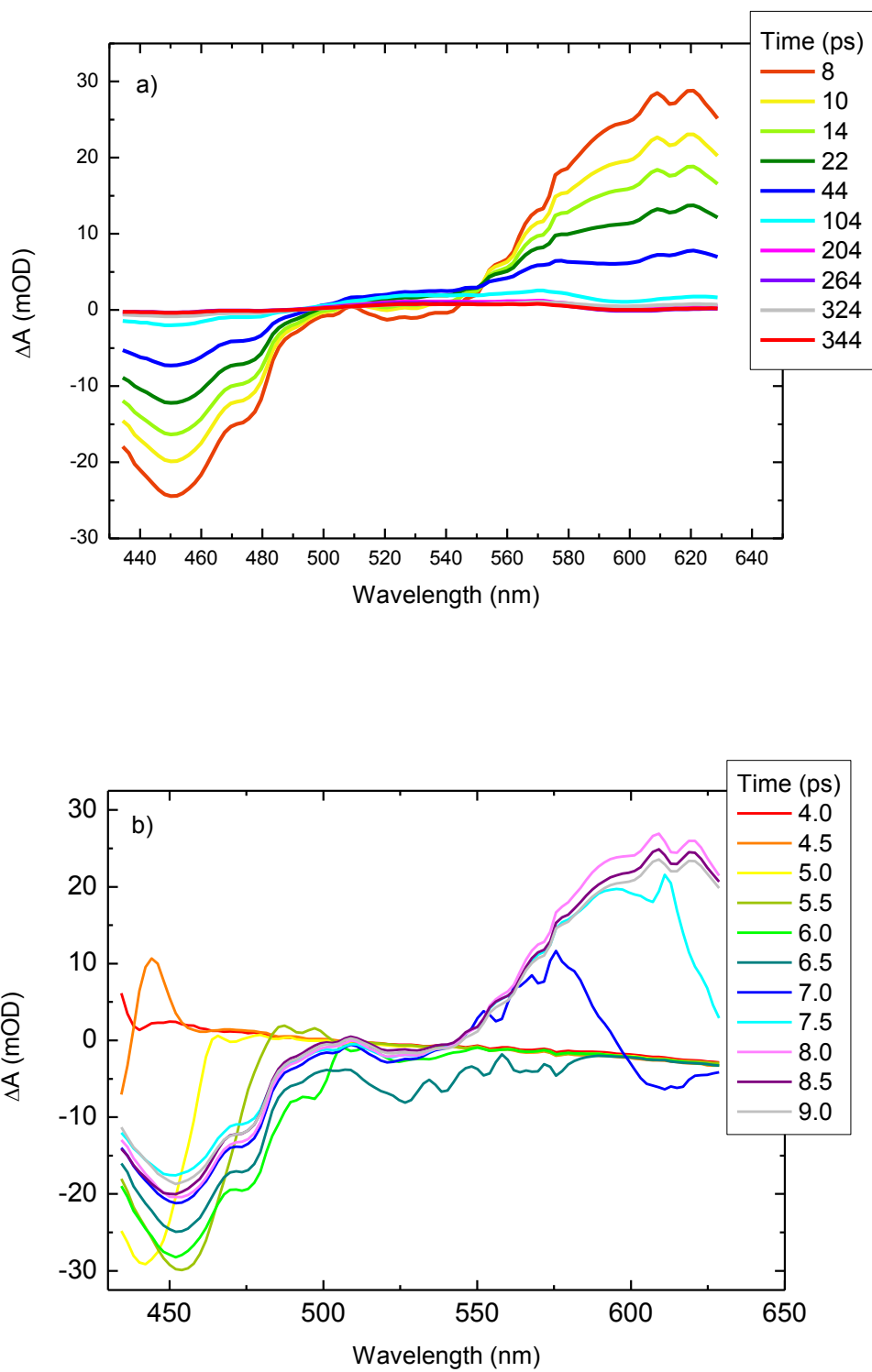
Figure 2.11. Ultrafast transient absorption spectra of the Kaede chromophore in methanol after removal of the coherent artefact (a) and before (b).

The kinetics for a particular wavelength can be extracted, as shown in Figure 2.12 for the ground-state bleach at 450 nm. The decays are fitted using the same procedure which will be described for the fluorescence measurements (Section 2.5.1). However, in this case the IRF is 300 fs, as determined by autocorrelation between the fundamental and second harmonic beams.
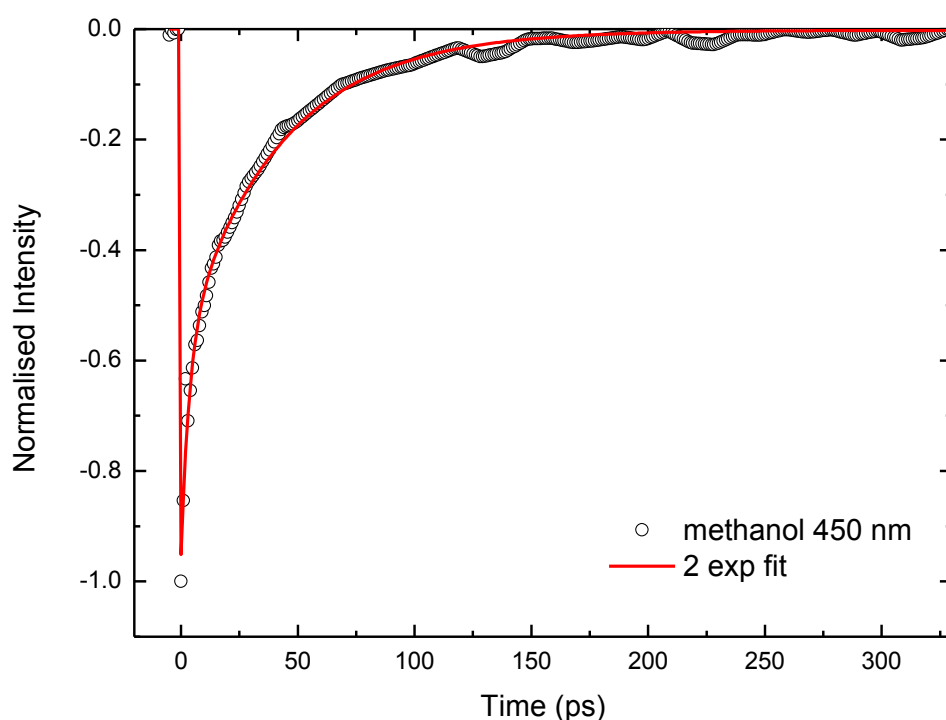
Figure 2.12. Kinetic of the Kaede chromophore in methanol at 450 nm (ground-state bleach). These data were fitted with a bi exponential function with time constants of 41.8 and 3.6 ps with an average lifetime of 26.3 ps.

A key part of analysis of the transient absorption data is the treatment of the coherent artefact (Figure 2.11 b). The high intensity pump pulse creates a non-linear optical response in the silica window and solvent. This produces a signal known as the coherent artefact,

which strongly distorts the measurement around time zero. Due to the frequency dependence of the non-linear response, the artefact propagates through the spectra and is no longer present after 8 ps. There is no standard procedure for subtraction of the artefact. Hence to ensure that the spectrum is not distorted by the artefact or by its incorrect removal, any measurement where the artefact is present is removed i.e. all measurements before 8 ps. For the transient absorption measurements, the error for individual kinetics was shown to be 11 %[26].

2.4. Time-resolved Infrared Spectroscopy

The time-resolved infrared spectroscopy (TRIR) system was used at the Central Laser Facility at the Rutherford Appleton Laboratory and has been described in detail elsewhere[27]. However, a brief description will be given in this section for completeness. An ultrafast laser with a 10 kHz repetition rate and 100 fs time resolution was used. The excitation wavelength was 450 nm, with a spot size of 100 μm and a pulse energy of 200 nJ. The IR probe transmission was measured as a function of delay time after the pump pulse to cover the range 500 fs to 2 ns. The polarization angle between the pump and probe was set to the magic angle to negate the effects of molecular orientation. The spectra are detected using two 128 pixel detectors, with a resolution of 3 cm^{-1} per pixel. For these measurements, the spectral window was 1270 to 1886 cm^{-1}.

TRIR difference spectroscopy provides both kinetic and structural information. The negative peaks (bleaches) indicate the depopulation of states absorbing the IR probe, while positive peaks (transients) indicate the population of transient or product states. The peaks can be

assigned to particular vibrational modes. In a number of cases DFT calculations using Gaussian can be used as an aid to assignment[28].

The data are collected, converted to absorption and then the difference calculated. The processed spectra have to be converted from pixel number to wavenumber. This is achieved using the measured IR transmission spectrum of *cis*-stilbene, where the peak positions are known, to create a calibration file. An example measurement is presented in Figure 2.13 for the GFP chromophore HBDI in methanol, showing the evolution of the spectra from 300 fs to 10 ps with the spectral features assigned.
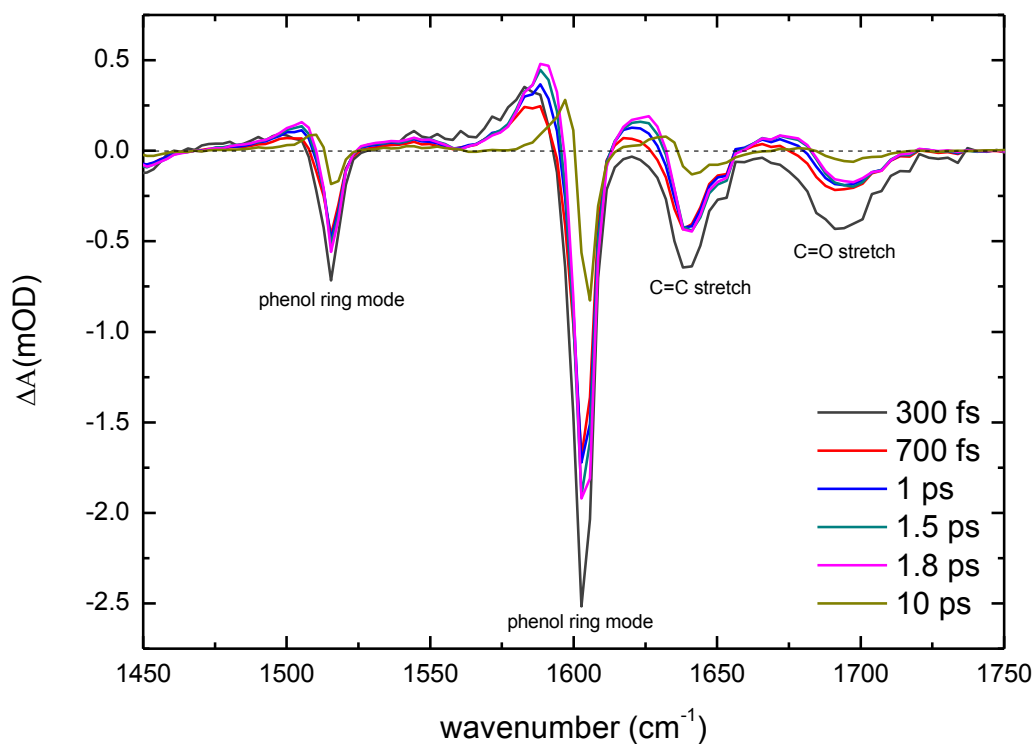
Figure 2.13. TRIR spectra HBDI in methanol from 300 fs to 10 ps.

Once peaks of interest are identified, the kinetics can be extracted. These are then fitted with a sum of exponentials function using the procedure which will be described for the time-resolved fluorescence in Section 2.5.1. Figure 2.14 shows a fit for HBDI at the main bleach (1602 cm^{-1}). These data were fitted with a single exponential function, giving a time constant of 6.9 ± 0.5 ps.
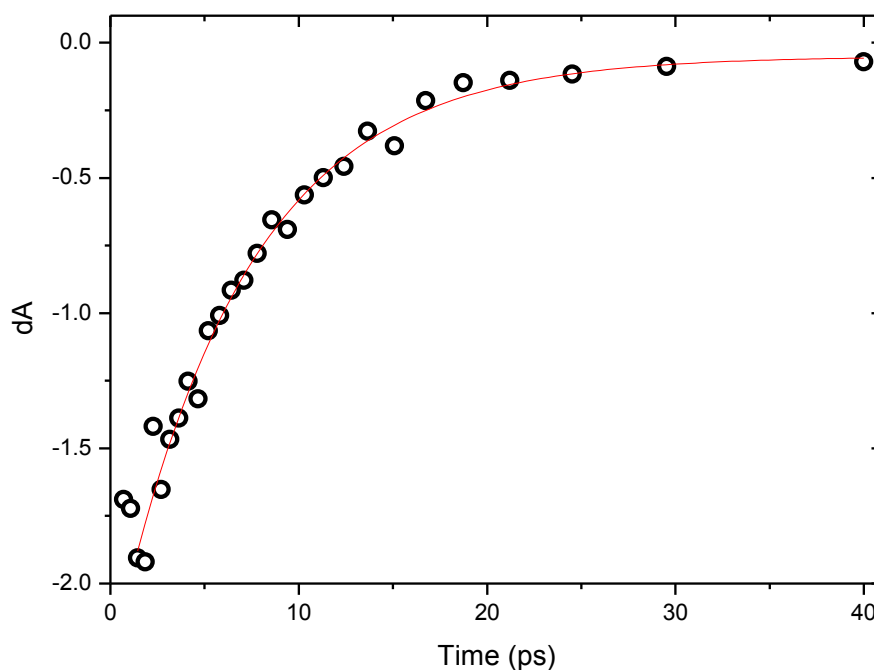
Figure 2.14. Kinetics of the 1602 cm^{-1} ground-state bleach of HBDI (circles) fitted to a single exponential (red).

2.5. Data Analysis

2.5.1. Fluorescence Measurements

As measured, the time-resolved fluorescence data are convoluted with the instrument response function (IRF)[14,29]. This distorts the data and therefore the information which can be obtained by fitting them. This distortion can be removed by deconvolution. The IRF for up-conversion data can be determined from the instantaneous up-converted Raman scattering (Figure 2.2) and is incorporated into the LabVIEW data fitting algorithm used. Here the IRF and measurement are deconvoluted, then the deconvoluted kinetics are fitted with the desired function. The convoluted kinetics are described with the following function,

$$I(t) = \int_{-\infty}^{t} E(t - t')R(t')dt', \qquad (2.21)$$

where the IRF is given by $R(t')$, $I(t)$ is the experimentally measured signal and $E(t - t')$ is the actual response of the sample [30]. To obtain the true deconvoluted kinetics, $I(t)$ can be fitted with a function $f(t)$ which is then convoluted with $R(t')$ to create a fit $F(t)$ which is compared to the measured $I(t)$. In this work all data were fitted with a sum of exponentials,

$$F(t) = \int_{-\infty}^{t} R(t') \sum_{i=1}^{n} a_i e^{-\frac{(t-t')}{\tau_i}} dt', \qquad (2.22)$$

where a_i and τ_i correspond to the amplitude and time constant of the ith exponential component. An evolutionary fitting algorithm is used to fit $F(t)$ to $I(t)$, where the best fit is generated by reducing the least squares error in the difference between the measured and fitted kinetics[31,32]. The user inputs the upper and lower limits of the time constants and a set of random fitting parameters is generated, where the quality of the fit is evaluated on each run and a new set of parameters are generated until the errors converge.

An example of a measured decay for the molecular motor DCVJ (Chapter 1) with the IRF and convoluted fit is shown in Figure 2.15. This was fitted with 2 exponentials and a rising exponential (exponential with a negative amplitude).
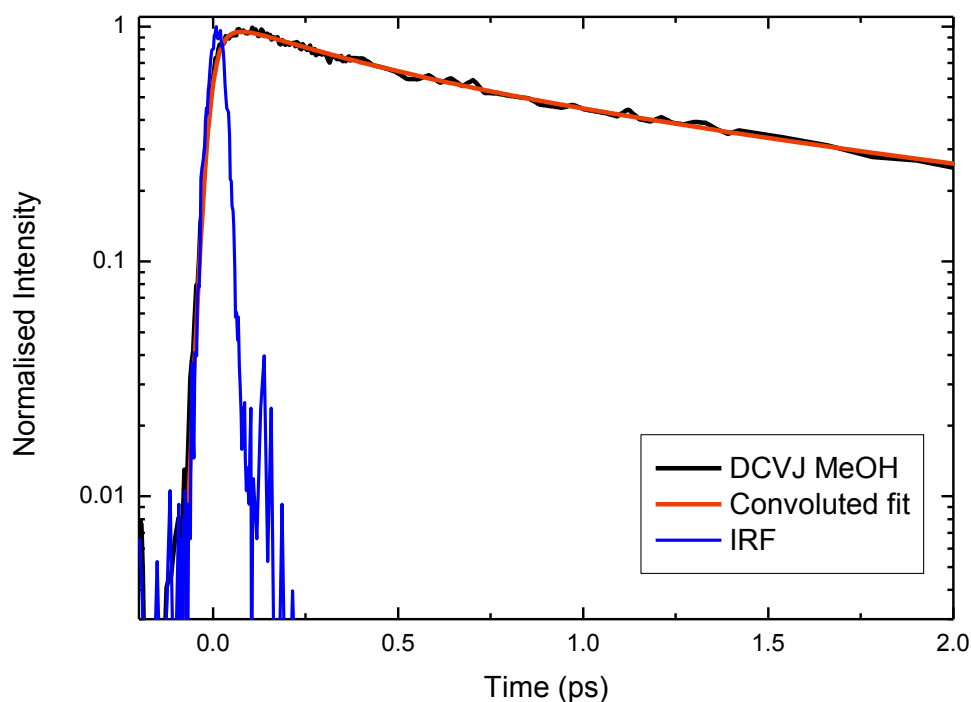
Figure 2.15. Time-resolved fluorescence decay of DCVJ in methanol.

2.5.2. Time-resolved Fluorescence Spectrum

Each up-conversion measurement reveals the kinetics at a single fluorescence wavelength. Time-resolved emission spectra ($S(\lambda, t)$) can be created by compiling measurements at several wavelengths across the emission spectrum (Figure 2.16)[29], to generate:

$$S(\lambda, t) = \frac{E(\lambda,t)S_0(\lambda)}{\int_0^\infty E(\lambda,t)dt},$$

(2.23)

where $E(\lambda, t)$ is the deconvoluted profile and $S_0(\lambda)$ is the steady-state intensity. Thus, the area under each individual decay has been normalised to the intensity of the steady-state spectrum to create a 3 dimensional intensity-time-wavelength surface. After constructing the surface, spectra at individual times can be selected to show the spectral evolution. The individual spectra may then be fitted to a log normal function as this accurately reproduces the shape of the spectrum, and provides a convenient function for further analysis. The log-normal is:

$$F(v, t) = h \left(e^{-\ln(2)\left[\frac{\ln(1+\alpha)}{\gamma}\right]^2} \right), \qquad (2.24)$$

where $\alpha = \frac{2\gamma(v-v_p)}{\Delta}$, h represents the amplitude, γ the asymmetry, Δ the width and v_p the peak wavenumber. Figure 2.17 shows the fluorescence spectrum of DCVJ from 50 fs to 12 ps. A rise over the first 150 fs is observed with a red shifting and narrowing of the spectrum, typical of polar solvent reorganisation[31,33].
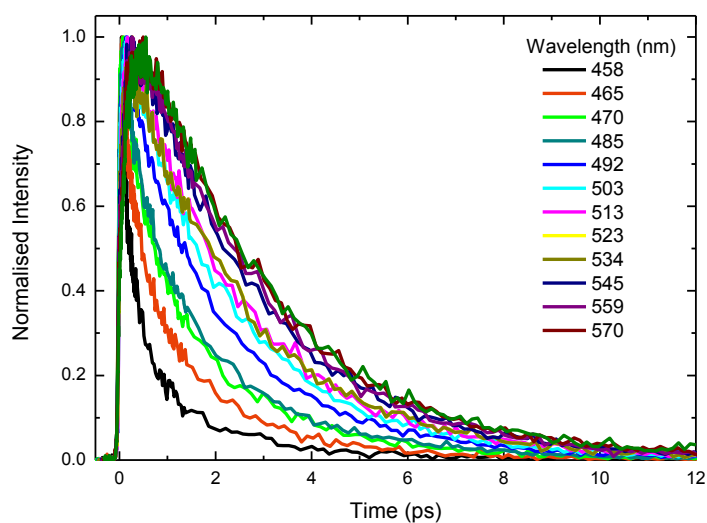
Figure 2.16. Multiple fluorescence decays, measured at wavelengths across the DCVJ

steady-state spectrum The fast decay on the blue edge and fast rise in the red are

characteristic of a red shift with time after excitation.
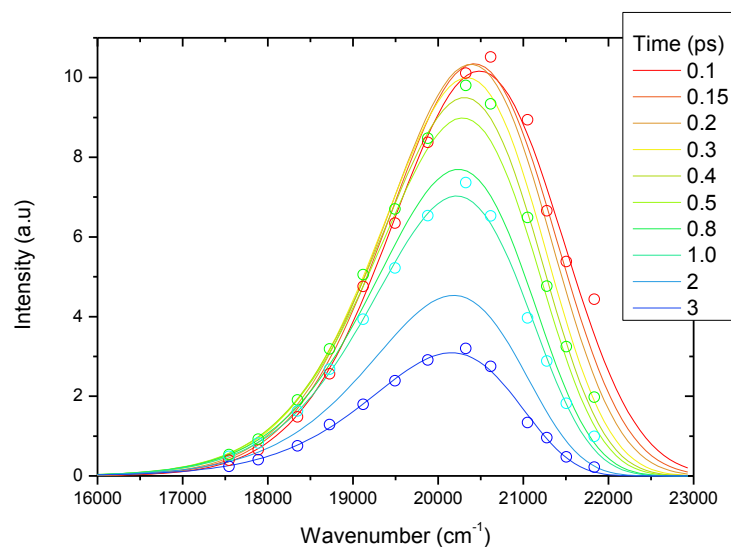
Figure 2.17. Reconstructed fluorescence spectrum of DCVJ in methanol from 100 fs (red) to

3 ps (dark blue). The measured data points at 100 fs (red), 400 fs (green), 1 ps (cyan) and 3

ps (dark blue) are shown as circles.

These spectral changes can be quantified in terms of the first moment ($\bar{v}(t)$), integrated area ($I(t)$) and FWHM ($\Gamma(t)$) of the log normal:

$$\bar{v}(t) = v_p(t) + \left(\frac{\Delta(t)}{2\gamma(t)}\right)\left[e^{\left(\frac{3\gamma(t)^2}{4\ln(2)}\right)} - 1\right], \tag{2.25}$$

$$I(t) = \left(\frac{\pi}{4\ln(2)}\right)^{\frac{1}{2}} h(t)\Delta(t)e^{\left(\frac{\gamma^2}{4\ln(2)}\right)}, \tag{2.26}$$

$$\Gamma(t) = \Delta(t)\left(\frac{\sinh(\gamma(t))}{\gamma(t)}\right), \tag{2.27}$$

where these functions are graphically illustrated in Figure 2.18[31]. The first moment describes the average wavelength of the spectrum and therefore quantifies the spectral shift. The integrated area and FWHM describe the rate of population decay of the excited state and the dispersion of the population, respectively.

Figure 2.18 a illustrates the time dependence of the first moment, showing a red shift of approximately 800 cm^{-1} over the first few picoseconds. This is accompanied by a spectral narrowing of approximately 600 cm^{-1} (Figure 2.18 c). Figure 2.18 b shows a linear plot of the log of the integrated intensity against time. Therefore the behaviour of the total fluorescence decay can be described to a good approximation by a single exponential.
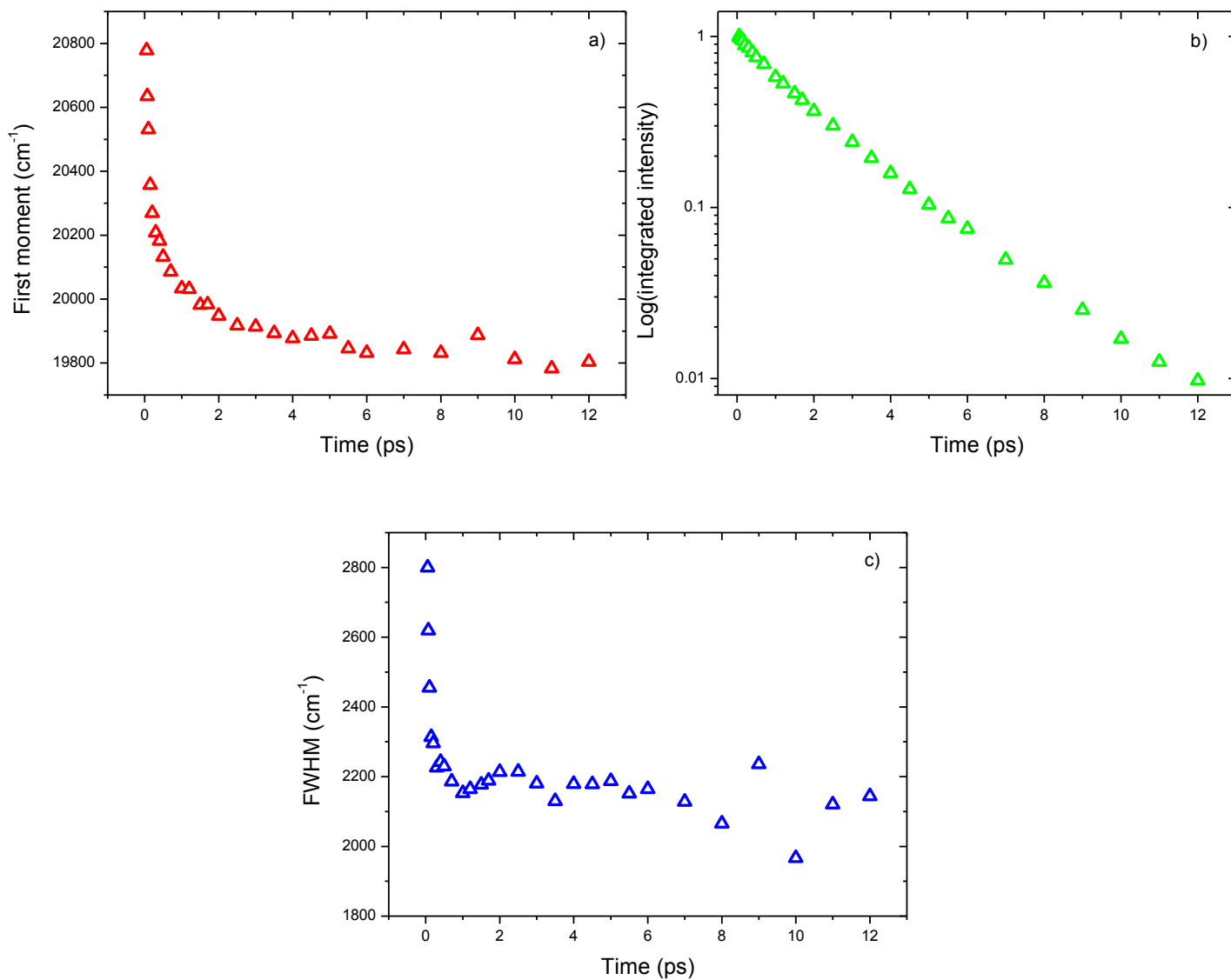
Figure 2.18. a) First moment b) integrated intensity c) FWHM of the time-resolved

fluorescence spectrum of DCVJ in methanol.

The errors on the up-conversion measurements were calculated by determining the error

from both repeated fits to the same measurement and also by fitting repeated

measurements of the same sample. Using this procedure (for some measurements on the

GFP chromophore (Chapter 3)) the error was less than 11%.

2.6. Excited State Modelling

This section describes the theoretical aspects of the model used to investigate the excited

state dynamics of HBDI and a kindling fluorescent protein-like chromophore (Chapter 6).

The path followed by an excited state population back to the ground-state is determined by

the potential energy surfaces (Chapter 1) but these are typically unknown. Individual decays

measured by ultrafast up-conversion can be constructed to produce a time-resolved

spectrum (Section 2.5.2.). If the forms of the potential energy surfaces are known or can be

modelled, it is possible to simulate the time-resolved spectra. These spectra can then be

compared with experimental results to gain insights into the excited state dynamics on the

reactive potential energy surface of the molecule.

The model used in this work is based on the Bagchi-Fleming-Oxtoby (BFO) theory which

describes the relaxation of excited states in solution with no activation barrier (Chapter 1)[34].

The time-dependent spectra are modelled using a generalised Smoluchowski equation. The

Smoluchowski equation describes the evolution of a population density $\rho(z,t)$ along a

reaction coordinate (z) for a particular potential energy surface (S_1) and diffusion coefficient

$D(t)$[34-37].

$$\frac{\partial}{\partial t}\rho(z,t) = D(t)\frac{\partial}{\partial z}\left(\frac{\partial}{\partial z} + \frac{1}{k_B T}\frac{\partial}{\partial z}S_1(z)\right)\rho(z,t) - k\Gamma(z)\rho(z,t). \tag{2.28}$$

The first term describes diffusive motion on the PES, whilst the last term allows nonradiative

decay back to the ground-state with a rate coefficient k via 'sink' functions $\Gamma(z)$. The rate of

nonradiative decay in this model can be varied along the reaction coordinate. In general in

this work the reaction coordinate is some torsional or pyramidalization coordinate and the $\Gamma(z)$ is a Gaussian function described by,

$$\Gamma(z) = k_{G1}\frac{1}{\sqrt{\pi}\sigma_1}e^{-\left[\frac{(z-z_{01})}{\sigma_1}\right]^2} + k_{G2}\frac{1}{\sqrt{\pi}\sigma_2}e^{-\left[\frac{(z-z_{02})}{\sigma_2}\right]^2},$$ (2.29)

where k_{G1} and k_{G2} are the amplitudes, σ_1 and σ_2 are the widths and z_{01} and z_{02} are the centres of the sinks connecting excited and ground-states; for simplicity we have set $k_{G1} = k_{G2}$, $\sigma_1 = \sigma_2$ and $z_{01} = z_{02}$. The form of the sinks is shown in Figure 2.19 where two sinks are required to allow decay following torsion in either direction. The z position of the sinks is set to correspond to the maximum twist angle as it has been shown that nonradiative decay is enhanced in nonplanar chromophores[7].

In previous work, the parameters of equation 2.28 were set by hand and $\rho(z,t)$ was calculated in Matlab before being loaded into LabVIEW where the time-dependent fluorescence spectra were created and compared to experimental data[38]. This procedure was repeated until a reasonable fit was achieved. However, to improve the accuracy of the simulations in this work, an evolutionary fitting algorithm was incorporated into the LabVIEW program. For a given pair (ground and excited states) of PESs, $\rho(z,t)$ is calculated in Matlab by solving equation 2.28 for a given $S_1(z)$ and $D(t)$ and choice of $\Gamma(z)$. Then the time-dependent fluorescence spectra are created in labVIEW following the procedure described below. The time-dependent fluorescence spectra can be calculated from[39,40],

$$I_{fl} \propto \int dz\, g(v_0(z), v(z) - v_0(z))M^2(z)\rho(z,t)v^3$$ (2.30)

and the absorption spectrum described by,

$$I_A \propto \int dz\, g(v_0(z), v(z) - v_0(z))M^2(z)\rho(z,0),$$ (2.31)

where $g(v_0(z), v(z) - v_0(z))$ is a line shape function describing the Franck-Condon factor, which is given by the log-normal function which accurately reproduces the shape of the emission spectrum (Section 2.5.2), $v_0(z)$ is the energy gap between the ground-state and the first excited state. The first measured fluorescence spectrum (t = 50 fs) and the measured absorption spectrum are fitted to the corresponding calculated fluorescence spectrum and the calculated absorption spectrum. v_0 is varied to raise or lower the S_1 energy, shifting the absorption and fluorescence spectra. The positions of the absorption and emission spectra are given by $x_a = v - v_0 - v_1$ and $x_f = v - v_0 + v_1$ respectively. v_1 is varied to change the separation between the absorption and fluorescence.

The transition moment ($M(z)$) in equation 2.30 is given by the matrix element,

$$M(z) = \langle \psi_{S1} | \mu | \psi_{S0} \rangle, \tag{2.33}$$

where μ is the dipole moment operator. $M^2(z)$ gives the probability of the transition, in this case from the first excited state to the ground-state. As the molecule's structure distorts during the excited state, its transition moment to the ground-state will reduce. In this model an inverse tangent function is used to represent the dependence of the transition moment on z, such that the twisted state becomes a dark state i.e. the probability of the transition is zero:

$$M^2(z) = -\operatorname{atan}\big(a(z - b)\big) - \operatorname{atan}(a(z + b)). \tag{2.34}$$

An evolutionary fitting algorithm is used to vary the sink parameters to obtain fits to measured data, where a satisfactory fit is achieved when the errors converge.

Figure 2.19 illustrates the main model parameters showing the energy of the S_0 and S_1

potential energy surfaces as a function of the reaction coordinate and the form of the

transition moment and sink function.
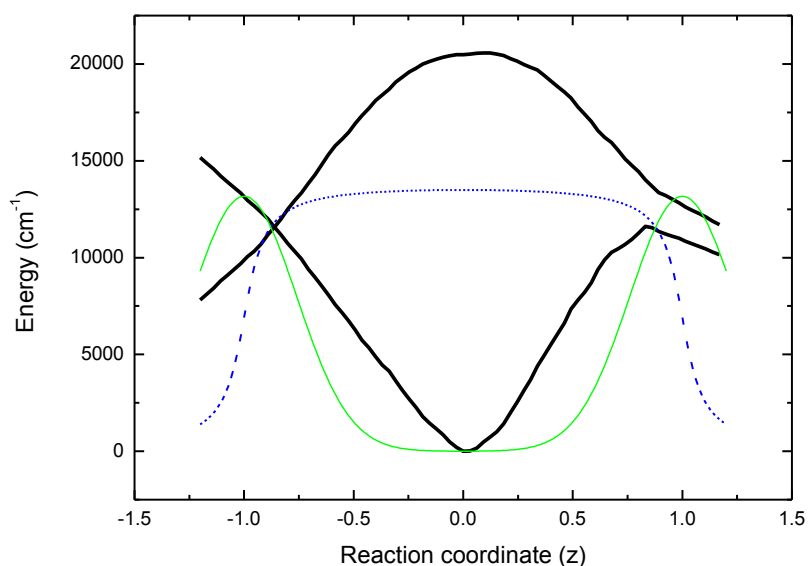
Figure 2.19 S_0 and S_1 potential energy surfaces of anionic HBDI as a function of reaction

coordinate (black), where 1.0 corresponds to a 90° twist of the bridge bonds. The transition

moment is shown in blue and the sink function in green.

The diffusion constant in Equation 2.28 can in general be time-dependent[38]. However, in

this model a time-independent diffusion coefficient of the form,

$$D = \frac{k_B T}{6\eta V} \tag{2.35}$$

is used, in which η is the solvent viscosity and V is the volume of the rotating group.

Details of the application of this model to understand the dynamics of FP chromophores will

be presented in Chapter 6.

2.7. References

(1)Gustavsson, T.; Baldacchino, G.; Mialocq, J. C.; Pommeret, S. *Chem. Phys. Lett.* **1995**, *236*, 587.
(2)Jimenez, R.; Fleming, G. R.; Kumari, P.; Maroncellll, M. *Natur* **1994**, *369*, 9.
(3)Zhang, L.; Kao, Y.-T.; Qiu, W.; Wang, L.; Zhong, D. *The Journal of Physical Chemistry B* **2006**, *110*, 18097.
(4)Qiu, W.; Zhang, L.; Okobiah, O.; Yang, Y.; Wang, L.; Zhong, D.; Zewail, A. H. *The Journal of Physical Chemistry B* **2006**, *110*, 10540.
(5)Addison, K.; Conyard, J.; Dixon, T.; Bulman Page, P. C.; Solntsev, K. M.; Meech, S. R. *The Journal of Physical Chemistry Letters* **2012**, *3*, 2298.
(6)Addison, K.; Heisler, I. A.; Conyard, J.; Dixon, T.; Bulman Page, P. C.; Meech, S. R. *Faraday Discuss.* **2013**.
(7)Conyard, J.; Kondo, M.; Heisler, I. A.; Jones, G.; Baldridge, A.; Tolbert, L. M.; Solntsev, K. M.; Meech, S. R. *The Journal of Physical Chemistry B* **2011**, *115*, 1571.
(8)Conyard, J.; Addison, K.; Heisler, I. A.; Cnossen, A.; Browne, W. R.; Feringa, B. L.; Meech, S. R. *Nat Chem* **2012**, *advance online publication*.
(9)Zgrablić, G.; Voïtchovsky, K.; Kindermann, M.; Haacke, S.; Chergui, M. *Biophys. J.* **2005**, *88*, 2779.
(10)Cannizzo, A.; Bräm, O.; Zgrablic, G.; Tortschanoff, A.; Oskouei, A. A.; van Mourik, F.; Chergui, M. *Opt. Lett.* **2007**, *32*, 3555.
(11)Mahr, H.; Hirsch, M. D. *OptCo* **1975**, *13*, 96.
(12)Shah, J. *Quantum Electronics, IEEE Journal of* **1988**, *24*, 276.
(13)Zhao, L.; Luis Perez Lustres, J.; Farztdinov, V.; Ernsting, N. P. *PCCP* **2005**, *7*, 1716.
(14)Schanz, H. R., Citeseer, 2002.
(15)Svelto, O. *Principles of Lasers*; 4 ed.; Plenum Press, 1998.
(16)Cui, G.; Lan, Z.; Thiel, W. *J. Am. Chem. Soc.* **2011**.
(17)Boyd, R. W. *Nonlinear optics*; 3rd ed.; Elsevier, 2008.
(18)Wynne, G. D. R. K. *Encyclopedia of Analytical Chemistry* **2000**, 13644.
(19)Roy, A.; Field, M. J.; Adam, V.; Bourgeois, D. *J. Am. Chem. Soc.* **2011**, *133*, 18586.
(20)Trebino, R. **2008**.
(21)Trebino, R. **2008**.
(22)Yarkony, D. R. *Chem. Rev.* **2011**.
(23)Radzewicz, C.; Band, Y. B.; Pearson, G. W.; Krasinski, J. S. *OptCo* **1995**, *117*, 295.
(24)Kim, C. H.; Joo, T. *Opt. Express* **2008**, *16*, 20742.
(25)Valeur, B.; Berberan-Santos, M. N. *Molecular fluorescence: principles and applications*; John Wiley & Sons, 2012.
(26)Conyard, J. **2013**.
(27)Greetham, G. M.; Burgos, P.; Cao, Q.; Clark, I. P.; Codd, P. S.; Farrow, R. C.; George, M. W.; Kogimtzis, M.; Matousek, P.; Parker, A. W.; Pollard, M. R.; Robinson, D. A.; Xin, Z.-J.; Towrie, M. *Appl. Spectrosc.* **2010**, *64*, 1311.
(28)Frisch, M.; Trucks, G.; Schlegel, H.; Scuseria, G.; Robb, M.; Cheeseman, J.; Montgomery Jr, J.; Vreven, T.; Kudin, K.; Burant, J. *Inc., Wallingford, CT* **2004**, *4*.
(29)Smith, N. A.; Meech, S. R.; Rubtsov, I. V.; Yoshihara, K. *Chem. Phys. Lett.* **1999**, *303*, 209.
(30)Tkachenko, N. V. *Optical Spectroscopy: Methods and Instrumentations*; Elsevier, 2006.
(31)Horng, M. L.; Gardecki, J. A.; Papazyan, A.; Maroncelli, M. *The Journal of Physical Chemistry* **1995**, *99*, 17311.
(32)Bäck, T.; Schwefel, H.-P. *Evol. Comput.* **1993**, *1*, 1.
(33)Pal, S. K.; Peon, J.; Bagchi, B.; Zewail, A. H. *The Journal of Physical Chemistry B* **2002**, *106*, 12376.
(34)Bagchi, B.; Fleming, G. R.; Oxtoby, D. W. *The Journal of Chemical Physics* **1983**, *78*, 7375.
(35)Bagchi, B.; Fleming, G. R. *The Journal of Physical Chemistry* **1990**, *94*, 9.
(36)Agmon, N.; Hopfield, J. *The Journal of Chemical Physics* **1983**, *79*, 2042.

(37)Chandrasekhar, S. *RvMP* **1943**, *15*, 1.
(38)Heisler, I. A.; Kondo, M.; Meech, S. R. *The Journal of Physical Chemistry B* **2009**, *113*, 1623.
(39)Tominaga, K.; Walker, G. C.; Kang, T. J.; Barbara, P. F.; Fonseca, T. *The Journal of Physical Chemistry* **1991**, *95*, 10485.
(40)Kang, T. J.; Jarzeba, W.; Barbara, P. F.; Fonseca, T. *Chem. Phys.* **1990**, *149*, 81.

Chapter 3 - *Cis-trans* Isomerisation of the Green Fluorescent Protein Chromophore

3.1. Introduction

Dronpa is a monomeric photoactivatable fluorescent protein (PAFP), which can be reversibly switched between fluorescent and non fluorescent states[1,2] (Chapter 1). In the fluorescent state, Dronpa has a high fluorescence quantum yield of 0.85 in the on state, whilst the off state remains stable for roughly 14 hours[3]. Furthermore, this PAFP can be photoswitched hundreds of times. These properties make Dronpa a valuable tool for applications such as ultra resolution imaging, labelling and tracking, dual colour imaging, optically activated molecular switches and high density optical storage[4-10].

Irradiation with 488 nm light creates the protonated (neutral) off state, whilst irradiation with 405 nm light restores the deprotonated (anionic) on form, recovering the green fluorescence[1]. The exact mechanism of photoconversion has been the subject of many studies. Whilst it is known that photoswitching results in different charge states of the chromophore, the precise pathway of the process is unclear with the importance of chromophore conformation, planarity, excited state proton transfer, hydrogen bonding and protein environment being widely debated[11-17].

Initially, crystal structure studies focused on the bright state and conflicting theories were presented[3,13]. Stiel et al. found that the chromophore adopts the *cis* form in the on-state[3]. Through comparisons with the on and off states of another photoswitchable protein, asFP595, they proposed that the off-state was likely to possess the *trans* chromophore[18]. From the on-state crystal structure they identified residues which may hinder isomerisation

(Val-157, Arg-66 and Met-159) and subsequently mutated them to facilitate easier isomerisation. This resulted in faster rates of photoswitching, supporting the hypothesis that isomerisation of the chromophore plays a role. It was also suggested that the *cis* form has a more rigid attachment to the protein and that the ability to isomerise, and subsequently modulate this attachment strength, is crucial for photoswitching[18]. Conversely Wilmann and co-workers, who also studied the crystal structure of the on state, proposed a model based on proton transfer via a polar network of residues around the chromophore[13]. They proposed that the protein environment would hinder the formation of a *trans* isomer, thus making the *cis-trans* isomerisation mechanism of photoswitching unrealistic. The crystal structures of both the on and off states were solved by Andresen et al. in 2007[19]. They revealed that photoswitching does in fact involve *cis-trans* isomerisation of the chromophore, but via a large scale movement of the hydroxyphenyl ring. This results in the displacement of four amino acid residues (Arg-66, Ser-142, Val-157 and His-193) located close to the chromophore, as shown in Figure 3.1. In the off-state (*trans)* the chromophore was shown to have a much more flexible attachment to the protein, with fewer hydrogen bonds. It also has a nonplanar geometry, where the imidazolinone and phenyl rings are twisted by approximately 30°.These structural changes result in very different electrostatic surface potentials surrounding the phenoxy ring of the chromophore, changing from a negative potential in the on state to a neutral/positive potential in the off state. These surfaces will influence the protonation state of the chromophore.
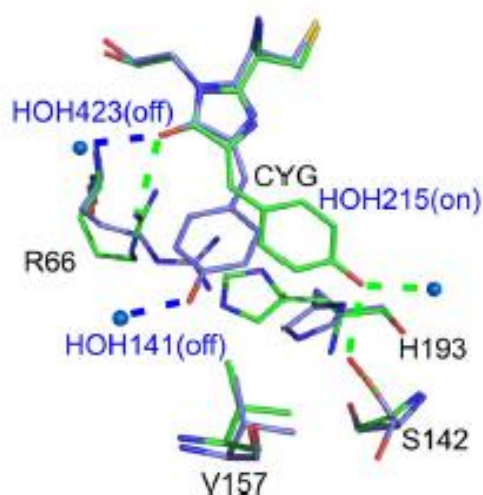
Figure 3.1. The on (green) and off (blue) positions of the chromophore, showing the different interactions with nearby amino acid residues and differences in the hydrogen bonding network (dashed lines)[19].

The importance of flexibility of the chromophore and protein environment has also been highlighted in other work. Mizuno et al. showed through NMR studies of the on and off states, that in the off state, the chromophore and a section of the β- barrel becomes more flexible, significantly enhancing the nonradiative decay[11]. Furthermore, by measuring the temperature dependence of the dark state recovery, Habuchi et al. showed that there is a large activation energy of 109 kJ mol^{-1} between the off and on forms[15]. They proposed that this is indicative of very different protein environments for the two states. In addition, Kao and co-workers demonstrated that the rate of photoswitching of Dronpa and the mutant Dronpa-3 can be modulated through the viscosity of the medium surrounding the protein, where the effect was greater for the more flexible mutant[20]. They revealed that the rate of photoswitching of the chromophore could be reduced by increasing the viscosity of the

medium surrounding the protein. This effect is expected if the structural changes, which facilitate isomerisation, are integral to photoswitching. In a molecular dynamics study presented by Li and co-workers, it was demonstrated that the chromophore environment and the flexibility of its attachment is crucial to the lifetime of the on-state[21]. A mutated Dronpa (H193T) was studied, revealing that nonradiative decay is enhanced for the mutant. This can be explained by the inability of the threonine to form π- stacking interactions with the anionic *cis* chromophore. These interactions increase the rigidity of the chromophore, suppressing nonradiative decay via movement of the bridging bonds.

This paper also addressed the mechanism of radiationless decay, where it was concluded that the process occurs through a flip of the C-C bridge bond. However, Koseki et al. presented a conflicting theoretical study of the photoconversion mechanism based on DFT and molecular dynamics methods[22], showing that photobleaching involves *cis-trans* isomerisation from an anionic to neutral form, where the first step is excited state proton transfer (ESPT) which is preceded by isomerisation via the hula twist rotation. In photoactivation this process is reversed.

The emission of the isolated chromophore of GFP (HBDI) (Figure 3.2) is (in contrast to GFP itself) very weak. The mechanism of decay is ultrafast internal conversion, involving a volume conserving motion around the bridging bonds[23-26]. Hence, the more flexible chromophore-protein attachment in the off-state of Dronpa is expected to enhance the rate of nonradiative decay via this path. Furthermore, it has been shown that nonplanarity of the chromophore enhances radiationless decay[27], meaning that radiationless decay will be further enhanced for the twisted *trans* chromophore in the off-state, compared to the planar *cis* chromophore in the on-state. HBDI, which is also the chromophore in Dronpa, has

been shown to undergo *cis-trans* isomerisation upon UV irradiation in solution (Figure 3.2.). In this chapter, the importance of isomerisation in the photoswitching behaviour of PAFPs is addressed by studying the isolated chromophore in solution, in the *cis* state and in a mixture of the *cis* and *trans* states. Firstly, the existence of both isomers was confirmed through NMR studies. Then both the steady-state and time-resolved fluorescence of both isomers are compared.
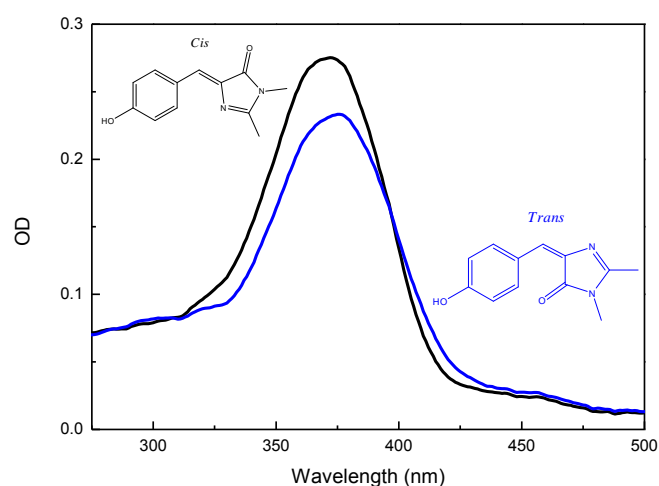
Figure 3.2. HBDI undergoes *cis-trans* isomerisation upon UV irradiation, causing a slight red shifting of the absorption spectrum.

3.2. Experimental Methods

The HBDI chromophore was synthesised by the group of Prof. Philip Page at the University of East Anglia, based on a modified version of the method described by Kojima et al.[28]. NMR spectra were recorded using a 400 MHz Varian spectrometer with samples prepared to a concentration of 10 mM. Steady-state absorption spectra were recorded using a

PerkinElmer XLS spectrometer and the emission with a Jobin Yvon fluorimeter with 5nm excitation and emission slit widths. As the emission of HBDI is very weak, the Raman scattering peak of the solvent can strongly distort the fluorescence spectra. However by measuring the emission of the pure solvent, the contribution from the Raman scattering can be subtracted from the sample. For the steady-state experiments, samples were prepared to a concentration of 16 µM in 1 cm quartz cuvettes, giving an optical density at the peak absorption wavelength of ~0.2. After steady-state and time-resolved measurements of the stable *cis* isomer, the samples were irradiated with UV light from a 385 nm 20 mW collimated light emitting diode (LED) from Thorlabs to induce photoisomerization.

The time-resolved fluorescence was measured by ultrafast laser up-conversion (Section 2). Measurements were made over 8 ps with a time resolution of 50 fs and an excitation wavelength of 400 nm. Samples for up-conversion were prepared to concentrations of 1 mM. The unirradiated (*cis*) sample was flowed through a 1mm quartz flow cell at a rate of 7ml/min and excited with an average power of 9 mW; this flow system prevented significant formation of the *trans* state during the measurement. This was checked by taking absorption spectra periodically. As shown in Figure 3.3, varying the pump power from 1 mW to 9 mW had no effect on the decay kinetics, nor did varying the flow rate from 4 ml/min to 10 ml/min. Hence the highest 9 mW pumping power was used to achieve the best signal-to-noise ratio. After measurements on the unirradiated sample the cell was then irradiated until the maximum *trans* population was attained (confirmed by steady-state measurements shown in Figure 3.5) and the up-conversion was re-measured in a static 1 mm cell under constant illumination by the LED to maintain the trans population throughout the measurement.
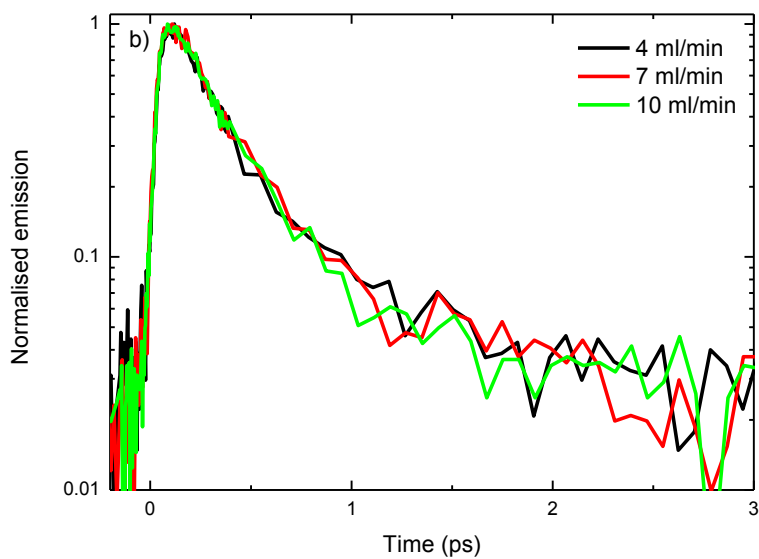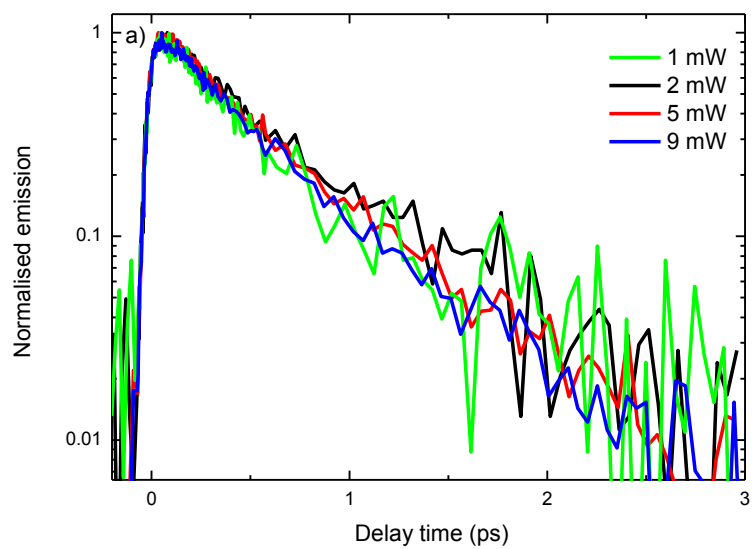
Figure 3.3 (a) Increasing the excitation power from 1 to 9 mW. (b) Increasing the flow rate

from 4 ml/min to 10 ml/min. Neither parameter has a measureable effect on the

fluorescence decay.

3.3. Results and Discussion

3.3.1. NMR Spectroscopy

UV irradiation of *cis* HBDI creates a metastable *trans* population which can return to the *cis* state in a thermal back reaction. The different isomers can be observed in NMR spectra taken before and after irradiation[29,30], where the peak assignments are shown in Figure 4. The maximum *trans* population can be determined by comparing the relative intensities of the *cis* and *trans* peaks in the unirradiated and irradiated spectra. In each case the peaks were normalised to the intensity of the methyl group (14 in Figure 3.4), as this environment is relatively unchanged by isomerisation. The percentage population in the *trans* form was calculated by comparing the intensity of a particular *cis* feature with the corresponding *trans* feature in the normalised irradiated spectrum. This process was repeated for every feature, for which a clear and separate *trans* form could be identified, and the values averaged. For neutral HBDI in methanol-d4, DMSO-d6 and acetonitrile-d3, the maximum *trans* populations were 40%, 57% and 45% respectively. For anionic HBDI in basic methanol-d4, 23% of the initial *cis* population was converted. The point where irradiation no longer continues to cause photoisomerisation indicates that *cis-trans* isomerisation is being balanced by thermal relaxation or photoconversion back to the *cis* isomer. It has been shown that the *trans* form is stable in some aprotic solvents and benzene but converts back to the *cis* isomer in protic solvents at room temperature[29-32].
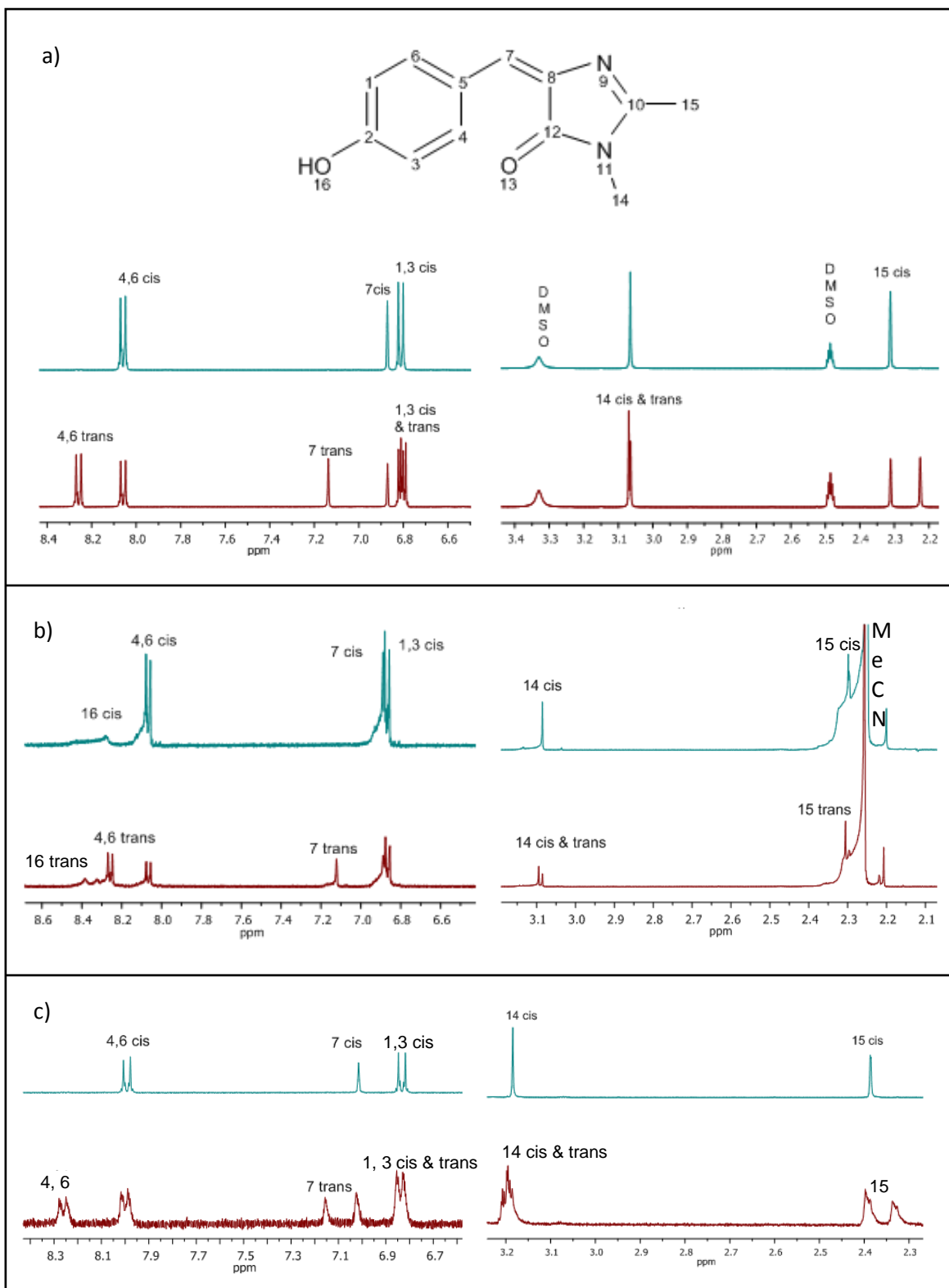
Figure 3.4. NMR spectra of dark (green) and irradiated (red) HBDI in DMSO-d6 (a),

acetonitrile-d3 (b) and methanol-d4 (c).

3.3.2 Steady-state Measurements

Upon photoisomerisation, a small shift and decrease in intensity in the steady-state UV-Vis and emission spectra is observed. Figure 3.5a shows the UV-Vis absorption spectra of neutral HBDI in methanol in the dark state and after 5 minutes and 5 hours of irradiation. In the light state the peak absorption is red-shifted by 4 nm, from 371 to 375 nm. This is in agreement with the work of Voliani et al. who observed a 5 – 15 nm red shift in the absorption spectrum after irradiation[29]. For the anion (Figure 3. 5b) the peak absorption wavelength was shifted by 5 nm, from 429 nm to 434 nm after 1 hour of irradiation. The spectral changes were complete within a few hours of irradiation, resulting in a 15% decrease in the optical density (OD) at the peak wavelength for the neutral form. However, a 12% decrease in the OD was observed after only 5 minutes of irradiation time. Whilst for the anion there was an 8% decrease in the OD.

The weak steady-state emission of neutral and anionic HBDI in methanol is shown in Figure 3.6. Similarly to the absorption, there is a small shift upon isomerisation and the intensity at the peak emission wavelength decreases slightly, with a 16% decrease in the integrated area for the neutral and an 8% decrease for the anion.
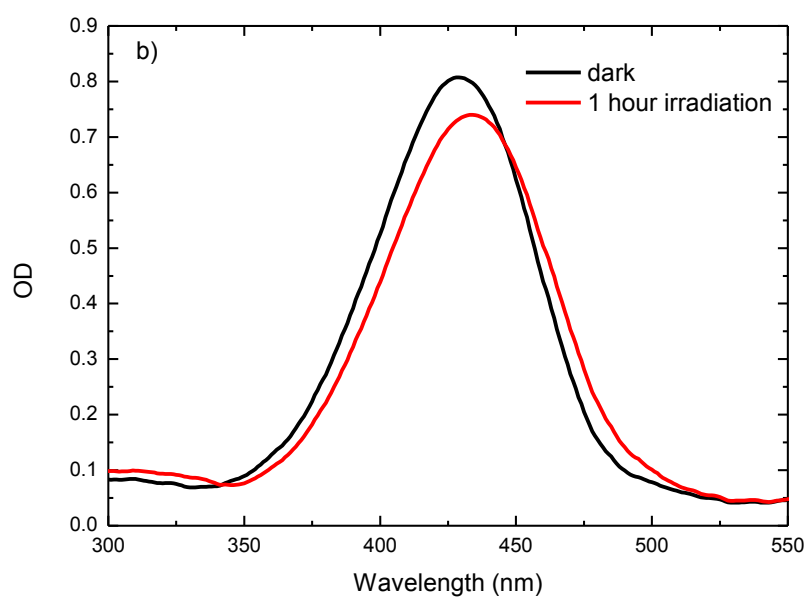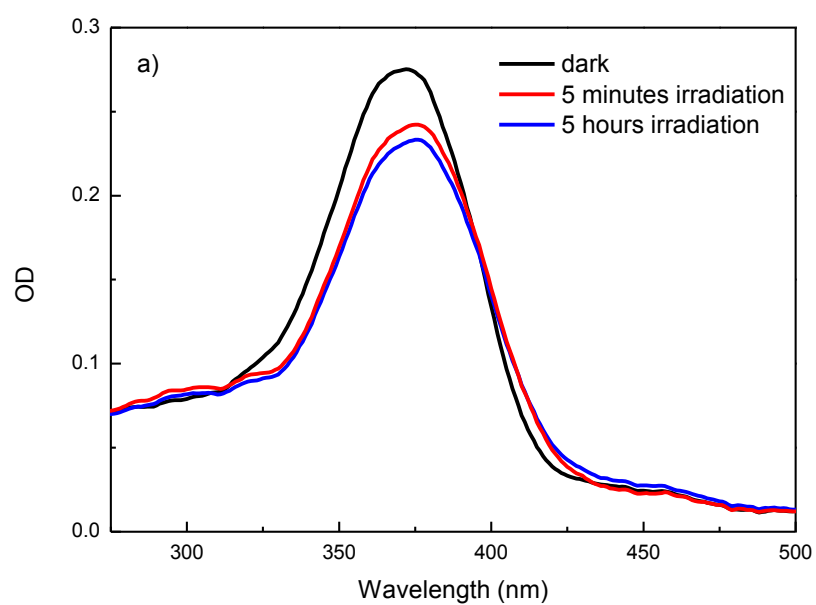
Figure 3.5. a) Steady-state measurements of neutral HBDI after 0 min (black), after 5 min (red) and after 5 hours (blue) of 385 nm irradiation. b) Corresponding measurements for anionic HBDI in methanol after 0 min (black) and 1 hour (red) of irradiation.
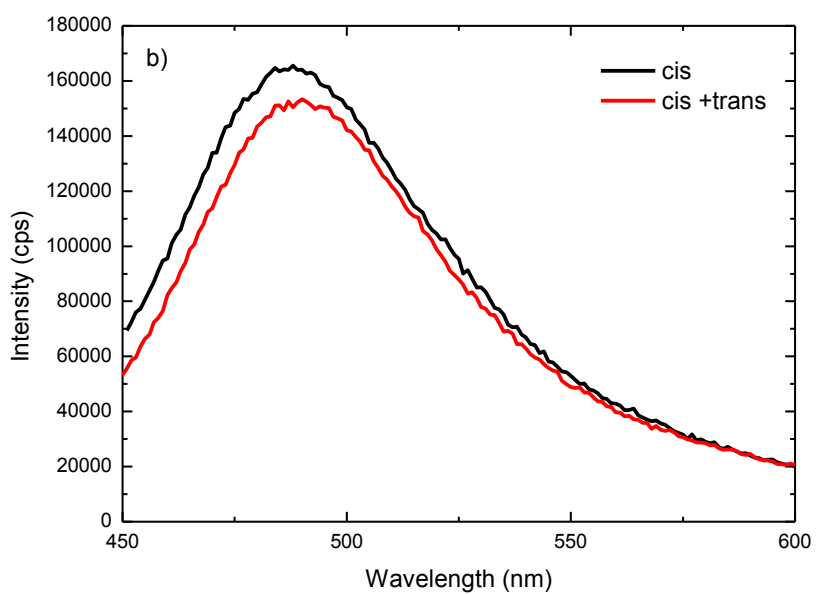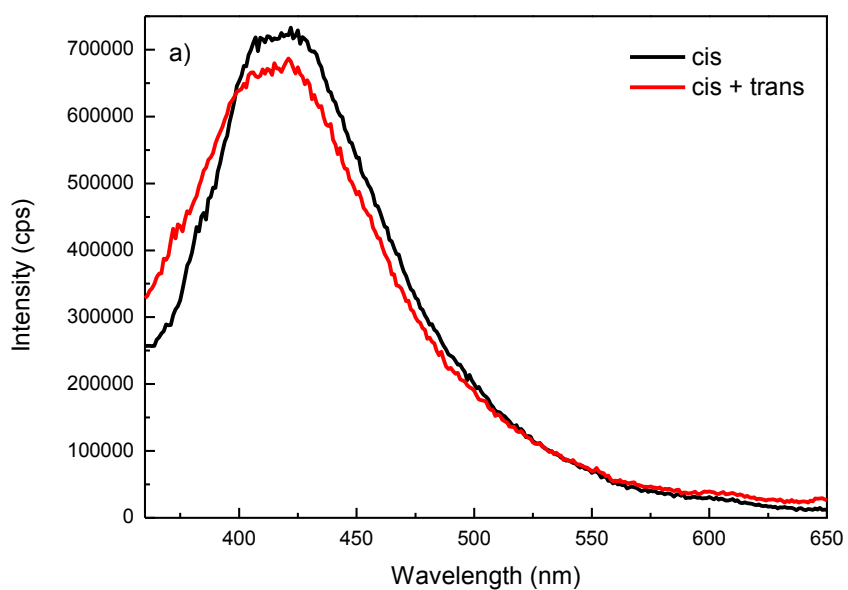
Figure 3.6. Emission of *cis* HBDI in methanol (black) and an equilibrated *cis/trans* mixture (red) for the neutral (a) excited at 340 nm and the anion (b) excited at 390 nm, where the Raman scattering of methanol has been subtracted.

3.3.3. Time-resolved Measurements

The results in Figure 3.7 show the fluorescence decays of neutral HBDI in methanol, acetonitrile and of the anion in methanol. As reported previously, the decays are complete within a few ps and the decay of the anion is slower than that of the neutral[26,27]. Significantly, in all cases the decays of the *cis* and *cis/trans* samples are experimentally indistinguishable. One possible explanation for the identical decays is that the *trans* state is a truly dark state (i.e with a lifetime below our 50 fs resolution). Hence for both the dark and light samples, only fluorescence from the *cis* state is being detected. This explanation would be consistent with *cis/trans* isomerisation being responsible for the lack of fluorescence in the off-state of Dronpa. However, whilst the steady-state emission for HBDI in methanol shows a 16% decrease in the integrated area, the corresponding NMR spectrum shows an isomer distribution which is 40% *trans*. So a larger decrease in the integrated area would be expected if the *trans* state was a dark state. It can therefore be concluded that both the *cis* and *trans* states are fluorescent.
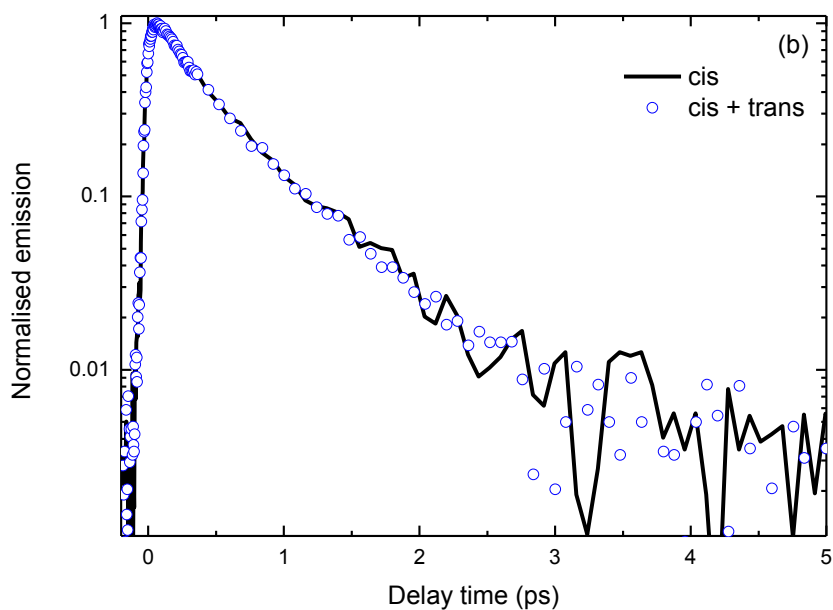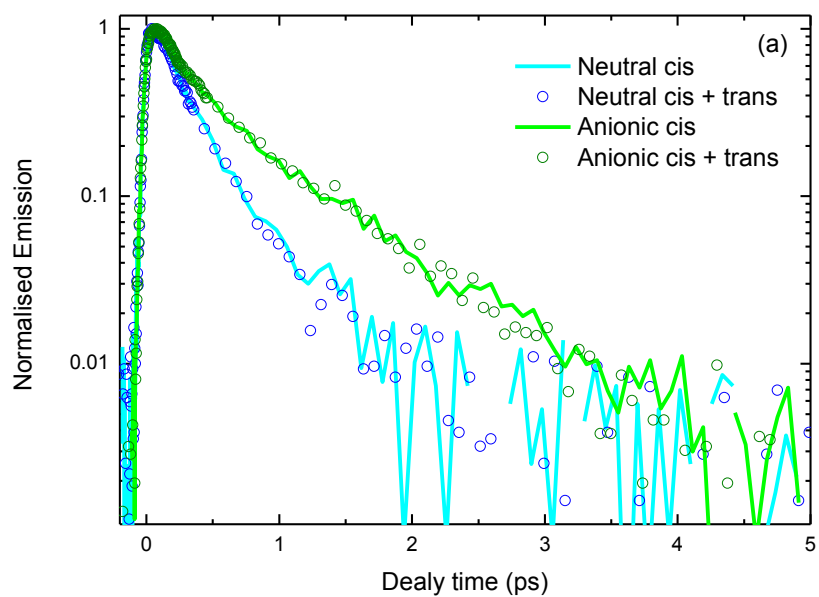
Figure 3.7. Fluorescence decays of *cis* (solid) and a *cis/trans* mixture (circles) of neutral (blue) and anionic (green) HBDI in methanol (a), acetonitrile (b) measured with a time resolution of 50 fs. The lack of a dependence on isomer is evident.

As indicated by the slight nonlinearity of the decays shown in Figure 3.7, the decays are not single exponential. Importantly, this is true for the pure *cis* state. Thus, indicating that this behaviour is not a result of contributions from both isomers, which might be expected to produce a multi-exponential decay[33-35]. Alternatively, this could indicate an intrinsically non-exponential relaxation on the excited state. The kinetics were fitted with a bi-exponential function, with the amplitudes and time constants given in Table 3.1. To test reproducibility of the fitting each trace was fitted three times and the results averaged. The standard deviation was calculated to determine the error on each fitting parameter. In all cases this error was less than 10%. Fits to repeated experiments with the same condition indicate that the intrinsic error of the measurement is 10% (Chapter 2). In all cases, the total error on the average lifetime was less than 11%. Therefore the average lifetimes given by these fitting parameters are identical within the errors.

	Acetonitrile		Octanol		Methanol		Anion in Methanol	
	Dark	Light	Dark	Light	Dark	Light	Dark	Light
τ_1/ps	0.25	0.22	0.20	0.19	0.17	0.18	0.17	0.17
a_1	0.70	0.66	0.68	0.69	0.80	0.78	0.66	0.66
τ_2/ps	0.75	0.69	0.71	0.62	0.49	0.42	0.79	0.79
a_2	0.30	0.34	0.32	0.31	0.20	0.22	0.34	0.34
$<\tau>/ps$	0.40	0.38	0.36	0.32	0.24	0.24	0.38	0.38

Table 3.1. Fitting parameters for unirradiated and irradiated neutral HBDI in acetonitrile, octanol and methanol and the anion in methanol.

The similarity of the *cis* and *trans* fluorescence decays suggests that the excited states of the isomers must also be very similar with comparable relaxation pathways back to the ground-state. This theory is supported by the work of Olsen and Smith who calculated the S_0 and S_1 potential energy surfaces for both isomers of anionic HBDI as a function of torsion of the phenoxy and imidazolinone bonds, which are proposed to be important coordinates in the radiationless decay pathway[36]. Figure 3.8a shows the potential energy surfaces calculated using a state-averaged CASSCF model. The calculated *cis* and *trans* surfaces are almost identical. Hence the excited state populations would follow approximately the same path back to the ground-state, producing the indistinguishable fluorescence decays observed. These surfaces were extracted and input into a model which simulates the time-resolved fluorescence spectra (The model is described in more detail in Chapter 6). Figure 3.8b shows the results of the simulation of the time-resolved spectra for *cis* and *trans* HBDI calculated between 50 fs and 1.5 ps. Clearly there is very little variation between the simulated *cis* and *trans* spectra.
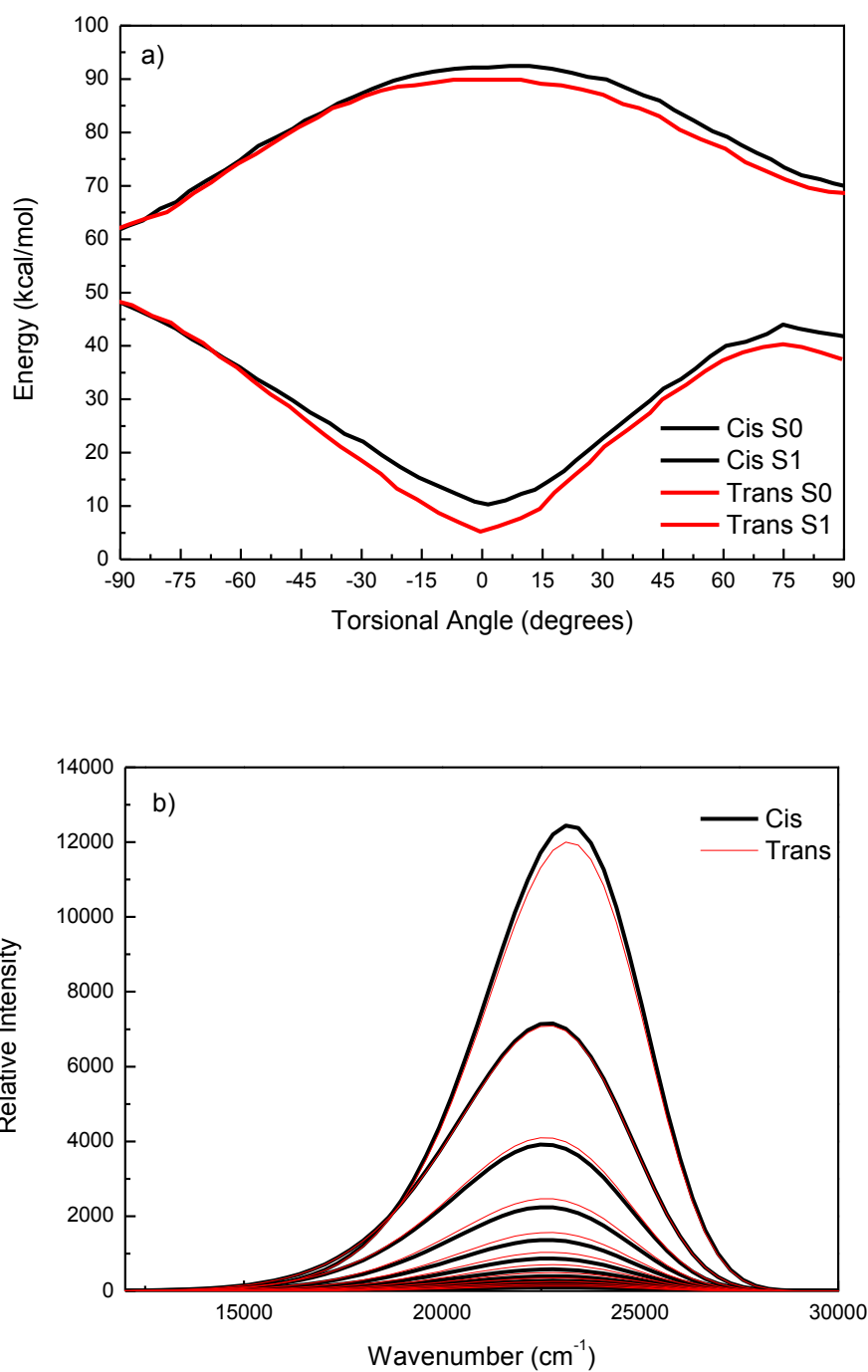
Figure 3.8. a) S_0 and S_1 potential energy surfaces for *cis* (black) and *trans* (red) anionic HBDI extracted from[36]. b): Fluorescence spectra of *cis* (black) and *trans* (red) anionic HBDI between 50 fs and 1.5 ps calculated using the model described in Chapter 6 with the ground and excited state surfaces above.

3.3.4. Simulations of Up-converted Data

The results displayed in Figure 3.7 and Table 3.1 indicate that the excited state decay of

HBDI is very similar for both ground-state isomers. In order to estimate the difference in

lifetime which would be observable in our measurements, the decays were simulated under

the assumption that the *trans* lifetimes (τ_{t1} and τ_{t2}) are some percentage of the known *cis*

lifetimes (τ_{c1} and τ_{c2}). A calculated decay was then obtained from:

$$I = A_c \left(e^{-\frac{t}{\tau_{c1}}} + e^{-\frac{t}{\tau_{c2}}} \right) + A_t \left(e^{-\frac{t}{\tau_{t1}}} + e^{-\frac{t}{\tau_{t2}}} \right), \tag{3.1}$$

where A_c and A_t are the relative populations of the *cis* and *trans* components respectively,

which were determined from the NMR spectra. Figure 3.9 shows the results of this

simulation for HBDI in acetonitrile. This demonstrates that if the *trans* lifetime were to differ

by more than 20% of the *cis* lifetime, then this should produce a difference which would be

observable in the experimental data.
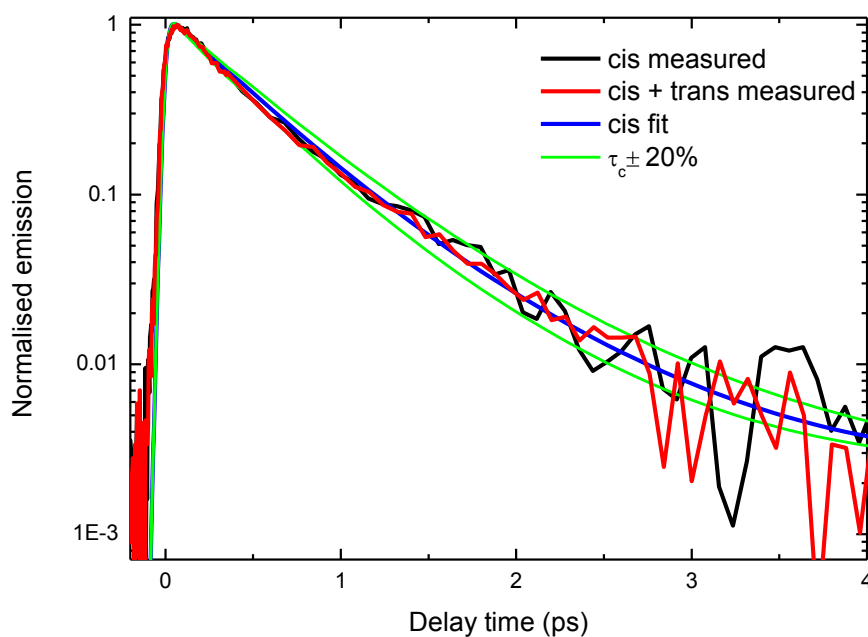
Figure 3.9. Experimental data and simulated decays of HBDI in acetonitrile, *cis* data (black), *cis/trans* data (red), *cis* bi-exponential fit (blue), bi-exponential fits with a 20% difference in the *cis* lifetimes (τ_{c1} and τ_{c2}) (green).

3.4. Conclusions

Structural studies have shown that the bright and dark forms of Dronpa possess the HBDI chromophore in the *cis* and *trans* forms respectively[3,19]. These states have dramatically different photophysics. The time-resolved fluorescence measurements presented here indicate that there is no observable difference in the lifetimes of the *cis* and *trans* states of the chromophore in solution. Therefore it cannot be the chromophore conformation alone which is responsible for the different behaviour of the isomers in Dronpa.

These results demonstrate that *cis-trans* isomerisation of the chromophore cannot be solely responsible for the on-off photoswitching behaviour of Dronpa and related PAFPs. Whilst the emissive part of a FP is the chromophore, this work highlights the importance of the protein structure in modulating the behaviour of FPs. The differential protein-chromophore interactions must be responsible for the contrasting behaviour of the on and off states of Dronpa. The exact mechanism is likely to involve a sequence of changes to the protein structure in the local chromophore environment which alter the bonding network and permits (or forbids) isomerisation.

3.5. References

(1)Habuchi, S.; Ando, R.; Dedecker, P.; Verheijen, W.; Mizuno, H.; Miyawaki, A.; Hofkens, J. *Proc. Natl. Acad. Sci. U. S. A.* **2005**, *102*, 9511.
(2)Ando, R.; Mizuno, H.; Miyawaki, A. *Sci* **2004**, *306*, 1370.
(3)Stiel, A. C.; Trowitzsch, S.; Weber, G.; Andresen, M.; Eggeling, C.; Hell, S. W.; Jakobs, S.; Wahl, M. C. *Biochem. J.* **2007**, *402*, 35.
(4)Brown, T. A.; Tkachuk, A. N.; Shtengel, G.; Kopek, B. G.; Bogenhagen, D. F.; Hess, H. F.; Clayton, D. A. *Mol. Cell. Biol.* **2011**, *31*, 4994.
(5)Marriott, G.; Mao, S.; Sakata, T.; Ran, J.; Jackson, D. K.; Petchprayoon, C.; Gomez, T. J.; Warp, E.; Tulyathan, O.; Aaron, H. L.; Isacoff, E. Y.; Yan, Y. *Proc. Natl. Acad. Sci. U. S. A.* **2008**, *105*, 17789.
(6)Hofmann, M.; Eggeling, C.; Jakobs, S.; Hell, S. W. *Proc. Natl. Acad. Sci. U. S. A.* **2005**, *102*, 17565.
(7)A. Schwentker, M.; Bock, H.; Hofmann, M.; Jakobs, S.; Bewersdorf, J.; Eggeling, C.; Hell, S. W. *Microsc. Res. Tech.* **2007**, *70*, 269.
(8)Lukyanov, K. A.; Chudakov, D. M.; Lukyanov, S.; Verkhusha, V. V. *Nat Rev Mol Cell Biol* **2005**, *6*, 885.
(9)Sauer, M. *Proc. Natl. Acad. Sci. U. S. A.* **2005**, *102*, 9433.
(10)Korpany, K. V.; Langat, P.; Kim, D. M.; Edelman, N.; Cooper, D. R.; Nadeau, J.; Blum, A. S. *J. Am. Chem. Soc.* **2012**, *134*, 16119.
(11)Mizuno, H.; Kumar Mal, T.; Wälchli, M.; Kikuchi, A.; Fukano, T.; Ando, R.; Jeyakanthan, J.; Taka, J.; Shiro, Y.; Ikura, M.; Miyawaki, A. *Proceedings of the National Academy of Sciences*.
(12)Nam, K.-H.; Kwon, O. Y.; Sugiyama, K.; Lee, W.-H.; Kim, Y. K.; Song, H. K.; Kim, E. E.; Park, S.-Y.; Jeon, H.; Hwang, K. Y. *Biochem. Biophys. Res. Commun.* **2007**, *354*, 962.
(13)Wilmann, P. G.; Turcic, K.; Battad, J. M.; Wilce, M. C. J.; Devenish, R. J.; Prescott, M.; Rossjohn, J. *J. Mol. Biol.* **2006**, *364*, 213.
(14)Schäfer, L. V.; Groenhof, G.; Boggio-Pasqua, M.; Robb, M. A.; Grubmüller, H. *PLoS Comput Biol* **2008**, *4*, e1000034.
(15)Habuchi, S.; Dedecker, P.; Hotta, J.-i.; Flors, C.; Ando, R.; Mizuno, H.; Miyawaki, A.; Hofkens, J. *Photochemical & Photobiological Sciences* **2006**, *5*, 567.
(16)Regis Faro, A.; Carpentier, P.; Jonasson, G.; Pompidor, G.; Arcizet, D.; Demachy, I.; Bourgeois, D. *J. Am. Chem. Soc.* **2011**, *133*, 16362.
(17)Lukacs, A.; Haigney, A. L.; Brust, R. J.; Addison, K.; Towrie, M.; Greetham, G. M.; Jones, G. A.; Miyawaki, A.; Tonge, P. J.; Meech, S. R. *The Journal of Physical Chemistry B* **2013**.
(18)Andresen, M.; Wahl, M. C.; Stiel, A. C.; Gräter, F.; Schäfer, L. V.; Trowitzsch, S.; Weber, G.; Eggeling, C.; Grubmüller, H.; Hell, S. W.; Jakobs, S. *Proc. Natl. Acad. Sci. U. S. A.* **2005**, *102*, 13070.
(19)Andresen, M.; Stiel, A. C.; Trowitzsch, S.; Weber, G.; Eggeling, C.; Wahl, M. C.; Hell, S. W.; Jakobs, S. **2007**, *104*, 13005.
(20)Kao, Y.-T.; Zhu, X.; Min, W. *Proceedings of the National Academy of Sciences* **2012**, *109*, 3220.
(21)Li, X.; Chung, L. W.; Mizuno, H.; Miyawaki, A.; Morokuma, K. *The Journal of Physical Chemistry Letters* **2010**, *1*, 3328.
(22)Koseki, J.; Kita, Y.; Nagashima, U.; Tachikawa, M. *Procedia Computer Science* **2011**, *4*, 251.
(23)Litvinenko, K. L.; Webber, N. M.; Meech, S. R. *The Journal of Physical Chemistry A* **2003**, *107*, 2616.
(24)Litvinenko, K. L.; Webber, N. M.; Meech, S. R. *Chem. Phys. Lett.* **2001**, *346*, 47.
(25)Webber, N. M.; Litvinenko, K. L.; Meech, S. R. *The Journal of Physical Chemistry B* **2001**, *105*, 8036.
(26)Mandal, D.; Tahara, T.; Meech, S. R. *The Journal of Physical Chemistry B* **2003**, *108*, 1102.
(27)Conyard, J.; Kondo, M.; Heisler, I. A.; Jones, G.; Baldridge, A.; Tolbert, L. M.; Solntsev, K. M.; Meech, S. R. *The Journal of Physical Chemistry B* **2011**, *115*, 1571.

(28)Kojima, S.; Ohkawa, H.; Hirano, T.; Maki, S.; Niwa, H.; Ohashi, M.; Inouye, S.; Tsuji, F. I. *Tetrahedron Lett.* **1998**, *39*, 5239.

(29)Voliani, V.; Bizzarri, R.; Nifosì, R.; Abbruzzetti, S.; Grandi, E.; Viappiani, C.; Beltram, F. *The Journal of Physical Chemistry B* **2008**, *112*, 10714.

(30)Yang, J.-S.; Huang, G.-J.; Liu, Y.-H.; Peng, S.-M. *Chem. Commun.* **2008**, 1344.

(31)Dong, J.; Abulwerdi, F.; Baldridge, A.; Kowalik, J.; Solntsev, K. M.; Tolbert, L. M. *J. Am. Chem. Soc.* **2008**, *130*, 14096.

(32)He, X.; Bell, A. F.; Tonge, P. J. *FEBS Lett.* **2003**, *549*, 35.

(33)Ben-Amotz, D.; Harris, C. B. *The Journal of Chemical Physics* **1987**, *86*, 4856.

(34)Bagchi, B.; Fleming, G. R.; Oxtoby, D. W. *The Journal of Chemical Physics* **1983**, *78*, 7375.

(35)Bagchi, B.; Fleming, G. R. *The Journal of Physical Chemistry* **1990**, *94*, 9.

(36)Olsen, S.; Smith, S. C. *J. Am. Chem. Soc.* **2008**, *130*, 8677.

Chapter 4 – The Kaede Chromophore

4.1. Introduction

Since the discovery of GFP, prolific research has resulted in the development of many new FPs with emission wavelengths covering the visible spectrum (Chapter 1). A series of red fluorescent proteins (RFPs), with chromophores having an extended conjugation compared to GFPs, have been discovered and developed from coral species[1-4]. The development of RFPs created better separation between the emission peak of GFP and other similar FPs which enabled multicolour *in vivo* imaging and Förster resonance energy transfer (FRET) studies with GFP variants[5]. Furthermore, excitation with longer wavelengths is less damaging to living cells and less autofluorescence is generated. The FPs DsRed, which emits at 583 nm, and HcRed (emitting at 645 nm) were two of the first RFPs discovered and subsequently used in imaging[6,7]. However, their applications were limited due to a tendency to oligomerize and by their relatively low fluorescence quantum yields. DsRed was engineered into mRFP1 (monomeric red fluorescent protein) and subsequently a series of brighter, more photostable mRFP1 variants, the mFruits, were produced[3,4,8].

The properties of photoactivatable fluorescent proteins (PAFPs) can be optically modulated (Chapter 1). PAFPs can be irreversibly or reversibly switched on and off or between different colours. The Kaede fluorescent protein (KaedeFP) was extracted and cloned from the stony coral, *Trachyphyllia geoffroyi*, by Ando in 2002[2]. It is an irreversible PAFP, which can be permanently changed from a green to a red emissive state upon UV irradiation. The red state is highly stable and of comparable brightness to the green state. Furthermore, photoconversion results in more than a 2000 fold increase in the red to green fluorescence

ratio, with well separated emission wavelengths. These features make KaedeFP highly useful for optical marking and tracking in cells, as a specific population tagged with KaedeFP can be photoconverted and its subsequent movement tracked. However it was shown that Kaede forms a tetrameric complex, which is not ideal for *in vivo* imaging, and a monomeric form of Kaede was developed[2].

The mechanism of KaedeFP photoconversion was revealed by Miyawaki and co-workers (Figure 4.1.). Unlike most FP chromophores which are composed of the amino acids Ser-Tyr-Gly, KaedeFP contains a chromophore (Kaede) formed from the residues His-62, Tyr-63 and Gly-64[9]. The active section of the green chromophore is the same as that of HBDI (Chapter 3). Upon irradiation of the chromophore the protein undergoes with a low yield a backbone cleavage at His-62 and subsequent reaction. This extends the π-conjugated system to the imidazole of His-62, thus lowering the energy of the transition resulting in the observed green to red conversion[2,9]. It has been shown through mutations that this His-62 residue is crucial for a bright photoconverted form[9].
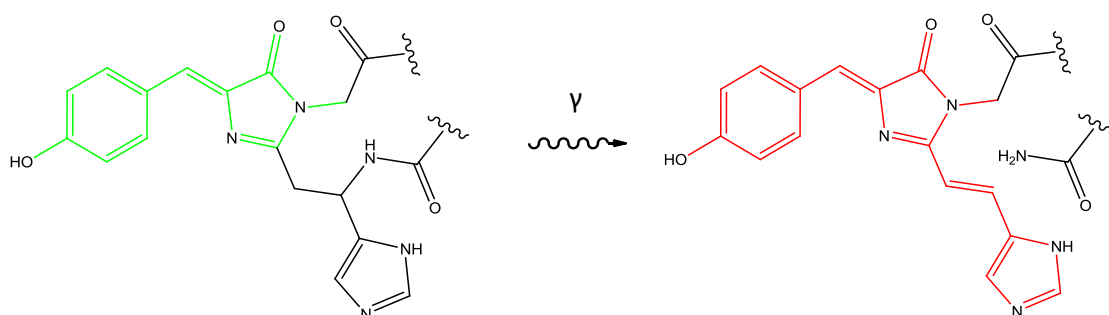
Figure 4.1. Photoconversion from the green to red Kaede chromophore occurs via backbone cleavage upon irradiation with UV light.

Studies of the crystal structure of KaedeFP before and after photoconversion show that the chromophore conformation is similar in both states. This is in contrast to the photochromic PAFP Dronpa, where the on - off photoswitching results in isomerization of the chromophore[10]. Excitation of neutral KaedeFP leads to photoconversion[9]. However, it has been shown that photoconversion (Figure 4.1) is likely to involve the protonated state of the chromophore as acidic conditions result in a higher rate of photoswitching[2]. The presence of a water molecule close to the His-62 imidazole ring in the green chromophore was revealed[10]. This molecule is thought to aid the cleavage process by providing favourable conditions for the protonated form of the chromophore.

A number of FPs containing the Kaede chromophore have now been discovered or synthesised. For example, EosFP and Dendra2 which both undergo green-to-red photoconversion via backbone cleavage[11,12]. Engineering of EosFP and Dendra2 has led to the development of IrisFp and NijiFP respectively. These FPs exhibit both reversible on-off photoswitching and irreversible green-to-red photoconversion[13,14]. This property makes these proteins highly useful for fluorescence imaging and has resulted in the development of new applications, such as super-resolution pulse chase imaging[15]. IrisFP was the first FP to exhibit these dual reversible and irreversible properties However the fast off-switching rate, low photostability and tendency to oligomerize presented practical problems. Through mutations of existing proteins, improved dual PAFPs, such as NijiFP, were developed with better on-off switching rates and greater photostability. NijiFP is a monomeric FP developed from Dendra2, where a mutation (F173S) allows greater conformational freedom and flexibility of the chromophore. Thus enabling more efficient on-off photoswitching[14].

In this chapter, the photophysics of the red KaedeFP chromophore (called Kaede) is studied, and compared to HBDI. Firstly the steady-state absorption and emission is investigated for different solvents, concentrations, pH values and temperatures. NMR spectroscopy is used to examine the possibility of photoisomerization, and ground-state DFT calculations are performed to determine the isomerisation barriers. The ground-state and excited state dynamics are probed using TRIR, ultrafast fluorescence up-conversion and transient absorption, where the dependence on solvent, wavelength and temperature is investigated.

4.2. Experimental Methods

The Kaede chromophore was synthesised by the group of Prof. Philip Page at the University of East Anglia.

Steady-state absorption spectra (Section 4.3.1) were recorded using a PerkinElmer XLS spectrometer and the emission with a Jobin Yvon fluorimeter with 5nm excitation and emission slit widths. A 1 cm quartz cell was used with solutions prepared to a concentration of 13 μM (unless stated otherwise). For the low temperature steady-state fluorescence measurements, a Gilden Photonics FluoroSENS spectrometer with cryostat attachment was used to vary the sample temperature between room temperature and 77 K (Section 4.3.4). NMR spectra were recorded using a Bruker 500 MHz spectrometer, where samples were prepared to a concentration of 10 mM (Section 4.3.3). Samples were irradiated using a 405 nm 20 mW collimated LED from Thorlabs, where the power was measured using a power meter from Coherent.

The time-resolved infrared (TRIR) spectra were measured at the Central Laser Facility at the Rutherford Appleton Laboratory (Section 4.3.6)[16]. The excitation wavelength was 450 nm, with a spot size of 100 μm and a pulse energy of 200 nJ at a 1 kHz repetition rate. The IR probe transmission was measured as a function of delay time after the pump pulse to cover the range 500 fs to 2 ns with a time resolution of 100 fs. The 450 nm pump beam was chopped at 500 Hz to allow collection of pumped and unpumped IR transmission, and the data are presented as difference spectra. The polarization angle between the pump and probe was set to the magic angle to negate the effects of molecular rotation[17]. The spectra were detected using two 128 pixel detectors, with a resolution of 3 cm^{-1} per pixel. For these measurements the spectral window was 1270 to 1886 cm^{-1}, where the spectral range is calibrated using *cis* stilbene transmission.

The time-resolved fluorescence (Section 4.4) was measured by ultrafast laser up-conversion (described in Chapter 2). Measurements were made over 250 ps with a time resolution of 50 fs. Samples were excited at 400 nm with a power of 9 mW and a monochromator was used to detect emission at the desired wavelength. Samples were prepared to concentrations of 0.5 mM and flowed through a 1mm quartz flow cell at a rate of 7ml/min using a Peri-Star Pro peristaltic pump. A water bath temperature controller was used to vary the sample cell temperature between 5 ^{o}C and 80 ^{o}C. The sample reservoir was placed in the water bath and flowed. A custom built copper sample cell holder, through which the thermostatted water was flowed, was used to ensure that the sample temperature was maintained during the measurement.

The transient absorption spectra were recorded up to 350 ps after excitation, covering the spectral range 430 nm to 630 nm with a time resolution of 300 fs. The coherent artefact

distorts the spectrum between 0 and 7.5 ps and data within this range is removed (Chapter 2). Samples were prepared to concentrations of 0.5 mM and flowed through a 1mm quartz flow cell at a rate of 7ml/min using a Peri-Star Pro peristaltic pump.

4.3. Results and Discussion

4.3.1 Steady-state Measurements

The steady-state UV-Vis absorption spectra of HBDI and Kaede are shown in Figure 4.2. The choice of solvents was limited by the poor solubility of the chromophore in nonpolar solvents. The extension of the conjugated system causes a redshift of the peak absorption wavelength from 370 nm for HBDI in methanol to 430 nm for Kaede in the same solvent. As observed for HBDI, there is little dependence of the maximum absorption wavelength on the solvent. The extinction coefficients (ε) were calculated at the maximum wavelength using the Beer-Lambert law (Chapter 1) and are given in Table 4.1. The values are typical of allowed π-π^* transitions. A solvent dependence is seen for the extinction coefficient of both chromophores, where for Kaede ε decreases with increasing polarity (Figure 4.3). For Kaede in formamide and HBDI in water, a shoulder is observed on the red side of the spectrum. The acid base investigation (Section 4.3.2) revealed that this is due to the stabilisation of the anion in these solvents.
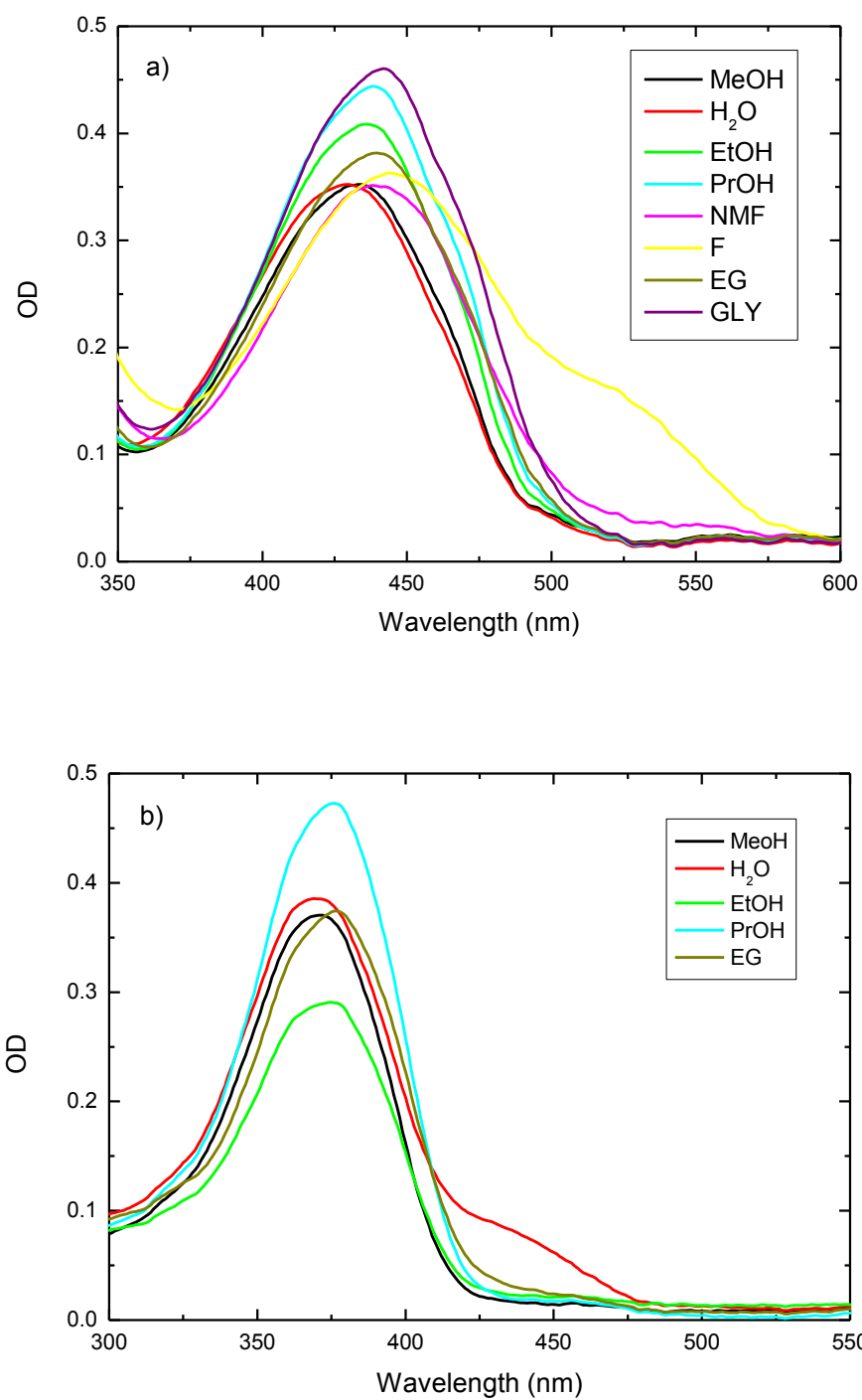
Figure 4.2. Steady-state absorption of Kaede (a) and HBDI (b) as a function of solvent measured at a concentration of 13 μM and 16 μM respectively.
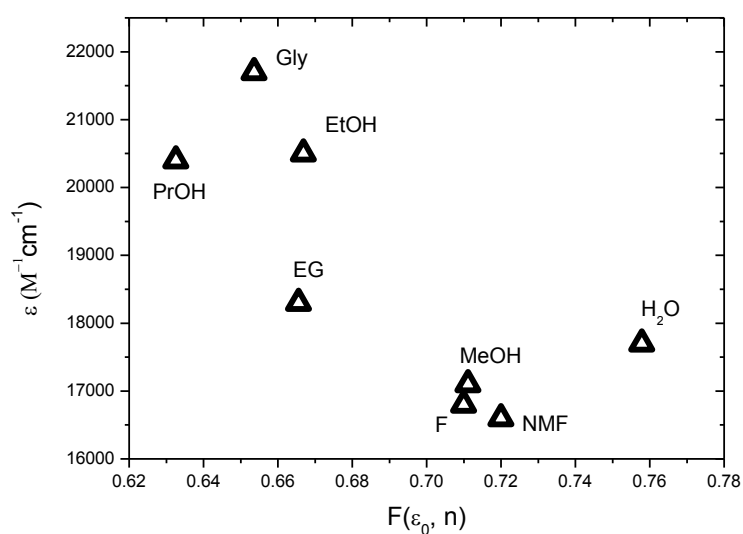
Figure 4.3. The extinction coefficient of Kaede at the maximum absorption wavelength in various solvents against the polarity function.

The red shift observed in the absorption between HBDI and Kaede is also seen in the emission (Figure 4.4), where the emission maximum is shifted from 430 nm for HBDI in methanol to approximately 505 nm for Kaede. Similarly to the absorption, neither chromophore exhibits a strong dependence of maximum emission wavelength or spectral width on solvent, as can most clearly be seen in the peak normalized spectra inset in Figure 4.4. However, there is a slight blue shift for Kaede in methanol.

Figure 4.4a shows that Kaede is much more fluorescent than HBDI, where the integrated area increases 15 times in methanol. The behaviour of the integrated intensity of the chromophores in the alcohols indicates a weak dependence on solvent viscosity. For Kaede, the integrated intensity of the emission increases almost 5 times from methanol to glycerol as the viscosity increases by a factor of 1700, and for both chromophores from methanol to

ethylene glycol the intensity doubles for a viscosity increases of 30 times, thus both chromophores show a weak viscosity dependence. One further difference between Kaede and HBDI is the clear structure in the Kaede spectra, with two distinct peaks separated by 20 - 30 nm. This structure is not seen in the absorption spectra and could indicate either vibronic structure in the emission or the presence of two distinct emitting states which are more energetically different in the excited state than the ground-state. Furthermore, the absorption and emission spectra of Kaede are broader than those of HBDI. This could also be due to the presence of multiple structures in the Kaede samples – we return to this point below in a concentration dependent study.
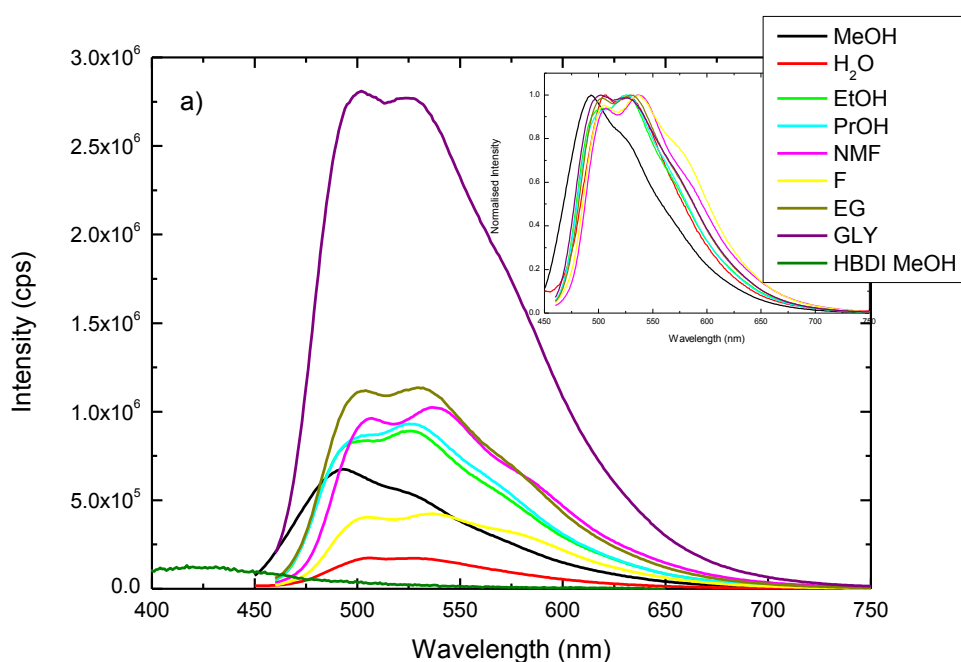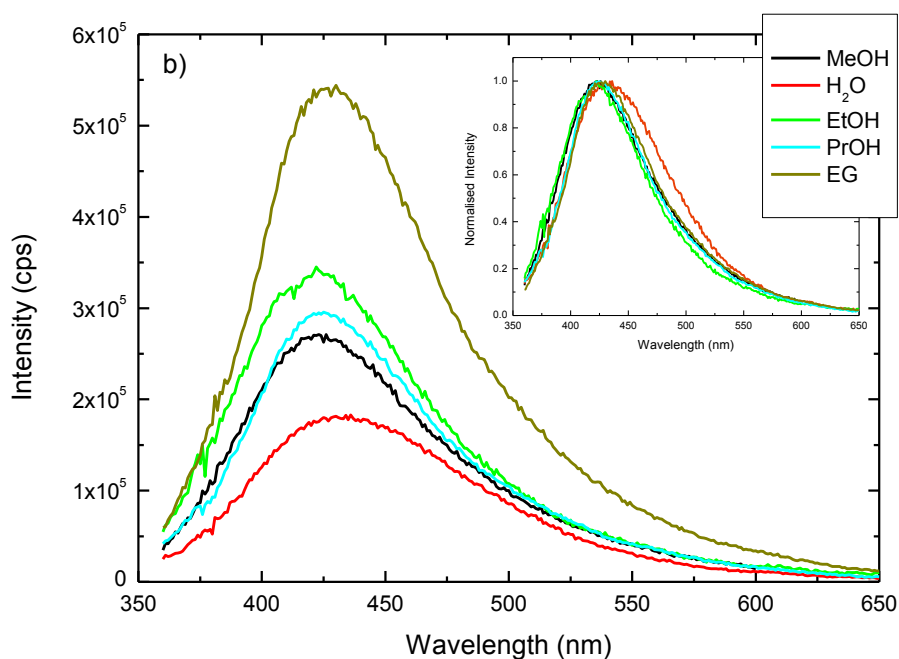
Figure 4.4. Absorption corrected emission of Kaede (a) and HBDI (b), with the normalised spectra inset. Measurements were made at a concentration of 13 μM and 16 μM respectively.

The Stokes shifts for Kaede and HBDI are listed in Table 4.1. For Kaede the shift was calculated from the maximum absorption wavelength to the top of the shortest wavelength peak in the emission. Both chromophores exhibit a moderate Stokes shift, where the shift is greater for HBDI in all cases. Neither chromophore exhibits a Stokes shift which shows a strong dependence on polarity, although for both the Stokes shift is greatest in water. This result suggests that there is not a large change in dipole moment between ground and excited state for either chromophore.

	Kaede				HBDI		
	λ_{abs} (nm)	λ_{fl} (nm)	Stokes Shift / nm (cm^{-1})	ε ($M^{-1}cm^{-1}$) at max	λ_{abs} (nm)	λ_{fl} (nm)	Stokes Shift / nm (cm^{-1})
MeOH	434	492	58 (2716)	1.71×10^4	371	423	52 (3314)
H$_2$O	429	504	75 (3467)	1.77×10^4	369	436	67 (4614)
EtOH	436	499	63 (2896)	2.05×10^4	375	423	48 (3026)
PrOH	438	499	61 (2791)	2.04×10^4	376	425	49 (3066)
NMF	438	506	68 (3068)	1.66×10^4	-	-	-
F	444	502	58 (2602)	1.68×10^4	-	-	-
EG	439	501	62 (2819)	1.83×10^4	377	430	53 (3269)
Gly	442	502	60 (2704)	2.17×10^4	-	-	-

Table 4.1. Maximum absorption and emission wavelength and Stokes shifts for Kaede and HBDI and extinction coefficients for Kaede at the maximum absorption wavelength.

Figures 4.5a and 4.5b illustrate that the peak wavelengths of the absorption and emission of the chromophores do not exhibit a dependence on either polarity or viscosity. Figure 4.5c indicates that for Kaede the fluorescence yield (measured from the integrated area of the emission for a fixed absorbance) has a slight negative dependence on solvent polarity, whilst there is negligible variation for HBDI. Figure 4.5 d illustrates the weak viscosity dependence of the quantum yield for both chromophores.
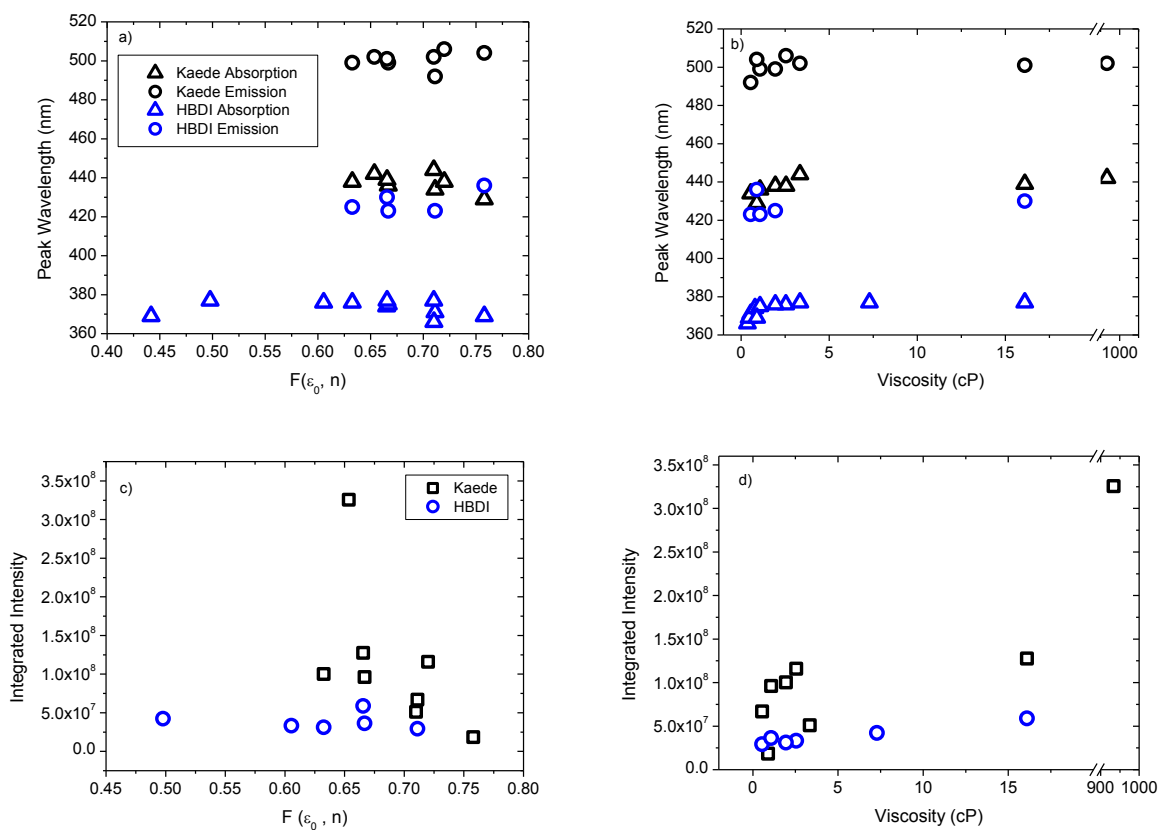
Figure 4.5. The first moment of the Kaede (black) and HBDI (blue) absorption spectra (triangles) and emission spectra (circles) against the polarity function (a) and viscosity (b), showing no dependence on either parameter. The integrated intensity of the emission of Kaede (black) and HBDI (blue) against the polarity function (c) and viscosity (d), showing a weak dependence on viscosity.

In contrast to HBDI, the emission spectrum of Kaede shows a strong dependence on the excitation wavelength. Such a dependence is unexpected for an isolated molecule in solution, which usually follows the Kasha's rule[18]. Figure 4.6 shows the evolution of the emission spectrum of Kaede in propanol when the excitation wavelength is tuned from 370 nm to 480 nm. As the excitation wavelength is increased, the spectrum shifts to the red by

up to 24 nm. The lower wavelength peak also becomes weaker relative to the higher

wavelength peak. This deviation from Kasha's rule could indicate the presence of multiple

states. A 'red edge effect' has been reported for other molecules and can give rise to

excitation dependent spectra, when a distribution of solvation sites causes inhomogeneous

broadening of the absorption spectra on a timescale longer than fluorescence decay. Often

in such cases a long 'tail' is seen in the low energy side of the absorption spectrum[19-22].

Figure 4.2a shows that this is not the case for the absorption of Kaede. Furthermore, the

shifting of the emission on red-edge excitation is not usually accompanied by a change in

shape. Hence an alternative explanation is that the emission observed is from species with

distinct spectra. Each species would then have a different emission spectrum, provided they

were not coupled by FRET, which is unlikely for such a short fluorescence lifetime and

relatively low sample concentration[22].
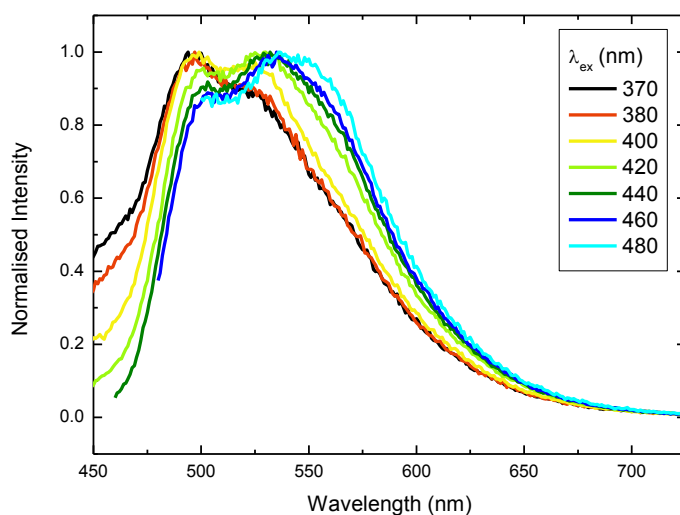
Figure 4.6. Normalised emission of Kaede in propanol excited between 370 nm and 480 nm.

The spectrum shows a dependence on the excitation wavelength and the existence of two

states is clear.

Similarly to Kaede, dyes in imidazolium ionic liquids exhibit excitation wavelength dependent emission spectra which are composed of two bands; one strong band and a second smaller band at higher wavelength. It has been shown that these features are due to the existence of a monomeric form of the dye and aggregated structures which differ in energy. Upon dilution, the higher wavelength peak gradually disappeared as the structures dissociated, eventually leaving just a monomer peak[21,23]. A solution of Kaede in propanol was gradually diluted from 0.5 mM to 0.0125 µM (Figure 4.7). For most measurements a 1mm quartz cuvette was used. However for concentrations above 63 µM, where the optical density was too high, a 1mm cuvette was used and the measurements scaled according to the Beer-Lambert Law (equation 1.1). This may have resulted in the underestimation of the emission intensity for these two measurements. As the sample was diluted, the spectrum blue shifted and narrowed, consistent with dissociation of an aggregate. At higher concentrations (≥ 250 µM), the lower wavelength peak is not visible. However this is likely to be due to reabsorption of emission below 500 nm. The emission spectra (Figure 4.7b) thus reveal the existence of monomeric (shorter wavelength) and higher aggregate (longer wavelength) forms. These data, together with the wavelength dependence (Figure 4.6), confirm the existence of an equilibrium between monomeric and aggregated forms of Kaede in solution. The aggregate evidently persists to quite low concentrations. However, Figure 4.7a shows that little change in the low energy part of the absorption spectrum is observed upon dilution from 0.5mM to 15uM (at very low concentrations additional contributions can be seen in the absorption spectrum at higher energy but not in the emission spectrum). This may suggest an enhanced absorption to higher electronic states in the monomer form or solvent effects. The same dilution causes a shift in the emission of approximately 20 nm, indicating that a greater change occurs in the excited state.
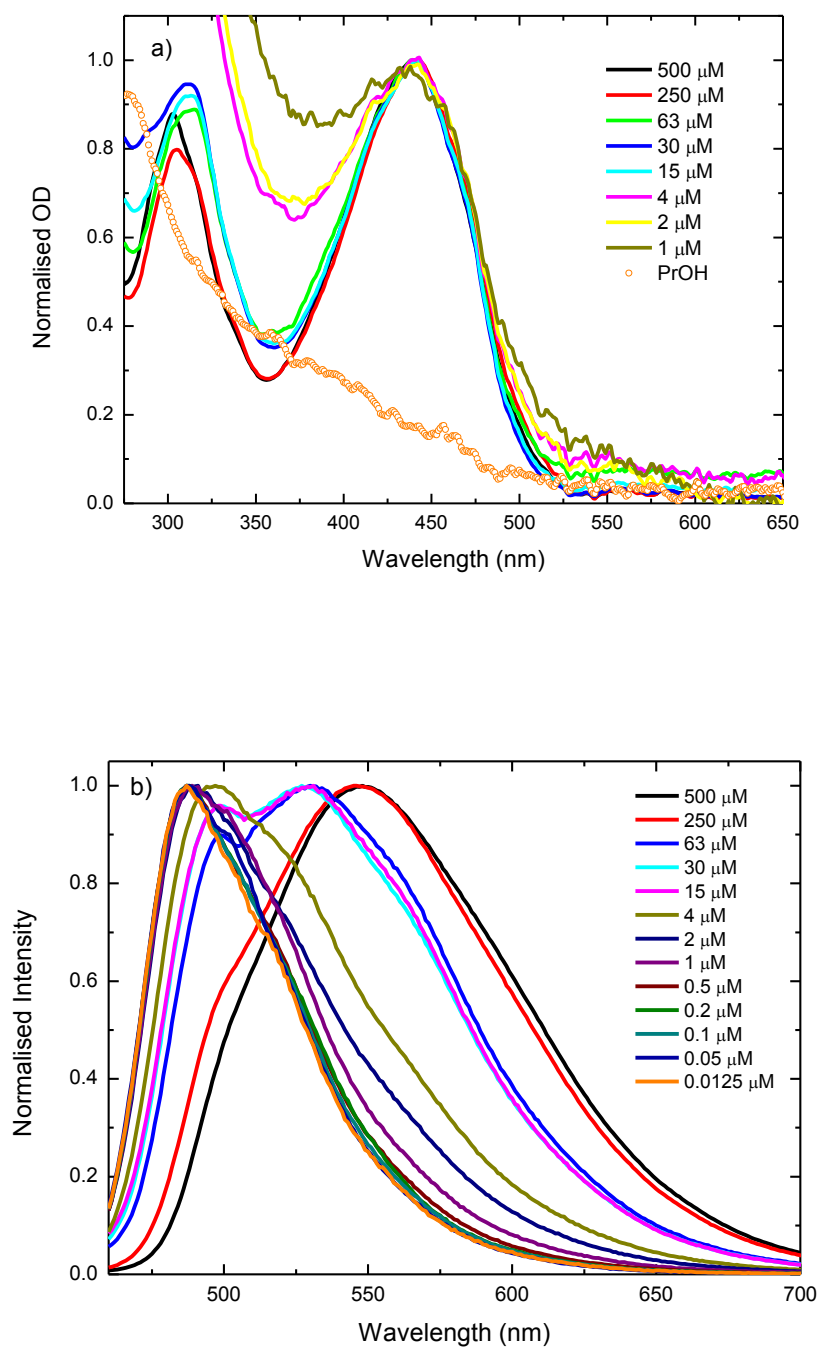
Figure 4.7. Normalised steady-state absorption (a) emission (b) spectra of Kaede in propanol diluted from c=0.5 mM to c = 0.0125 μM. While dilution has little effect on the lowest energy absorption, the emission spectrum clearly blue shifts and narrows.

Figure 4.8 shows the integrated intensity of the emission spectrum of Kaede in propanol plotted against sample concentration. In contrast to what would be expected for emission from monomeric species, the fluorescence displays a nonlinear dependence on concentration. Figure 4.7b shows that the shape of the emission spectrum does not change when increasing the concentration from 0.0125 μM to 0.45 μM. Thus, the integrated intensities obtained from concentrations between these points can be fitted with a straight line function and extrapolated to predict the dependence on concentration expected for a monomeric sample. This analysis is shown as a red line in Figure 4.8. It is clear that aggregate formation enhances the emission above that which would be expected solely from the monomer. For example at a concentration of 0.5 mM, the integrated intensity is over double that which would expected for a completely monomeric sample. Thus aggregation seems to enhance emission. Most chromophores exhibit fluorescence quenching upon aggregation[24]. However it has already been shown that some fluorophores experience aggregation-induced emission (AIE) and have found use as optical LEDs and biosensors[25-27]. AIE generally arises from the restriction of the motions which are associated with non-radiative decay[28]. Thus, enhancing the fluorescence quantum yield of the aggregated form compared to the monomer. This will be discussed further for Kaede in the light of the time-resolved fluorescence.
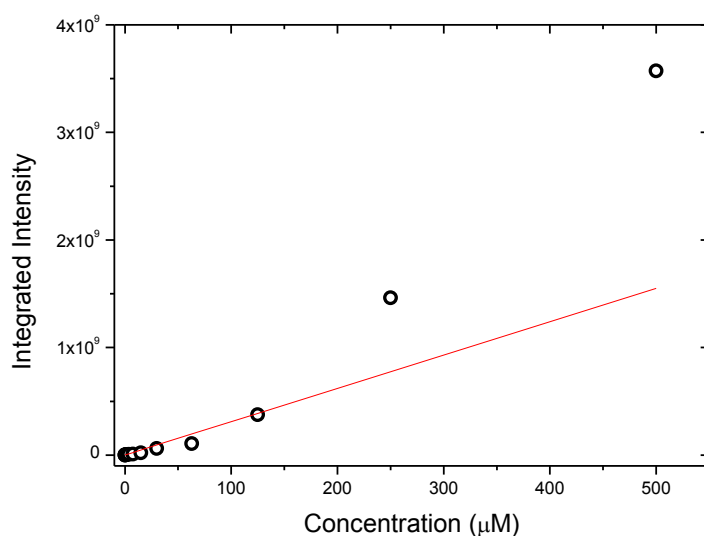
Figure 4.8. The integrated area of the emission of Kaede in propanol as a function of sample concentration exhibits a non-linear dependence due to emission from the dimer.

4.3.2. pH Dependence

The pH dependence of the absorption was investigated for Kaede in water at a concentration of 13 μM, where both monomers and aggregates exist. Hydrochloric acid and potassium hydroxide were used to alter the pH between 1.2 and 13, with selected spectra shown in Figure 4.9. The anion begins forming at pH 7 and the neutral/anion pK_a was determined to be 7.9, close to that of HBDI which is 7.8[29]. Upon formation of the anion, the maximum absorption wavelength is redshifted to 486 nm. In contrast to HBDI no clear isosbestic point is observed for anion formation, this could be due to the influence of the oligomer. However, the narrow single peak of the steady-state emission spectrum (Figure 4.10b) of the anion suggests that the anionic chromophore is monomeric. This may reflect

stabilization of the anion by solvation and aggregate dissociation due to Coulombic repulsion.

At low pH (pH = 1) a small, 10 nm blueshift of the absorption is observed compared to the neutral. For HBDI, the cation/neutral pK_a was found to be 2.7[29], indicating that HBDI is relatively hard to protonate. However, for Kaede in water the pK_a of the cation could not be determined and no isosbestic point is observed. This may be because of the existence of multiple ground-states, but also because the cation and neutral forms could have very similar spectra; there are changes in the spectra between pH 1 and 5, but they are small and not readily assigned to an equilibrium between two distinct states.
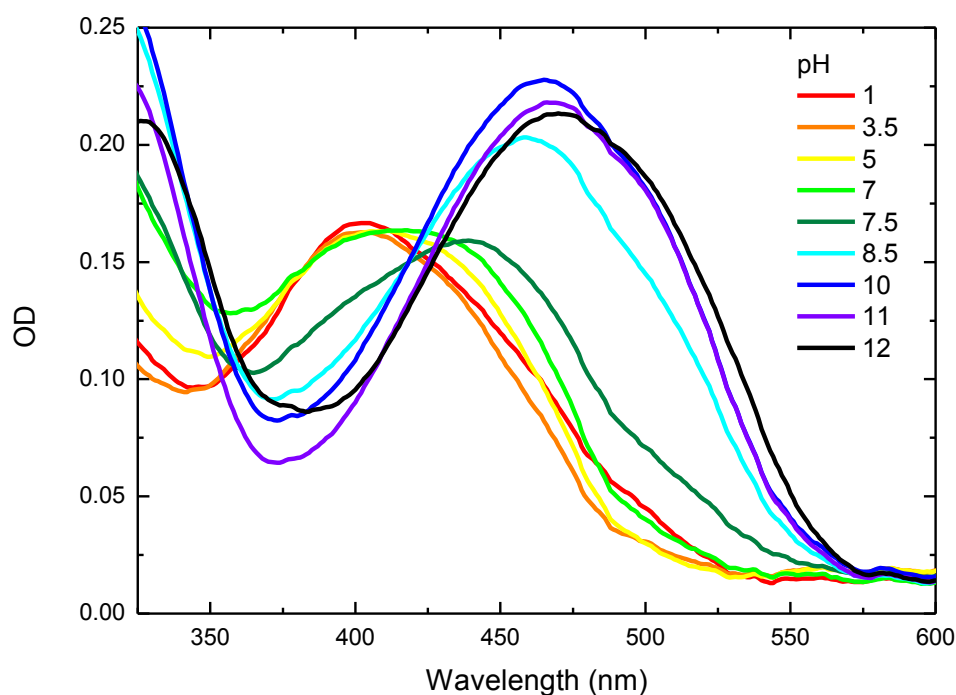
Figure 4.9. The pH dependence of the absorption of Kaede in water from pH = 1 to 12. The anion is red shifted to 486 nm and the cation is blue shifted by 10 nm.

The acid/base behaviour of the steady-state absorption and emission of Kaede in formamide (Figure 4.10) and ethylene glycol was also investigated. Sodium hydroxide was added to form the anion and hydrochloric acid added to form the cation. Similarly to the result in water and that of HBDI, in both solvents the absorption of the anion is red shifted by 60 - 80 nm and the OD at the peak wavelength increases. However, in contrast to the behaviour in water, lowering the pH results in a small (15 nm) redshift of the maximum absorption wavelength. This is similar to the behaviour seen in formation of the HBDI cation which is redshifted by roughly 23 nm from the neutral[29]. This behaviour is reflected in the steady-state emission, where the cation fluorescence is red shifted by approximately 30 nm and the anion by roughly 70 nm (Figure 4.10b) compared to the neutral state. The emission spectrum of the anion is significantly narrower than those of the neutral and cation. This suggests that the anion exists as the monomer in non-aqueous solvents.
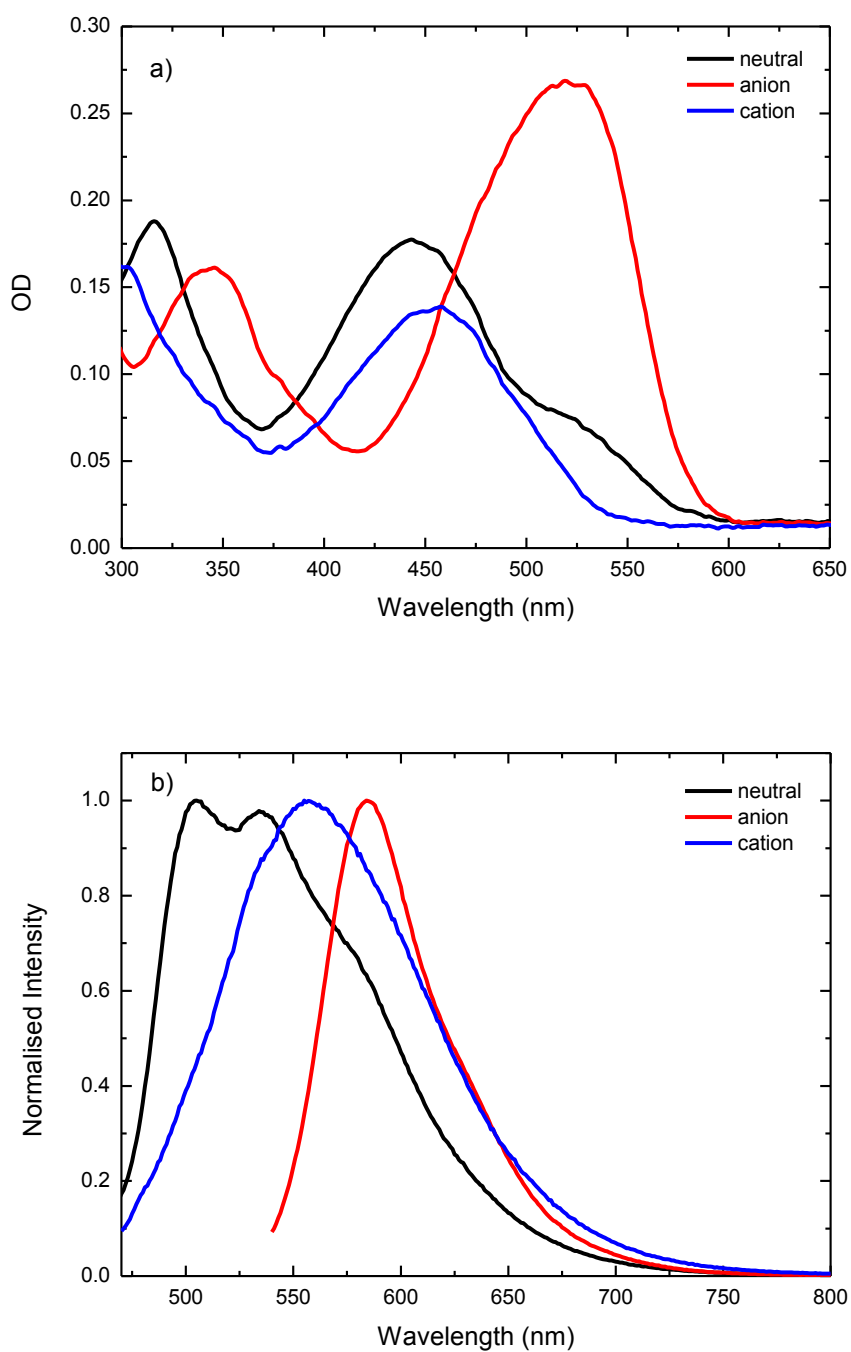
Figure 4.10. The UV-Vis absorption (a) and steady-state fluorescence (b) of neutral (black), anionic (red) and cationic (blue) Kaede in formamide.

4.3.3. NMR Spectroscopy

The NMR spectrum of Kaede in D_2O at a concentration of 10 mM was measured using a Bruker 500MHz spectrometer – clearly at such a high concentration aggregates are expected. The spectrum was assigned as shown in Figure 4.11 and indicates the presence of a single ground-state isomer. Multiple ground-state isomers exchanging at a fast rate could be present within the solution leading to averaged spectra. However the calculations presented in Section 4.3.5 suggest that the isomers would not be able to exchange freely due to the large energy barriers. Simulations of the NMR spectra of other possible isomers indicate that the spectra should be sufficiently different from these to be detected. Thus we conclude there is a single ground-state isomer.
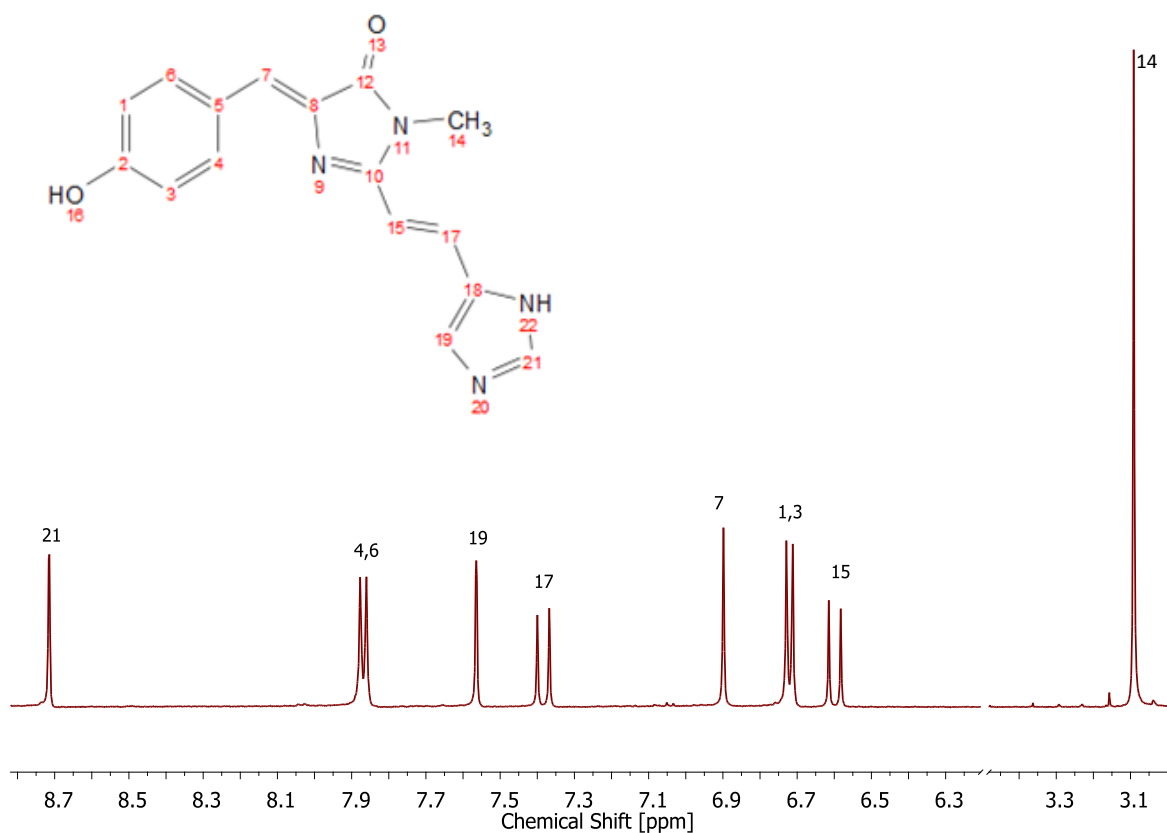
Figure 4.11. The NMR spectrum of Kaede in D_2O shows a single ground-state configuration.

95

HBDI undergoes *cis-trans* isomerisation upon irradiation with UV light[30-32]. This creates a metastable *trans* population, the concentration of which can be measured quantitatively using NMR spectroscopy (Chapter 3). Furthermore, the *trans* population can be detected through small shifts in the steady-state electronic absorption and emission spectra. To determine whether the Kaede chromophore undergoes photoisomerisation, a 10mM solution was prepared in methanol-d4 and irradiated with a 405 nm, 20 mW collimated LED. NMR and steady-state absorption spectra were recorded after different irradiation times to check for the presence of a new isomer. As Figure 4.12 shows, irradiation does not result in the creation of a new set of well defined resonances in addition to the original peaks, as was previously observed for HBDI and shown to be characteristic of isomerization (Chapter 3). However, some of the original peaks do shift to higher ppm and this shift increases with irradiation time. Additionally, the intensities relative to the solvent peaks decrease and the spectrum becomes noisy, indicating a change in the sample. No change in the sample was observed when leaving the sample overnight before irradiating. Thus, the spectral changes are a result of a photoinduced process. Two possible explanations for these observations are photoinduced aggregation of the chromophore or the formation of radicals. Both processes can cause shifting of peaks as well as changes in the number, shape and intensity of resonances[33,34]. However, upon adding a radical initiator (AIBN), no increase in the rate of spectral change was observed. Thus it is likely that photoinduced aggregation is observed at these high concentrations. As the aggregated species persists after irradiation, there must exist a barrier to disaggregation in the ground state.
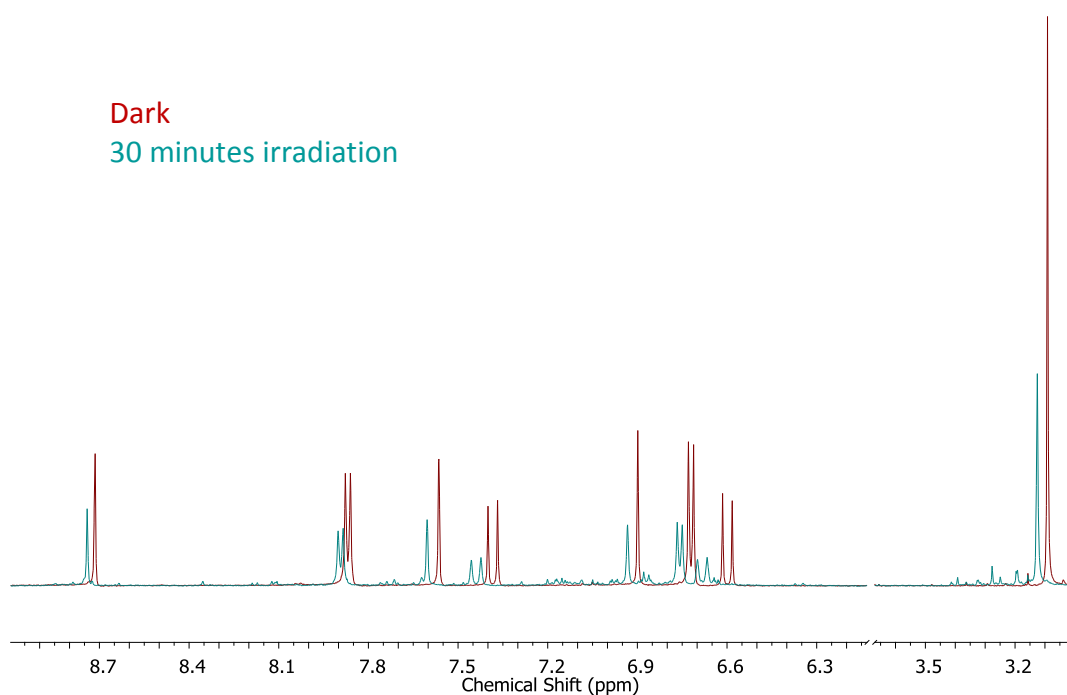
Figure 4.12. NMR spectra of Kaede in MeOH-d4 before (red) and after (green) irradiation. After irradiation new peaks appear with the original resonances shifting and decreasing in intensity.

It was shown in Chapter 3 that for HBDI, photoisomerisation causes shifting of the steady-state absorption and emission spectra. Figure 4.13 shows the equivalent measurements for Kaede in MeOH-d4 at a concentration of 13µM. Whilst a decrease in the intensity was observed, there was no observable shifting or shape change of the spectra. Thus, again there is no evidence for the formation of new isomers in the electronic spectra.
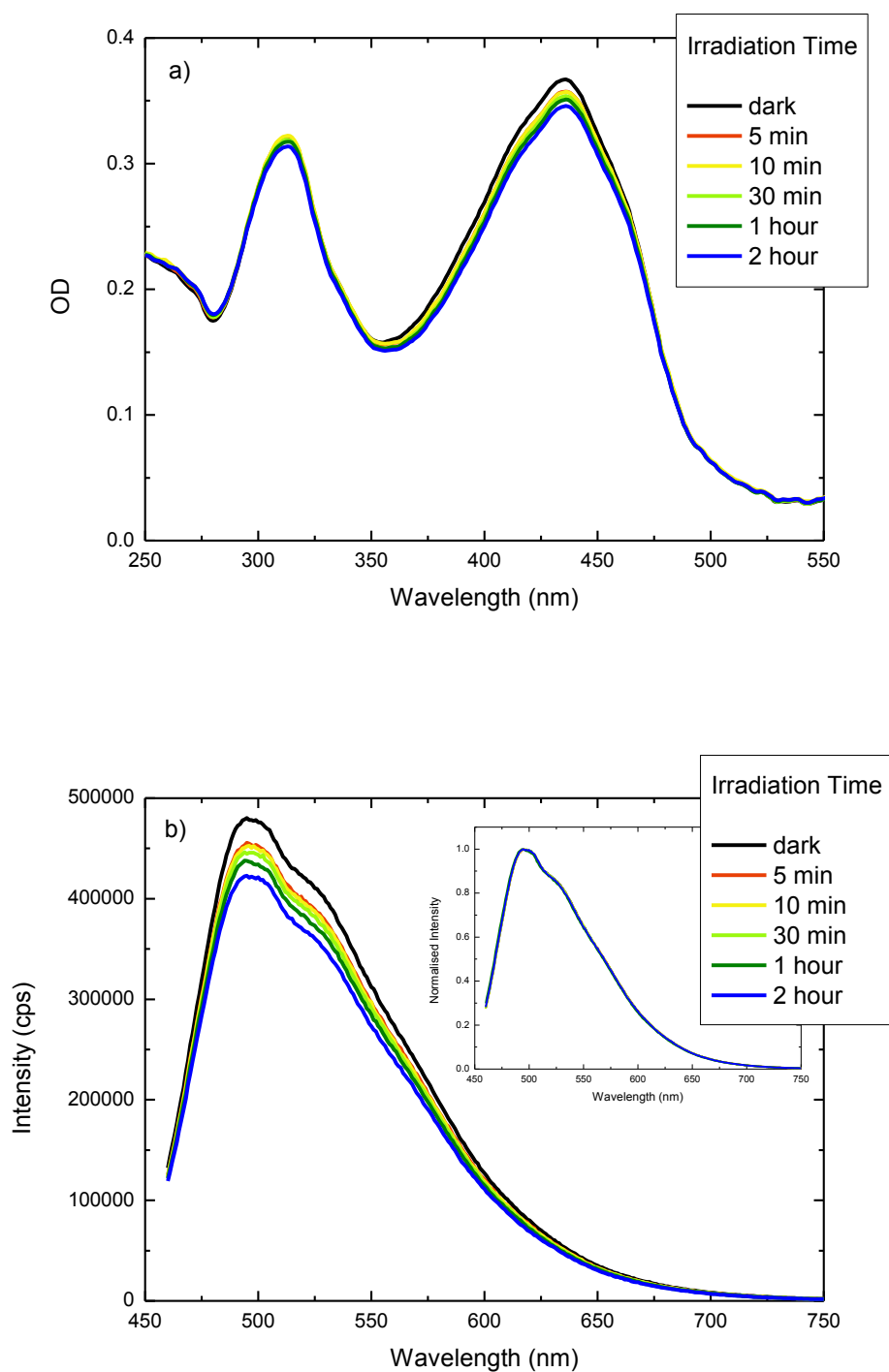
Figure 4.13. (a) UV-Vis absorption of Kaede in MeOH before irradiation (black) and after increasing irradiation times up to 2 hours (blue). (b) Fluorescence of Kaede in MeOH after the same irradiation times with the normalised spectra inset. The Intensity of the spectrum decreases with no shifting or change in spectral profile.

4.3.4 Steady-state Temperature Dependence

For HBDI the fluorescence quantum yield increases more than 1000 times upon lowering the temperature from 295K to 77K[35]. An enhancement of the fluorescence is also observed for Kaede upon cooling. Figure 4.14 shows the emission spectrum of Kaede in a 13µM 3:1 mixture of ethanol:methanol as the temperature is reduced from room temperature (300 K) to the glass transition temperature (77 K). As the temperature is lowered, the quantum yield increases over 100 times and strong vibronic structure is observed. The spectrum of HBDI is broad and structureless in some solvents[36]. However, in non-hydrogen bonding solvents, weak vibronic structure is observed at very low temperatures[37]. From the HBDI vibronic structure, a frequency of 1470 ± 60 cm^{-1} was determined and was assigned to the C=N + exocyclic C=C stretching mode from comparison to the resonance Raman spectrum[37]. This is close to the value of 1400 cm^{-1} given by the strong vibronic progression of the Kaede low temperature spectrum (Figure 4.14). Clearly for Kaede, the most probable transition is the 0-1 rather than 0 -0. This was also found for HBDI, where it was proposed that this is indicative of significant structural change between the excited and ground-states.
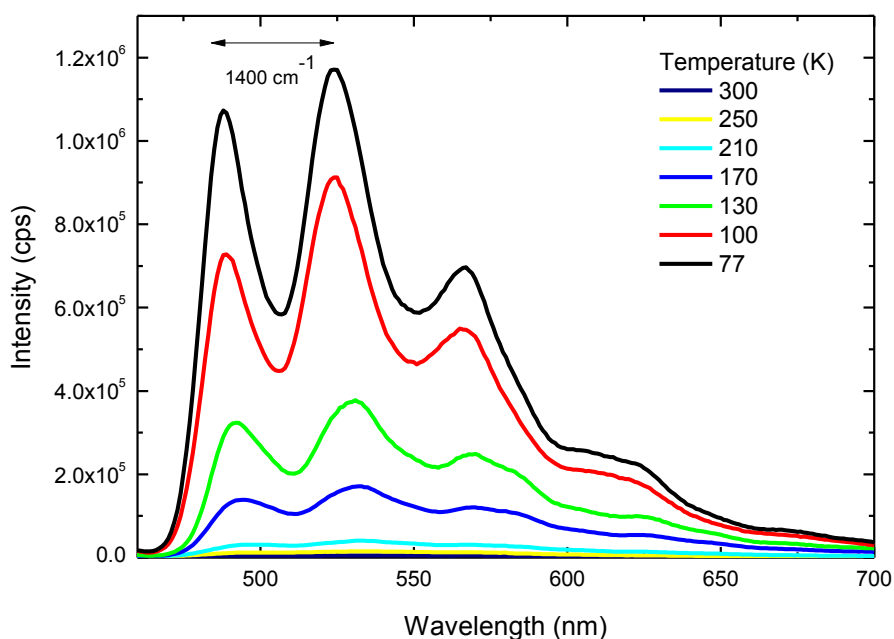
Figure 4.14. The evolution of the steady-state fluorescence of Kaede in a 3:1 ethanol:methanol mixture from 300K to 77K. As the temperature is lowered, the intensity increases and vibronic structure appears in the spectrum.

The increase in the quantum yield upon cooling indicates that as the temperature is decreased, non-radiative decay channels are hindered. Cooling to the glass transition temperature strongly restricts the ability of the chromophore to move. This is analogous to the effect of the protein matrix, where interactions restrict the freedom of the chromophore, thus suppressing the radiationless decay and enhancing the quantum yield[38].

Arrhenius analysis of the low temperature data reveals the activation energy for the radiationless decay process. The rate of nonradiative decay (k_{nr}) at each temperature was calculated from the emission spectrum according to,

$$k_{nr} = k_f \left(\frac{1-\varphi_F^R}{\varphi_F^R} \right),$$

(4.1)

where k_f is the radiative rate constant and φ_F^R is the quantum yield relative to that at 77K,

measured from the integrated area of the spectrum[38]. As k_f is unknown for Kaede, the

radiative rate constant was calculated using the relation,

$$k_f = \frac{\varphi}{\tau},$$

(4.2)

where φ (0.33) and τ (4.8 ns) are the quantum yield and lifetime of the Kaede chromophore

in the protein respectively[2,39]. This gives a radiative rate constant of 6.9 x 10^7 s^{-1}.

The activation energy for the radiationless decay can be determined from the gradient of a

linear fit to a plot of $\ln(k_{nr})$ against 1/T. Unlike the biphasic Arrhenius plot of HBDI,

analysis of Figure 4.15 yields a single activation energy of 10.8 kJ mol^{-1} for Kaede[38]. This is

higher than the value of 6 ± 3 kJ mol^{-1} determined for HBDI above the solvent melting

temperature (T_m) and comparable to the activation energy of 12 ± 2 kJ mol^{-1} below T_m. This

increase in the activation energy for radiationless decay above T_m is consistent with the

increased quantum yield of Kaede compared to HBDI.
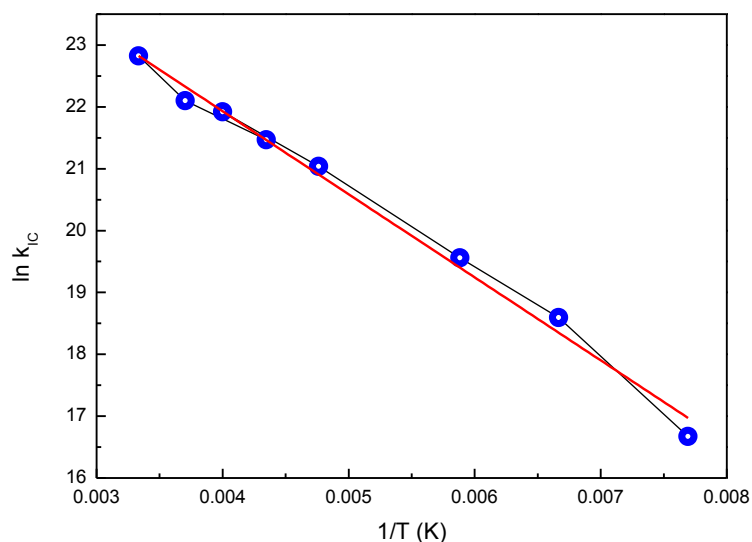
Figure 4.15. Arrhenius analysis of Kaede gives an activation energy of 10.8 kJ mol^{-1}.

For the sample concentration used in these measurements (13 µM), the aggregate will contribute to the emission spectrum (Figure 4.7). Therefore it would be desirable to repeat the measurement at a sufficiently low concentration such that only fluorescence from the monomer is detected.

4.3.5. Ground-state Calculations

The ground-state structures of HBDI and Kaede were optimized using Gaussian software to determine the minimum energy geometry. Calculations were made at the DFT B3LYP level using the basis set 6-31G++ (d,p), ensuring that there were no imaginary frequencies upon completion. The dipole moment of Kaede was found to be 3.8 D, higher than that of HBDI (1.6 D). Figure 4.16 shows the HOMO molecular orbital surface for Kaede, indicating that the

conjugation is extended across the whole molecule. The extended conjugation is consistent with the redshifted absorption spectrum compared to HBDI.

The NMR spectra of Kaede before and after irradiation suggest the presence of a single ground-state isomer (Section 4.3.3). Whilst for HBDI, irradiation induces *cis-trans* isomerisation creating a metastable *trans* form (Chapter 3). To investigate the possibility that different isomeric forms of Kaede could be created photochemically then exchange freely to repopulate the original ground-state, the barriers to ground-state isomerisation should be calculated.
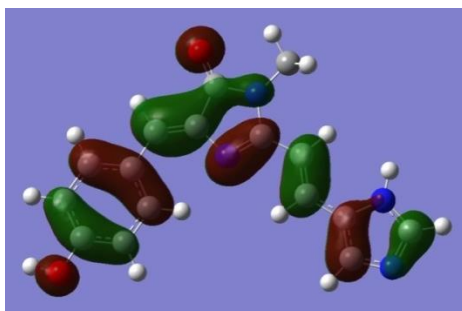
Figure 4.16. The HOMO surface for Kaede shows that the conjugation extends across the whole molecule.

4.3.6. IR Spectroscopy

The ground-state IR spectra of Kaede and HBDI were calculated for the optimised structures using Gaussian software as described in Section 4.3.5. The calculated frequencies were corrected using the recommended scaling factor of 0.9613 (Figure 4.17)[40]. Some peaks associated with structures shared by both chromophores are unchanged. For example the strong carbonyl stretching mode at 1700 cm^{-1} and the peaks at 1452 cm^{-1} and 1446 cm^{-1}

associated with bends of the methyl groups on the im1 ring. The extended conjugation of

Kaede resulted in the shifting of some peaks to lower frequencies. For example the intense

ring modes at 1627 cm^{-1} and 1589 cm^{-1} in HBDI, are downshifted in Kaede to 1618 cm^{-1} and

1583 cm^{-1} respectively. The extended structure of Kaede also results in closely spaced

modes which may cause broadening of certain features in the measured spectrum, such as

the 1618 cm^{-1} peak which contains two modes. There are also some modes exclusive to the

Kaede spectrum, such as the strong peak at 1439 cm^{-1} due to a delocalized stretching mode

of both the imidazole rings and the connecting bridge. In addition there is a weak mode at

1530 cm^{-1} due to the stretching of the C=C bond between the imidazole rings.
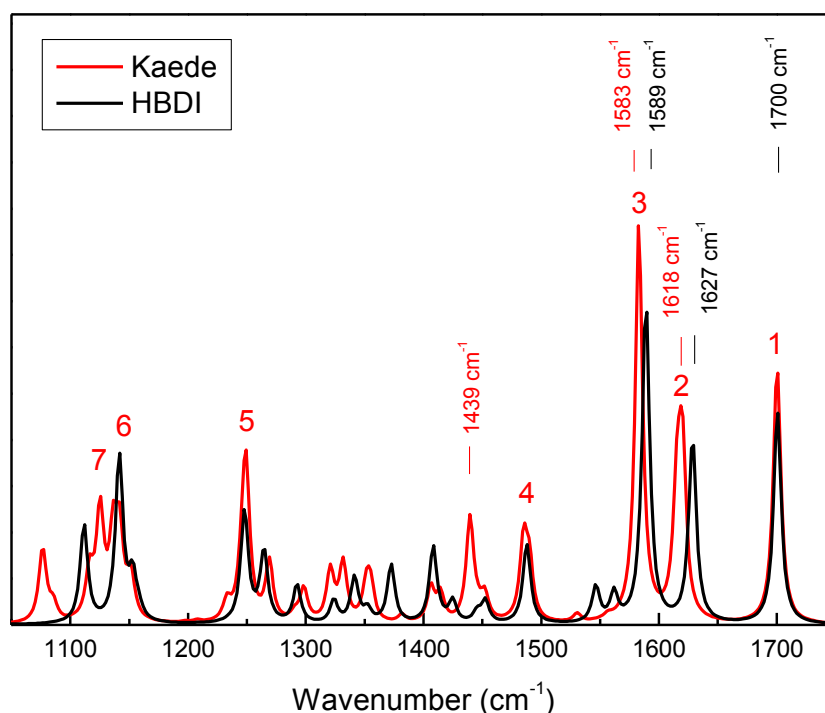
Figure 4.17. Calculated ground-state IR spectra of Kaede (red) and HBDI (black). For both

chromophores the carbonyl peak is located at 1700 cm^{-1}. Some peaks in the Kaede spectrum

are shifted relative to those of HBDI due to the extended conjugated structure. The feature

at 1439 cm^{-1} is exclusive to the Kaede spectrum. The numbers 1-7 correspond to peaks observed in the measured steady-state IR spectrum (Figure 4.18).

The steady-state IR spectrum of Kaede was obtained by mixing with Nujol to create a mull. Figure 4.19 shows the spectrum of Nujol (black) and that of the mixture (red). The numbered peaks correspond to those labelled in Figure 4.17. The carbonyl peak is observed at 1694 cm^{-1} and the two modes underlying the broad peak at 1618 cm^{-1} in the calculated spectrum are resolved as two peaks at 1650 cm^{-1} and 1632 cm^{-1} in the measured spectrum.
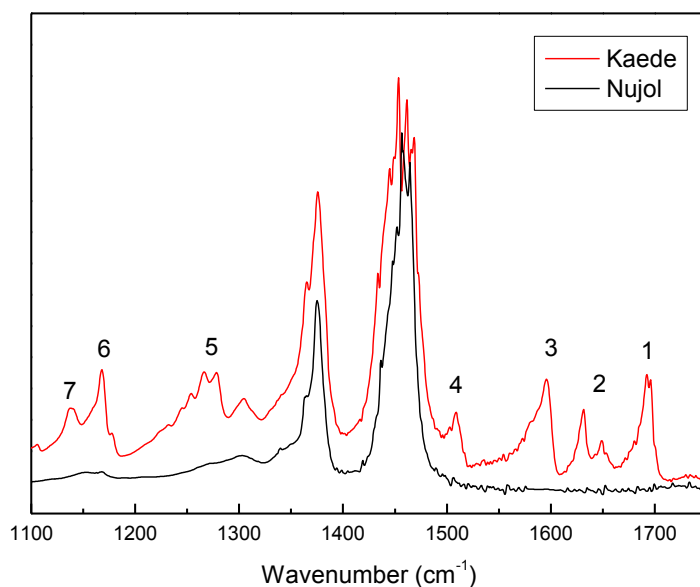
Figure 4.18. The steady-state IR spectrum of a Kaede – Nujol mull (red) and pure Nujol (black). The numbered peaks correspond to those in the calculated spectrum in Figure 4.18.

The time-resolved IR (TRIR) spectra of Kaede and HBDI in methanol were recorded at the

Rutherford Appleton Laboratory as described in Chapter 2. Figure 4.19 shows the spectra at

selected times after the pump pulse. The labelled peaks in Figure 4.19a, correspond to those

in Figures 4.17 and 4.18. For HBDI the broad carbonyl band is clearly visible around

1700 cm^{-1}, whereas for Kaede the band is very small. The steady-state IR spectrum (Figure

4.18), shows that the carbonyl band (1) should be of comparable intensity to the main

bleach (3). Thus the 1700 cm^{-1} must be obscured by excited state absorption in the TRIR

difference spectrum (Figure 4.19a), suggesting that this mode is unchanged by electronic

excitation.
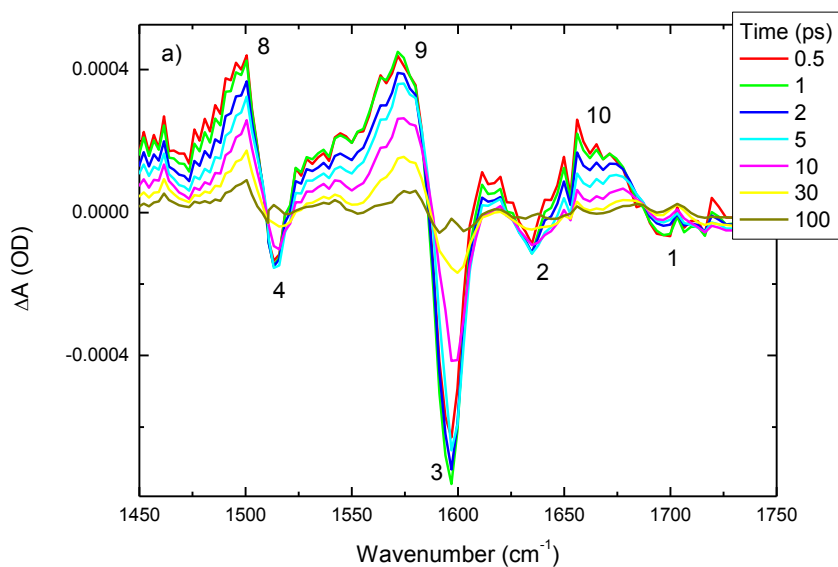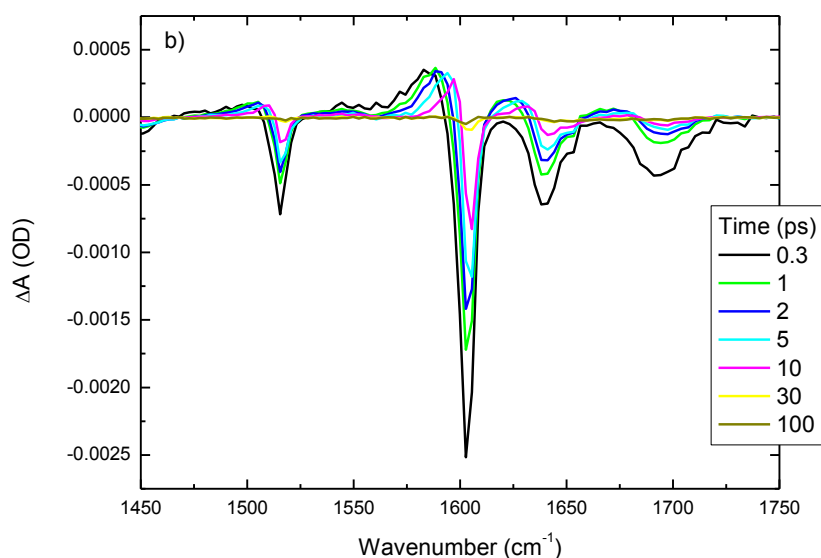
Figure 4.19. Selected TRIR spectra of Kaede (a) and HBDI (b) in methanol. The numbered

peaks correspond to those labelled in the calculated spectrum (Figure 4.17) and the steady-

state IR spectrum (Figure 4.18).

Figure 4.20 shows the TRIR spectra of Kaede and HBDI 1 ps after the pump pulse. The

spectra have been normalised to the main bleach around 1600 cm^{-1}. As predicted by

calculations (Figure 4.17), peaks 2, 3 and 4 in the Kaede spectrum are shifted to lower

frequency compared to the corresponding peaks in the HBDI spectrum. Where the C=C

stretch mode (2) is shifted from 1640 cm^{-1} in HBDI to 1634 cm^{-1} in Kaede and the phenyl ring

modes (3 and 4) at 1602 cm^{-1} and 1516 cm^{-1} in HBDI are downshifted to 1597 cm^{-1} and

1514 cm^{-1} respectively in Kaede.
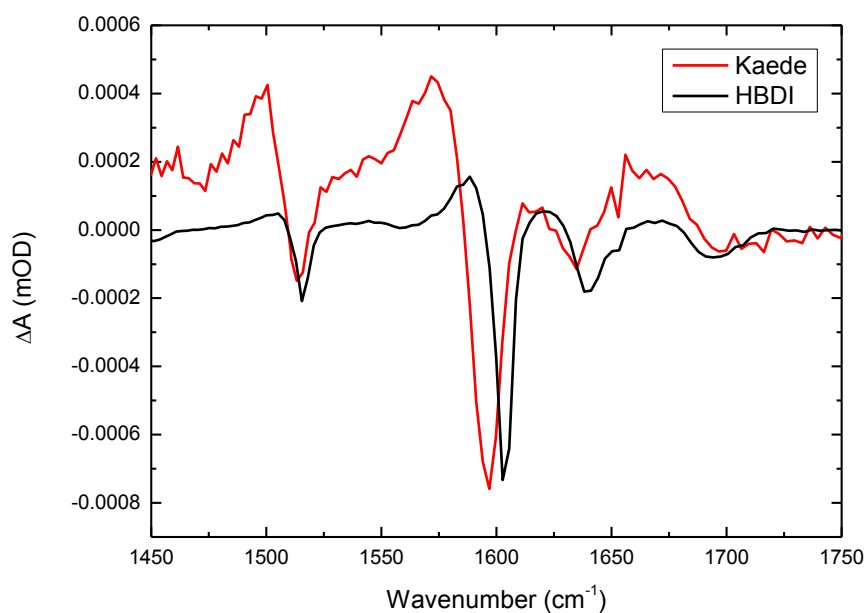
Figure 4.20. TRIR spectra of Kaede (red) and HBDI (black) 1ps after the pump pulse. The spectrum of Kaede is downshifted compared to HBDI.

The kinetics of the main bleach are shown in Figure 4.21. The recovery of the main bleach of Kaede is much slower and more complex than that of HBDI. For HBDI, the main bleach was fitted with a single exponential with a lifetime of 7 ps. On the other hand, for Kaede a biexponential function was required with a main component of 15 ps and a minor long component of 131 ps, giving an average lifetime of 38 ps.
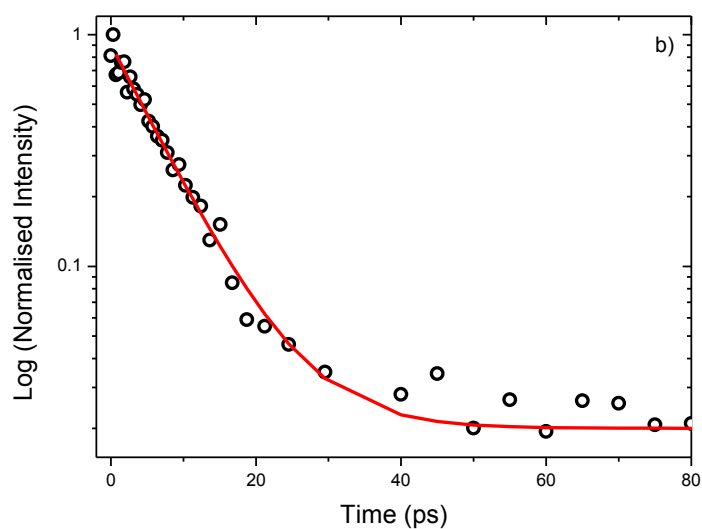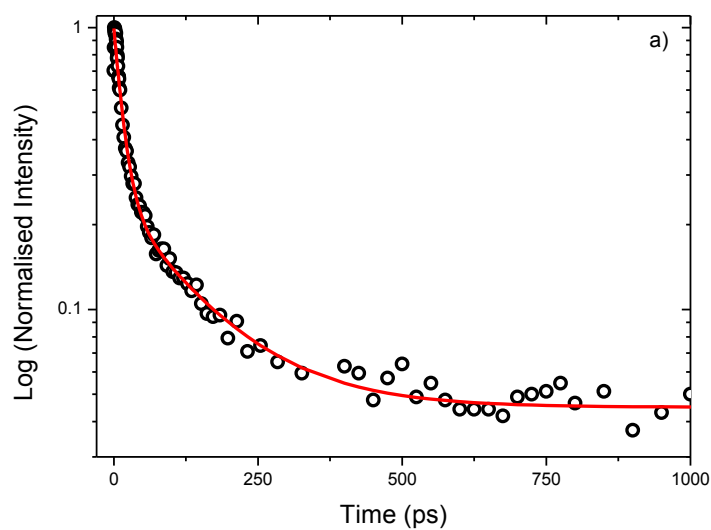
Figure 4.21. The recovery of the main bleach of Kaede (a) and HBDI (b) in methanol. Data shown as black circles and fits as a red line. Note the different time scales.

The fitting parameters for all peaks observed in Figure 4.20 are given in Table 4.2. For Kaede a biexponential function was required. This was composed of a long component ranging from 56 ps to 262 ps, and a shorter component of a few tens of ps. For HBDI either a single

or double exponential function was used. Where a double exponential was required, there was a shorter component of approximately 1 ps and a longer component of 5 – 10 ps which is comparable to the lifetimes recovered in the single exponential fits. The presence of the second exponential may be due to the formation of the aggregated form. In all cases, the kinetics of Kaede are longer than the corresponding kinetics of HBDI, and on average the lifetime is 5 – 15 times longer. Peaks 8 and 9 correspond to excited state modes and whilst this is not in agreement with the fluorescence lifetimes (Table 4.3), this could be due to the large errors in the TRIR measurements of Kaede.

		a_1	τ_1 (ps)	a_2	τ_2 (ps)	$<\tau>$ (ps)	Mode
8	K 1500 cm^{-1}	0.28	190	0.72	19	67	
4	K 1513 cm^{-1}	-0.17	222	-0.83	15	51	Phe ring
	H 1516 cm^{-1}	-1	8.0	-	-	8.0	Phe ring
9	K 1572 cm^{-1}	0.64	56	0.36	15	42	
	H 1592 cm^{-1}	0.48	5.9	0.52	1.2	5.9	
3	K 1597 cm^{-1}	-0.2	131	-0.8	15	38	Phe ring
	H 1602 cm^{-1}	-1	7.0	-	-	7.0	Phe ring
2	K 1635 cm^{-1}	-0.18	262	-0.82	31	73	C=C st
	H 1638 cm^{-1}	-1	5.1	-	-	5.1	C=C st
10	K 1657 cm^{-1}	1	37	-	-	37	
1	K 1698 cm^{-1}	0.21	144	0.79	14	42	C=O
	H 1691 cm^{-1}	-0.22	9.2	-0.78	0.83	2.7	C=O

Table 4.2. Fitting parameters for the kinetics of the TRIR spectra of Kaede (K) and HBDI (H) in methanol. The error on the average lifetime is at least 10%.

Glotaran software was used to perform global analysis on these TRIR data[41]. Rather than focusing on the kinetics at specific wavelengths, global analysis is performed on the complete time-resolved spectrum. Hence, this allows the determination of mechanisms and processes through the calculation of rate constants describing the whole system, rather

than just individual rate constants at each wavelength[42]. The rates can be determined using a sequential model, where each component decays sequentially (1 → 2 →…→n_{comp}), or a parallel model where each component decays individually. Both methods were applied to these TRIR data and almost identical results were obtained. Presented here are the results for the sequential analysis. The global analysis revealed two components were revealed; one short with a lifetime of 7.6 ps and one long with a lifetime of 98 ps. These components could be associated with the monomer (short component) and oligomer (long component). Figure 4.22 shows the decay associated spectra (DAS) recovered from the global analysis with the short component in black and the longer component in red. The spectra are similar although the long component has a lower amplitude. This is in agreement with the lifetimes obtained by fitting the kinetics of the individual peaks in the TRIR spectrum (Table 4.3.).
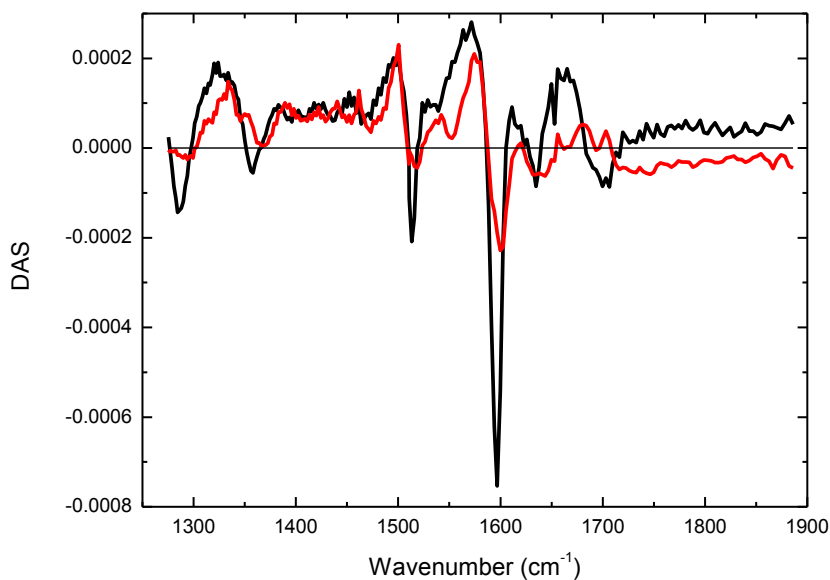
Figure 4.22. Decay associated spectra of the TRIR spectrum of Kaede in methanol. The shorter (7.6 ps) component is shown in black and the longer (98 ps) component in red.

4.4. Time-Resolved Fluorescence

4.4.1. Solvent Dependence

The time-resolved fluorescence gives insights exclusively into the excited state dynamics of a molecule. The time-resolved emission of Kaede was measured using ultrafast fluorescence up-conversion with a time resolution of 50 fs (Chapter 2).

The time-resolved fluorescence was measured at the peak wavelength of the steady-state emission (Figure 4.4.) in a variety of solvents at a concentration of 0.5 mM. Figure 4.23 shows that the decays are highly non exponential. There is also an observable viscosity dependence in the alcohol solvents, with the lifetime increasing with viscosity, although this behaviour does not extend to non-alcohol solvents. As Figure 4.24 shows the behaviour correlates with the steady-state quantum yields. The lifetime is significantly shorter in water, which could indicate a polarity effect. However, the decays are relatively long in the very polar solvents NMF and formamide. Suggesting an important role for the hydrogen bonding nature of the solvent in determining the radiationless decay rate.
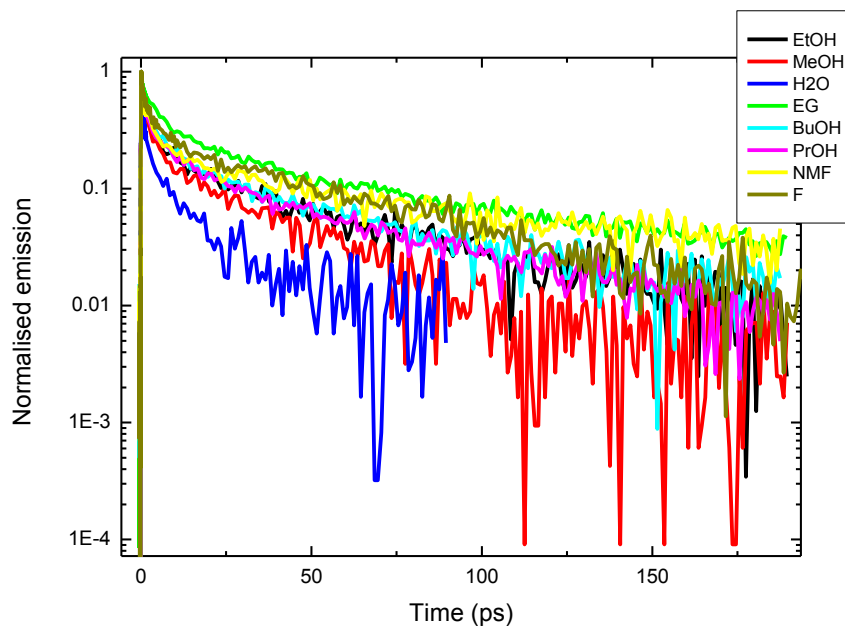
Figure 4.23. The time-resolved fluorescence of Kaede in ethanol (black), methanol (red), water (blue), ethylene glycol (green), butanol (light blue), propanol (pink), n-methyl formamide (yellow) and formamide (gold).
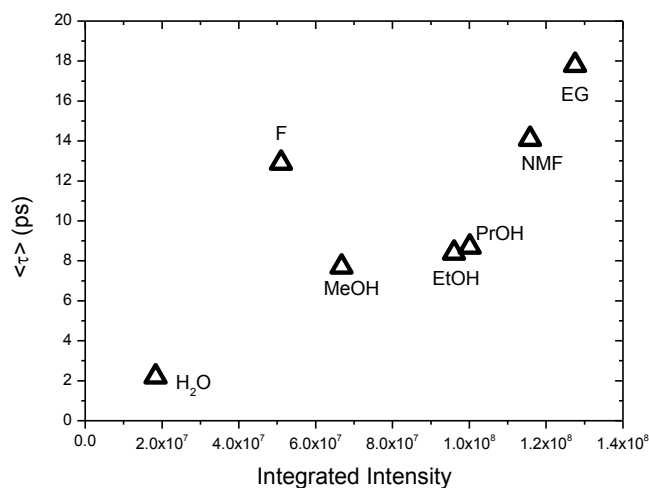
Figure 4.24. The average lifetime of the time-resolved fluorescence increases with the integrated area of the steady-state emission, showing the expected correlation between lifetime and quantum yield.

As Figure 4.23 shows, the decays are highly non monoexponential and accurate fitting requires 4 exponential components. The fitting parameters are reported in Table 4.3 where the amplitudes have been normalised to sum to unity. The sample concentration used for the up-conversion measurements was 0.5 mM and the detection wavelength 530 nm. As Figure 4.7 indicates, at this concentration and wavelength, emission from the aggregate will contribute to the measured decay. Thus the complexity of the kinetics is likely to be due, at least in part, to fluorescence from both the monomer and aggregate. In Section 4.3.6 it was shown that the global analysis of the TRIR spectrum of Kaede in methanol could be described by two DAS. The short component has a lifetime of 7 ps which is comparable to the average fluorescence lifetime (Table 4.3).

	MeOH	H$_2$O	EtOH	PrOH	BuOH	NMF	F	EG
τ_1 *(ps)*	36	13.2	51.8	49.4	60.6	93.4	46.5	81.5
a_1	0.12	0.13	0.13	0.15	0.11	0.14	0.25	0.18
τ_2 *(ps)*	6.7	-	5.7	5.4	11.9	5.9	-	9.6
a_2	0.41	-	0.17	0.18	0.15	0.2	-	0.25
τ_3 *(ps)*	2.1	1.1	1.03	1.18	1.53	0.97	2.8	1.63
a_3	0.24	0.39	0.33	0.33	0.35	0.35	0.34	0.22
τ_4 *(ps)*	0.4	0.17	0.15	0.18	0.17	0.13	0.26	0.12
a_4	0.24	0.48	0.36	0.34	0.39	0.31	0.41	0.34
<τ> (ps)	7.7	2.2	8.4	8.7	8.9	14.1	12.9	17.8

Table 4.3. Fitting parameters for the time-resolved fluorescence of Kaede in various solvents measured at the peak emission wavelength. The error on the average lifetime is less than 11 %.

Figure 4.25 shows the dependence of τ_1 and $\langle\tau\rangle$ on viscosity and τ_1 on polarity. Both parameters show a positive dependence on the solvent viscosity for the alcohols. However, τ_1 and $\langle\tau\rangle$ are both low in water and relatively high in NMF. As both solvents are highly polar, this again suggests a role for hydrogen bonding in the excited state decay of Kaede. More specifically, unlike water, NMF cannot donate hydrogen bonds. Thus the fast decay in water may be due to hydrogen bonds donated from the solvent which quench the fluorescence.

τ_1 decreases with polarity, as shown in Figure 4.25, in an almost linear fashion for the n-alcohols. However, the values in ethylene glycol and NMF do not fit this trend. The high value in ethylene glycol is likely due to the viscosity of the solvent, while that in NMF could be due to the distinct highly polar, aprotic nature of the solvent, as mentioned above.
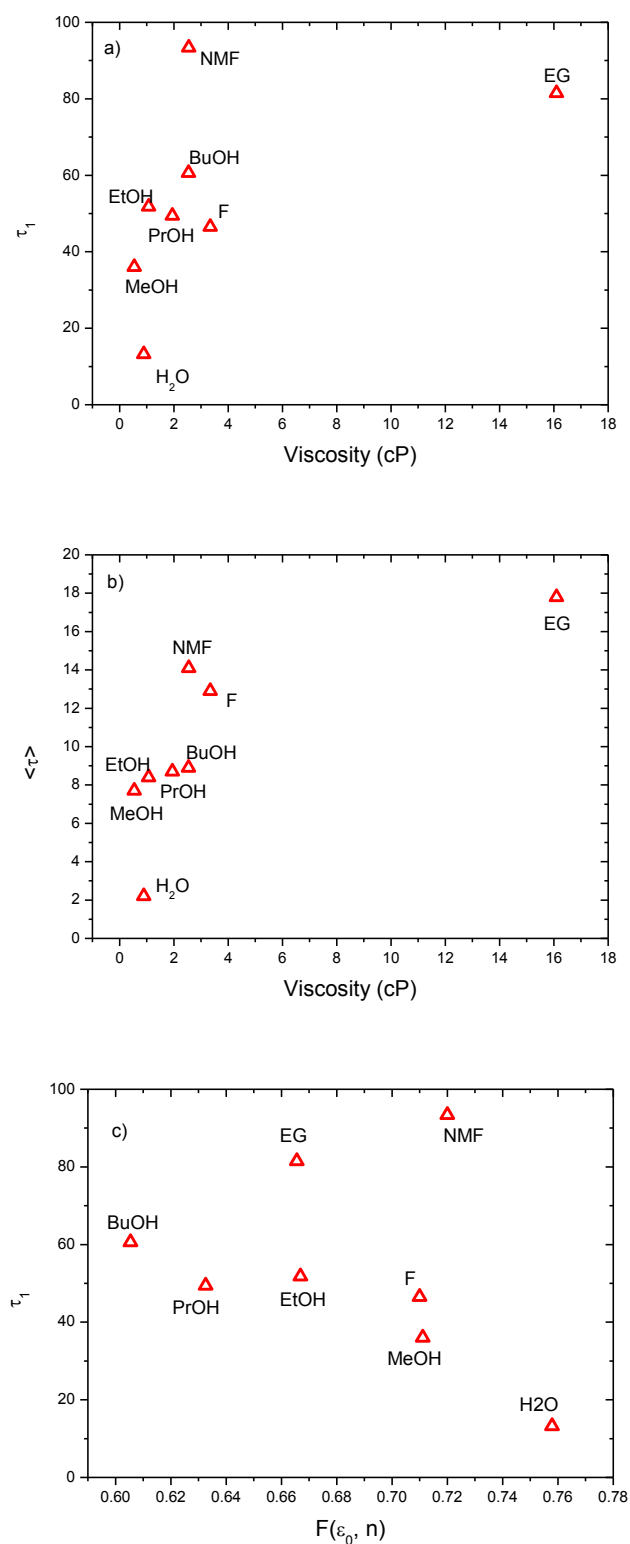
Figure 4.25. The dependence of the fitting parameters τ_1 and $<\tau>$ on viscosity, (a) and (b) respectively, and τ_1 on the polarity function (c).

Figure 4.26 shows the time-resolved fluorescence of HBDI in methanol, acetonitrile, octanol and ethylene glycol. In agreement with the higher quantum yield seen in steady-state measurements (Section 4.3.1), the fluorescence decays of Kaede are significantly longer than those of HBDI. The kinetics of HBDI are also less complex as they can be fitted with a biexponential function. This is likely to be because HBDI is monomeric. Table 4.4 lists the biexponential fitting parameters of the decays of HBDI, where the amplitudes have been normalised. The average lifetime in methanol is 7.7 ps for Kaede and only 0.24 ps for HBDI, an increase of over 30 times. In ethylene glycol the average lifetime increases 36 times, from 0.5 ps in HBDI to 17.8 ps in Kaede.
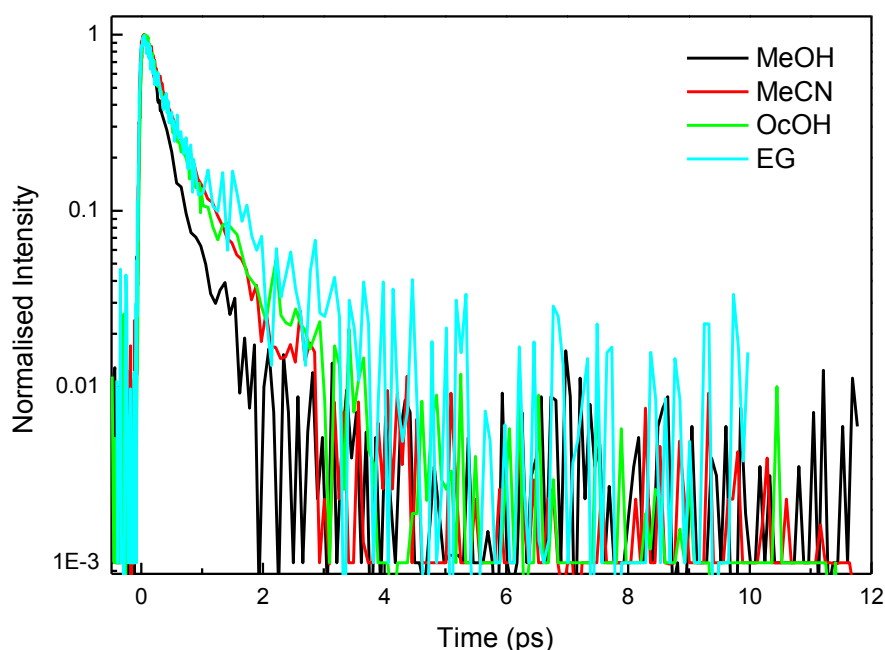
Figure 4.26. Time-resolved fluorescence of HBDI in methanol (black), acetonitrile (red), octanol (green) and ethylene glycol (blue).

	MeCN	OcOH	MeOH	EG
τ_1 *(ps)*	0.25	0.20	0.17	0.3
a_1	0.70	0.68	0.80	0.73
τ_2 *(ps)*	0.75	0.71	0.49	1.1
<τ>(ps)	0.40	0.36	0.24	0.50

Table 4.4. Fitting parameters for the time-resolved fluorescence decays of HBDI.

4.4.2. Wavelength Dependence

The complex decay of Kaede can be attributed to the presence of both monomers and higher aggregates within the sample. As Figure 4.7 shows, the aggregate is observed at relatively low concentrations (above 0.45 µM). Hence it was not possible to measure the time-resolved fluorescence of the monomer individually. However, the aggregate emission is redshifted compared to that of the monomer (Figure 4.7). Therefore their relative contributions to the time-resolved fluorescence should change as the detection wavelength is altered, where the aggregate will contribute more to the red side of the spectrum. The wavelength dependence of the time-resolved emission of Kaede in methanol is shown in Figure 4.27. Measurements were made at nine wavelengths from 470 nm to 580 nm. As the detection wavelength is moved to the red, the fluorescence decay becomes longer. This effect cannot be attributed to solvation as a rise time is not seen on the red edge of the spectrum. However, the aggregate is more fluorescent than the monomer (Figure 4.8) and emits at longer wavelengths. Therefore, the wavelength dependence of the fluorescence lifetime could be due to the enhanced fluorescence (hence longer lifetime) of the aggregate. Figure 4.27 shows that the decay time increases with wavelength from 470 nm to 520 nm. Subsequently little change is observed from 520 nm to 538 nm. Finally the kinetics become

longer from 538 nm to 551 nm, after which there is little further change. This behaviour

could indicate a transition from predominantly monomer emission to aggregate emission,

with the aggregate dominating the kinetics measured beyond 551 nm. This observation

would be expected from the form of the steady-state emission spectrum (Figure 4.7).
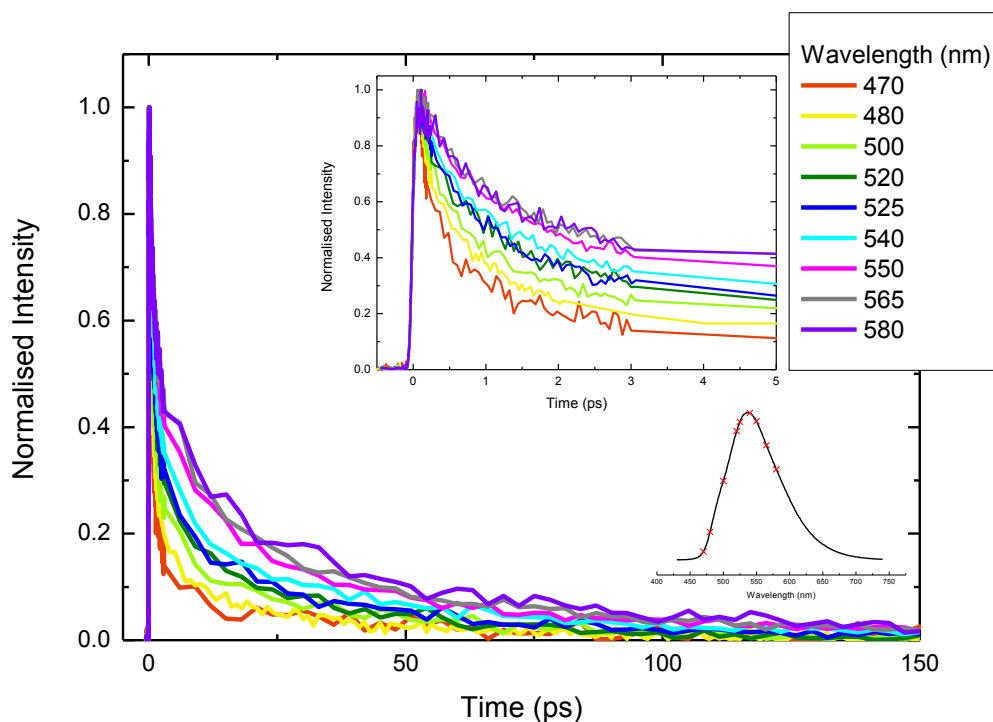
Figure 4.27. The time-dependent fluorescence of Kaede in methanol measured across the

steady-state spectrum from 470 nm (red) to 580 nm (purple), showing a wavelength

dependence in the kinetics. The insets show the kinetics between 0 and 5 ps and the

measured points marked on the steady-state emission spectrum.

The wavelength dependence of the time-resolved fluorescence of Kaede is in contrast to the behaviour of HBDI. Figure 4.28 shows that no wavelength dependence is observed for HBDI in methanol measured at nine wavelengths covering the range 465 nm to 570 nm.
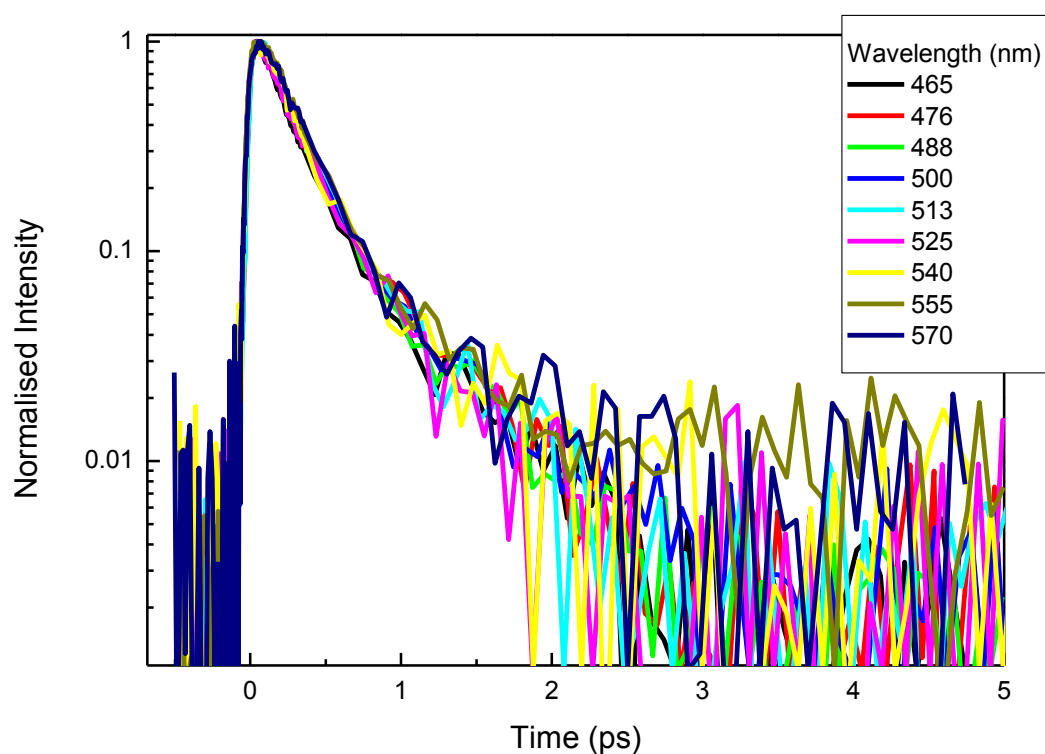
Figure 4.28. The time-resolved fluorescence of HBDI in methanol from 465 nm (black) to 570 nm (red). The kinetics show no wavelength dependence.

The decays of Kaede in methanol shown in Figure 4.27 were fitted with 4 exponentials (Table 4.5). Figure 4.29 shows the parameters τ_1, τ_2, τ_3, τ_4 and $<\tau>$ plotted as a function of wavelength. While τ_1, τ_3, τ_4 and $<\tau>$ increase with wavelength, τ_2 decreases. The behaviour of the second component could indicate the decreasing contribution of the monomer to the emission spectrum as the detection wavelength is moved to the red.

	Emission Wavelength / nm							
	470	480	500	520	525	540	550	580
τ_1 (ps)	16	17	29	33	36	38	41	39
a_1	0.10	0.12	0.10	0.12	0.12	0.12	0.18	0.18
τ_2 (ps)	8.4	8.2	7.3	8.1	6.7	7	6.6	5.9
a_2	0.24	0.24	0.42	0.3	0.42	0.42	0.42	0.36
τ_3 (ps)	1.1	1.0	1.8	2.3	2.1	2.2	2.4	3.2
a_3	0.24	0.36	0.24	0.30	0.24	0.30	0.30	0.18
τ_4 (ps)	0.2	0.1	0.3	0.3	0.4	0.4	0.3	0.6
a_4	0.42	0.42	0.36	0.3	0.24	0.24	0.24	0.24
$<\tau>$ (ps)	3.8	3.9	5.9	7.3	7.7	8.5	9.4	10.8

Table 4.5. Fitting parameters for the time-resolved emission of Kaede in methanol measured from 470 nm to 580 nm. The average time constant has an error of less than 11 %.
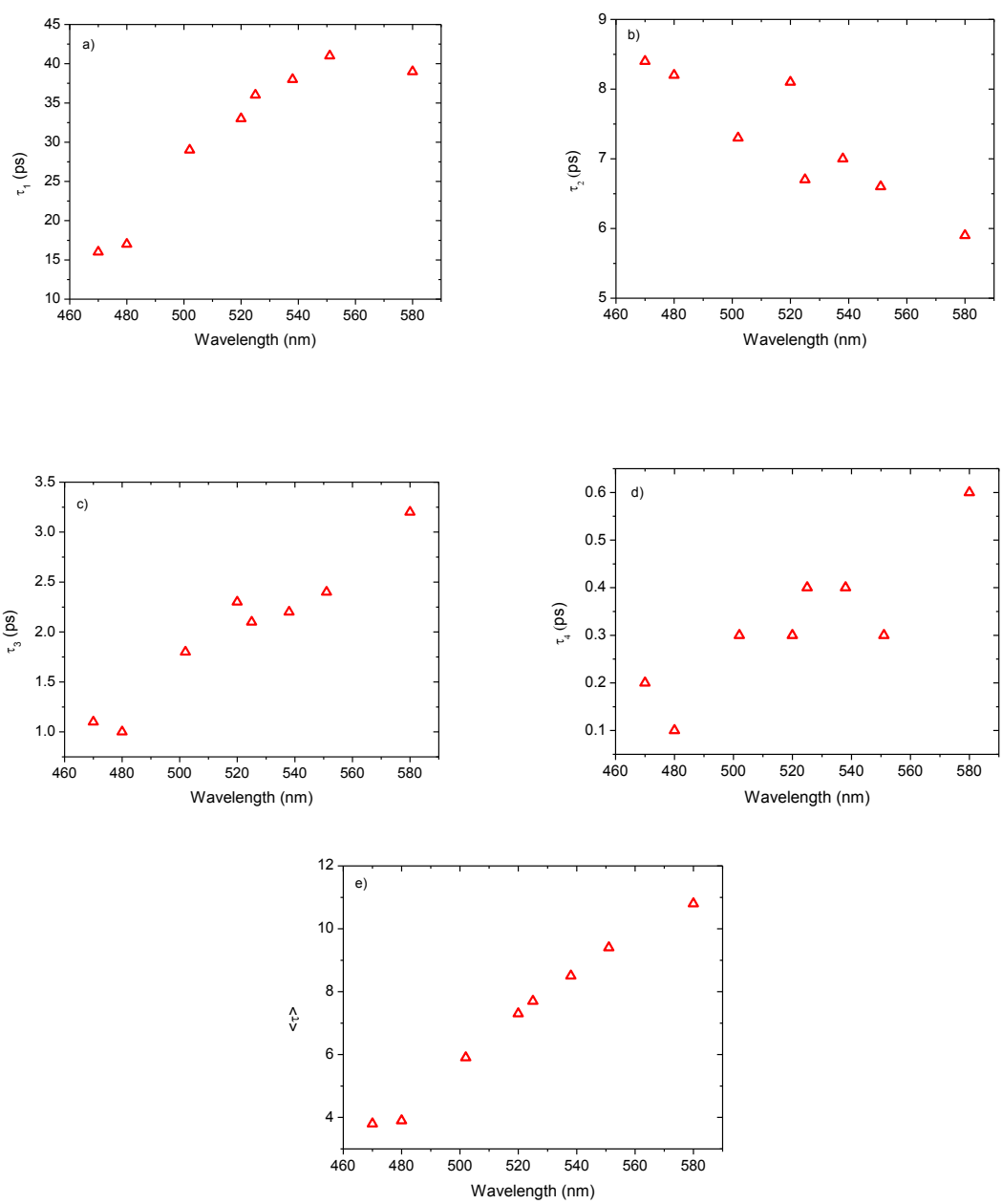
Figure 4.29. The fitting parameters τ_1 (a), τ_2 (b), τ_3 (c), τ_4 (d) and <τ> (e) for the kinetics of

Kaede in methanol plotted against emission wavelength.

The individual decays shown in Figure 4.26 were compiled to create a time-resolved

spectrum (as described in Chapter 2). Figure 4.30 shows the evolution of the time-resolved

spectrum of Kaede in methanol between 50 fs and 50 ps. In this case, measured data points

have been used to create the spectrum rather than fitting a log normal function as

described in Chapter 2. This is due to the presence of structure in the steady-state spectrum

(Figure 4.4), which is not well described by a log normal function. The inset shows the

normalised 0.05, 0.1, 1, 20 and 50 ps spectra. At later times (50 ps) the spectrum is broader

and red-shifted and thus may indicate predominantly the aggregate emission spectrum
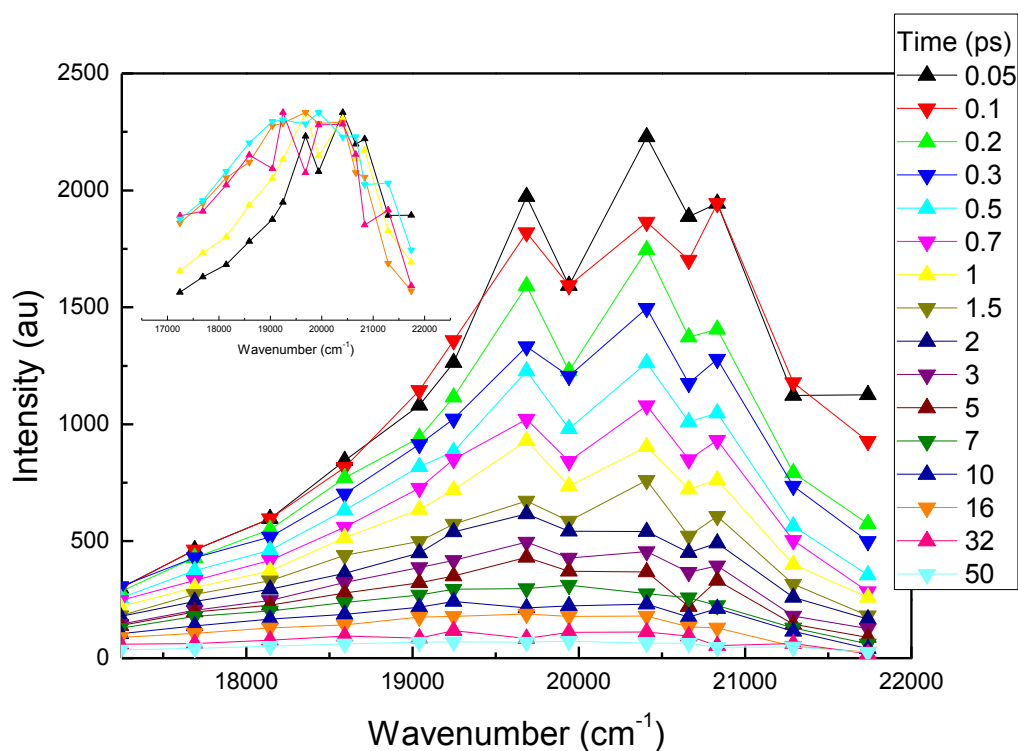
(Figure 4.7).

Figure 4.30. The time-resolved fluorescence spectra of Kaede in methanol from 50 fs to

50 ps with selected normalised spectra inset.

Figure 4.31 shows the time-dependent first moment, integrated intensity and FWHM extracted from the time-resolved spectra of Kaede in methanol (Figure 4.30). The wavelength dependence of the kinetics is reflected in the first moment. Figure 4.30a shows that over the first 10 ps, the first moment is red-shifted by almost 1250 cm^{-1}. This is in contrast to HBDI in methanol, where a negligible shift of roughly 100 cm^{-1} was observed (Chapter 7). On the same timescale, the FWHM increases by approximately 1000 cm^{-1}. Both the first moment and integrated intensity display non-single-exponential behaviour. This is again in contrast to the behaviour of HBDI (Chapter 7), where the decay of the integrated intensity is almost single exponential. The more complex behaviour of Kaede is consistent with the initial decay of the monomer combined with the longer decay of the red-shifted aggregate.
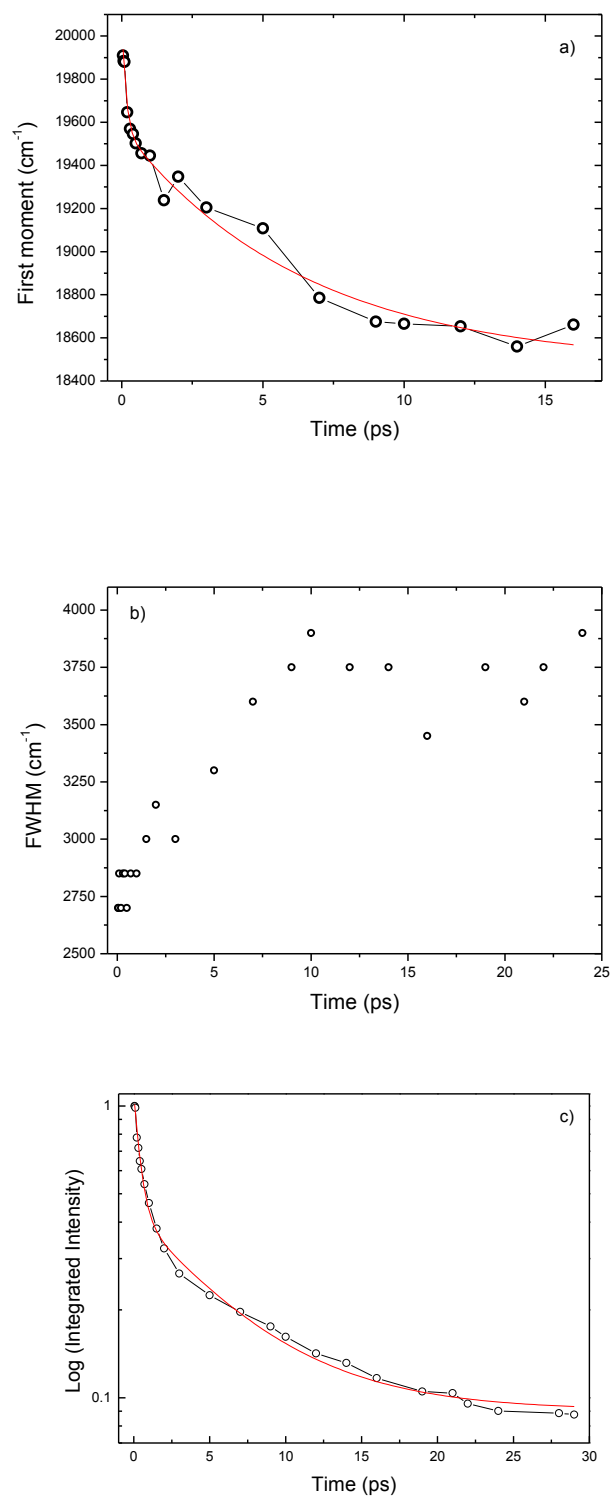
Figure 4.30. Time dependence of the first moment (a), FWHM (b) and integrated intensity

(c) of Kaede emission in methanol.

4.4.3. pH Dependence

The time-resolved fluorescence decays of neutral, anionic and (what is assumed to be) cationic Kaede in H_2O are shown in Figure 4.31. Both the cation and anion exhibit longer decays compared to the neutral form as was also found for HBDI[29]. The anion and cation fits are similar at early times but start to deviate after 15 ps, with the cation decay longer than the anion. The decays were fitted with a sum of 3 exponentials (Table 4.6). Comparing the fitting parameters, all components become longer going from neutral to anion to cation. Also, for the neutral form, the long component has a much lower amplitude than for the anion or cation. The steady-state concentration study indicates that aggregation enhances the fluorescence quantum yield (Figure 4.8) and the steady-state fluorescence indicates that anionic Kaede is monomeric, while the neutral and cationic forms contain higher aggregates (Figure 4.10). The wavelength dependence of the time-resolved fluorescence is also consistent with the aggregate being longer lived than the monomer (Section 4.4.2). Although the anion is longer than the neutral in HBDI, this result for Kaede indicates a large change in lifetime between the neutral and anionic forms when taking into account the monomer-aggregate effect.

126
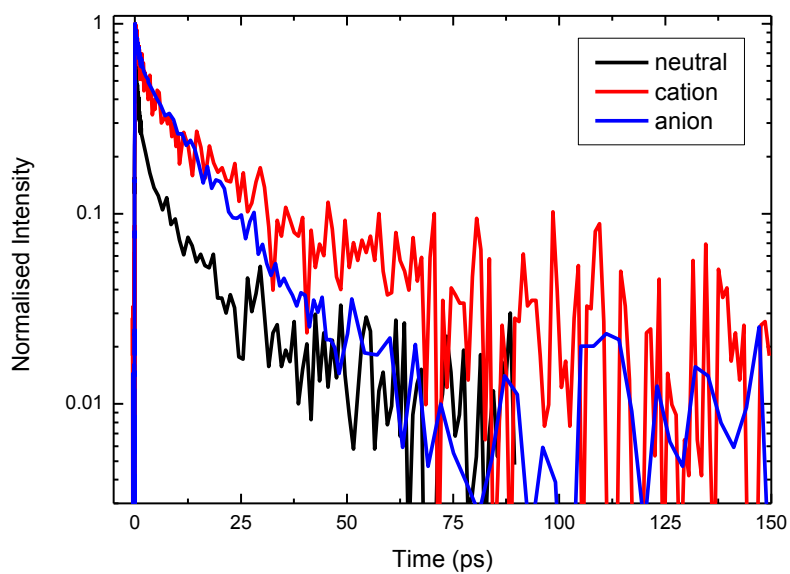
Figure 4.31. Time-resolved fluorescence decays of neutral (black), cationic (red) and anionic

(blue) Kaede in H2O.

	Neutral	Anion	Cation
τ_1 *(ps)*	13.2	14.2	36.5
a_1	0.13	0.53	0.26
τ_2 *(ps)*	1.1	2.0	5.6
a_2	0.39	0.25	0.37
τ_3 *(ps)*	0.17	0.35	0.74
a_3	0.48	0.22	0.37
<τ> (ps)	2.2	8.1	11.7

Table 4.6. Fitting parameters for the fluorescence decays of neutral, anionic and cationic

Kaede in H_2O. The errors on the average lifetimes are less than 12%.

4.4.4. Temperature Dependence and Isoviscosity Analysis

It was shown in Section 4.3.4, that the steady-state emission exhibits a dependence on temperature with an activation energy of 10.8 kJ mol^{-1} for the radiationless decay. The temperature dependence of the time-resolved emission was measured for Kaede in ethylene glycol. Measurements were made using a temperature controlled water bath to vary the sample temperature from 278 to 353 K (Section 4.2). This covers the viscosity range 46 cP to 3.5 cP. The solution was flowed and the sample reservoir placed in the water bath. The 1mm flow cell was placed in a copper holder which was thermally stabilised with water flowing from the water bath to maintain the sample temperature. The measured decays indicate no observable change from 278 to 303 K (Figure 4.32.). However, at 353 K the decay is clearly faster. The decays were fitted with 4 exponentials and the parameters are given in Table 4.7.
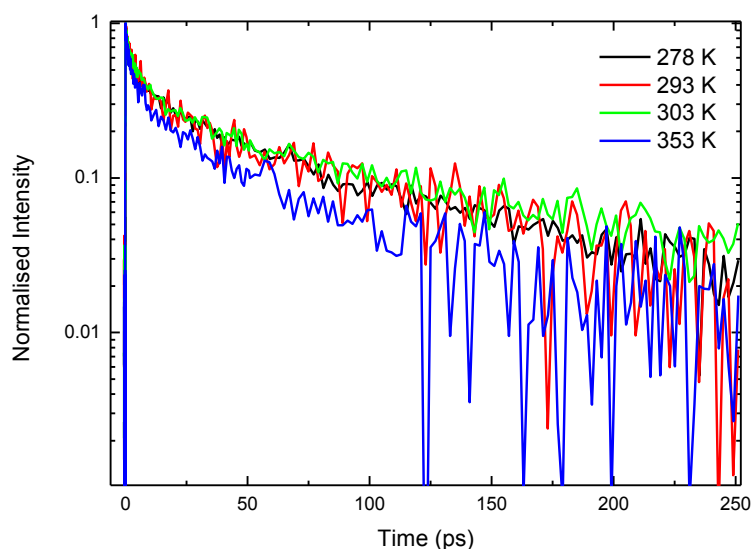
Figure 4.32. Time-resolved fluorescence of Kaede in ethylene glycol at 278 K (black), 293 K (red), 303 K (green) and 353 K (blue).

T (K)	278	293	303	353
η (cP)	46	21	14	3.5
τ_1 (ps)	66.6	83.7	78.4	57.9
a_1	0.27	0.22	0.21	0.24
τ_2 (ps)	9.6	8.30	8.0	7.1
a_2	0.22	0.29	0.31	0.32
τ_3 (ps)	1.7	0.86	0.90	1.4
a_3	0.26	0.22	0.17	0.23
τ_4 (ps)	0.18	0.08	0.21	0.37
a_4	0.25	0.27	0.31	0.22
$<\tau>$ (ps)	20.6	20.7	19.3	16.6

Table 4.7. Fitting parameters for the time-resolved fluorescence of Kaede in ethylene glycol at 278, 293, 303 and 353 K. The error on the average lifetime is less than 15 %.

The time-resolved emission of Kaede was also measured in propanol, ethanol and butanol at a range of temperatures (Figure 4.33). In ethanol and propanol, there is no obvious temperature dependence over the given temperature range. In butanol however, a small decrease in the lifetime is observed as the temperature is increased. The temperatures measured for ethanol, propanol and butanol correspond to a small, approximately 3 fold, change in viscosity. In ethylene glycol, a 13 fold decrease in the viscosity resulted in only a 20% decrease in the average lifetime (Table 4.7.). Hence it is not surprising that little or no effect is observable in the decays shown in Figure 4.32, as a significant change in viscosity is required to produce observable changes in the time-resolved fluorescence. Moreover, the barrier determined from the low temperature steady-state fluorescence data (Figure 4.15), predicts a negligible change in the lifetime across the measured temperature range.
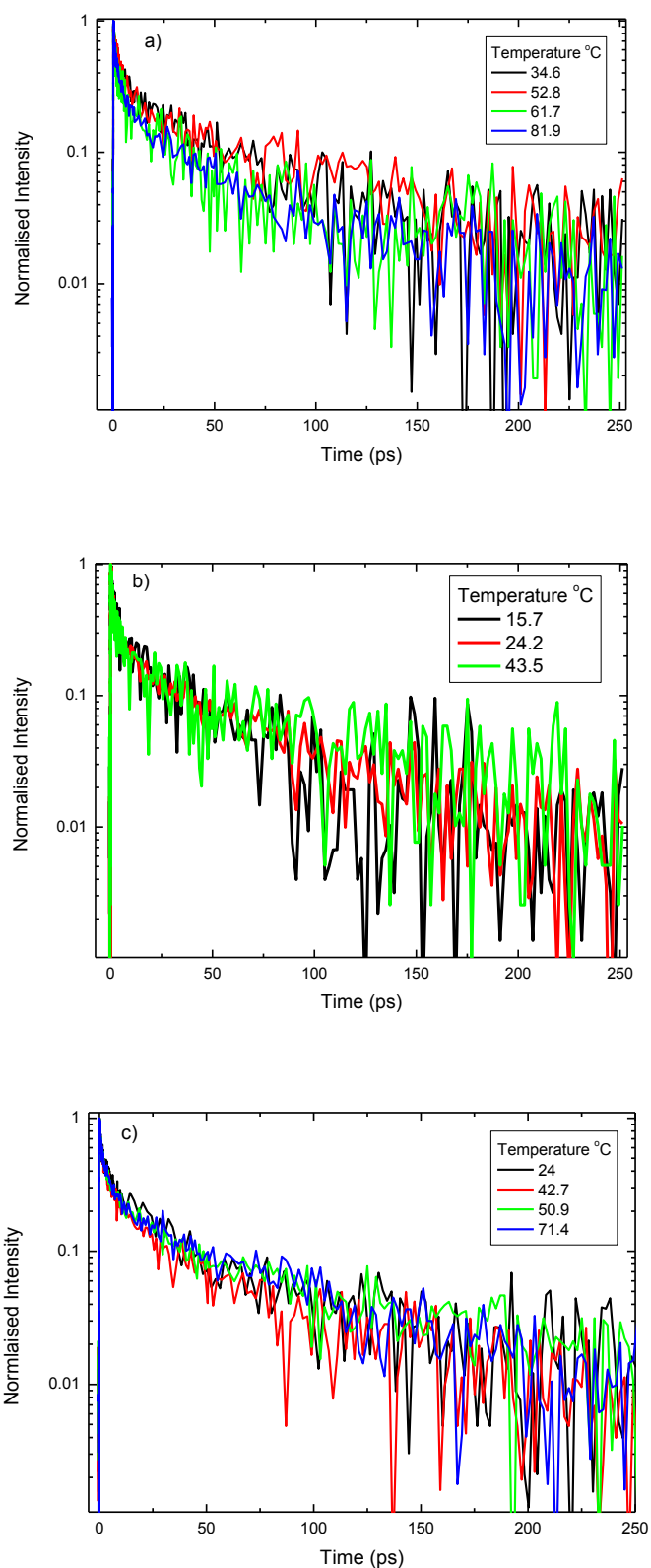
Figure 4.33. Fluorescence decays of Kaede in butanol (a), ethanol (b) and propanol (c)

measured at a range of temperatures selected to yield the same viscosity.

The decays were fitted with 4 exponentials and the parameters are reported in Table 4.8. The average lifetime was used to obtain the rate of nonradiative decay (k_{nr}) using,

$$k_{nr} = \frac{1}{<\tau>}.$$
(4.3)

Combining these with the results obtained for Kaede in ethylene glycol, a plot of *ln k_{nr}* against viscosity was created (Figure 4.34). The rate of nonradiative decay exhibits a very weak dependence on viscosity, where analysis of the ethylene glycol data yields a gradient of 0.0044 ± 0.0026.

	Butanol				Propanol				Ethanol		
T (K)	308	326	335	355	297	316	324	345	289	297	317
η (cP)	2.163	1.402	1.164	0.788	2.163	1.402	1.164	0.788	1.402	1.164	0.788
τ_1 (ps)	80	88	70.6	67.4	48.9	56	61	70.9	41.5	68.9	94
a_1	0.21	0.16	0.14	0.12	0.2	0.14	0.17	0.22	0.09	0.13	0.13
τ_2 (ps)	16.1	10.6	15.7	12.1	19.3	10.6	12.9	8.3	21.3	15.6	13.4
a_2	0.13	0.19	0.11	0.14	0.1	0.2	0.17	0.1	0.17	0.16	0.14
τ_3 (ps)	4.4	2.9	3	2.4	2.5	1.8	2.3	4	1.8	3.4	3.3
a_3	0.28	0.31	0.3	0.36	0.32	0.39	0.36	0.31	0.39	0.28	0.26
τ_4 (ps)	0.65	0.3	0.54	0.32	0.28	0.31	0.48	0.66	0.43	0.64	0.56
a_4	0.37	0.34	0.44	0.38	0.38	0.27	0.29	0.37	0.36	0.43	0.46
<τ> (ps)	20.7	17	12.9	10.6	12.6	10.8	13.5	17.6	8	12.4	15.1

Table 4.8. Fitting parameters for Kaede in butanol, propanol and ethanol measured at temperatures selected to yield the same viscosity. The error of the average lifetime is less than 14%.
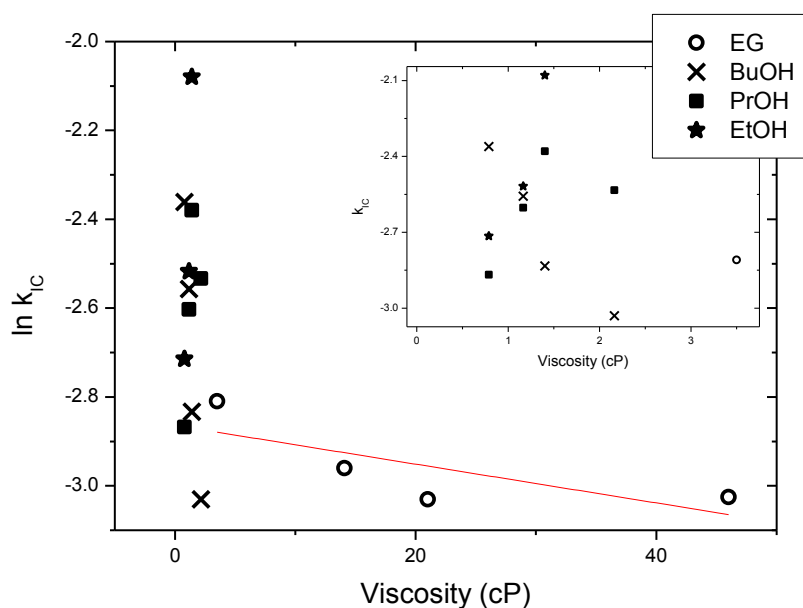
Figure 4.34. The rate of nonradiative decay exhibits a very weak dependence on viscosity. The red line is the fit to the ethylene glycol data, giving a gradient of 0.0044 ± 0.0026. The inset shows the low viscosity (0 − 3.5 cP) data.

In order to separate the effects of solvent friction and a thermal barrier crossing on the nonradiative decay process, an isoviscosity analysis was performed. The rate of nonradiative decay can be described by,

$$k_{nr} = F(\eta)e^{-\left(\frac{E_0}{RT}\right)},$$
(4.4)

where $F(\eta)$ is a function of viscosity and E_0 is the intrinsic barrier height[43]. The gradient obtained by plotting $\ln(k_{nr})$ against $1/T$ (Figure 4.35) at a constant viscosity yields E_0. Temperatures were selected to yield the same set of viscosities in the solvents butanol, propanol and ethanol. In propanol and ethanol, k_{nr} decreases with decreasing temperature. Whilst in butanol, the opposite is true. The activation energy is determined by calculating

the gradient of the points of equal viscosity (indicated by dashed lines in Figure 4.35.).   For

η = 1.402 cP, an activation energy of 14 ± 6 kJ mol^{-1} was obtained, whilst for η = 1.164 cP, a

small barrier of 1 ± 1 kJ mol^{-1} was determined and for η = 0.788 cP a negative barrier of

-5 ± 11 kJ mol^{-1} was calculated. All determined activation energy values have large errors

and the behaviour is similar to that observed for HBDI[38]. At the measured temperatures, kT

ranges from 2.4 to 3 kJ mol^{-1}. Therefore taking into account the large errors on these

measurements and the fact that the fluorescence lifetime of Kaede is significantly longer

than that of HBDI, these results suggest there may exist a non-negligible barrier to

nonradiative decay of Kaede. This is in contrast to HBDI, where internal conversion is

barrierless[38].
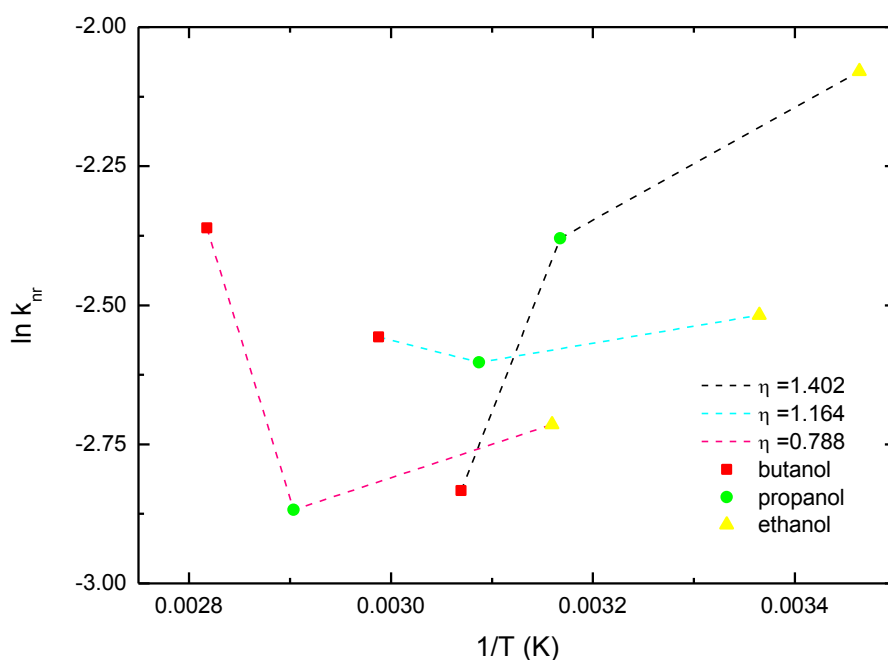
Figure 4.35. The rate of nonradiative decay of Kaede in butanol (red), propanol (green) and

ethanol (yellow) against inverse temperature, where dashed lines join points of equal

viscosity.

4.5. Transient Absorption

Transient absorption measurements (Chapter 2) were made to investigate both the excited state and ground-state dynamics of Kaede and those of any potential non emissive intermediates. Transient absorption measures the change in the population of states. Hence, these measurements can reveal the existence of dark excited states not detected by ultrafast fluorescence up-conversion measurements. The transient absorption of Kaede in methanol, ethanol, butanol, ethylene glycol, water, formamide and propanol were measured, over the spectral range 425 nm to 625 nm with a time resolution of 300 fs. The transient absorption spectra of Kaede in methanol are shown in Figure 4.37. All measurements show a broad ground-state bleach centred around 450 nm (see Figure 4.2). In addition all also show an excited state absorption at 610 nm and a feature with negative ΔOD around 530 nm.

The negative feature around 530 nm, where there is no ground-state absorption, must have a contribution from stimulated emission which causes gain in intensity in the probe and therefore a negative signal. Figure 4.4 shows that 530 nm, being close to the emission maximum is the appropriate wavelength for stimulated emission.
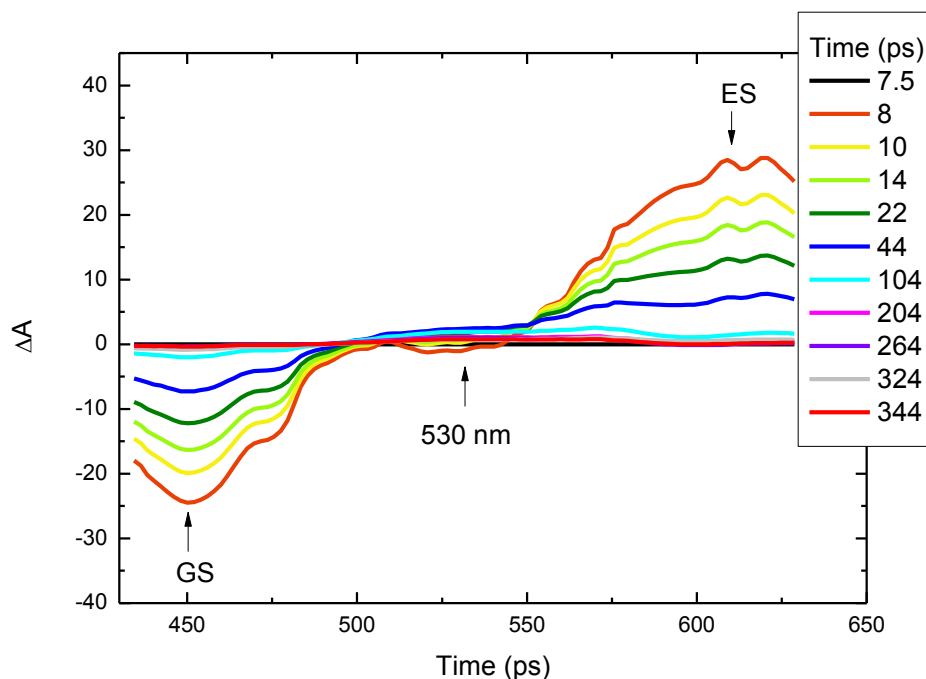
Figure 4.36. Transient absorption spectra of Kaede in methanol showing the ground-state recovery at 450 nm and excited state decay at 610 nm.

After removal of the coherent artefact (Chapter 2), the kinetics at 450 nm, 530 nm and 610 nm were extracted. Figure 4.37 shows the kinetics of Kaede in methanol. Clearly the ground and excited states recover and decay respectively on approximately the same time scale. This is consistent with internal conversion being the dominant decay mechanism, as was found for HBDI[35]. The inset of Figure 4.37 shows the small 530 nm component is initially negative but begins to rise in a few ps, becoming positive after 10 ps. This behaviour could indicate stimulated emission followed by the absorption of a long-lived excited state. The spectra show structure, for example in the ground-state recovery two peaks are observed centred at 450 nm and 475 nm. Analysis of the kinetics at these wavelengths yields the

same parameters. Hence it is likely that the structure is associated with the same ground-state.
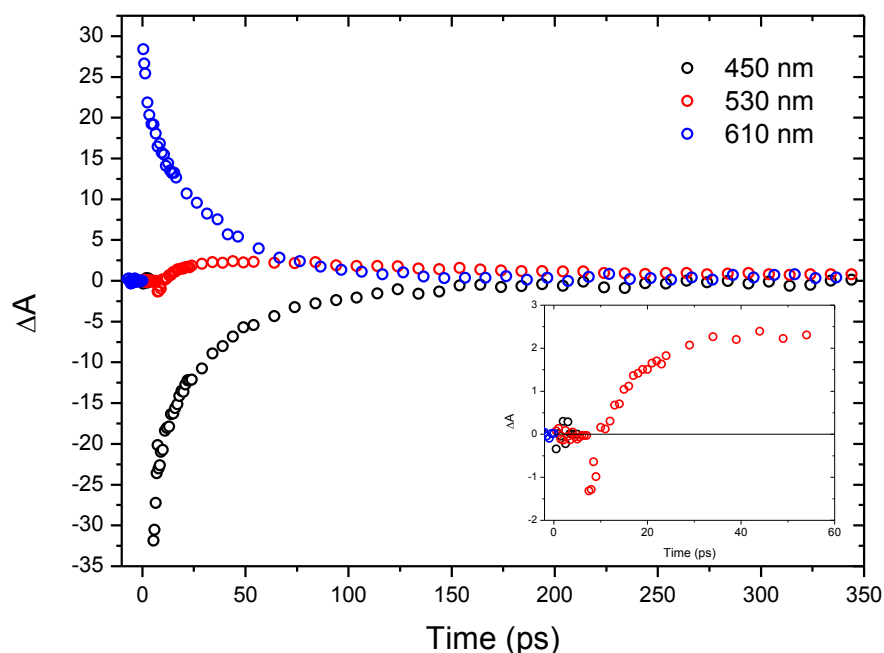
Figure 4.37. Kinetics of the transient absorption of Kaede in methanol at 450 nm (black), 530 nm (red) and 610 nm (blue). The ground and excited states recover on approximately the same timescale. The 530 nm feature is initially negative (stimulated emission), becoming positive after roughly 10 ps.

Global analysis of the transient absorption data was performed in Glotaran using a sequential model with three rates (Section 4.3.6). This revealed 3 spectral components, as illustrated in Figure 4.38a for Kaede in methanol. One component is associated with a lifetime of a few ps, there is an intermediate component of tens of ps and a longer component of over 100 ps corresponding to the final state (Table 4.9). The short and

intermediate components are spectrally similar, with the longer component differing in
shape and amplitude. Figure 4.38 also shows the DAS recovered in water, ethanol, propanol,
butanol, NMF, formamide and ethylene glycol. For NMF and formamide only 2 components
were required, this will be discussed later.
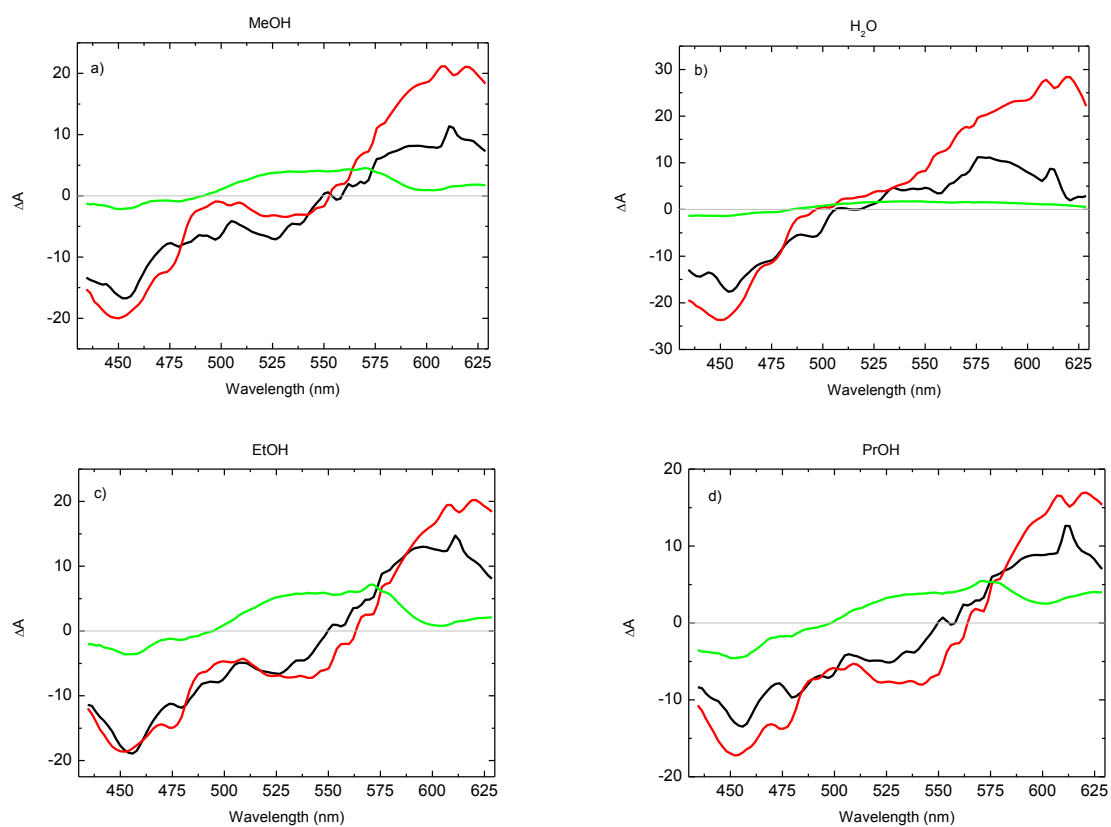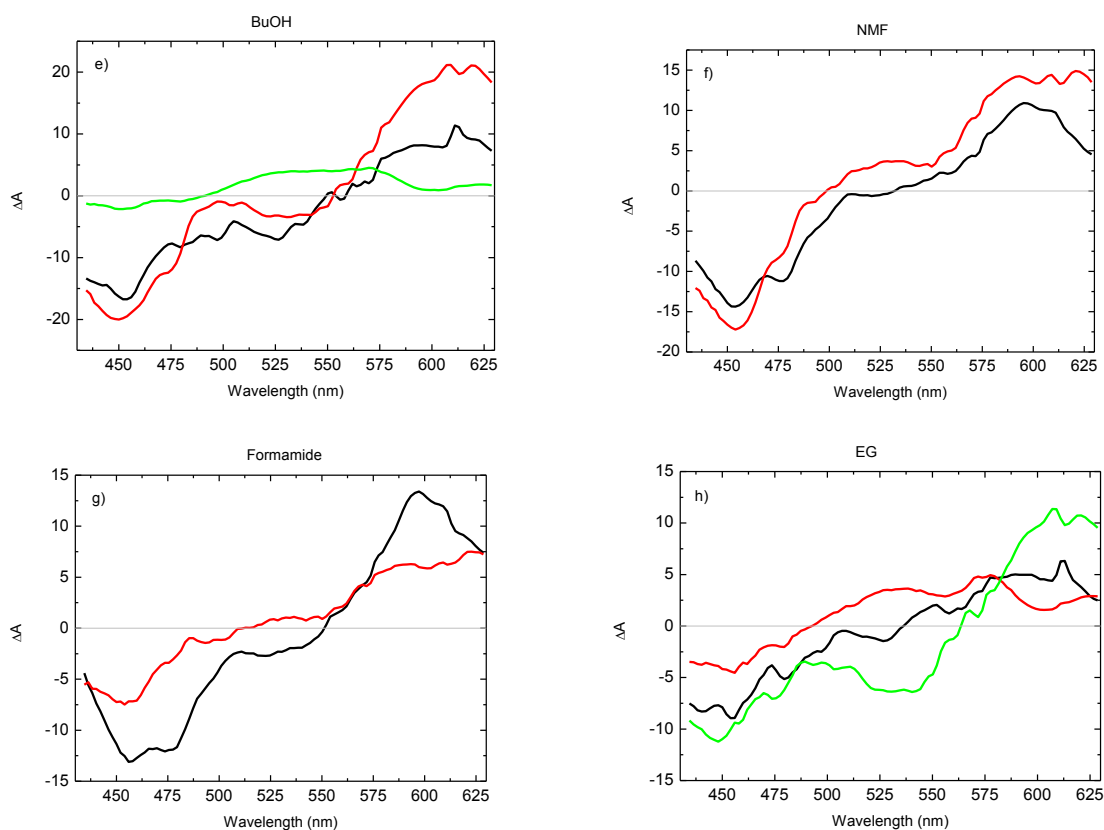
Figure 4.38. Decay associated spectra recovered from global analysis of the transient absorption of Kaede in (a) methanol, (b) water, (c) ethanol, (d) propanol, (e) butanol, (f) n-methylformamide, (g) formamide and (h) ethylene glycol, showing the short (black), intermediate (red) and long (green) components.

	MeOH	H2O	EtOH	PrOH	BuOH	NMF	F	EG
τ_1 (ps)	1.5	1.2	2.7	3.2	2.6	17	27	3.6
τ_2 (ps)	28	10	39	33	37	119	108	182
τ_3 (ps)	161	1100	173	187	259			47

Table 4.9. Time constants of the components recovered from global analysis of the transient absorption spectra of Kaede in various solvents. The errors are less than 10%.

The time constants recovered from global analysis do not show a strong dependence on viscosity or polarity (Figure 4.39.). Although τ_2 in EG is high, no significant viscosity dependence is seen in the alcohols. However, the τ_2 DAS is similar to the τ_3 DAS in other solvents. For τ_3, the lifetime in water is very long (over 1 ns) and corresponds to the lifetime of the 530 nm excited state, as the amplitude of the third component is concentrated around this wavelength. In contrast, the fluorescence decay in water is fast ($<\tau> = 2.2$ ps) with no evidence of emission from the state seen in the global analysis of the transient absorption. Figure 4.42 shows that the time constants in the highly polar, aprotic solvents NMF and formamide are anomalously long compared to the alcohols. In these solvents only 2 components are recovered from the global analysis. In both cases these components are spectrally similar and more like the shorter two in the other solvents. The third component, which is concentrated around 530 nm and very long in water, is not present in the global analysis of NMF and formamide. This highlights the importance of the hydrogen bonding nature of the solvent. As no sign of the third, long component is observed in the fluorescence, it is likely that this is a dark state.

As mentioned earlier, the short and intermediate components (black and red in Figure 4.38) are spectrally similar and may correspond to the monomer and aggregate states respectively. For methanol and water, the fluorescence lifetimes τ_3 and τ_1 are in agreement with the short and intermediate components respectively. Therefore these fluorescence components may correspond to the lifetimes of the monomer and aggregate.
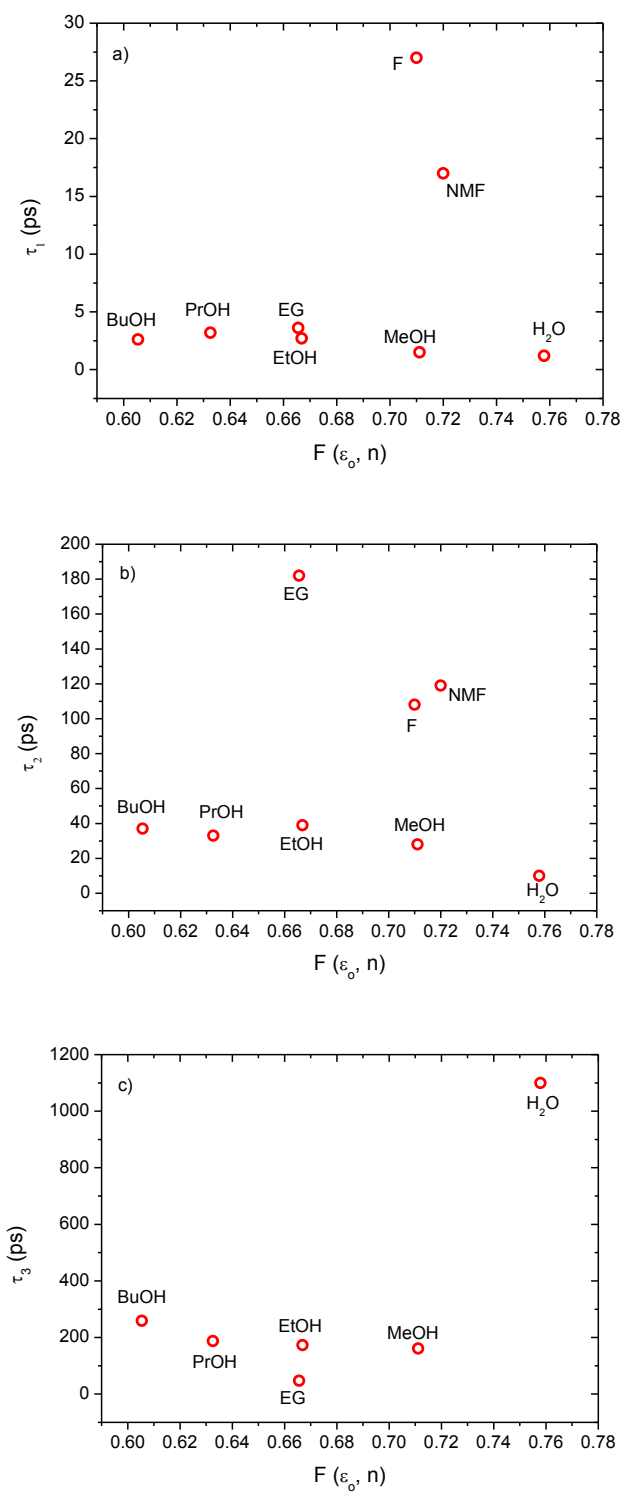
Figure 4.39. The time constants τ_1 (a), τ_2 (b) and τ_3 (c) of the DAS recovered from global analysis of the Kaede transient absorption spectra plotted against the polarity function.

4.6. Conclusions

The fluorescence of Kaede is 15 times more intense than that of HBDI. Due to the extended conjugated structure, the Kaede chromophore also exhibits redshifted absorption and emission compared to HBDI. Whilst the steady-state fluorescence spectrum of HBDI is featureless and relatively narrow, the Kaede emission spectrum shows clear structure (Section 4.3.1.). The dependence on excitation wavelength and sample concentration reveals that these features are due to emission from monomeric and brighter, aggregated forms of Kaede. Whilst the dependence upon excitation wavelength indicates that the aggregate is present in the ground-state, the monomer and aggregate states are not distinguishable in the absorption spectrum. This indicates that the excited states of the monomer and aggregate differ more than the ground-states. The steady-state emission spectrum of the Kaede anion formed in basic solution is structureless and relatively narrow (Section 4.3.2). This indicates that the aggregate has dissociated at high pH.

Excited HBDI relaxes to the ground-state predominantly via ultrafast IC and as such has a very low quantum yield. However upon cooling to the glass transition temperature, the strong fluorescence observed in GFP is restored. At low temperatures, the high viscosity of the medium restricts the freedom of motion of the chromophore. The fluorescence of Kaede also increases at low temperature, by over 100 times between 300 K and 77K (Section 4.3.4.). The activation energy for the nonradiative decay (shown to be internal conversion in Section 4.5) was found to be 10.8 kJ mol^{-1}. This is higher than the value of 6 ± 3 kJ mol^{-1} determined for HBDI above T_m and comparable to the activation energy of 12 ± 2 kJ mol^{-1} below T_m. The variable temperature time-resolved fluorescence measurements show that a large change in viscosity is required to make an observable

change in the fluorescence lifetime of Kaede (Section 4.4.4.). Furthermore, in agreement with the steady-state analysis, it was shown that the rate of internal conversion exhibits a weak dependence on viscosity. Thus it is likely that the extension of the fluorescence lifetime of Kaede compared to HBDI is due to a greater intrinsic barrier to internal conversion (Section 4.4.4).

In agreement with the steady-state behaviour, the time-resolved fluorescence decays of Kaede are longer than those of HBDI and display a weak dependence on viscosity (Section 4.4.). The fluorescence lifetime is shortest in water indicating that hydrogen bonding enhances radiationless decay. Consistent with this, in the highly polar, aprotic solvents NMF and formamide, the lifetime is relatively long. The kinetics of the Kaede fluorescence requires 3 or 4 exponential fitting components. This complexity is likely to be due to the combination of emission from both the monomer and higher aggregate. In contrast to the behaviour of HBDI, Kaede displays a strong wavelength dependence, where the decay time increases on the red side of the spectrum. Emission from the more fluorescent aggregate is redshifted compared to that of the monomer and analysis of the kinetics suggests a transition from mainly monomer to mainly aggregate fluorescence as the detection wavelength is moved to the red.

The change in nature of the emission is also reflected in the evolution of the fluorescence spectrum of Kaede, which shows much more variation than that of HBDI. The wavelength dependent behaviour is reflected in the first moment and FWHM of the time-resolved spectra, which redshifts and narrows by 1250 cm^{-1} and 1000 cm^{-1} respectively over the first 10 ps. For HBDI, the decay of the integrated intensity is almost single exponential. Whilst for

Kaede the biexponential decay is again likely due to the separate contributions of monomer and aggregate.

Transient absorption measurements suggest the presence of a long-lived, excited state at 530 nm in certain solvents. Global analysis revealed 3 components, 2 shorter components with similar spectral profiles corresponding to the monomer and aggregate and 1 long component corresponding to the final state with the amplitude concentrated around the 530 nm excited state. The lifetime associated with this component does not correspond to any component of the fluorescence. This suggests that the 530 nm feature is a dark state. This excited state is very long-lived in water (over 1 ns), whilst the fluorescence decays within a few ps. In formamide and NMF only two DAS were recovered, where these were similar to the two shorter components found for the other solvents and the fluorescence lifetime is extended in these solvents. These results highlight the importance of the hydrogen bonding nature of the solvent on the photophysics of Kaede as although NMF and formamide are highly polar solvents like water, they lack the ability to donate hydrogen bonds.

4.7. References

(1)Matz, M. V.; Fradkov, A. F.; Labas, Y. A.; Savitsky, A. P.; Zaraisky, A. G.; Markelov, M. L.; Lukyanov, S. A. *Nat. Biotechnol.* **1999**, *17*, 969.
(2)Ando, R.; Hama, H.; Yamamoto-Hino, M.; Mizuno, H.; Miyawaki, A. *Proc. Natl. Acad. Sci. U. S. A.* **2002**, *99*, 12651.
(3)Campbell, R. E.; Tour, O.; Palmer, A. E.; Steinbach, P. A.; Baird, G. S.; Zacharias, D. A.; Tsien, R. Y. *Proceedings of the National Academy of Sciences* **2002**, *99*, 7877.
(4)Shaner, N. C.; Lin, M. Z.; McKeown, M. R.; Steinbach, P. A.; Hazelwood, K. L.; Davidson, M. W.; Tsien, R. Y. *Nat. Methods* **2008**, *5*, 545.
(5)Müller-Taubenberger, A.; Anderson, K. *Appl. Microbiol. Biotechnol.* **2007**, *77*, 1.
(6)Lounis, B.; Deich, J.; Rosell, F. I.; Boxer, S. G.; Moerner, W. E. *The Journal of Physical Chemistry B* **2001**, *105*, 5048.
(7)Gurskaya, N. G.; Fradkov, A. F.; Terskikh, A.; Matz, M. V.; Labas, Y. A.; Martynov, V. I.; Yanushevich, Y. G.; Lukyanov, K. A.; Lukyanov, S. A. *FEBS Lett.* **2001**, *507*, 16.
(8)Shu, X.; Shaner, N. C.; Yarbrough, C. A.; Tsien, R. Y.; Remington, S. J. *Biochemistry (Mosc).* **2006**, *45*, 9639.
(9)Mizuno, H.; Mal, T. K.; Tong, K. I.; Ando, R.; Furuta, T.; Ikura, M.; Miyawaki, A. *Mol. Cell* **2003**, *12*, 1051.
(10)Hayashi, I.; Mizuno, H.; Tong, K. I.; Furuta, T.; Tanaka, F.; Yoshimura, M.; Miyawaki, A.; Ikura, M. *J. Mol. Biol.* **2007**, *372*, 918.
(11)Wiedenmann, J.; Ivanchenko, S.; Oswald, F.; Schmitt, F.; Röcker, C.; Salih, A.; Spindler, K.-D.; Nienhaus, G. U. *Proc. Natl. Acad. Sci. U. S. A.* **2004**, *101*, 15905.
(12)Adam, V.; Nienhaus, K.; Bourgeois, D.; Nienhaus, G. U. *Biochemistry (Mosc).* **2009**, *48*, 4905.
(13)Adam, V.; Lelimousin, M.; Boehme, S.; Desfonds, G.; Nienhaus, K.; Field, M. J.; Wiedenmann, J.; McSweeney, S.; Nienhaus, G. U.; Bourgeois, D. *Proceedings of the National Academy of Sciences* **2008**, *105*, 18343.
(14)Adam, V.; Moeyaert, B.; David, Charlotte C.; Mizuno, H.; Lelimousin, M.; Dedecker, P.; Ando, R.; Miyawaki, A.; Michiels, J.; Engelborghs, Y.; Hofkens, J. *Chem. Biol.* **2011**, *18*, 1241.
(15)Fuchs, J.; Böhme, S.; Oswald, F.; Hedde, P. N.; Krause, M.; Wiedenmann, J.; Nienhaus, G. U. *Nat. Methods* **2010**, *7*, 627.
(16)Greetham, G. M.; Burgos, P.; Cao, Q.; Clark, I. P.; Codd, P. S.; Farrow, R. C.; George, M. W.; Kogimtzis, M.; Matousek, P.; Parker, A. W.; Pollard, M. R.; Robinson, D. A.; Xin, Z.-J.; Towrie, M. *Appl. Spectrosc.* **2010**, *64*, 1311.
(17)Valeur, B.; Berberan-Santos, M. N. *Molecular fluorescence: principles and applications*; John Wiley & Sons, 2012.
(18)Kasha, M. *Discuss. Faraday Soc.* **1950**, *9*, 14.
(19)Demchenko, A. P. *Luminescence* **2002**, *17*, 19.
(20)Mandal, P. K.; Sarkar, M.; Samanta, A. *The Journal of Physical Chemistry A* **2004**, *108*, 9048.
(21)Paul, A.; Mandal, P. K.; Samanta, A. *The Journal of Physical Chemistry B* **2005**, *109*, 9148.
(22)Samanta, A. *The Journal of Physical Chemistry B* **2006**, *110*, 13704.
(23)Paul, A.; Mandal, P. K.; Samanta, A. *Chem. Phys. Lett.* **2005**, *402*, 375.
(24)Ebeid, E. Z. M.; Abdel-Halim, S. T.; Abdel-Kader, M. H. *The Journal of Physical Chemistry* **1988**, *92*, 7255.
(25)Jacky, W.; SingáKwok, H.; ZhongáTang, B. *Chem. Commun.* **2001**, 1740.
(26)Zhang, X.; Liu, M.; Yang, B.; Zhang, X.; Chi, Z.; Liu, S.; Xu, J.; Wei, Y. *Polym. Chem.* **2013**, *4*, 5060.
(27)Wang, M.; Zhang, G.; Zhang, D.; Zhu, D.; Tang, B. Z. *J. Mater. Chem.* **2010**, *20*, 1858.
(28)Tou, S.-L.; Huang, G.-J.; Chen, P.-C.; Chang, H.-T.; Tsai, J.-Y.; Yang, J.-S. *Chem. Commun.* **2014**, *50*, 620.

(29)Conyard, J.; Kondo, M.; Heisler, I. A.; Jones, G.; Baldridge, A.; Tolbert, L. M.; Solntsev, K. M.; Meech, S. R. *The Journal of Physical Chemistry B* **2011**, *115*, 1571.

(30)Voliani, V.; Bizzarri, R.; Nifosì, R.; Abbruzzetti, S.; Grandi, E.; Viappiani, C.; Beltram, F. *The Journal of Physical Chemistry B* **2008**, *112*, 10714.

(31)Addison, K.; Conyard, J.; Dixon, T.; Bulman Page, P. C.; Solntsev, K. M.; Meech, S. R. *The Journal of Physical Chemistry Letters* **2012**, *3*, 2298.

(32)Dong, J.; Solntsev, K. M.; Poizat, O.; Tolbert, L. M. *J. Am. Chem. Soc.* **2007**, *129*, 10084.

(33)Draney, D.; Kingsbury, C. A. *J. Am. Chem. Soc.* **1981**, *103*, 1041.

(34)LaPlante, S. R.; Carson, R.; Gillard, J.; Aubry, N.; Coulombe, R.; Bordeleau, S.; Bonneau, P.; Little, M.; O'Meara, J.; Beaulieu, P. L. *J. Med. Chem.* **2013**, *56*, 5142.

(35)Webber, N. M.; Litvinenko, K. L.; Meech, S. R. *The Journal of Physical Chemistry B* **2001**, *105*, 8036.

(36)Stavrov, S. S.; Solntsev, K. M.; Tolbert, L. M.; Huppert, D. *J. Am. Chem. Soc.* **2006**, *128*, 1540.

(37)Webber, N. M.; Meech, S. R. *Photochemical & Photobiological Sciences* **2007**, *6*, 976.

(38)Litvinenko, K. L.; Webber, N. M.; Meech, S. R. *The Journal of Physical Chemistry A* **2003**, *107*, 2616.

(39)Hosoi, H.; Mizuno, H.; Miyawaki, A.; Tahara, T. *The Journal of Physical Chemistry B* **2006**, *110*, 22853.

(40)Jensen, F. *Introduction to Computational Chemistry*; WILEY, 2007.

(41)Snellenburg, J. J.; Laptenok, S.; Seger, R.; Mullen, K. M.; Van Stokkum, I. H. *Journal of Statistical Software* **2012**, *49*.

(42)van Stokkum, I. H.; Larsen, D. S.; van Grondelle, R. *Biochimica et Biophysica Acta (BBA)-Bioenergetics* **2004**, *1657*, 82.

(43)Velsko, S. P.; Waldeck, D. H.; Fleming, G. R. *The Journal of Chemical Physics* **1983**, *78*, 249.

Chapter 5 – Photophysics of Two HBDI Analogues

5.1. Introduction

Many HBDI analogues have been developed which involve modifications at the ortho, meta and para positions of the phenolic ring. Measurements on these molecules show that small modifications can have dramatic effects on the photophysics of the chromophores. Modifications give rise to a diverse range of effects including intermolecular and intramolecular charge transfer, aggregation-induced fluorescence, hydrogen bonding which can enhance or suppress fluorescence[1-9]. This behaviour can be exploited for use in a many applications. For example a strong dependence of the fluorescence on solvent polarity can be useful as a biological probe and sensor; for example, o- and p- amino HBDIs have been synthesised which can detect the presence of Cr^{3+}, an important biological ion[6].

One such analogue is o-HBDI (4-(2-hydroxybenzylidene)-1, 2-dimethyl-1H-imidazol-5(4H)-one), where the hydroxyl has been moved to the ortho position of the benzene ring. The emission is enhanced compared to HBDI by approximately a factor of 10^{2-4}. Hsieh and co-workers demonstrated that this chromophore forms a seven-membered ring via an intramolecular hydrogen bond, and undergoes excited state intramolecular proton transfer (ESIPT) (Figure 5.1)[2]. They state that the behaviour of this chromophore more closely resembled that of HBDI in GFP rather than the isolated chromophore, as the emission was stronger and proton transfer was allowed.
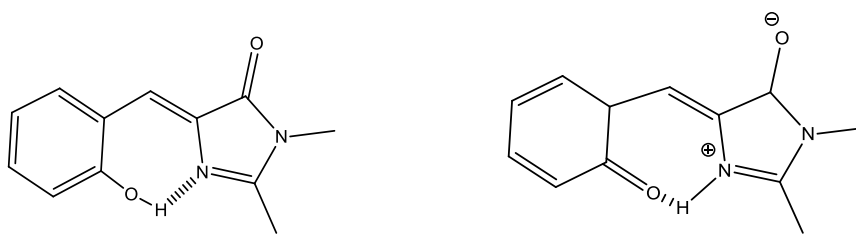
Figure 5.1. The molecular structure of o-HBDI before (left) and after (right) proton transfer.

Some meta substituted analogues of HBDI have also been investigated (Figure 5.2)[9-11]. It was shown that for m-HBDI, nonradiative decay is suppressed due to a higher barrier of photoisomerisation and, in aqueous solutions, ultrafast intermolecular excited state proton transfer (ESPT) competes with isomerisation[10]. This is analogous to the behaviour of m- and p- hydroxystilbenes[12]. Yang and co-workers synthesised the chromophores m-ABDI and m-DMABDI shown in Figure 5.2[9,11]. For m-ABDI it was found that the fluorescence is strongly quenched in protic solvents, where solvent-solute hydrogen bonding leads to excited state proton transfer[11]. For m-DMABDI, a strong solvent polarity dependence was observed in the steady-state emission, where the spectrum shifted significantly upon changing the solvent from cyclohexane to acetonitrile. Whilst the quantum yield was larger for m-DMABDI, in both chromophores the quantum yield decreased with increasing solvent polarity, with very low fluorescence in MeOH. Through further modifications, they also showed that H-bonding to the carbonyl oxygen is better at deactivating the excited state than H-bonding to the imino nitrogen.
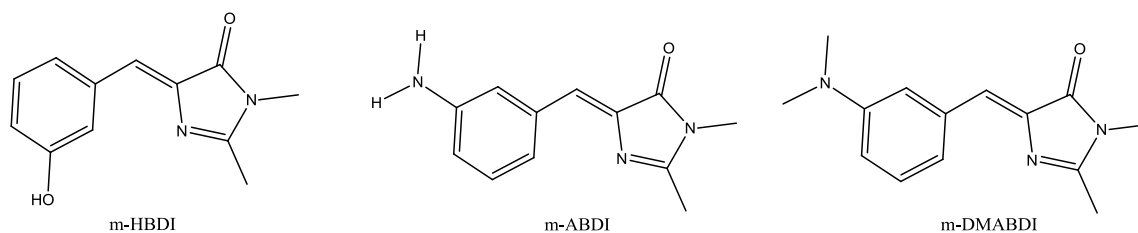
Figure 5.2. Molecular structure of some meta HBDIs.

Recently, a group of chromophores which display aggregation-induced emission have been developed[13]. These chromophores have long alkyl chains attached which facilitates aggregation. The restriction of movement caused upon formation of the aggregate structure suppresses the non-radiative decay channels and raised the quantum yield to as high as 0.53, comparable to that of chromophores in proteins[14].

In this chapter the photophysics of two new HBDI analogues are investigated (Figure 5.3). The first molecule, labelled *p*NR2, has a diethylamino substituent in the para position of the benzene ring. The second molecule also has a hydroxyl group at the ortho position of the benzene ring, and will be referred to as *o*OH*p*NR2. These chromophores allow the study of the effect of the substitution of the para hydroxyl of HBDI for the larger, strongly electron donating diethylamino substituent in combination with the effect of the *o*-HBDI modification, which may form the intramolecular hydrogen bond reported for *o*-HBDI. The hope was that these new chromophores would have some utility as fluorescent probes, as well as telling us more about HBDI photophysics.
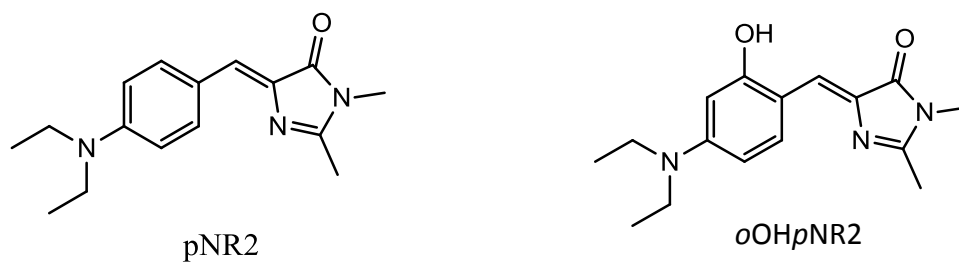
Figure 5.3. The molecular structure of the HBDI analogues pNR2 (left) and *o*OH*p*NR2 (right).

5.2. Experimental Methods

The chromophores were synthesised by Dr Kyril Solntsev (Georgia Institute of Technology, USA). The steady-state and time-resolved measurements were made under the same conditions as those described in Chapter 3. The fluorescence decays were measured and fitted using the procedure described in Chapter 2.

5.3. Steady-state Spectroscopy

The UV-Vis absorption spectra of *p*NR2 and *o*H*p*NR2 in various solvents are shown in Figure 5.4. The absorption spectra of both molecules are red-shifted by 70 – 80 nm compared to HBDI, such that in methanol the absorption maxima are at 443 nm and 453 nm in *p*NR2 and *o*OH*p*NR2 respectively compared with 371 nm in HBDI. Comparing *p*NR2 to another analogue (referred to as *p*-D1A16 in the literature where only two methyl groups are attached to the para nitrogen), the absorption is 10 nm to the blue, at 433 nm in methanol[13]. The maximum absorption wavelengths of *p*NR2 and *o*OH*p*NR2 in various solvents are listed in Table 5.1. Both molecules exhibit a complex dependence on the solvent, with no obvious correlation with the solvent polarity function. However, the

149

absorption of both chromophores is blue-shifted in cyclohexane and acetonitrile and
redshifted in water relative to other solvents, where the shift is greatest for *p*NR2. The OD is
strongly enhanced in water for both molecules and in MeOH for *o*OH*p*NR2.
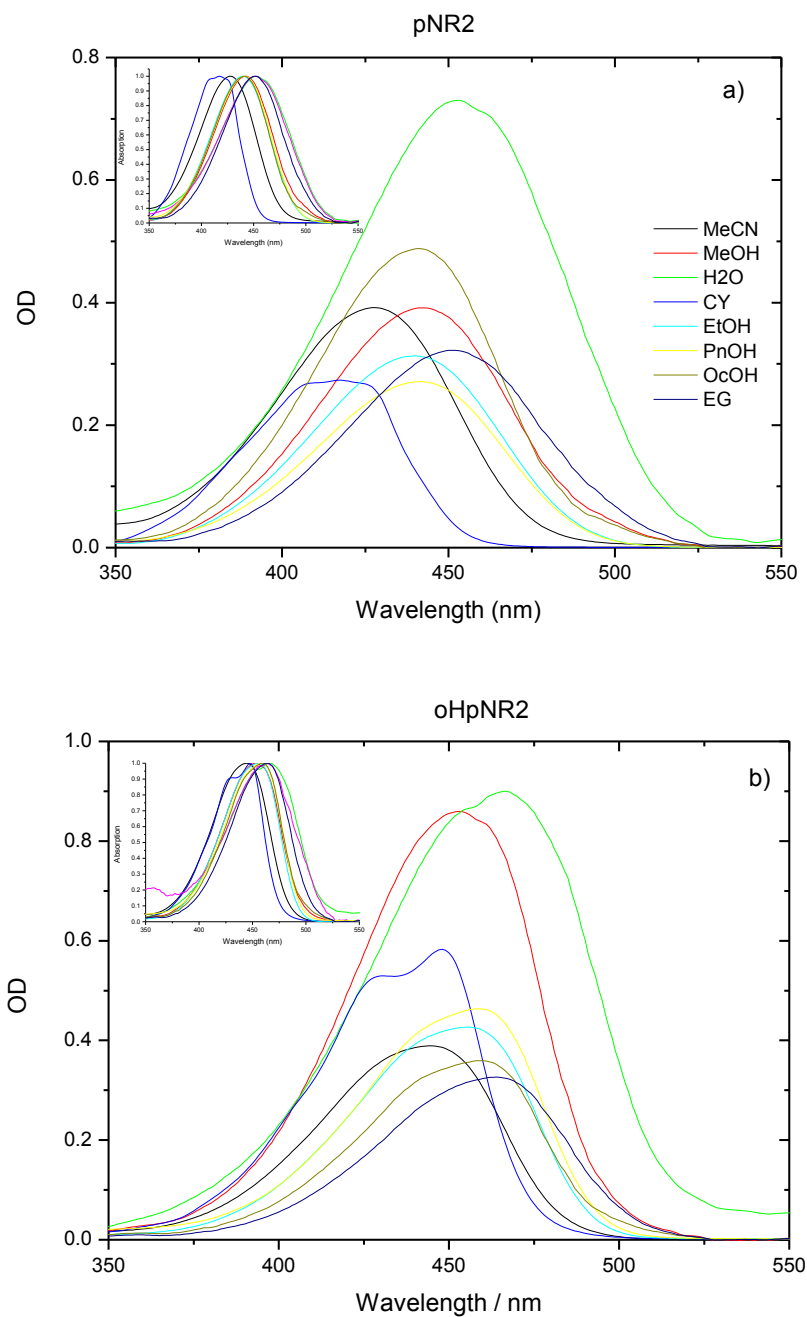
Figure 5.4. UV-Vis absorption spectra of *p*NR2 (a) and *o*OH*p*NR2 (b) with the normalised

spectra inset.

	η /cP	$F(\varepsilon_0,n)$	$\lambda_{abs}^{o\text{OH}}$ /nm	$\lambda_{abs}^{p\text{NR2}}$ /nm	$\lambda_{fl}^{o\text{OH}}$ /nm	$\lambda_{fl}^{p\text{NR2}}$ /nm	$\Delta\lambda o\text{OH}$ /cm^{-1}	$\Delta\lambda p\text{NR2}$ /cm^{-1}	Integrated Area of Emission oOHpNR2	Integrated Area of Emission pNR2
MeCN	0.369	0.7102	444	428	493	493	2238	3080	2.1E+05	4.3E+04
CY	0.894	0.56552	440	417	485	462	2108	2336	2.2E+05	7.9E+04
EtOH	1.074	0.66686	455	440	499	489	1938	2277	2.0E+05	4.0E+04
EG	16.1	0.66558	464	451	507	512	1828	2642	6.4E+05	1.1E+05
H2O	0.89	0.7579	465	453	525	525	2457	3027	-	-
OcOH	7.288	0.49777	459	440	497	485	1665	2108	7.5E+05	1.2E+05
PnOH	3.619	0.56516	459	440	499	489	1746	2277	3.3E+05	4.9E+04
MeOH	0.544	0.71112	453	443	502	497	2155	2452	-	-
D2O	1.132	0.75964	464	452	525	525	2504	3076	-	-

Table 5.1. Steady-state absorption and emission properties of pNR2 and oOHpNR2.

The absorption corrected steady-state emission spectra of pNR2 and oOHpNR2 are shown in Figures 5.5 and 5.6 respectively, with the spectrum of HBDI in ethanol included for comparison. The integrated area of emission is listed in Table 5.1. For both chromophores the integrated area increases with solvent viscosity (Figure 5.7), where this dependence is much stronger for oOHpNR2. Comparing the two analogues, oOHpNR2 is more fluorescent than pNR2 (by 3 – 7 times depending on solvent). Both molecules are more fluorescent than HBDI, where in EtOH the integrated intensity of pNR2 is over 70 times greater and that of oOHpNR2 is almost 500 times higher. Similarly to the absorption spectra, the emission is red-shifted by approximately 70 nm relative to that of HBDI. However, the maximum fluorescence wavelength of p-D1A16 is approximately the same as those of pNR2 and oOHpNR2[13].
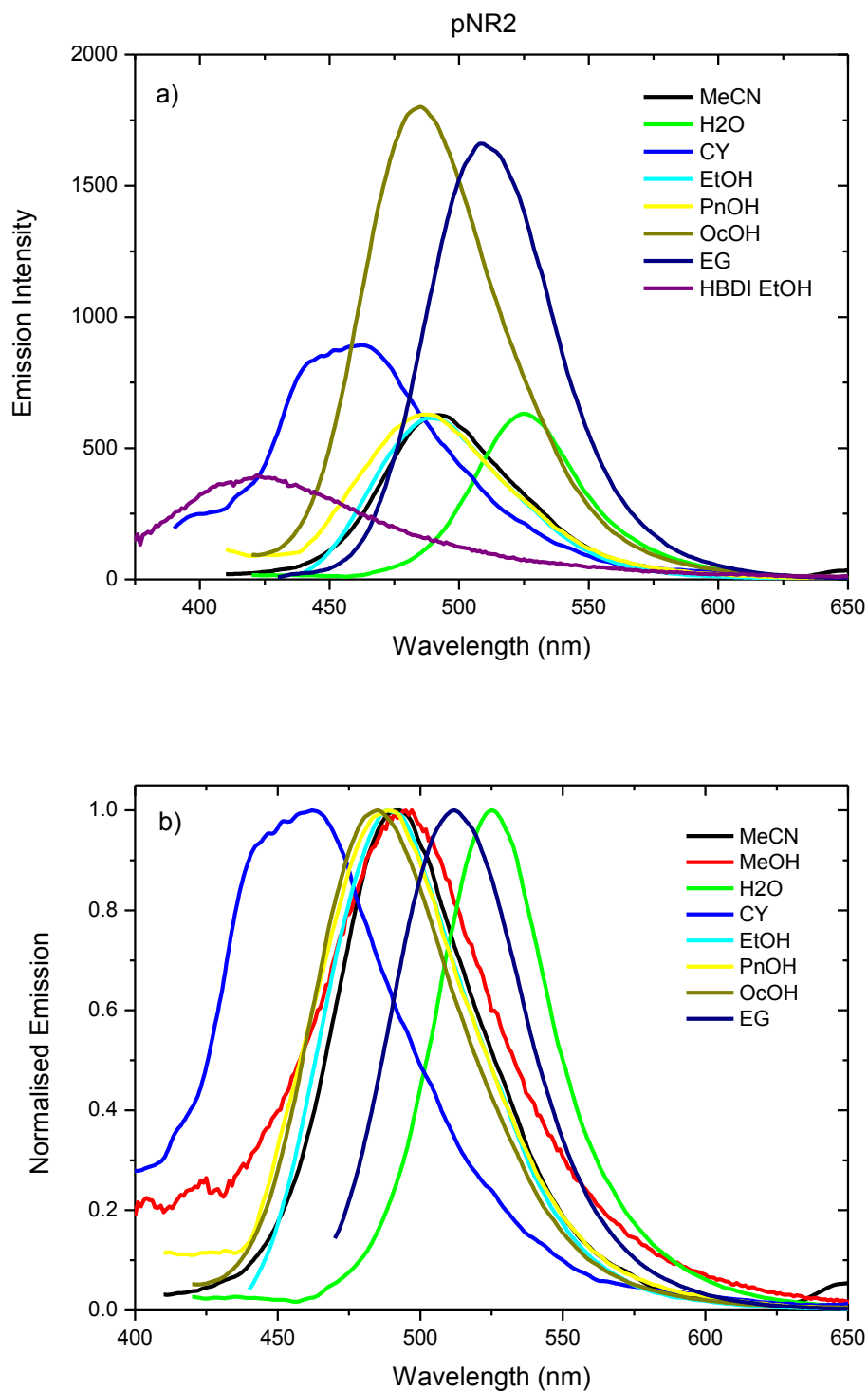
Figure 5.5. Steady-state emission spectra of pNR2, absorption corrected (a) and
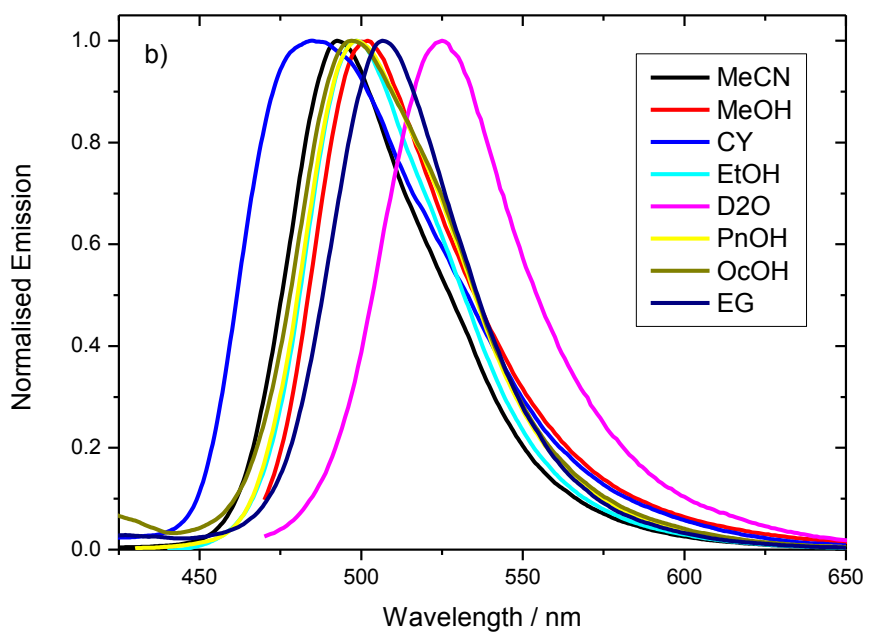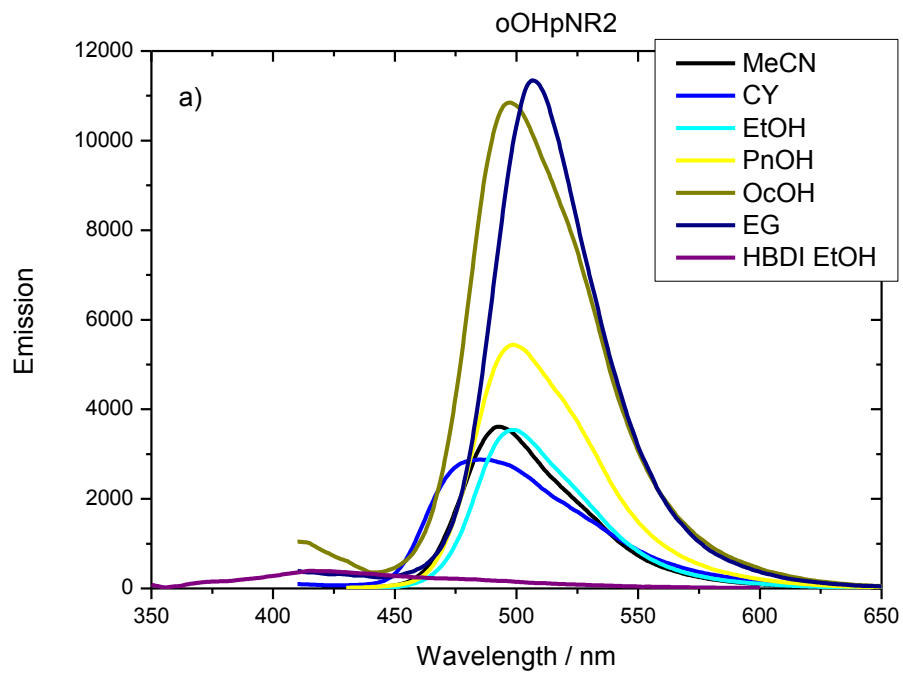
normalised (b).

Figure 5.6. Steady-state emission spectra of *o*OH*p*NR2, absorption corrected (a) and normalised (b).
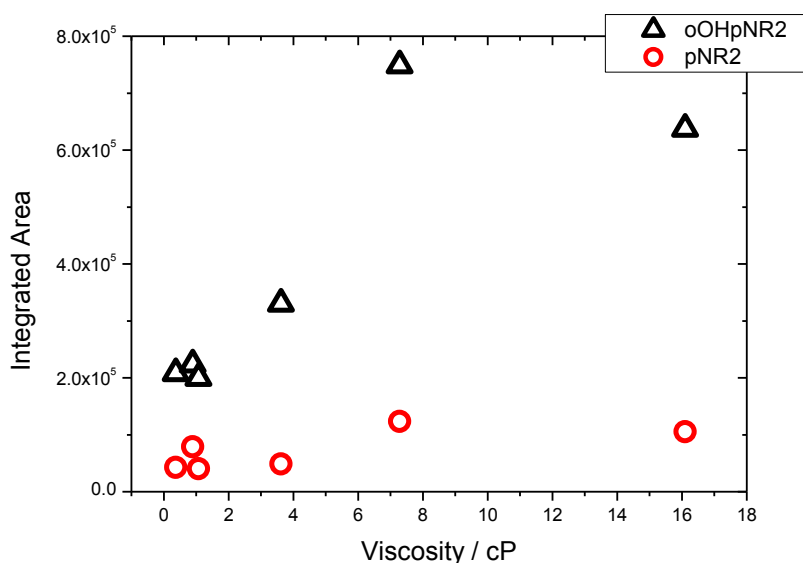
Figure 5.7. Integrated emission intensity of *o*OH*p*NR2 and *p*NR2 against viscosity.

The Stokes shifts of both molecules are considerably lower than those of HBDI and the *p*-D1A16 analogue. For example, in MeCN the Stokes shift was 2238 cm^{-1} for *o*OH*p*NR2 and 3080 cm^{-1} for *p*NR2, significantly less than those of *p*-D1A16 and HBDI in the same solvent which are 3443 cm^{-1} and 3848 cm^{-1} respectively[13]. Both analogues show a dependence of the Stokes shift on polarity where the shift increases with solvent polarity (Figure 5.8). This is consistent with an increased permanent dipole moment between the ground and excited state. The slope is greater for *p*NR2 indicating a larger dipole moment change. The hydrogen bond donating strength of the solvent seems to have very little effect for *o*OH*p*NR2 but a reasonably large effect for *p*NR2. The Stokes shift of *o*OH*p*NR2 in MeOH and MeCN (approximately the same polarity) is exactly the same, whilst for pNR2 the Stokes shift is over 600 cm^{-1} greater in MeCN.
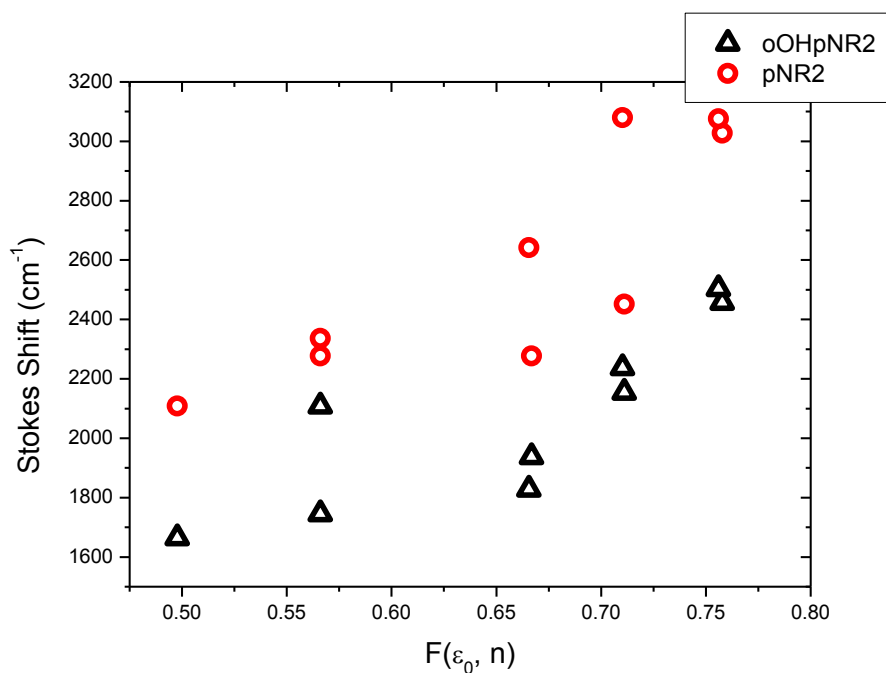
Figure 5.8. Stokes shift of *o*OH*p*NR2 (black) and *p*NR2 (red) as a function of the polarity

function.

5.4. Time-resolved Fluorescence Measurements

To investigate the excited state dynamics of these HBDI analogues, the time-resolved

fluorescence of the chromophores was measured using ultrafast fluorescence up-conversion

(Chapter 2). Measurements were made at the peak of the steady-state emission for samples

prepared to a concentration of 0.5mM. Firstly the measurements of *p*NR2 will be described,

followed by those of *o*OH*p*NR2. Finally, the time-resolved emission of both chromophores

will be compared.

5.4.1 Time-resolved Fluorescence of *p*NR2

Figure 5.9 shows the solvent dependence of the time-resolved emission of *p*NR2 with the corresponding fitting parameters listed in Table 5.2. The kinetics are complex and were fitted with 2 exponential components or 3 exponentials for the more viscous solvents pentanol, octanol and ethylene glycol. The behaviour of *p*NR2 in the alcohols displays a viscosity dependence, where the long component increases with viscosity.
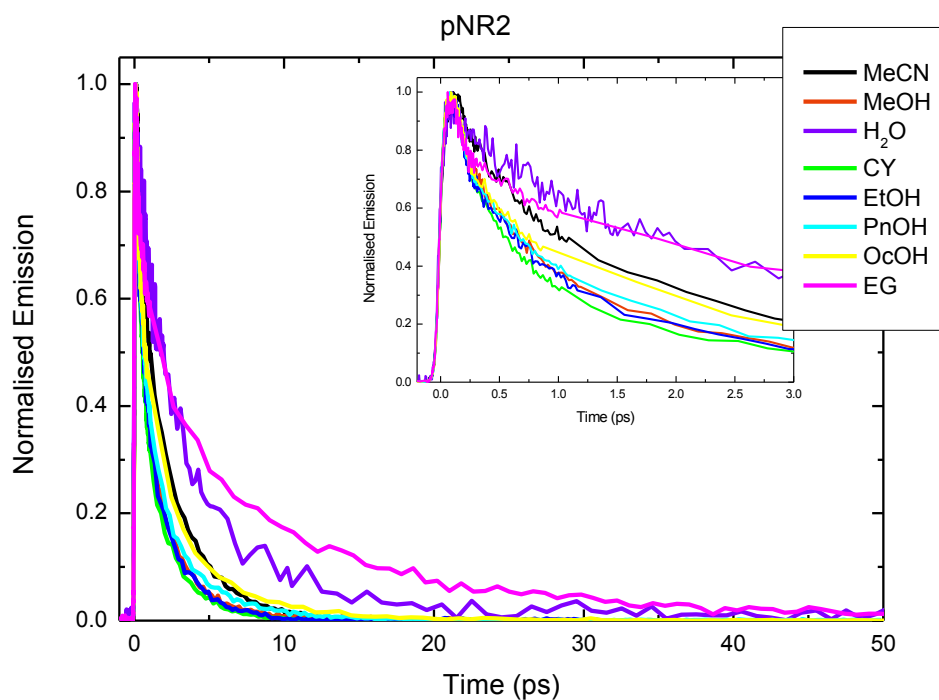
Figure 5.9. Time-resolved fluorescence of *p*NR2 with the inset showing the early time data.

pNR2	MeCN	MeOH	H_2O	CY	EtOH	D_2O	PnOH	OcOH	EG
τ_1 /ps	0.36	0.36	1.4	0.28	0.24	1.7	0.13	0.15	0.13
a_1	0.41	0.54	0.44	0.59	0.50	0.48	0.48	0.49	0.44
τ_2 /ps	2.5	2.1	5.7	1.9	1.8	6.0	1.0	1.4	2.2
a_2	0.59	0.46	0.56	0.41	0.50	0.52	0.37	0.36	0.32
τ_3 /ps	-	-	-	-	-	-	3.8	5.0	14.0
a_3	-	-	-	-	-	-	0.15	0.14	0.24
$<\tau>$ /ps	1.6	1.2	3.8	0.9	1.0	3.9	1.0	1.3	4.1

Table 5.2. Fitting parameters for the time-resolved fluorescence of pNR2.

The lifetime of pNR2 shows no clear dependence on the polarity function, although the decays are extended in H_2O and D_2O. In Figure 5.10, the average lifetime is plotted against solvent viscosity. The average lifetime shows a dependence on viscosity in the alcohols, where the lifetime is significantly extended in EG. This is reflected in the long component whilst the short lifetime displays no dependence on solvent viscosity, suggesting different origins for the two decays. For m-HBDI, the fluorescence yield is enhanced due to a higher barrier of photoisomerisation[10]. The hydrogen bond stabilises the planar geometry, resulting in a higher barrier to C=C torsion. However in aqueous solutions, it was shown that ultrafast intermolecular proton transfer provides a means to quench the fluorescence. Solvent-solute hydrogen bonding may supress radiative decay by enabling excited state proton transfer[11]. As the fluorescence lifetime of pNR2 is not significantly reduced in the strongly hydrogen bonding solvent H_2O, it is unlikely that ESPT occurs.
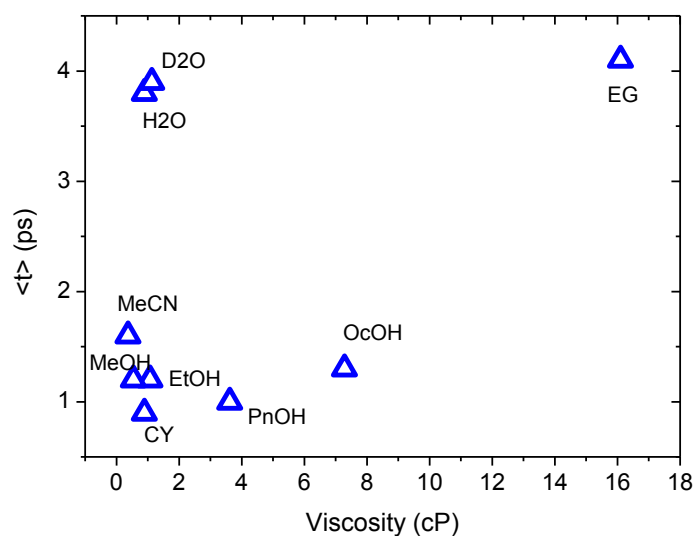
Figure 5.10. The dependence of the average lifetime of pNR2 on solvent viscosity. $\langle\tau\rangle$

increases with viscosity in the alcohols.

5.4.2. Time-resolved Fluorescence of *o*OH*p*NR2

The fluorescence decays of *o*OH*p*NR2 are shown in Figure 5.11. The decays were fitted as

for pNR2 with the parameters listed in Table 5.3. There is a clear viscosity dependence

indicated by the behaviour of the alcohols. In contrast to pNR2, in aqueous solvents the

decays are substantially shortened.
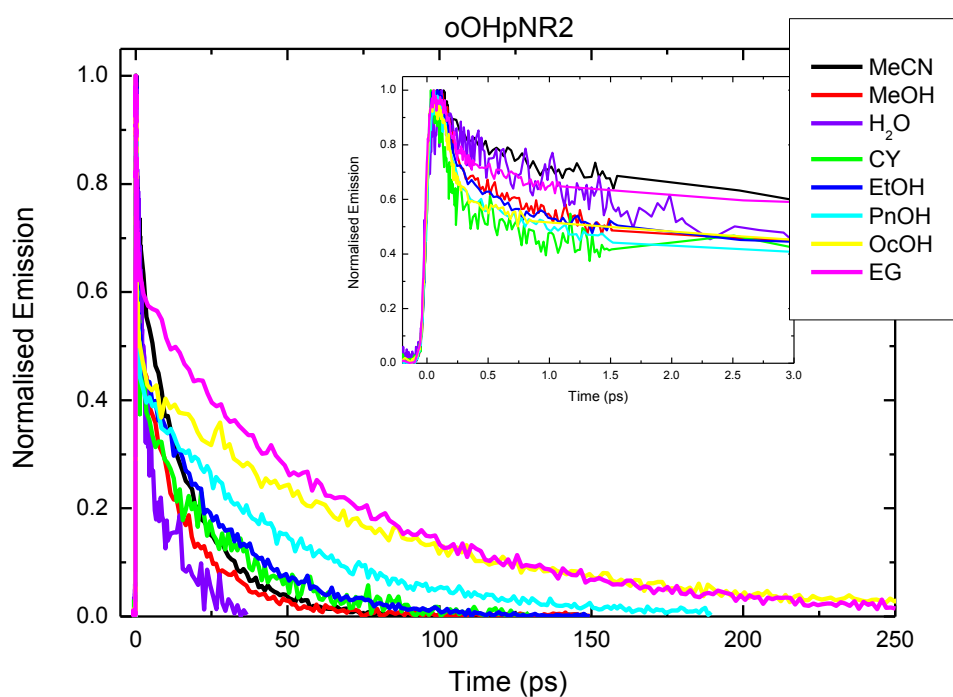
Figure 5.11. Time-resolved emission of *o*OH*p*NR2 with the inset showing the early time data.

oOHpNR2	MeCN	MeOH	H2O	CY	EtOH	D2O	PnOH	OcOH	EG
τ_1 /ps	0.30	0.25	1.7	0.18	0.28	1.6	0.12	0.12	0.17
a_1	0.32	0.54	0.53	0.61	0.56	0.63	0.61	0.63	0.48
τ_2 / ps	15.4	14.1	11.6	23.0	24.5	14.3	0.90	2.0	5.8
a_2	0.68	0.46	0.47	0.39	0.44	0.37	0.12	0.09	0.08
τ_3 / ps	-	-	-	-	-	-	42.2	76.4	69.3
a_3	-	-	-	-	-	-	0.27	0.28	0.44
$<\tau>$ / ps	10.6	6.7	6.4	9.0	10.9	6.3	11.7	21.6	30.7

Table 5.3. Fitting parameters for the time-resolved fluorescence of *o*OH*p*NR2.

For *o*OH*p*NR2 the average lifetime tends to increase with viscosity and decrease with polarity (Figure 5.12). Similarly to *p*NR2, the short lifetime displays no dependence on viscosity or the polarity function but appears to be significantly extended in H_2O and D_2O. The longest component decreases with polarity and increases with viscosity. The decays are shortened in the strong hydrogen bonding solvents water and methanol.
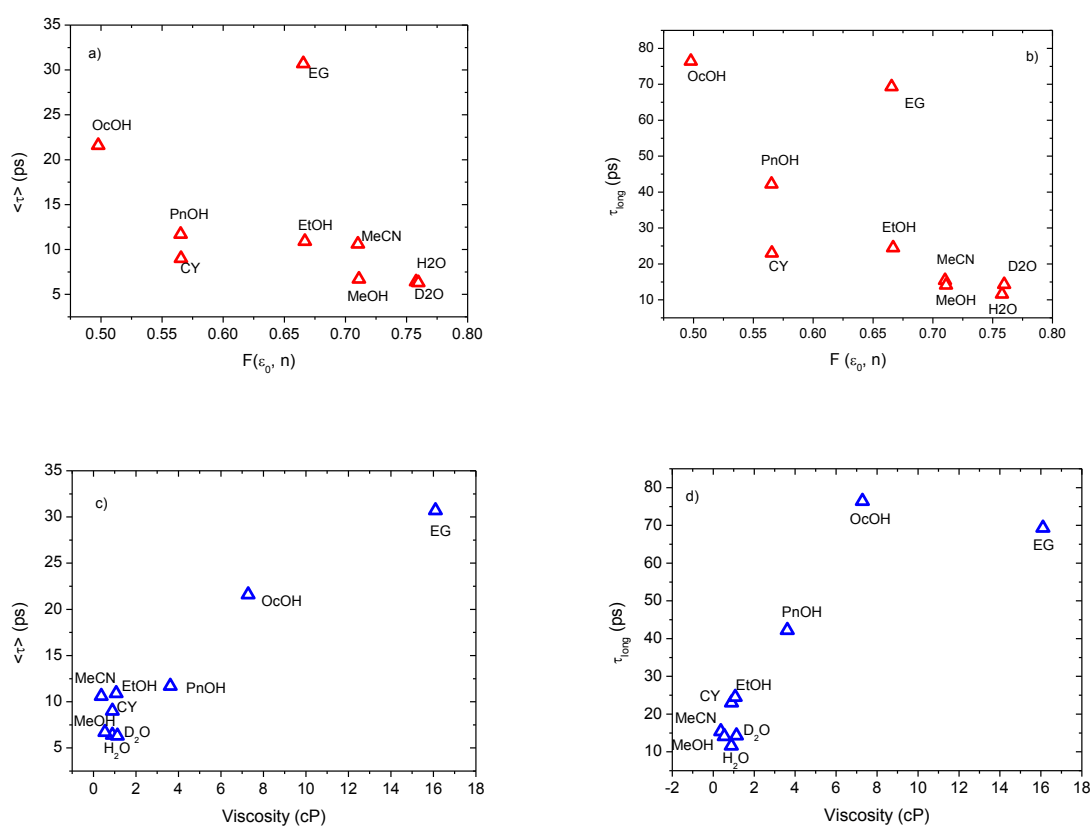
Figure 5.12. Top: The dependence of the average lifetime (a) and long lifetime (b) of *o*OH*p*NR2 on polarity. Bottom: The dependence of the average lifetime (c) and long lifetime (d) of *o*OH*p*NR2 on viscosity.

The reduced fluorescence lifetime of oOHpNR2 in the strong hydrogen bond donating solvents water and methanol could indicate ESPT enable by solvent-solute hydrogen bonding[2,11]. To investigate the possibility of ESPT, an isotope exchange experiment was performed and the kinetics compared in H_2O and D_2O. If a proton transfer process is involved, the kinetics may be slowed upon substitution for the heavier atom. It has been shown that exchange of protons when charge transfer is involved, can have a dramatic effect on the excited state kinetics, where the isotope effect has been shown to slow the proton transfer rate of GFP[15]. In this case the isotope effect was relatively large, with the kinetics slowing by about a factor of 5 upon deuteration[16].

The fluorescence decays of oOHpNR2 in H_2O and D_2O are shown in Figure 5.13. The results of the isotope exchange show no significant difference in D_2O, suggesting that either ESPT does not occur or that it is ultrafast. Similarly, for o-HBDI , which undergoes ultrafast ESPT, no changes resulted from deuterium substitution[2]. However other indications of ESPT were observed such as a large Stokes shift of approximately 200 nm in the steady-state data, indicative of tautomer emission, and oscillations in the time-resolved kinetics due to the modulation of the OH bond length. Neither of these signals were observed for oOHpNR2, thus it is unlikely that ESPT occurs in this molecule.
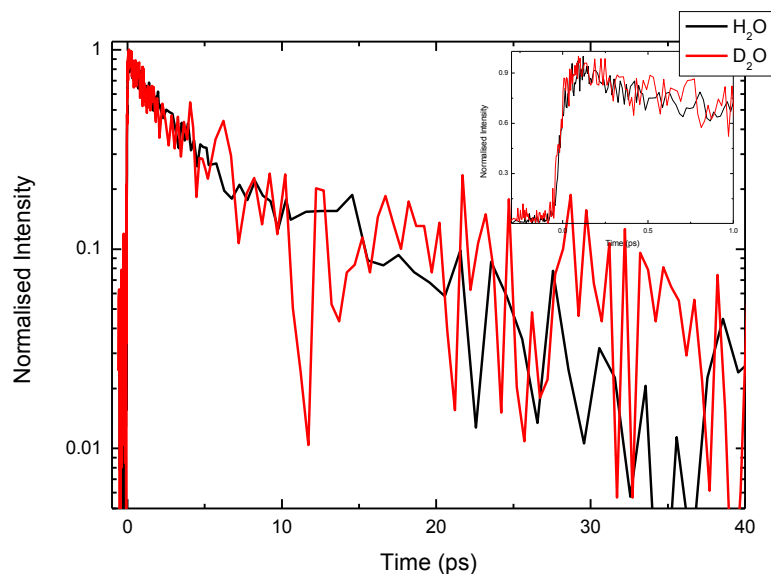
Figure 5.13. The fluorescence decays of *o*OH*p*NR2 in H_2O and D_2O.

5.4.3. Comparison of *p*NR2 and *o*OH*p*NR2

The long the average fitting components of the time-resolved fluorescence of both molecules shows a dependence on viscosity in the alcohol solvents. This behaviour in $\langle\tau\rangle$ originates from the longest component, suggesting different origins for the decays corresponding to the different exponential fitting components. However, only *o*OH*p*NR2 exhibits a solvent polarity dependence. The time-resolved fluorescence decays of *p*NR2 are approximately 4 -5 times longer than those of HBDI (Chapter 3). For *o*OH*p*NR2, the fluorescence lifetime is further extended where the average lifetime is 27 times longer in MeCN, 28 times longer in MeOH and 60 times longer in octanol. The average lifetime of *o*OH*p*NR2is consistently longer than that of *p*NR2, consistent with the increased fluorescence quantum yield of *o*OH*p*NR2, indicating an effect of the ortho OH group. The

extension of the *o*OH*p*NR2 average lifetime is greatest in non-polar solvents (Figure 5.14). The polarity effect indicates change in the electronic structure upon the addition of the ortho hydroxyl. For *p*NR2, the decays are extended in H_2O and D_2O, suggesting that ESPT does not occur in this molecule. Conversely, for *o*OH*p*NR2, the decays are shortened in the strong hydrogen bond donating solvents methanol and water. However, the lack of effect upon isotope exchange suggests that ESPT does not occur in *o*OH*p*NR2.
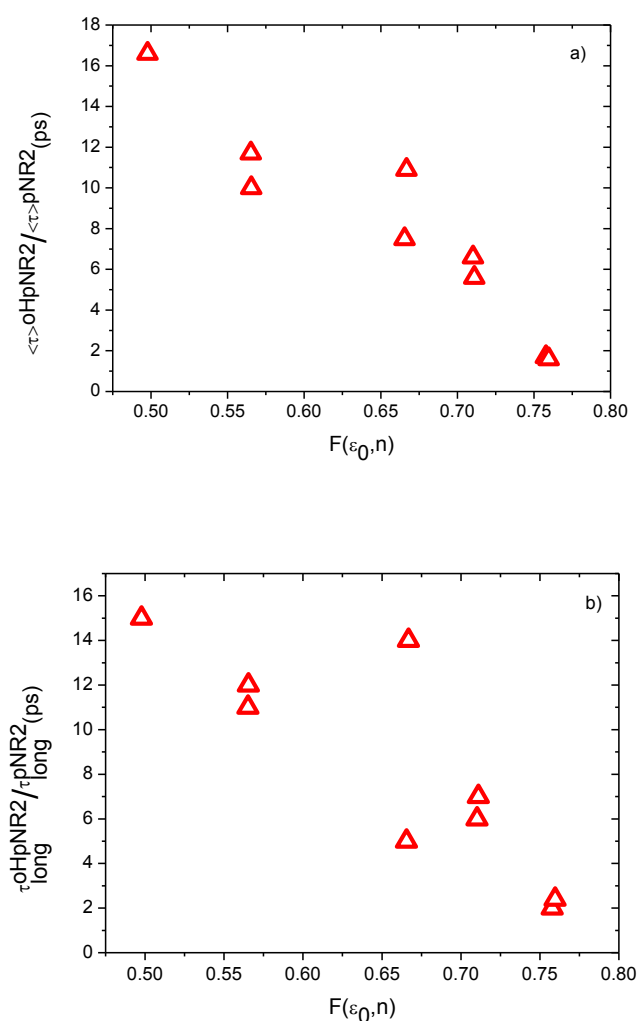
Figure 5.14. The extension of the *p*NR2 average fluorescence lifetime (a) and long component of the fluorescence (b) relative to that of *o*OH*p*NR2 is greatest in non-polar solvents.

5.5. Conclusions

Comparing the chromophores studied in this work to HBDI, the modifications cause a red shift of the absorption and emission spectra, an increase in the quantum yield and extension of the fluorescence lifetime. The effects are greatest for the *o*OH*p*NR2molecule, where the average emission lifetime can be up to 60 times longer than for HBDI in the same solvent.

HBDI decays via ultrafast internal conversion, where the rate of nonradiative decay does not depend on viscosity (Chapter 1). It has been shown that the mechanism of IC involves a near barrierless volume conserving motion. Conversely, the fluorescence decays of *p*NR2 and *o*OH*p*NR2 do exhibit a viscosity dependence, where this dependence is much stronger for *o*OH*p*NR2 than for *p*NR2. This suggests that whilst the para group does hinder IC, it is the ortho modification which is most significant. In agreement with this, a strong viscosity dependence was also observed for *o*-HBDI[2].

The addition of the ortho hydroxyl group significantly extends the fluorescence lifetime of the molecule, affecting the long component in a polarity sensitive manner. The OH group can form an intramolecular hydrogen bond with the N on the imino ring (Figure 5.1)[2]. This interaction restricts the ability of the chromophore to rotate around the bridging bonds, suppressing the radiationless decay mechanism and enhancing the fluorescence lifetime. For *o*OH*p*NR2, the decays are shortened in hydrogen bond donating solvents. The average lifetime is similar in the hydrogen bond donating solvents water and methanol (6.4 ps and 6.7 ps respectively), whilst in the aprotic solvent acetonitrile, $<\tau>$ increases to 10.6 ps (Table 5.3). Thus indicating that protic solvents disrupt the intramolecular hydrogen bond, facilitating IC and enhancing nonradiative decay.

The short component is similar for both molecules, with a lifetime of a few hundred femtoseconds which does not correlate with solvent viscosity or polarity. The lifetime of this component is also comparable to the short component of HBDI (Chapter 3), so could relate to a process which is not strongly affected by the modifications. It is possible that this decay relates to vibrational relaxation or solvation. Future work to measure the wavelength dependence of the time-resolved emission, could reveal the nature of this component.

5.6. References

(1)Dong, J.; Solntsev, K. M.; Poizat, O.; Tolbert, L. M. *J. Am. Chem. Soc.* **2007**, *129*, 10084.
(2)Hsieh, C.-C.; Chou, P.-T.; Shih, C.-W.; Chuang, W.-T.; Chung, M.-W.; Lee, J.; Joo, T. *J. Am. Chem. Soc.* **2011**, *133*, 2932.
(3)Kang, J.; Zhao, G.; Xu, J.; Yang, W. *Chem. Commun.* **2010**, *46*, 2868.
(4)Chen, K.-Y.; Cheng, Y.-M.; Lai, C.-H.; Hsu, C.-C.; Ho, M.-L.; Lee, G.-H.; Chou, P.-T. *J. Am. Chem. Soc.* **2007**, *129*, 4534.
(5)Vengris, M.; van der Horst, M. A.; Zgrabli, G.; van Stokkum, I. H. M.; Haacke, S.; Chergui, M.; Hellingwerf, K. J.; van Grondelle, R.; Larsen, D. S. *Biophys. J.* **2004**, *87*, 1848.
(6)Chen, Y.-H.; Lo, W.-J.; Sung, K. *The Journal of Organic Chemistry* **2012**, *78*, 301.
(7)Conyard, J.; Kondo, M.; Heisler, I. A.; Jones, G.; Baldridge, A.; Tolbert, L. M.; Solntsev, K. M.; Meech, S. R. *The Journal of Physical Chemistry B* **2011**, *115*, 1571.
(8)Baranov, M. S.; Lukyanov, K. A.; Borissova, A. O.; Shamir, J.; Kosenkov, D.; Slipchenko, L. V.; Tolbert, L. M.; Yampolsky, I. V.; Solntsev, K. M. *J. Am. Chem. Soc.* **2012**, *134*, 6025.
(9)Huang, G.-J.; Ho, J.-H.; Prabhakar, C.; Liu, Y.-H.; Peng, S.-M.; Yang, J.-S. *Org. Lett.* **2012**, *14*, 5034.
(10)Solntsev, K. M.; Poizat, O.; Dong, J.; Rehault, J.; Lou, Y.; Burda, C.; Tolbert, L. M. *The Journal of Physical Chemistry B* **2008**, *112*, 2700.
(11)Yang, J.-S.; Huang, G.-J.; Liu, Y.-H.; Peng, S.-M. *Chem. Commun.* **2008**, 1344.
(12)Lewis, F. D.; Crompton, E. M. *J. Am. Chem. Soc.* **2003**, *125*, 4044.
(13)Tou, S.-L.; Huang, G.-J.; Chen, P.-C.; Chang, H.-T.; Tsai, J.-Y.; Yang, J.-S. *Chem. Commun.* **2014**, *50*, 620.
(14)Chudakov, D. M.; Matz, M. V.; Lukyanov, S.; Lukyanov, K. A. *Physiol. Rev.* **2010**, *90*, 1103.
(15)Huppert, D.; Leiderman, P.; Ben-Ziv, M.; Genosar, L.; Cohen, L. *The Journal of Physical Chemistry B* **2005**, *109*, 4241.
(16)Chattoraj, M.; King, B. A.; Bublitz, G. U.; Boxer, S. G. *Proceedings of the National Academy of Sciences* **1996**, *93*, 8362.

Chapter 6 - Modelling the Excited State Dynamics of HBDI

6.1. Introduction

6.1.1. Relaxation of HBDI

As described in Chapter 1, the excited state of the GFP chromophore (HBDI) recovers via ultrafast internal conversion[1,2]. Accordingly, the emission of the isolated chromophore is very weak with a quantum yield of approximately 0.2×10^{-4} and decays within a few picoseconds[1,3]. The mechanism of internal conversion is proposed to involve a near barrierless, volume-conserving movement through some kind of torsion or pyramidalisation of the bridging methylene bonds[4-6].

The strong fluorescence of the protein can be recovered for the isolated chromophore in solution by cooling to the solvent glass transition temperature[1,4]. This scenario is equivalent to placing the chromophore in a rigid medium. Here the freedom of motion of the bridging bonds is restricted, such that the radiationless decay channels are hindered, enhancing the quantum yield. Furthermore, it has been shown that a sterically crowded derivative of HBDI, where the ground-state geometry is twisted, results in a further enhancement of the radiationless decay rate, consistent with the radiationless decay coordinate involving twisting of the bridging bonds[7].

Many theoretical studies of the excited state dynamics of HBDI have been presented. However most concern the chromophore in the gas phase with few focusing on the chromophore in solution. Gas phase calculations suggest that the nature of the excited state isomerization pathway to the ground-state depends on the protonation state and initial

167

isomer of the chromophore[8-10]. Some calculations suggest that the most probable path

involves torsion of the single bond, although torsion of both bonds can occur[6].

A quantum chemical calculation presented by Altoe et al. included solvent effects through

the polarizable continuum model[11]. In agreement with the gas phase calculations of Olsen &

Smith, they showed that torsion around both bonds was possible for anionic HBDI[10].

However, rotation about the double bond was suggested as the preferred radiationless

decay channel. It was determined that rotation around the double bond is associated with a

very small barrier (4.2-8.4 kJ mol^{-1}) and does not displace a large volume of solvent. Where

torsion around the single bond could account for the 5% of the excited population which

goes to a bottleneck in the ground-state recovery cycle[2]. Furthermore, they showed that

this motion would be hindered in the protein cavity, consistent with the high fluorescence

quantum yield in GFP itself. The calculations of Toniolo and co-workers addressed the

effects of environment by filling the first solvation shell[12,13]. These calculations showed that

in solution, the excited state decayed faster than in the gas phase and the results indicated

that torsion around both bridging bonds occurred in a volume conserving manner for both

regimes.

6.1.2. Previous Models

Several studies have used models based on the Smoluchowski equation to simulate the

dynamics of molecules undergoing barrierless excited state reactions[14,15] (Chapter 2).

Originally, Tominaga et al. used the model applied here to simulate charge transfer in the

excited state[16,17]. The excited state surface was described by strongly coupled harmonic

radiative and dark excited states, where the coupling forms the reactive potential energy surfaces (PESs).

A similar method has been used to study the excited state dynamics of other molecules in solution, with Meech and Glasbeek presenting studies on confined and free Auramine O[18-21] and Huppert et al. applying the model to the fluorescent marker Thioflavin-T[22,23]. In both studies of Auramine, the rate of radiative decay was chosen to have a dependence on the twisting angle of the phenyl rings. To account for the ultrafast radiative decay and the observation of a long-lived dark state, the excited state PESs were modelled by coupling an emissive locally excited state and a dark state.

These studies all rely on simulated PESs and when modelling the dynamics, the parameters which define the shapes and coupling of the surfaces had to be determined, or were used as fitting parameters. In this work calculated PESs for HBDI and FHBMI are used directly as input to the model, removing the complication and uncertainty introduced by simulating them. Thus we address the question: does the gas phase calculated PES reproduce the dynamics observed in solution?

6.1.3. Kindling Fluorescent Protein

The kindling fluorescent protein (KFP), is so called because it 'kindles' between fluorescent and nonfluorescent states[24]. Initially dark, the protein becomes fluorescent upon irradiation with intense green light. The emission then relaxes or can be quenched with blue light through a reversible mechanism. Certain properties of KFP, such as fluorescence relaxation lifetime, have been improved and tuned and there is now a family of KFPs. These

modifications have made KFPs extremely useful tools for *in vivo* photolabelling and tracking[25-27]. The mechanism of kindling has been investigated through studies of mutated versions of KFP. It has been proposed that the primary process involved is chromophore (Figure 6.1c) torsion or *cis-trans* isomerisation and that certain amino acids surrounding the chromophore are critical for kindling function[26,28].

The photophysics of the GFP and KFP proteins are very different[29]. To investigate the relative importance of the chromophore structure and protein-chromophore interactions, the behaviour of the GFP chromophore (HBDI) (Figure 6.1c) and a chromophore (FHBMI) closely related to the KFP chromophore (AHBMI) will be compared (Figure 6.1).
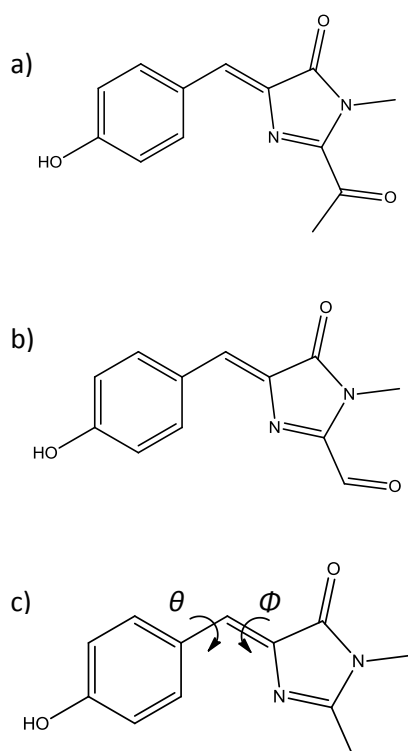
Figure 6.1. Molecular structure of the KFP chromophore AHBMI (a) and a related chromophore FHBMI (b). The structure of HBDI (c) showing torsional angles θ and Φ.

6.2. Experimental and Methods

The HBDI and FHBMI chromophores were synthesised at the University of East Anglia based on the methods described in literature and provided to us by the group of Philip Page[3,30].

The ground-state optimized geometries of the chromophores were calculated using Gaussian software. Calculations were made at the DFT B3LYP level using the basis set 6-31G++ (d,p) (Section 6.3.2).

The samples were flowed at a rate of 7 ml/min and excited with a power of up to 9 mW. The excitation wavelength was usually 400 nm. However for some measurements the two-photon setup was required to enable full coverage of the emission spectrum (Chapter 2). In these cases, an excitation wavelength of 800 nm was used for two-photon excitation.

6.2.1. Model

The theory underlying the diffusional model was outlined in Chapter 2. The model here uses calculated potential energy surfaces, rather than modelled ones. These were taken from the calculations of Olsen and Smith who determined the ground and excited state surfaces for HBDI and AHBMI (Figure 6.2) as a function of the torsion angles Φ and θ (Figure 6.1c). Two different methods were employed by Olsen to calculate the PESs, giving two sets of surfaces for the anionic state of each chromophore. The first method was based on a state-averaged CASSCF model (CAS) and the second on a perturbation theory-corrected CASSCF model (MR). The active space used was spanned by three Boys localised orbitals centred on the bridge, phenoxy and imidazolinone moieties. The reaction coordinate was the twist of the

methine bridge bonds which were both varied between 0° and 90^0. Surfaces were also

calculated for the molecules in both the *cis* and *trans* states. However, the surfaces are very

similar and it has been shown experimentally that the decays for both isomers are

essentially identical (Chapter 3)[31]. Thus, only the *cis* surfaces have been used in this work.

The surfaces are input to the Smoluchowski equation (Chapter2),

$$\frac{\partial}{\partial t}\rho(z,t) = D\frac{\partial}{\partial z}\left(\frac{\partial}{\partial z} + \frac{1}{k_B T}\frac{\partial}{\partial z}S_1(z)\right)\rho(z,t) - \Gamma(z)\rho(z,t). \qquad (6.1)$$

The Smoluchowski equation describes the evolution of a population density $\rho(z,t)$ along a

reaction coordinate (z) for a particular potential energy surface (S_1) and diffusion coefficient,

$$D = \frac{k_B T}{6\eta V}, \qquad (6.2)$$

in which η is the solvent viscosity and V is the volume of the rotating group.
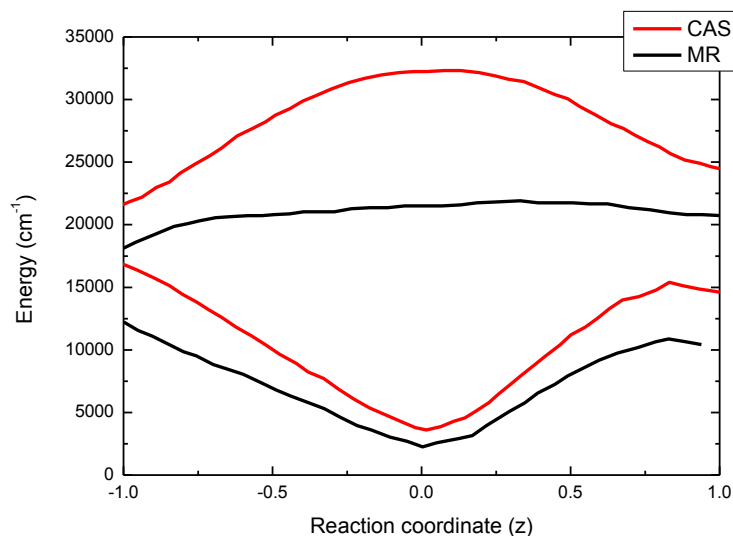
Figure 6.2. The S_0 and S_1 PESs for anionic HBDI were calculated by Olsen using two methods, CAS (red) and MR (black)[10].

6.3. Results and Discussion

6.3.1. Steady-state Spectroscopy of HBDI and FHBMI

HBDI and FHBMI differ structurally at the imidazolinone ring, where one of the attached methyl groups of HBDI has been substituted for an electron withdrawing formyl group in FHBMI (Figure 6.1). Figure 6.3 shows the steady-state absorption and emission of HBDI and FHBMI in the neutral (a) and anionic (b) states. The absorption and emission of both charge states of FHBMI are red-shifted by a few nm compared to HBDI. Clearly the molecular modification has little effect on the steady-state properties.
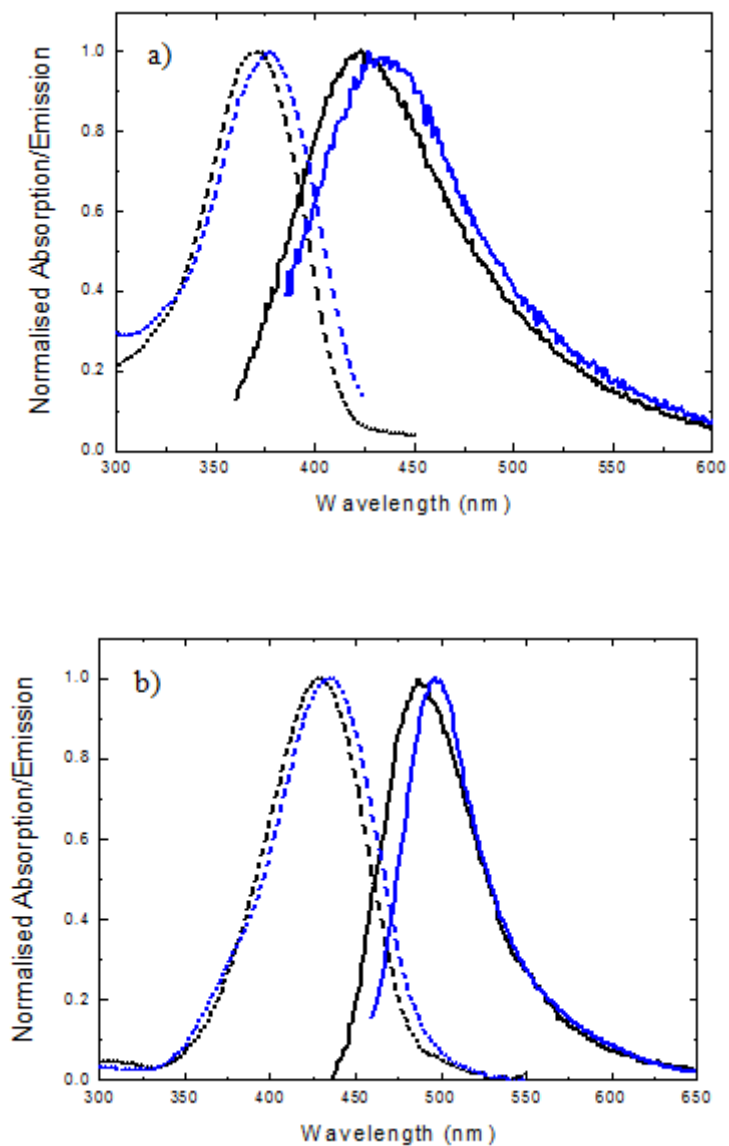
Figure 6.3. Steady-state absorption (dashed line) and emission (solid line) spectra of HBDI (black) and FHBMI (blue) in methanol: (a) neutral form (b) anionic form.

6.3.2. Ground-state Calculations on HBDI and FHBMI

The ground-state optimised structures of neutral and anionic HBDI and FHBMI were calculated at the DFT B3LYP level using the basis set 6-31G++ (d,p). Figure 6.4 shows that both chromophores are planar in their ground-states. Compared to neutral HBDI, the conjugation is increased slightly (across the formyl substituent) for neutral FHBMI, explaining the small red shift observed in the electronic spectra (Figure 6.3). The ground-state dipole moments (μ) were found to be 1.6 D and 4.8 D for neutral HBDI and FHBMI respectively, consistent with charge redistribution to the substituent. Turning to the anionic forms, the dipole moment of the HBDI anion increases significantly to 11.4 D, while that of anionic FHBMI is relatively unchanged at 4.7 D. The values calculated for HBDI are in agreement with those in the literature[32].
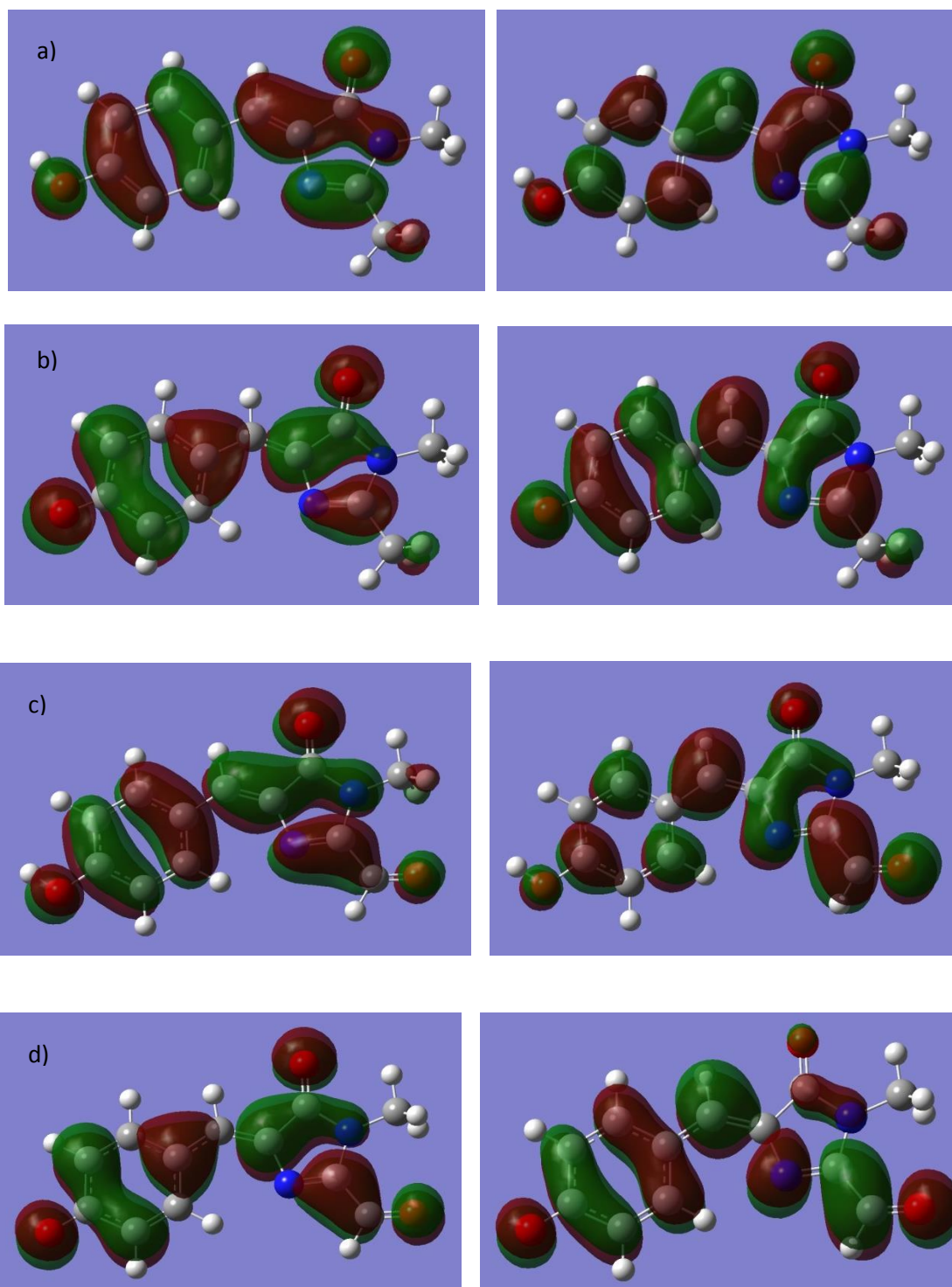
Figure 6.4. Optimized ground-state structures showing the HOMO (left) and LUMO (right) of neutral HBDI (a), anionic HBDI (b), FHBMI (c) and anionic FHBMI (d).

6.3.3. Time-resolved Fluorescence of HBDI and FHBMI

The time-resolved fluorescence decays of the chromophores were measured at the peak emission wavelengths in methanol. The decays are both ultrafast and very similar (Figure 6.5). For both chromophores the decay of the anion is significantly longer than that of the neutral. The kinetics were fitted with a single exponential for neutral HBDI and a biexponenital function for the other molecules. Table 6.1 gives the fitted time constants and normalised amplitudes. For both HBDI and FHBMI, the average lifetime increases approximately 1.5 times from neutral to anionic form. Comparing HBDI and FHMBI, for both the neutral and anionic chromophores there is a very small increase in the average lifetime of 1.3 and 1.2 times respectively.
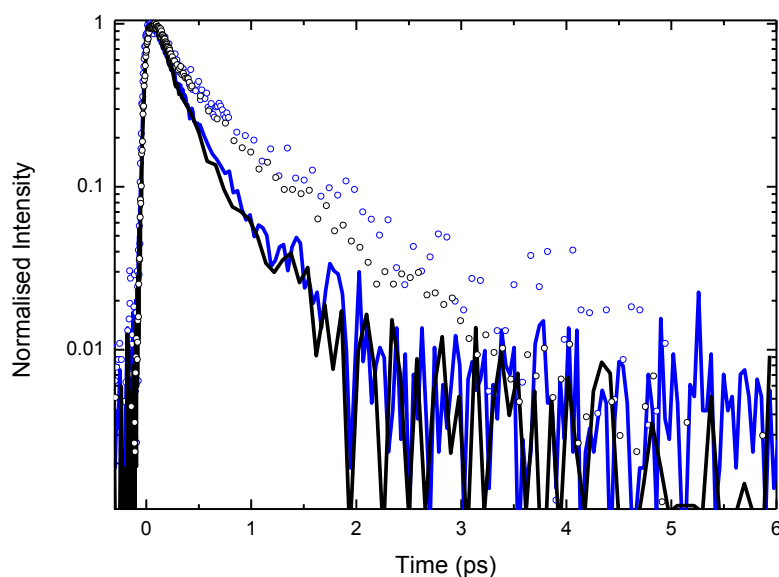
Figure 6.5. Time-resolved fluorescence decays of neutral (solid) and anionic (circles) HBDI (black) and FHMBI (blue).

	Neutral HBDI	Anionic HBDI	Neutral FHBMI	Anionic FHBMI
τ_1/ps	0.26	0.36	0.17	0.20
a_1	1.0	0.52	0.65	0.60
τ_2/ps	-	0.53	0.64	0.97
a_2	-	0.48	0.35	0.40
$<\tau>$/ps	0.26	0.44	0.34	0.51

Table 6.1. Fitting parameters for time-resolved fluorescence decays of HBDI and FHBMI.

Time-resolved fluorescence measurements were made spanning the steady-state emission spectrum of each chromophore. The individual decays were compiled to create time-resolved spectra (Figure 6.6). Spectra corresponding to particular times after excitation were extracted and fitted with a log normal function (Chapter 2). From the fitted spectra, the first moment, integrated intensity and FWHM were extracted (Figure 6.7).
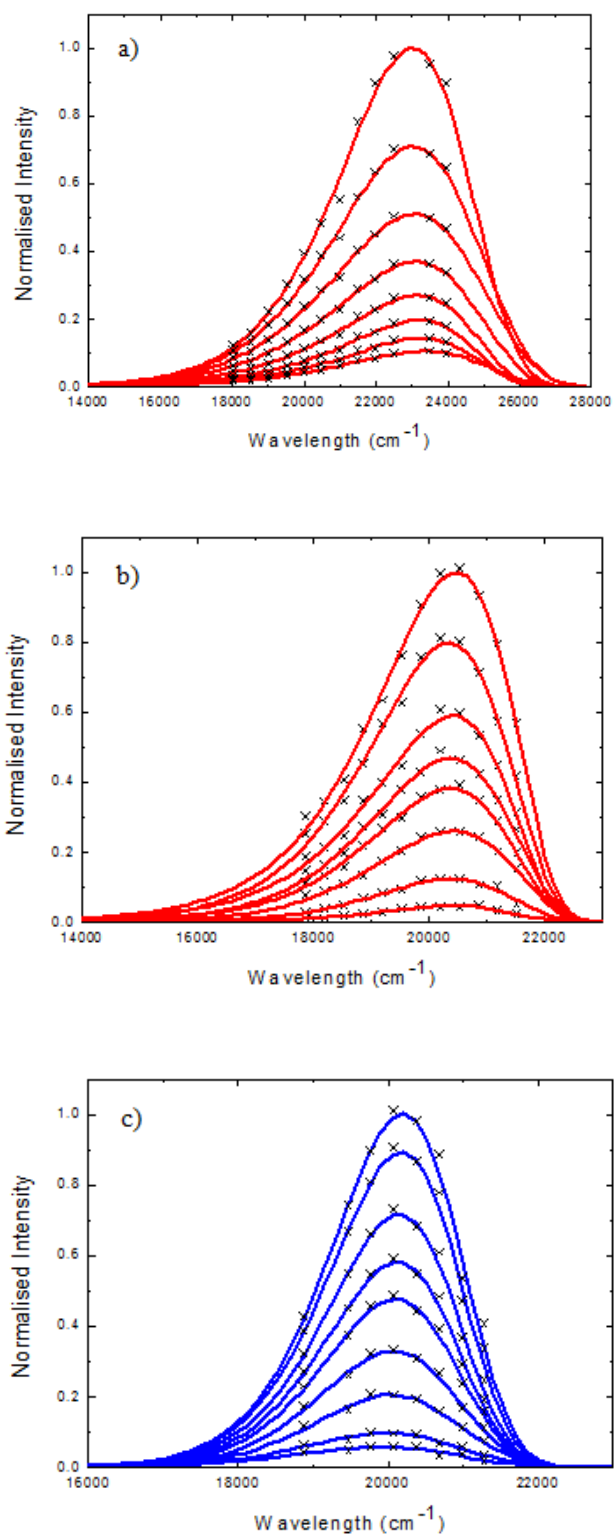
Figure 6.6. Time-resolved emission spectra (points) fit to the log normal function (lines) for

(a) neutral HBDI 50 fs to 800 fs (b) anionic HBDI 50 fs to 2ps (c) anionic FHBMI 50 fs to 2 ps.

For all measurements the solvent was methanol.

Figure 6.7 shows that there is negligible time dependence in the first moment of the fluorescence spectra of the chromophores. If the dipole moment of the excited state differed greatly to that of the ground-state, solvation would stabilise the excited state over the timescale of solvent reorganisation. This would result in a time-dependent red shift in the emission spectrum[33]. However calculations for HBDI have suggested only a small change in dipole moment between the S_0 and S_1 states (~2 D) for both the anion and neutral[32], consistent with our observation. A red shift might also be expected if the excited state population decays across a surface where the energy gap between the ground and excited states decreases with time (see below). Thus the observation of a negligible time-resolved Stokes shift limits the kind of excited state dynamics these solutes can exhibit.

In agreement with the single wavelength measurements presented above, the integrated intensity indicates non-single exponential dynamics for both chromophores and a longer decay for anionic HBDI. Overall the photophysics and spectra of HBDI and FHBMI are very similar, despite the strongly electron withdrawing formyl substituent. This contrasts with the strong effect on spectroscopy of substitution on the phenolic ring[7], or the greatly extended conjugation in Kaede (Chapter 4) The photophysical properties of the proteins GFP and KFP are very different[29]. Therefore, the similarity of the behaviour of HBDI and FHBMI highlights the importance of the protein-chromophore interactions in determining the protein photophysics.
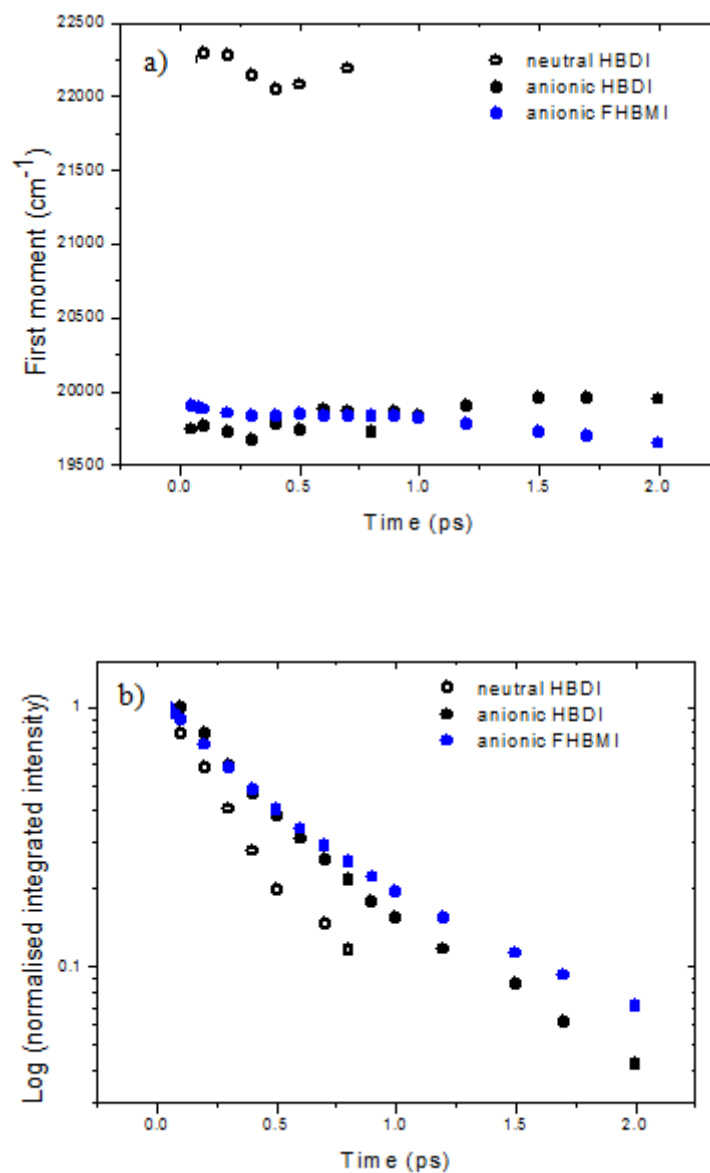
Figure 6.7. Time dependence of the (a) first moment and (b) integrated intensity for HBDI

(black) and FBHMI (blue) recovered from the log normal plots. Open symbols neutral, closed

anion.

6.3.4. Simulation Results

Before excitation the chromophores exist in a planar state, corresponding to the minimum of the S_0 surface (Figure 6.8). Excitation creates a Franck-Condon excited state where the chromophore is promoted to an almost flat region of the PES where barrierless torsion around one or both of the bridging bonds is possible. As the bonds twist, the energy of the ground-state is increased and excited state decreased until the surfaces merge at a conical intersection or become sufficiently close to allow fast internal conversion from the excited state to ground-state.

As described in Section 6.2.1, two different calculated PESs were used in these simulations in combination with two different volumes (required to calculate the diffusion coefficient (Equation 6.2)). The volume used represents the volume of the isomerising section of the chromophore and was estimated to be equivalent firstly to the actual volume of a benzene ring and secondly to the hydrodynamic volume of benzonitrile[34].

The parameters for the fit for the surface calculated using the MR method with the hydrodynamic volume of benzene are represented in Figure 6.8.The Franck - Condon geometry is planar and has a strong transition moment. It has been shown that a twisted chromophore has a lower transition moment as well as enhanced radiationless decay[7]. Thus the form of the transition moment (*M(z)*) (Chapter 2) shown in Figure 6.8 was used, where the *M(z)* is maximised at 0^0 (planar geometry) and minimised at a 90° degree twist around either bridge bond.
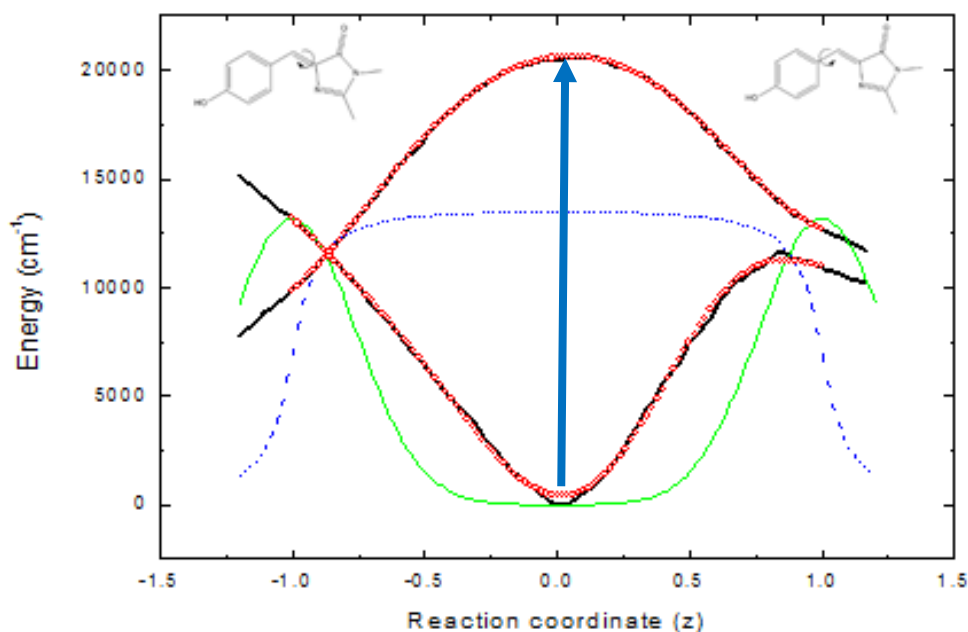
Figure 6.8. Representation of the parameters used in the simulations. Solid and dashed

black lines are the ground and excited state PESs calculated by Olsen[10]. The red circles are

polynomial fits to the PES used in the simulation. The green line is the Gaussian decay

functions and the dashed blue line is the coordinate-dependent transition moment. The

blue arrow represents excitation from the ground-state to the Franck-Condon region on the

excited state.

To investigate the importance of the inclusion of the transition moment and the rate of

radiationless decay in the model, the second term of Equation 6.1 was set to zero with the

M(z) shown in Figure 6.8 used for the HBDI anion in methanol. This is equivalent to a

scenario where no radiationless decay to the ground-state is permitted. Figure 6.9 shows

the evolution of the excited state population along the PES. The population collects at the

maximum twist angles as expected, resulting in an emission spectrum which red shifts and

broadens with time. This is as expected for the approach of the ground and excited state

PES, but is not consistent with experimental observations, highlighting the importance of

the inclusion of the radiationless decay rate in the model.
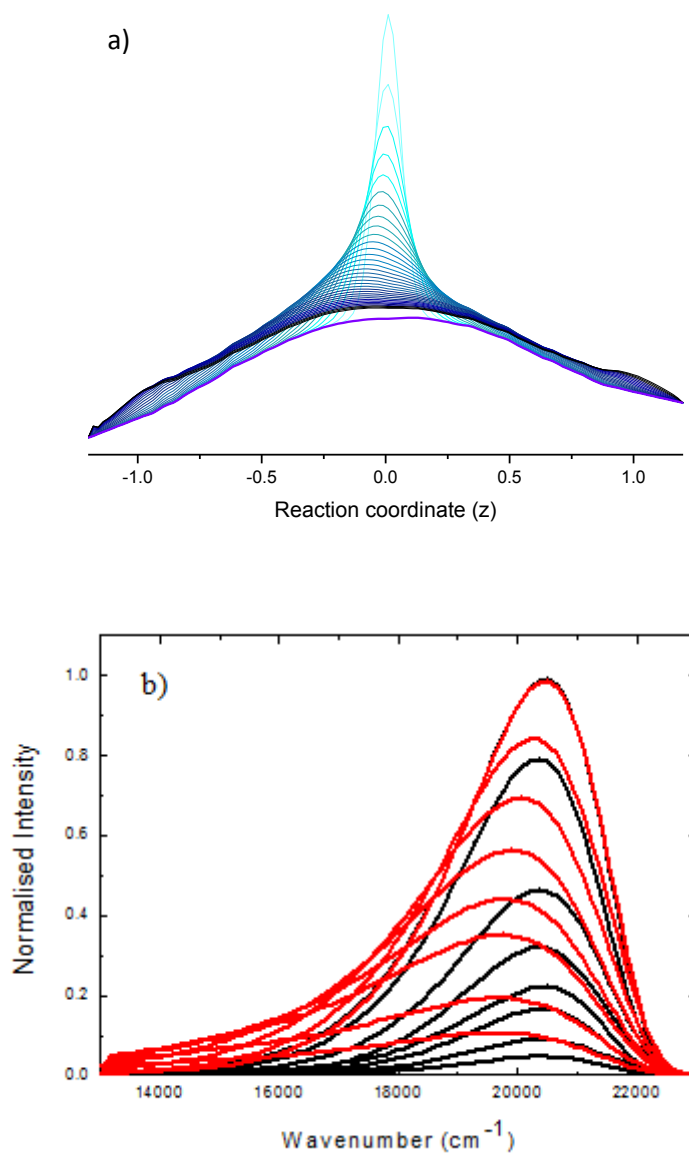
Figure 6.9. (a) The $\rho(z, t)$ calculated from (6.1) with the final term omitted (no decay

function). (b) The spectra calculated for the data in (a).

To simulate the spectra, $\rho(z,t)$ is first calculated by inputting the theoretically determined

PESs and assuming *M(z)* is of the form of that shown in Figure 6.8 and a time independent

diffusion coefficient (Equation 6.2) reflecting the chosen volume. To obtain best fits to the

time-resolved emission spectra, the amplitudes (k_G) and widths (σ) of the sinks were varied

using an evolutionary fitting algorithm, while keeping their positions along the reaction

coordinate fixed at the maximum twist angles. Figure 6.10 shows the fits produced for the

HBDI anion using the MR and CASSCF surfaces with the hydrodynamic volume of

benzonitrile or the volume of a benzene ring used for the calculation of *D* (Equation 6.2).

The surfaces provide reasonable fits to the measured data at early times, where the best fit

was obtained for using the hydrodynamic volume of benzonitrile and the MR PESs.
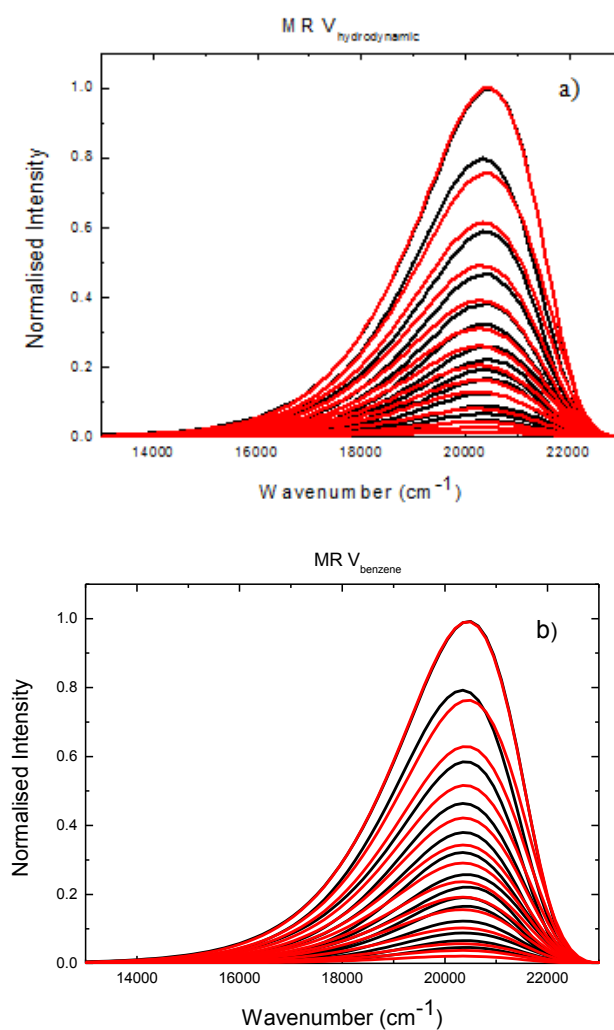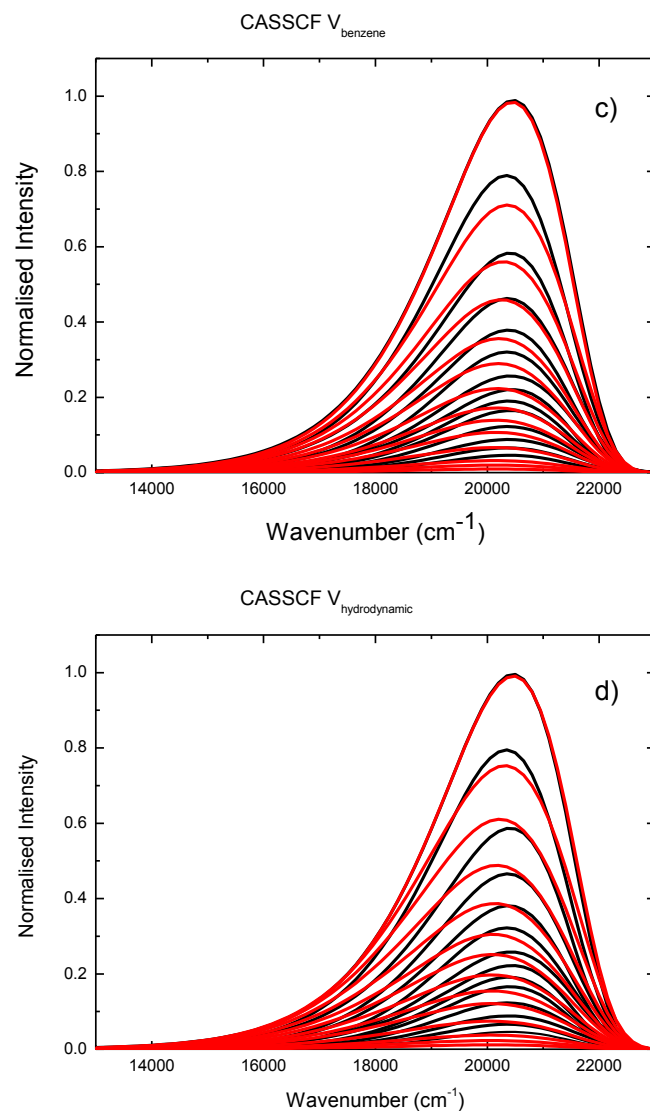
Figure 6.10. Comparison of the calculated spectra (red) and the log normal fits to the data (black), for HBDI anion in methanol using the hydrodynamic volume of benzonitrile and the MR surfaces (a), the volume of benzene and the MR surfaces (b), the volume of benzene and the CASSCF surfaces (c) and the hydrodynamic volume of benzonitrile with the CASSCF surfaces (d).

The time dependence of the first moment and integrated intensity for all combinations are shown in Figure 6.11. As Figure 6.11 shows, the very small blue shift observed experimentally in the first moment is not reproduced by the fits. However the fits show only small redshifts, on the order of a few hundred cm^{-1}, and the MR PESs with the volume of benzene provides the closest fit to the first moment.

The fitting parameters are given in Table 6.2. All fits require a broad (large σ) and deep (large k_G) sink. A narrower sink and a smaller rate produced a spectrum which red shifts in time and is therefore not consistent with the experimental results. As mentioned earlier the fits were created with a coordinate-dependent transition moment and sink function ($\Gamma(z)$), where the width and amplitude of the sinks are varied in the fitting procedure. As $M(z)$ and $\Gamma(z)$ control the rates of radiative and nonradiative decay respectively, they can be interchanged to a certain extent to achieve similar fits. However they are not perfectly interchangeable and less good fits were achieved by varying $M(z)$ and keeping the parameters of the sink function fixed. As Figure 6.9 indicates, a large $M(z)$ but small $\Gamma(z)$ would result in population collection in the twisted states. The transition moment rapidly decreases to 0 around high $|z|$. Thus radiative decay is not permitted from the highly twisted states. Such dark states are detectable by transient absorption, but have not been observed for HBDI. Transient infra-red spectroscopy of neutral HBDI in solution shows that the excited state decays on the sub-picosecond timescale to a vibrationally hot ground-state which subsequently cools on the picosecond timescale. Thus, the relatively strong sink function recovered from the simulations is consistent with the efficient nonradiative decay observed experimentally.
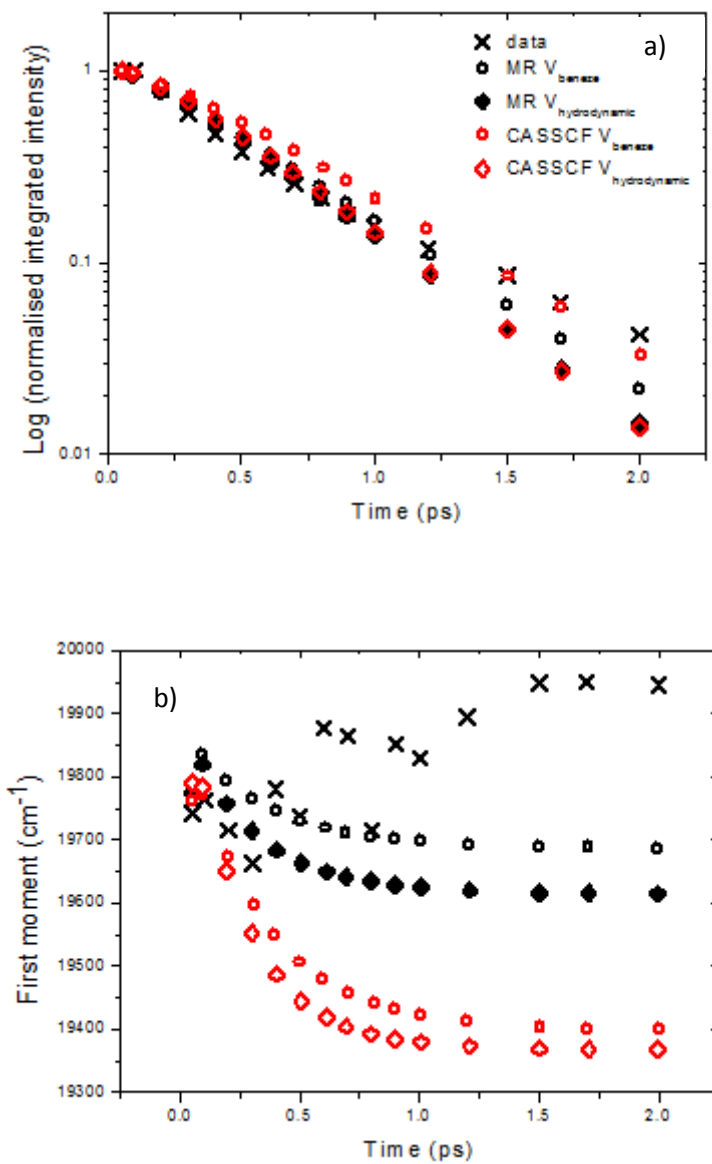
Figure 6.11. Calculated integrated intensity (a) and first moment (b) of the spectra using the volume of benzene (circles) and the hydrodynamic volume (diamonds) for *D* in (6.2) for the MR surfaces (black) and the CASSCF surfaces (red). Data are for HBDI (black crosses).

	$V_{benzene}$		$V_{hydrodynamic}$	
	CASSCF	MR	CASSCF	MR
k_G	3900	4020	4000	1340
σ	0.32	0.32	0.31	0.34

Table 6.2. The fitting parameters, width (σ) and amplitude (k_G), of the sink function for anionic HBDI recovered using combinations of the two volumes and two PESs.

The MR and CASSCF surfaces from Olsen's paper differ by approximately 1300 cm^{-1} for the S_0 PES and roughly 10,700 cm^{-1} for the S_1 PES at 0°[10]. However, after the surfaces have been vertically adjusted to match the measured absorption and first (t = 50 fs) emission spectra, there is no energy difference in the S_1 states at 0°, which is a consequence of the fitting. However at 90° the MR surface is still approximately 7000 cm^{-1} higher in energy. The MR surface is also much flatter than the CASSCF surface which may slow the evolution of the excited state population along the PES (Figure 6.2).

Whilst the model works well for anionic HBDI, the same method applied to the FHBMI anion failed. Although the measured spectra are similar (Figure 6.3), it is likely that the PESs used are not suitable for this molecule. Either the larger, more complex molecule requires a more sophisticated calculation method or the aldehyde to formyl substitution is in fact significant (the calculation is for AHBMI while our measurements are on FHBMI). Figure 6.12 shows the AHBMI PESs used for the FHBMI simulations. The minimum energy geometry in the ground-

state is nonplanar. However, calculations have revealed the optimized ground-state geometry of FHBMI to be planar (Section 6.3.2). Furthermore, the excited state surface appears to have a barrier to isomerization which is not consistent with the observed ultrafast decay of FHBMI (Section 6.3.3).
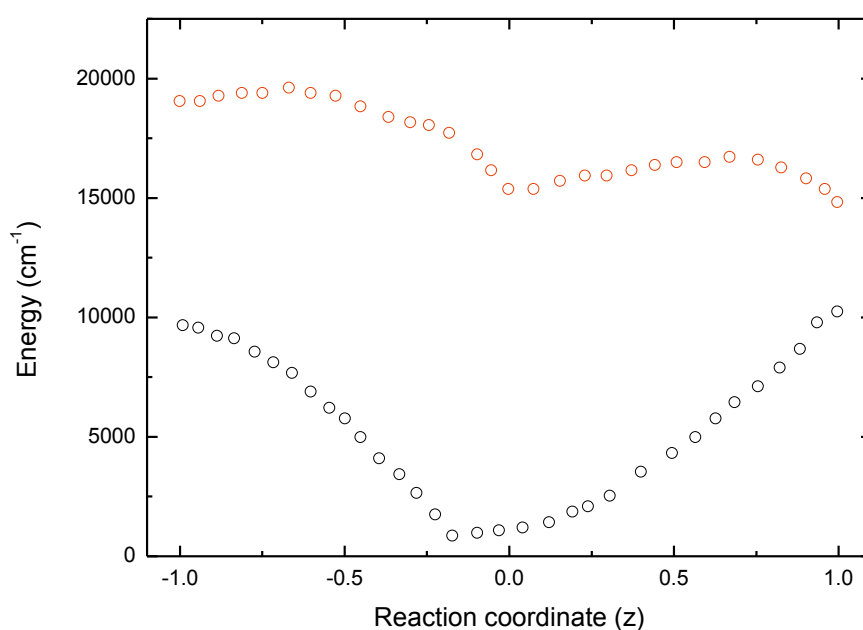
Figure 6.12. Calculated S_0 (black) and S_1 (red) PESs of FHBMI[10].

Calculations of the neutral species are more challenging than those of the anion. Hence there is little theoretical data with which to compare the experimental results. However, the energies of the ground and excited states were recently calculated for the neutral species at 0° and 90° torsion about the double bond[8]. As only two points are available, the anionic MR

surface was scaled to the two neutral points (Figure 6.13). First the energy differences between the two points and the surface were used to calculate a gradient. This gradient was applied to the anionic surface, producing a coordinate-dependent neutral PES. This method predicts a flatter S_1 PES for the neutral form than for the anion. The PESs were vertically shifted to reproduce the measured absorption and emission spectra, assuming the same *M(z)* described previously. Contrary to experimental data, the calculated time dependence of the integrated area predicts a faster decay for the anion than the neutral (Figure 6.13). Whilst calculations have indicated that in the gas phase, the anion does decay faster than the neutral[6]. However, the PESs created for this work cannot adequately reproduce the observed dynamics of the neutral chromophore in solution. More detailed calculations of the neutral chromophore surface are required. This is an important objective for calculation as the neutral state is important because it is often responsible for the excited state reactions of second generation fluorescent proteins[35-37].
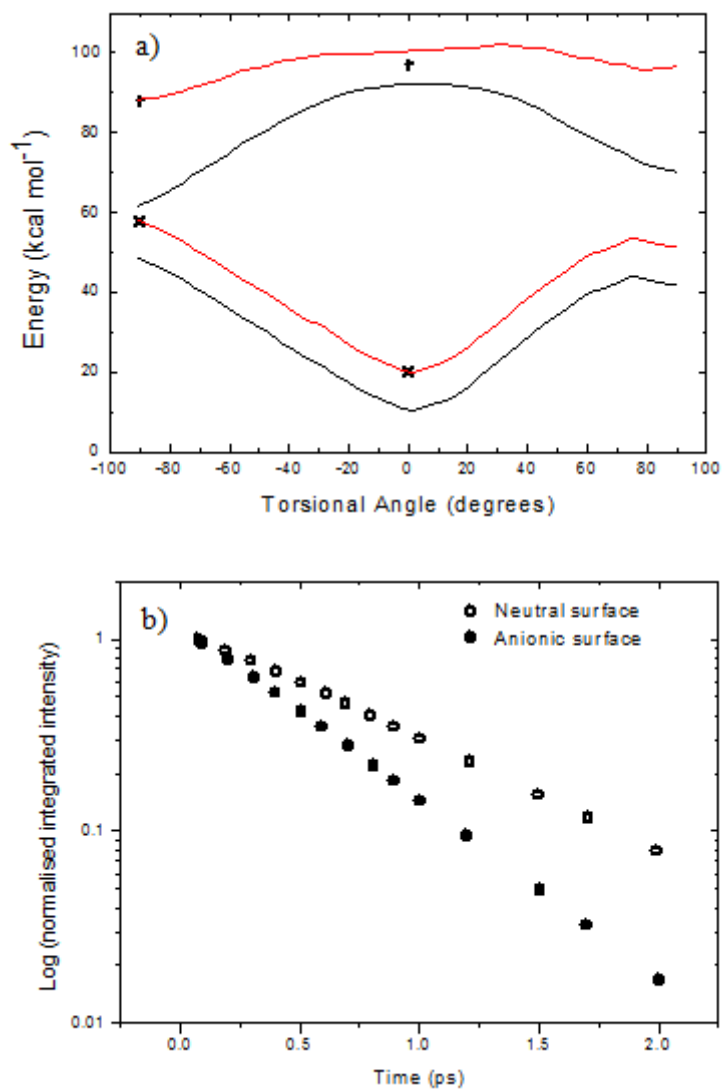
Figure 6.13. (a) Anionic HBDI S_0 and S_1 surfaces calculated by Olsen (black)[10]. Calculated S_0 and S_1 neutral HBDI points are shown (black crosses). Neutral surfaces were created by scaling the anionic surfaces to the neutral points (red). (b) Time dependence of the integrated intensity of HBDI predicted by the neutral surface (open circles) and Olsen's anionic surface (filled circles).

An important feature of the model presented here is the inclusion of solvent friction effects on the dynamics of the excited state population through D (Equation 6.2). The decays of HBDI in solvents of various viscosities are shown in Figure 6.14. The measured decays are shown to be only slightly dependent on the solvent viscosity, in agreement with the volume conserving mechanism predicted previously[1,4]. However, upon changing the viscosity in the model, a strong solvent dependence is observed. This indicates a significant failure of the model. The model behaved well for the fluid solvent methanol, in which the measured decay times are similar to those in the gas phase[38]. However, the viscosity dependence indicates that frictional contributions to the model are too large. Thus it may be the shape of the PES which is dominant in determining the dynamics in low friction media with frictional contributions becoming important in less fluid solvents. Alternatively the model for the diffusion coefficient may be incorrect. More sophisticated time-dependent diffusion coefficients were used to simulate ultrafast decay in Auramine[19].
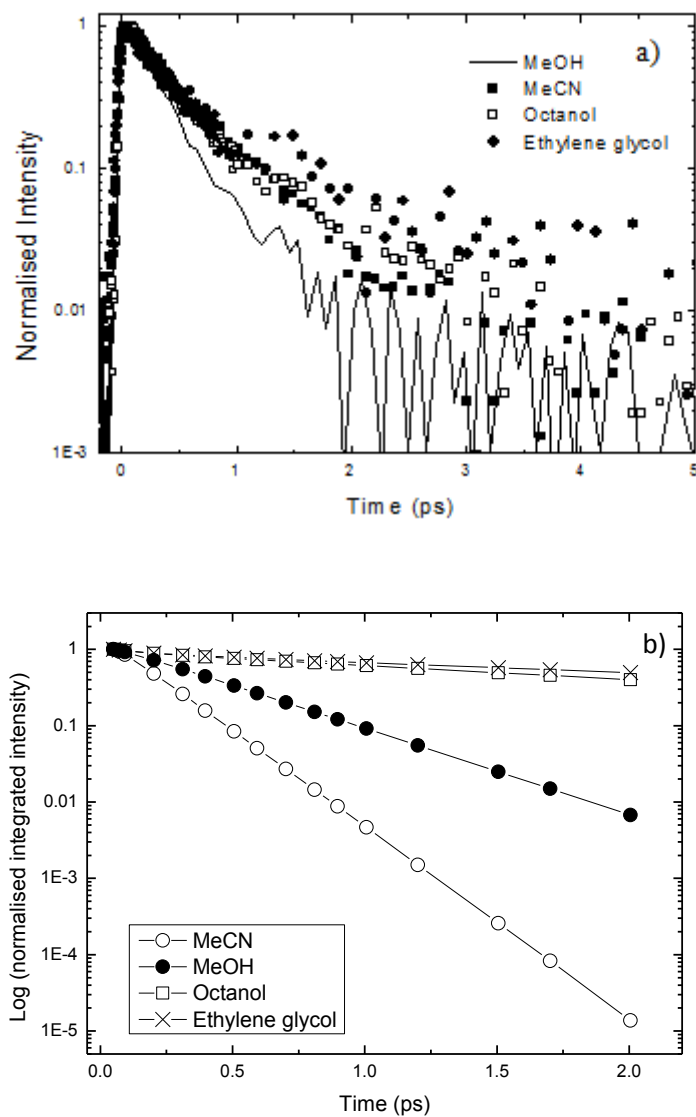
Figure 6.14. (a) Time-resolved fluorescence decay for HBDI neutral in a range of solvents. (b)

Calculated integrated intensity from (a) where *D* for the appropriate solvent viscosity was

used and other parameters fixed as for methanol.

6.4. Conclusions

The steady-state and ultrafast fluorescence spectroscopy of HBDI and FHBMI, a molecule closely related to the KFP chromophore, were measured in solution in their neutral and anionic forms. In contrast to the very different behaviour of the GFP and KFP proteins, the spectra and kinetics of the chromophores are similar. Both molecules exhibit ultrafast excited state dynamics, with the time-resolved fluorescence spectra showing negligible shifting with time. This result highlights the importance of the influence of the protein structure and the chromophore-protein dynamics in altering the behaviour of FPs.

The excited state dynamics of anionic HBDI in methanol were simulated using the Smoluchowski equation (Equation 2) to describe the evolution of the excited state population along calculated PESs[10]. Qualitative fits to experimental data were obtained. The model requires both a coordinate-dependent radiationless decay rate and coordinate-dependent transition moment. Also, radiationless decay to the ground-state has to be allowed early along the S_1 PES rather than just at the twisted geometry. This is contrary to the simple models of excited state dynamics where the excited state population relaxes along a PES, reaching a twisted geometry at which internal conversion occurs via a pinhole sink or conical intersection. The simulations failed for the FHBMI chromophore and for neutral HBDI. This is attributed to the lack of appropriate data for neutral HBDI PES and the unsuitability of the PESs used for FHBMI. More accurate calculations on the neutral chromophore are required, as this is an important state for FPs, such as in KaedeFP, where it is the neutral form which undergoes the photochemical reaction to form the Kaede chromophore.

The model worked well for the HBDI anion in the fluid solvent methanol. However, the model fails to reproduce the very weak solvent viscosity dependence observed experimentally. The lack of a viscosity dependence suggests that internal conversion involves a volume conserving (hence viscosity independent) coordinate. Originally proposed to explain the isomerisation of the chromophore within rhodopsin proteins, the "hula twist" is a highly volume conserving motion[39]. However, calculations have suggested that this route is energetically uphill and therefore inconsistent with the almost barrierless, ultrafast decay of the excited state of HBDI[6,40]. Another volume conserving route involves pyramidalisation around the central carbon atom connecting the bridging bonds[6,12,13]. Pyramidalisation has been shown to be important in the photoinduced *cis-trans* photoisomerisation of stilbene and ethylene and has also been proposed to explain the ultrafast excited state double bond rotation observed in a collection of molecular motors[41-43].

The volume conserving route observed is not consistent with full rotations of both bridging bonds which were the reaction coordinates for the PESs used in this work. However, the fits recovered do not allow a complete rotation – the sink functions were broad (Figure 6.8). In addition, a recent calculation has indicated that relaxation of the excited planar structure to the 90° twisted intermediate structure through torsion of the phenoxy bond does not displace more solvent than the HT mechanism[6]. It was also shown that torsion around both bonds occurs, where phenoxy torsion is strongly favoured due to a small barrier associated with the torsion of the imidazolinone bridge bond. Conversely, the calculations of Altoe (Section 6.1.1) suggest that the opposite is true for HBDI when taking into account the medium[11].

Incorporation of the chromophore into the protein structure causes significant changes to the spectral properties, with a red shift of roughly 80 nm for the neutral[44]. This suggests that the protein induces significant changes in the electronic structure as well as enhancing the fluorescence yield. Therefore the excited state PESs calculated in the gas phase may change significantly when the chromophore is inside the protein. However, if the PESs are not significantly altered, the interactions between the chromophore and protein may be sufficient to provide the friction required to resist the decay along the PES. Although, it has been shown that there is sufficient space within the protein cavity to allow significant rotation of the phenoxy bond as well as minor rotation of the double bridging bond[45,46]. Therefore it seems unlikely that steric crowding alone could prevent isomerization along a volume-conserving coordinate. Furthermore our simulations indicate that full rotation of the bridging bonds is not required to deactivate the excited state. In the wtGFP cavity, the fluorescent state of the protein is strongly H-bonded at both rings. Torsion and pyramidalisation of the chromophore will lead to a modulation of the chromophore length. The hydrogen bonds in the protein cavity could generate the friction or high energy barrier required to suppress the relaxation mechanism. These results again highlight the importance of protein-chromophore interactions in determining the photophysical behaviour of fluorescent proteins.

6.5. References

(1)Mandal, D.; Tahara, T.; Meech, S. R. *The Journal of Physical Chemistry B* **2003**, *108*, 1102.
(2)Litvinenko, K. L.; Webber, N. M.; Meech, S. R. *Chem. Phys. Lett.* **2001**, *346*, 47.
(3)Kojima, S.; Ohkawa, H.; Hirano, T.; Maki, S.; Niwa, H.; Ohashi, M.; Inouye, S.; Tsuji, F. I. *Tetrahedron Lett.* **1998**, *39*, 5239.
(4)Litvinenko, K. L.; Webber, N. M.; Meech, S. R. *The Journal of Physical Chemistry A* **2003**, *107*, 2616.
(5)Meech, S. R. *Chem. Soc. Rev.* **2009**, *38*, 2922.
(6)Martin, M. E.; Negri, F.; Olivucci, M. *J Am Chem Soc* **2004**, *126*, 5452.
(7)Conyard, J.; Kondo, M.; Heisler, I. A.; Jones, G.; Baldridge, A.; Tolbert, L. M.; Solntsev, K. M.; Meech, S. R. *The Journal of Physical Chemistry B* **2011**, *115*, 1571.
(8)Polyakov, I. V.; Grigorenko, B. L.; Epifanovsky, E. M.; Krylov, A. I.; Nemukhin, A. V. *Journal of Chemical Theory and Computation* **2010**, *6*, 2377.
(9)Olsen, S.; Lamothe, K.; Martínez, T. J. *J. Am. Chem. Soc.* **2010**, *132*, 1192.
(10)Olsen, S.; Smith, S. C. *J. Am. Chem. Soc.* **2008**, *130*, 8677.
(11)Altoe, P.; Bernardi, F.; Garavelli, M.; Orlandi, G.; Negri, F. *J. Am. Chem. Soc.* **2005**, *127*, 3952.
(12)Toniolo, A.; Olsen, S.; Manohar, L.; Martinez, T. *Faraday Discuss.* **2004**, *127*, 149.
(13)Toniolo, A.; Granucci, G.; Martínez, T. J. *The Journal of Physical Chemistry A* **2003**, *107*, 3822.
(14)Bagchi, B.; Fleming, G. R.; Oxtoby, D. W. *The Journal of Chemical Physics* **1983**, *78*, 7375.
(15)Bagchi, B.; Fleming, G. R. *The Journal of Physical Chemistry* **1990**, *94*, 9.
(16)Tominaga, K.; Walker, G. C.; Jarzeba, W.; Barbara, P. F. *The Journal of Physical Chemistry* **1991**, *95*, 10475.
(17)Tominaga, K.; Walker, G. C.; Kang, T. J.; Barbara, P. F.; Fonseca, T. *The Journal of Physical Chemistry* **1991**, *95*, 10485.
(18)van der Meer, M. J.; Zhang, H.; Glasbeek, M. *J. Chem. Phys.* **2000**, *112*.
(19)Heisler, I. A.; Kondo, M.; Meech, S. R. *The Journal of Physical Chemistry B* **2009**, *113*, 1623.
(20)Kondo, M.; Heisler, I. A.; Conyard, J.; Rivett, J. P. H.; Meech, S. R. *The Journal of Physical Chemistry B* **2009**, *113*, 1632.
(21)Glasbeek, M.; Zhang, H.; van der Meer, M. J. *J. Mol. Liq.* **2000**, *86*, 123.
(22)Amdursky, N.; Erez, Y.; Huppert, D. *Acc. Chem. Res.* **2012**, *45*, 1548.
(23)Erez, Y.; Liu, Y.-H.; Amdursky, N.; Huppert, D. *The Journal of Physical Chemistry A* **2011**, *115*, 8479.
(24)Lukyanov, K. A.; Fradkov, A. F.; Gurskaya, N. G.; Matz, M. V.; Labas, Y. A.; Savitsky, A. P.; Markelov, M. L.; Zaraisky, A. G.; Zhao, X.; Fang, Y. *J. Biol. Chem.* **2000**, *275*, 25879.
(25)Chudakov, D. M.; Belousov, V. V.; Zaraisky, A. G.; Novoselov, V. V.; Staroverov, D. B.; Zorov, D. B.; Lukyanov, S.; Lukyanov, K. A. *Nat. Biotechnol.* **2003**, *21*, 191.
(26)Chudakov, D. M.; Feofanov, A. V.; Mudrik, N. N.; Lukyanov, S.; Lukyanov, K. A. *J. Biol. Chem.* **2003**, *278*, 7215.
(27)Henderson, J. N.; Remington, S. J. *Physiology* **2006**, *21*, 162.
(28)Andresen, M.; Wahl, M. C.; Stiel, A. C.; Gräter, F.; Schäfer, L. V.; Trowitzsch, S.; Weber, G.; Eggeling, C.; Grubmüller, H.; Hell, S. W.; Jakobs, S. *Proc. Natl. Acad. Sci. U. S. A.* **2005**, *102*, 13070.
(29)Quillin, M. L.; Anstrom, D. M.; Shu, X.; O'Leary, S.; Kallio, K.; Chudakov, D. M.; Remington, S. J. *Biochemistry (Mosc).* **2005**, *44*, 5774.
(30)Yampolsky, I. V.; Kislukhin, A. A.; Amatov, T. T.; Shcherbo, D.; Potapov, V. K.; Lukyanov, S.; Lukyanov, K. A. *Bioorg. Chem.* **2008**, *36*, 96.
(31)Addison, K.; Conyard, J.; Dixon, T.; Bulman Page, P. C.; Solntsev, K. M.; Meech, S. R. *The Journal of Physical Chemistry Letters* **2012**, *3*, 2298.
(32)Das, A. K.; Hasegawa, J.-Y.; Miyahara, T.; Ehara, M.; Nakatsuji, H. *J. Comput. Chem.* **2003**, *24*, 1421.

(33) Horng, M. L.; Gardecki, J. A.; Papazyan, A.; Maroncelli, M. *The Journal of Physical Chemistry* **1995**, *99*, 17311.

(34) Smith, N. A.; Meech, S. R. *The Journal of Physical Chemistry A* **2000**, *104*, 4223.

(35) Mizuno, H.; Mal, T. K.; Tong, K. I.; Ando, R.; Furuta, T.; Ikura, M.; Miyawaki, A. *Mol. Cell* **2003**, *12*, 1051.

(36) Adam, V.; Lelimousin, M.; Boehme, S.; Desfonds, G.; Nienhaus, K.; Field, M. J.; Wiedenmann, J.; McSweeney, S.; Nienhaus, G. U.; Bourgeois, D. *Proceedings of the National Academy of Sciences* **2008**, *105*, 18343.

(37) Adam, V.; Moeyaert, B.; David, Charlotte C.; Mizuno, H.; Lelimousin, M.; Dedecker, P.; Ando, R.; Miyawaki, A.; Michiels, J.; Engelborghs, Y.; Hofkens, J. *Chem. Biol.* **2011**, *18*, 1241.

(38) Mooney, C. R.; Horke, D. A.; Chatterley, A. S.; Simperler, A.; Fielding, H. H.; Verlet, J. R. *Chemical Science* **2013**, *4*, 921.

(39) Liu, R. S. *Pure Appl. Chem.* **2002**, *74*, 1391.

(40) Weber, W.; Helms, V.; McCammon, J. A.; Langhoff, P. W. *Proceedings of the National Academy of Sciences* **1999**, *96*, 6177.

(41) Conyard, J.; Addison, K.; Heisler, I. A.; Cnossen, A.; Browne, W. R.; Feringa, B. L.; Meech, S. R. *Nat Chem* **2012**, *advance online publication*.

(42) Kazaryan, A.; Kistemaker, J. C.; Schäfer, L. V.; Browne, W. R.; Feringa, B. L.; Filatov, M. *The Journal of Physical Chemistry A* **2010**, *114*, 5058.

(43) Quenneville, J.; Martínez, T. J. *The Journal of Physical Chemistry A* **2003**, *107*, 829.

(44) Nienhaus, G. U.; Wiedenmann, J. *ChemPhysChem* **2009**, *10*, 1369.

(45) Maddalo, S. L.; Zimmer, M. *Photochem. Photobiol.* **2006**, *82*, 367.

(46) Chen, M. C.; Lambert, C. R.; Urgitis, J. D.; Zimmer, M. *Chem. Phys.* **2001**, *270*, 157.

Chapter 7 – Preliminary Studies of Three Novel Chromophores

7.1. Introduction

As mentioned in Chapter 1, the photophysics of fluorescent protein chromophores is not fully understood. Studies of HBDI analogues with modifications to the ortho, meta and para positions of the phenoxy ring with apparently weakly perturbing methyl groups have been shown to introduce a wide variety of behaviours and were discussed in Chapter 5[1-11]. In contrast, in Chapter 6 it was shown that the substitution of a formyl group for a methyl group on the imidazole ring of HBDI has very little effect on the photophysics[12]. In Chapter 4 it was shown that extension of the conjugated system of HBDI via the addition of an imidazole ring bridged to the imidazolinone of HBDI to form the Kaede chromophore red shifts the emission by approximately 75 nm and increases the intensity of emission 15 times through aggregation-induced effects. The systematic design of new FP chromophores thus presents the possibility of tuning the properties of FPs.

In this chapter the preliminary investigations of the photophysics of three new versions of the Kaede chromophore are described. The structures of these are similar to Kaede, the difference being substitution of the imidazole ring of Kaede for a pyridine ring with the position of the nitrogen atom on the ring changed from the meta to para to ortho position. The three molecular structures are shown in Figure 7.1 and are labelled HBPXI ((Z)-4-(4-hydroxybenzylidene)-1-methyl-2-((E)-2-(pyridin-X-yl)vinyl)-1H-imidazol-5(4H)-one) where X is 2, 3 or 4 depending on the position of the nitrogen.
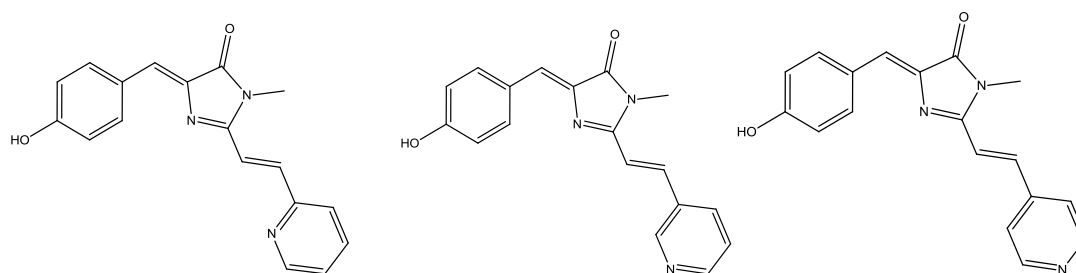
Figure 7.1. Structures of HBP2I (left), HBP3I (middle) and HBP4I (right).

Firstly the steady-state absorption and fluorescence spectra are compared (Section 7.2.1).

Then the low temperature steady-state emission measurements and NMR spectra of HBP3I

are described (Sections 7.2.2 and 7.2.3). This is followed by ground-state DFT calculations of

the three chromophores (Section 7.2.4). Finally the time-resolved fluorescence

measurements are discussed, including temperature dependent measurements of HBP3I

(Section 7.3).

7.2. Results and Discussion

7.2.1. Steady-state Absorption and Emission

The steady-state UV-Vis absorption spectra of the three chromophores in methanol are

shown in Figure 7.2 and the maximum absorption wavelengths and extinction coefficients

listed in Table 7.1. Samples were prepared to a concentration of 13 μM and measured in a

1 cm cell. The maximum absorption wavelengths (λ_{max}^{abs}) range from 426 nm to 453 nm

depending on the solvent and chromophore, where the absorption of HBP3I is blueshifted

by a few nm compared to that of HBP2I and HBP4I. The spectra are shifted by a few nm

compared to Kaede and by roughly 65 nm compared to HBDI. The extinction coefficients are

typical of allowed π-π* transitions.
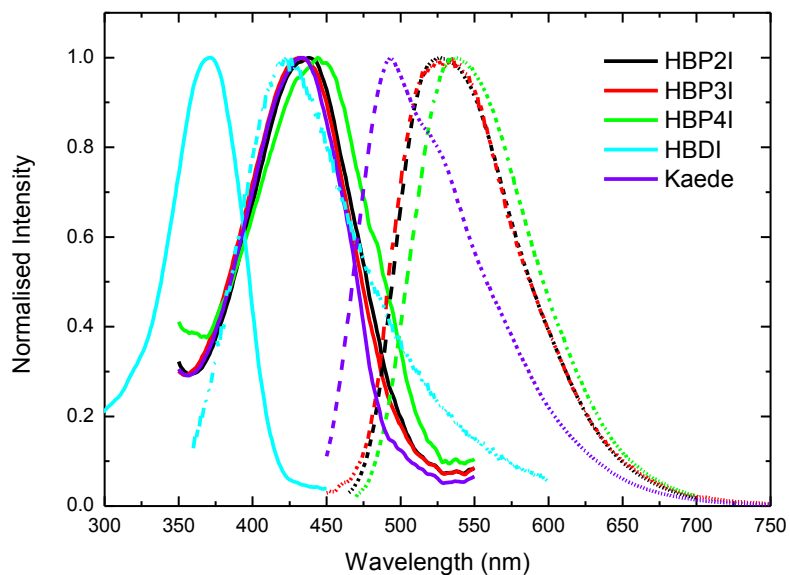
Figure 7.2. The normalised absorption (solid) and emission (dashed) spectra of HBP2I

(black), HBP3I (red), HBP4I (green), HBDI (blue) and Kaede (purple) in methanol.

Solvent	λ_{max}^{abs} / λ_{max}^{em} (nm)			ε ($M^{-1}cm^{-1}$) at max		
	HBP2I	HBP3I	HBP4I	HBP2I	HBP3I	HBP4I
THF	439 / 514	434 / 514	440 / 519	2.61E+04	1.75E+04	4.38E+03
MeCN	426 / 513	426 / 507	429 / 533	1.69E+04	1.46E+04	9.23E+03
MeOH	436 / 525	432 / 518	446 / 534	2.23E+04	2.23E+04	8.46E+03
DMF	-	437 / 516	443 / 530	1.62E+04	2.77E+04	8.46E+03
EtOH	442 / 526	437 / 516	443 / 537	1.92E+04	2.77E+04	6.92E+03
PrOH	446 / 525	441 / 519	446 / 535	2.23E+04	2.00E+04	9.23E+03
BuOH	451 / 528	444 / 517	446 / 536	2.54E+04	1.85E+04	8.15E+03
OcOH	451 / 521	447 / 518	453 / 531	2.54E+04	1.92E+04	7.69E+03
EG	444 / 530	438 / 517	441 / 541	1.77E+04	2.92E+04	7.62E+03

Table 7.1. Maximum absorption and emission wavelengths and extinction coefficients at the

absorption maximum of the HBPXI chromophores.

Figure 7.3 shows the solvent dependence of the absorption for each chromophore. The

maximum absorption wavelength and OD at this wavelength as a function of the solvent

polarity parameter are illustrated in Figure 7.4. For all chromophores λ_{max}^{abs} is blueshifted in

acetonitrile and tetrahydrofuran. Acetonitrile is a highly polar solvent whilst THF has a

relatively low polarity. However both solvents are aprotic, thus indicating the importance of

the hydrogen bonding nature of the solvent. Turning to the OD, Figure 7.3b shows that the

OD of HBP4I is lower than that of both HBP2I and HBP3I by a factor of about 4. This result

could be further investigated using TD-DFT methods to calculate the transition moment

associated with this absorption.
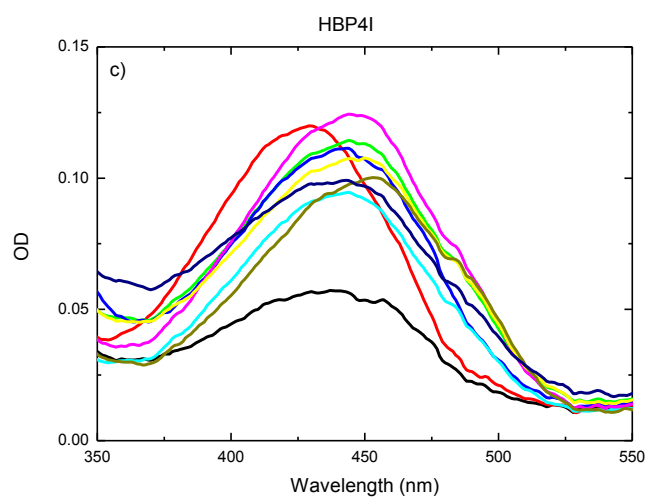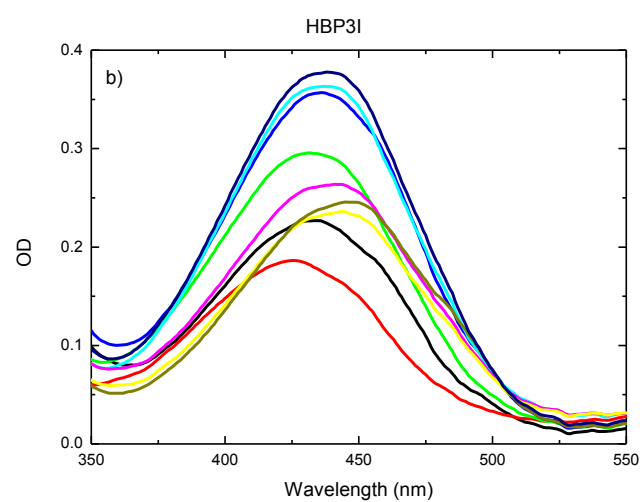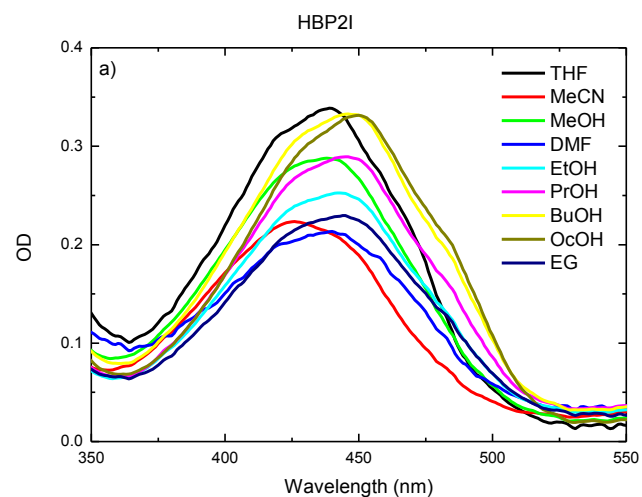
Figure 7.3. UV-Vis absorption spectra of HBP2I (a), HBP3I (b) and HBP4I (c) as a function of

solvent measured at a concentration of 13 μM.
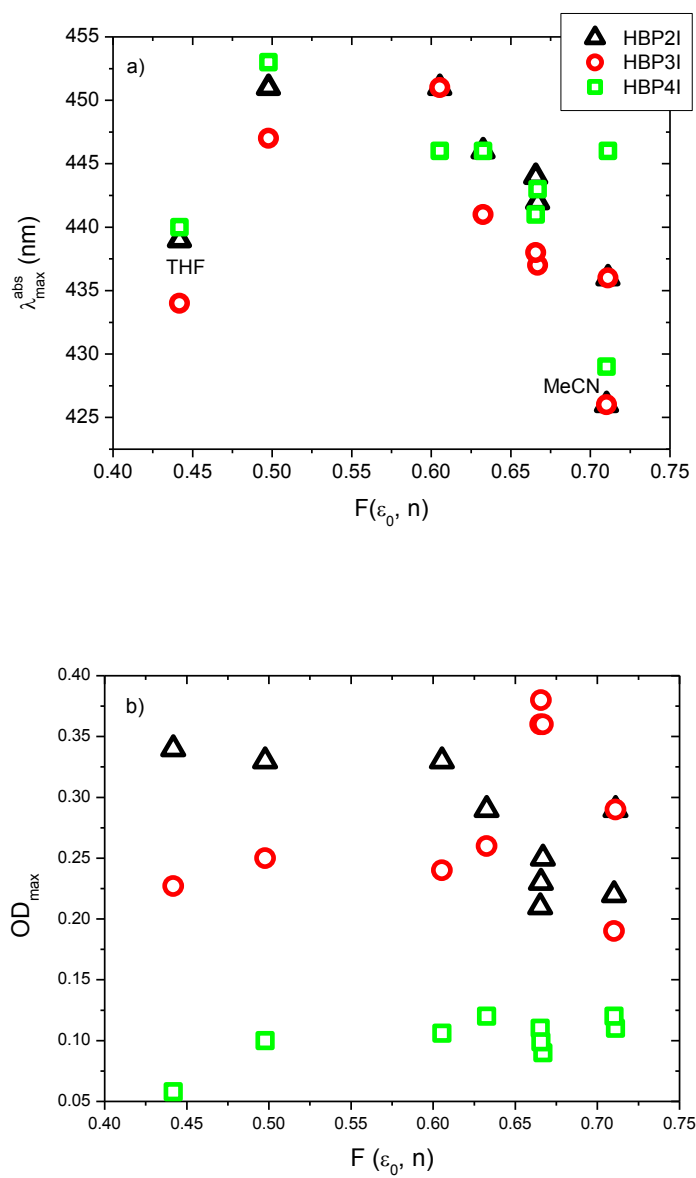
Figure 7.4. The maximum absorption wavelength (a) and OD at this wavelength (b) of HBP2I (black), HBP3I (red) and HBP4I (green) as a function of polarity. λ_{max}^{abs} is blueshifted in THF and MeCN for all chromophores.

The absorption corrected fluorescence of the three chromophores is shown in Figure 7.5 and the maximum emission wavelengths (λ_{max}^{em}) given in Table 7.1. These chromophores show a strong solvent dependence with the fluorescence clearly enhanced in MeCN and THF. The emission spectra of Kaede and HBDI in methanol are included in Figure 7.5b, the fluorescence is strongly enhanced compared to HBDI and comparable to that of Kaede, although redshifted by approximately 30 – 40 nm. Figure 7.5c shows that the fluorescence of HBP4I is strongly suppressed in water. This was found for Kaede (Chapter 4) and the HBDI analogues which were discussed in Chapter 5. HBP2I and HBP3I should also be measured in water to assess the effect of hydrogen bonding on the spectra of these chromophores.

The fluorescence spectra contain structure similar to that seen for Kaede (Chapter 4), suggesting that the HBPXIs also form aggregates at relatively low concentrations. The form of structure varies for each chromophore and solvent. However when separate peaks cannot be resolved, the spectral width does not change significantly (Figure 7.5 insets). This indicates that higher aggregates are present in these samples, otherwise a narrowing of the spectrum would be expected (discussed in Chapter 4)[13,14]. To investigate the effects of aggregation further, variable concentration and excitation wavelength measurements should be performed.
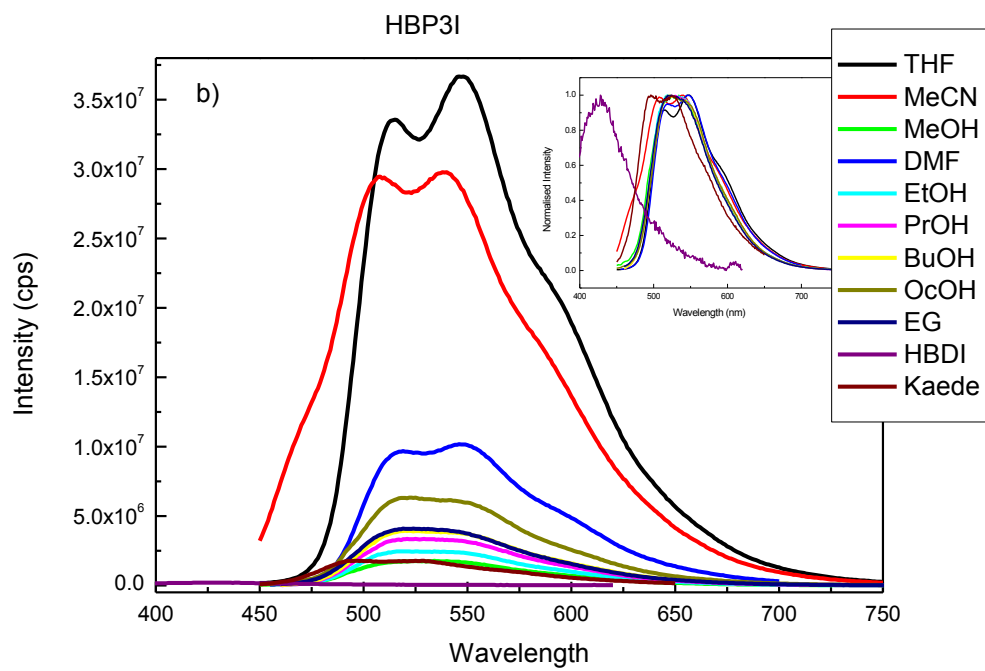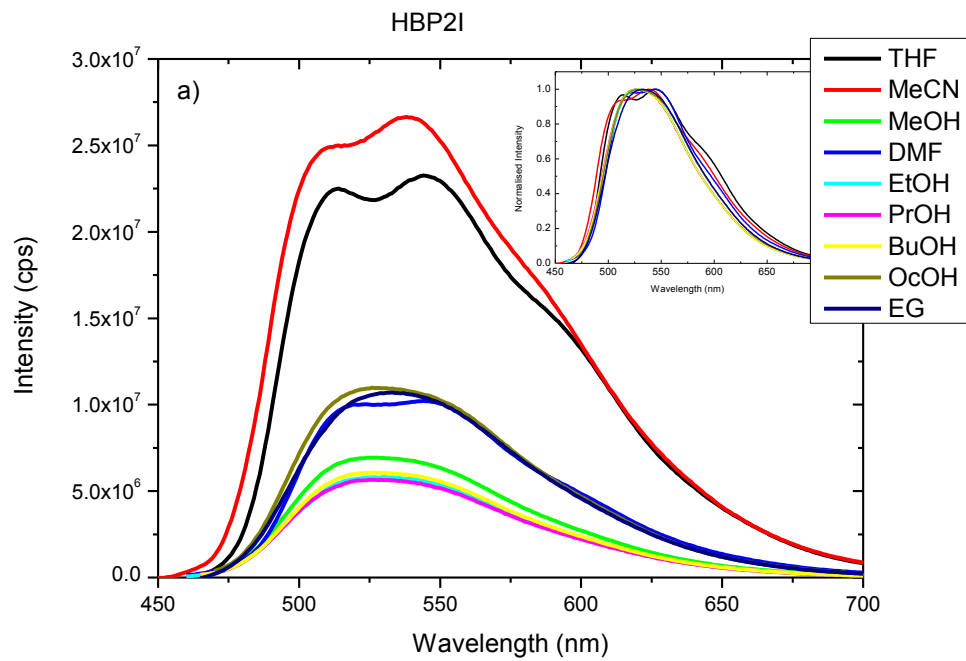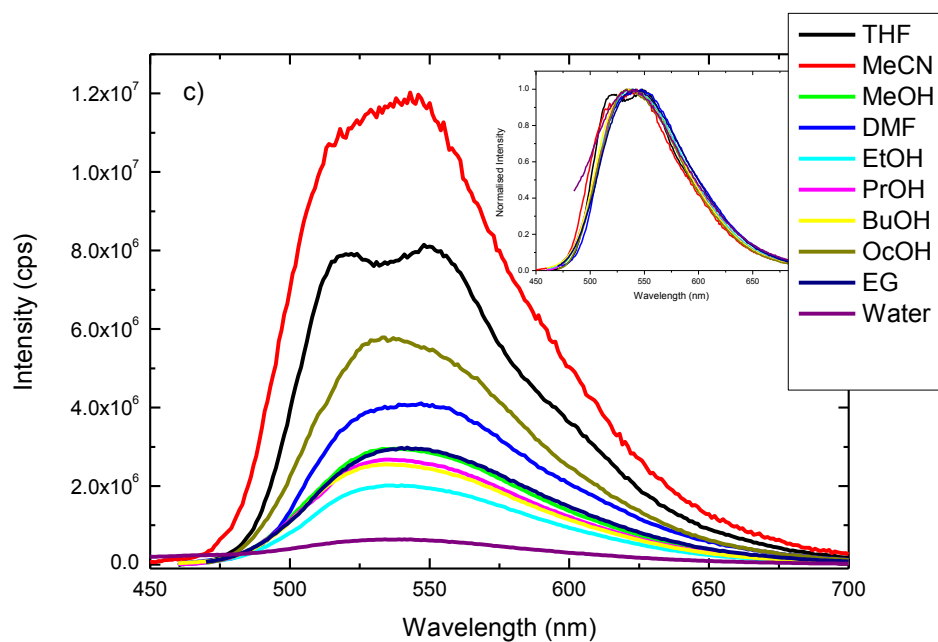
Figure 7.5. The steady-state fluorescence of HBP2I (a), HBP3I (b) and HBP4I (c) measured at a concentration of 13 μM. The normalised spectra are shown in the insets.

The quantum yield of the fluorescence has a slight tendency to decrease with increasing solvent polarity (Figure 7.6). For HBP4I, the integrated intensity increases over 7 times between water and octanol. However, the quantum yield is anomalously high in THF and MeCN for HBP3I and HBP2I, with a much smaller effect observed for HBP4I. In contrast to MeCN, THF has a relatively low polarity, however both chromophores are aprotic. It was shown in Chapter 4, that the quantum yield and fluorescence lifetime of Kaede are also enhanced in aprotic solvents.
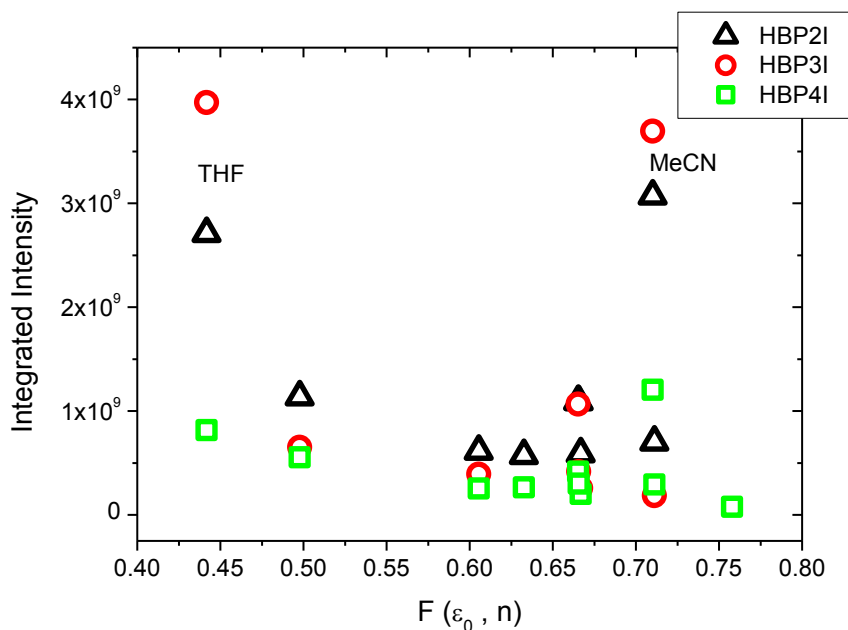
Figure 7.6. The dependence of the integrated intensity of the steady-state fluorescence of HBP2I (black), HBP3I (red) and HBP4I (green) on the solvent polarity function.

Figure 7.7a shows the peak emission wavelength plotted against the polarity function. This again highlights the solvent dependence of HBP2I and HBP3I, where the maximum emission wavelength is blueshifted in acetonitrile. Also, for all chromophores the peak is blueshifted in THF. There is also a tendency for the peak of the emission to redshift with increasing polarity for HBP2I and HBP4I. The Stokes shifts as a function of polarity are plotted in Figure 7.7b and listed in Table 7.2. In all cases the shifts are higher than those of Kaede and HBDI (Chapter 4). In contrast to Kaede and HBDI, the Stokes shifts of the HBPXIs increase strongly with increasing solvent polarity. The shifts are greatest for HBP4I, with the largest shift in MeCN. For all the HBPXI chromophores the Stokes shift is relatively high in THF.
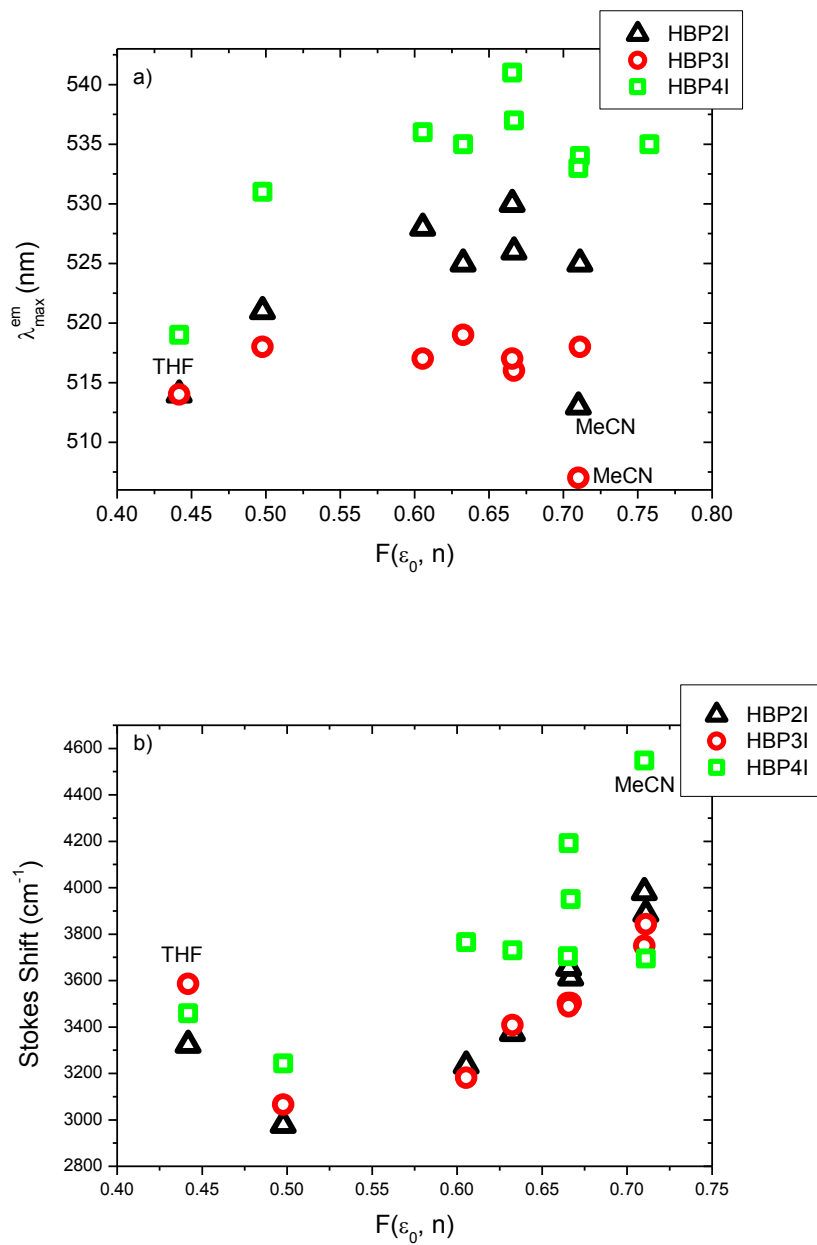
Figure 7.7. The maximum fluorescence wavelength (a) and Stokes shift (b) of HBP2I (black), HBP3I (red) and HBP4I (green) against the solvent polarity function. The emission is blueshifted for HBP2I and HBP3I in MeCN and for all chromophores in THF. The Stokes shift increases with polarity.

	Stokes Shift (cm^{-1})		
Solvent	HBP2I	HBP3I	HBP4I
THF	3324	3586	3459
MeCN	3981	3750	4548
MeOH	3888	3843	3695
DMF	-	3503	3705
EtOH	3613	3503	3951
PrOH	3374	3408	3730
BuOH	3234	3181	3765
OcOH	2979	3066	3243
EG	3655	3489	4192

Table 7.2. The Stokes shifts of the HBPXI chromophores.

7.2.2. Low Temperature Steady-state Fluorescence of HBP3I

The steady-state emission of HBP3I in a 3:1 ethanol:methanol mixture was measured

between 290 K and 80 K, as described in Section 4.2. Similarly to Kaede and HBDI, the

fluorescence of HBP3I is strongly enhanced at low temperatures (Figure 7.8). The integrated

intensity of HBP3I increases 50 times from room temperature to the glass transition

temperature. Vibronic structure is also resolved at low temperature, with a separation of

approximately 550 cm^{-1}. In comparison to Kaede, these peaks are less well defined, more

numerous and more closely spaced (Chapter 4). A significant difference between these

results and those obtained for Kaede, is the 55 nm blueshift of the spectrum upon cooling.

As the fluorescence quantum yield exhibits a dependence on viscosity in the alcohols

(excluding ethylene glycol), the shift is likely to be due to solvation on the molecule (Chapter

1). Furthermore, the spectrum begins to shift below 210 K, a temperature which would

correspond to a large increase in viscosity.
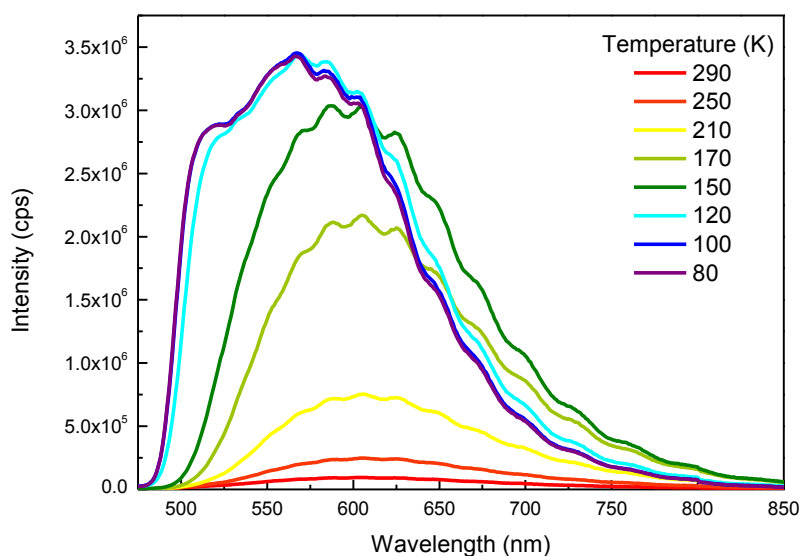
Figure 7.8. Temperature dependence of the steady-state emission of HBP3I in a 3:1 ethanol:methanol solution. At low temperatures the integrated intensity of the fluorescence is enhanced, the spectrum blueshifts and vibronic structure is observed.

The activation energy for radiationless decay was calculated according to Equation 4.1 (Section 4.3.4). As the radiative rate is unknown, the natural lifetime τ_n was estimated using the Strickler-Berg equation,

$$\tau_n^{-1} = 2.88\text{x}10^{-9}n^2 \frac{\int_{\Delta v_e} F(v)\, dv}{\int_{\Delta v_a} F(v)v^{-3}\, dv} \int_{\Delta v_a} \varepsilon(v)\, dlnv, \qquad (7.1)$$

where n is the refractive index of the solvent, Δv_e and Δv_a are the limits of the absorption and emission bands, $F(v)$ is the spectral distribution of the emission and $\varepsilon(v)$ is the extinction coefficient[15]. The natural lifetime is the lifetime in the absence of nonradiative decay channels. At low temperature the flexibility of the chromophore is greatly reduced, thus suppressing the nonradiative decay mechanisms. Hence the fluorescence spectrum

measured at 80 K was used for $F(\upsilon)$. The reciprocal of the natural lifetime yields the radiative rate k_f. The nonradiative rate at each temperature was then determined following the procedure described in Section 4.3.4.

Analysis of the Arrhenius plot (Figure 7.9) yields a very high activation energy of 263 ± 30 kJ mol^{-1}. This is significantly higher than the values of 10.8 ± 0.5 kJ mol^{-1} for Kaede and 6 ± 3 kJ mol^{-1}, determined for HBDI above T_m and 12 ± 2 kJ mol^{-1} for HBDI below T_m[16]. To determine if this barrier is intrinsic to the molecule or a result of solvent friction requires further investigation through an isoviscosity analysis (Chapter 4).
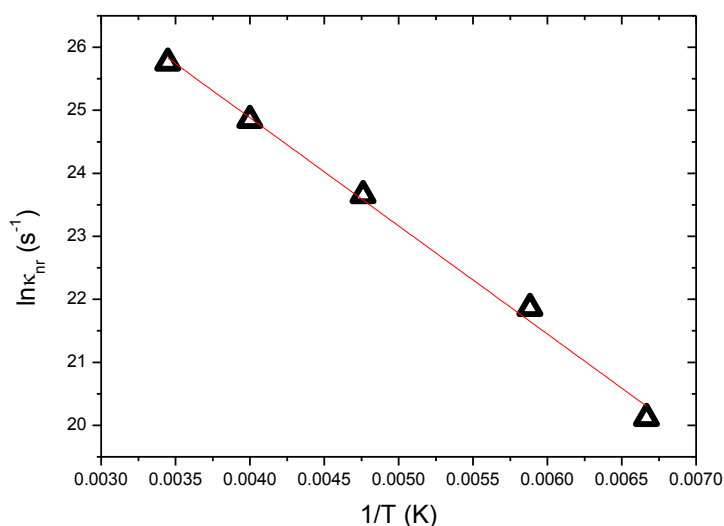
Figure 7.9. Arrhenius analysis of the low temperature steady-state fluorescence of HBP3I gives an activation energy of 263 ± 30 kJ kJ mol^{-1}.

7.2.3. NMR Spectroscopy

The NMR spectrum of a 10 mM solution of HBP3I in deuterated methanol is shown in Figure 7.10 and suggests the presence of a single isomer in the ground-state. In Chapter 3 it was shown that HBDI undergoes *cis-trans* photoisomerisation when irradiated with UV light. The relative amounts of the *cis* and the metastable *trans* population can then be quantitatively measured using NMR spectroscopy[17,18]. In contrast, Kaede does not undergo photoisomerisation and instead aggregates upon irradiation (Chapter 4). To investigate the possibility of light induced changes occurring in the HBPXI chromophores, a sample of HBP3I in deuterated methanol was irradiated with a 405 nm, 20 mW collimated LED lamp and the NMR spectrum recorded before and at increasing irradiation times. Figure 7.10 shows that after 3 hours of irradiation, no signs of isomerisation or aggregation are observed.
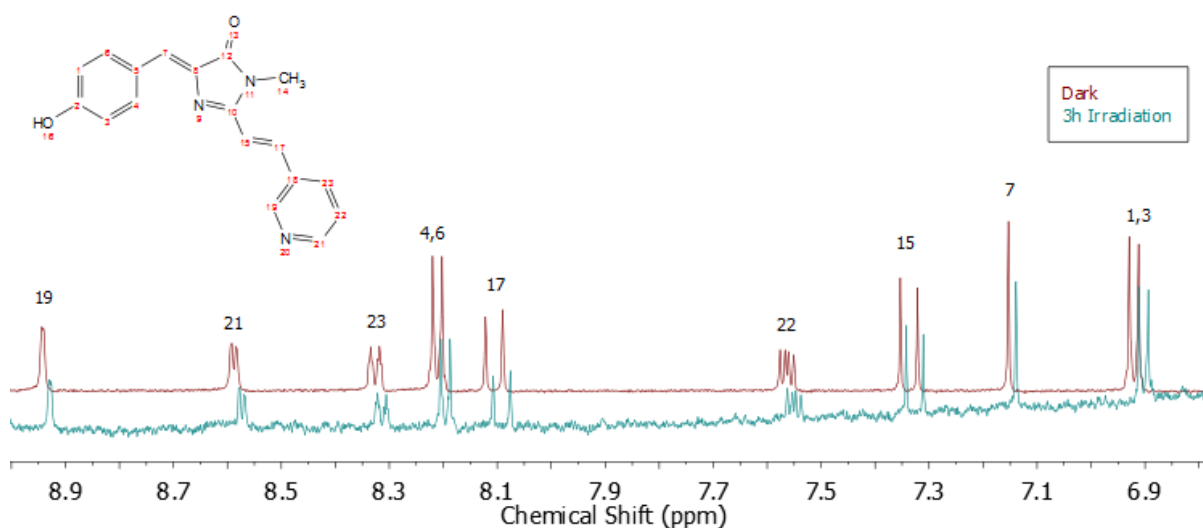
Figure 7.10 NMR spectra of dark (red) and irradiated (green) HBP3I in MeOH-d4. The irradiated spectrum shows no signs of photoisomerisation or aggregation.

7.2.4. DFT Calculations

The ground-state optimised structures of the HBPXI chromophores were calculated using Gaussian software at the DFT B3LYP level using the basis set 6-31G++ (d,p). Figure 7.11 indicates that the minimum energy structures are planar for all chromophores. Also, the structures show extended conjugation through the pyridine ring. Thus explaining the redshifted absorption spectrum compared to that of HBDI (and similar to our findings for Kaede). The dipole moment of HBP2I was calculated to be 3.1 D (slightly lower than that of Kaede which was 3.8 D), while those of HBP3I and HBP4I were lower at 1.4 D and 1.6 D respectively and comparable to that of HBDI (1.6 D). TD –DFT calculations to determine the dipole moments in the excited state are required to investigate the solvent sensitivity observed in the steady-state measurements (Section 5.2.1).

Figure 7.11 illustrates the highest occupied molecular orbital (HOMO) and lowest unoccupied molecular orbital (LUMO) for each chromophore using DFT. For all molecules, the electron density shifts from the phenoxy ring to the pyridine from the HOMO to the LUMO. It is also clear that for the HOMOs, the electron density is not distributed evenly across the pyridine ring due to the electronegativity of the nitrogen atom. In comparison to the HBPXIs, for Kaede the electron density is distributed much more evenly across the molecule. However, as for the HBPXIs, the electron density does shift away from the phenoxy ring from the HOMO to the LUMO.
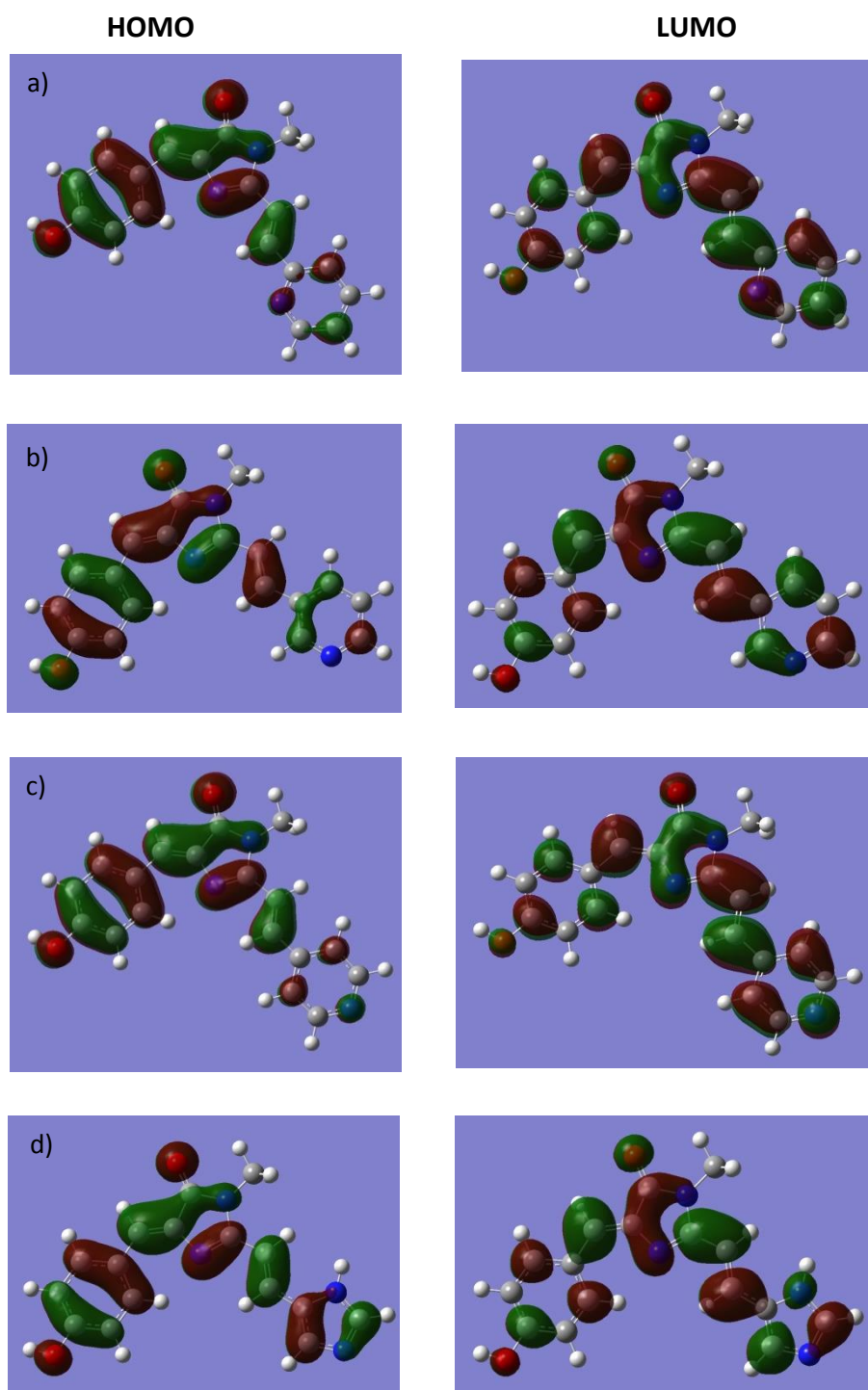
HOMO   **LUMO**

Figure 7.11. Ground-state optimised structures of HBP2I (a), HBP3I (b), HBP4I (c) and Kaede (d) showing the HOMO (left) and LUMO (right). The minimum energy configuration corresponds to planar geometry for all chromophores.

7.3. Time-resolved Fluorescence

To study the effect of the pyridine substitutions on the excited state dynamics, the time-resolved emission of each chromophore was measured using ultrafast fluorescence up-conversion (Chapter 2). Samples were prepared to a concentration of 0.5 mM in the solvents methanol, acetonitrile, octanol and ethylene glycol and measured at four wavelengths across the steady-state spectrum following the method described in Chapter 4. It will be shown that the fluorescence lifetime exhibits a strong dependence on solvent and wavelength as well as the position of the pyridine nitrogen atom.

7.3.1. Solvent and Wavelength Dependence

Figure 7.12 shows the time-resolved fluorescence of each chromophore in acetonitrile, methanol, octanol and ethylene glycol at the peak emission wavelength (Figure 7.5). Like Kaede, the decays are highly non-exponential and were fitted with 2, 3 or 4 exponentials depending on the chromophore and solvent (Tables 7.3, 7.4 and 7.5). As discussed in Chapter 4 the complexity is likely to be due, in part, to aggregation effects. The decays exhibit a clear solvent dependence which differs at early and late times. Looking firstly at the behaviour at late times, for HBP2I and HBP3I the decays are fastest in methanol, become longer in octanol and ethylene glycol and longest in acetonitrile. Little difference is observed between methanol and ethylene glycol, indicating a lack of sensitivity to solvent viscosity. Contrastingly, for HBP4I the decays are fastest in acetonitrile and ethylene glycol, becoming slightly longer in methanol and longest in octanol.

Turning to the early time behaviour, it can be seen in the inset of Figure 7.12b that the decays of HBP3I are initially fastest in methanol and acetonitrile, becoming longer in octanol and ethylene glycol. This behaviour is followed for HBP2I, although the decay in acetonitrile is slightly longer than that in methanol. For HBP4I the decays are fastest in acetonitrile and become progressively longer from ethylene glycol to methanol to octanol, mirroring the long-time behaviour. These observations suggests a viscosity effect in the early time behaviour which then becomes dominated by solvent polarity and hydrogen bonding effects at later times.
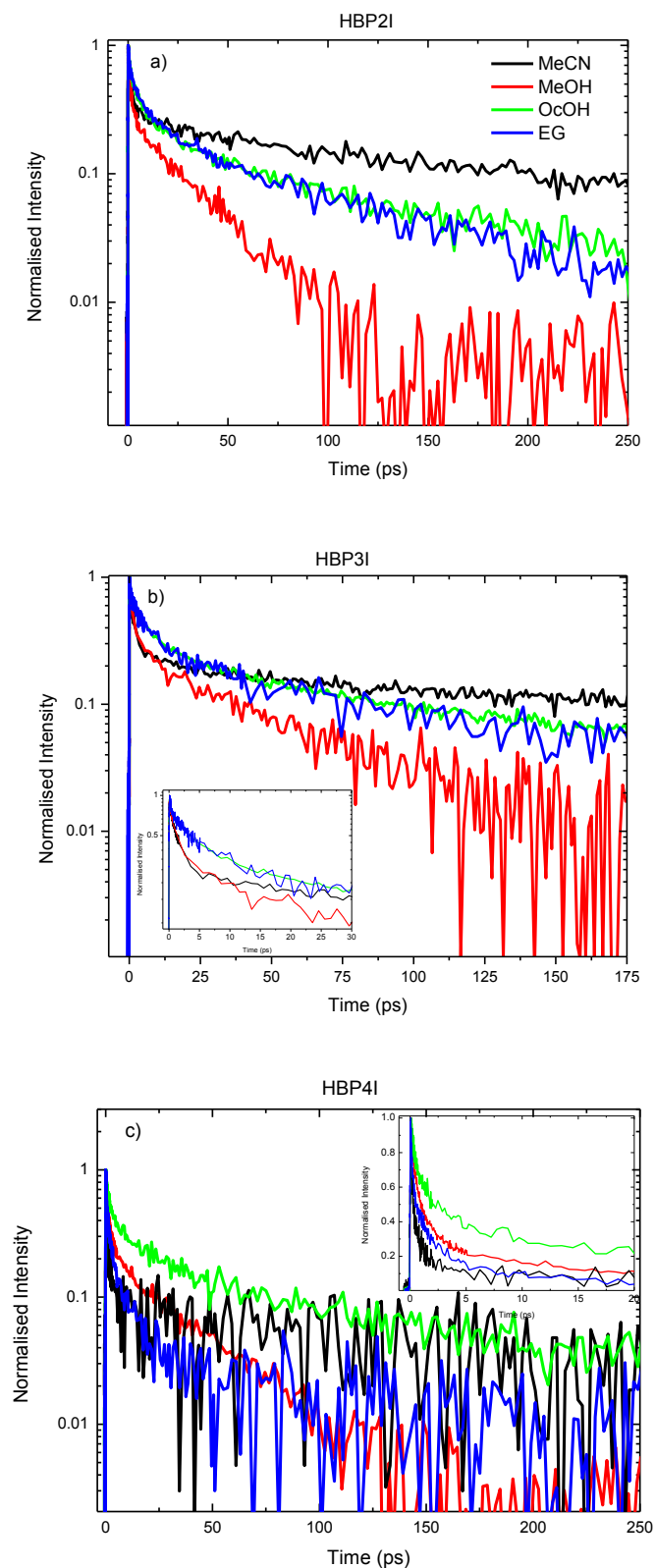
Figure 7.12. The time-resolved fluorescence of HBP2I (a), HBP3I (b) and HBP4I (c) in MeCN

(black), MeOH (red), OcOH (green) and EG (blue). The insets show the early time data.

At the peak emission wavelength (530 nm), the average lifetimes ($<\tau>$) of HBP2I in methanol

(7.8 ps) and ethylene glycol (19.7 ps) are in agreement with that of Kaede in the same

solvents (7.7 ps and 17.8 ps in methanol and ethylene glycol respectively). For HBP3I the

lifetimes increase slightly to 11.9 ps and 23.3 ps. For HBP4I, the lifetime in methanol (7.8 ps)

is in agreement with that of Kaede and HBP2I. However in ethylene glycol the average

fluorescence lifetime decreases to only 3.3 ps, indicating a lack of sensitivity to solvent

viscosity for HBP4I.

	HBP2I															
	MeCN				MeOH				OcOH				EG			
	Emission Wavelength (nm)															
	496	530	556	580	496	530	556	580	496	530	556	580	496	530	556	580
τ_1 (ps)	83	89	82	82	25	28	27	30	43	61	69	71	68	68	66	73
a_1	0.14	0.21	0.24	0.28	0.16	0.25	0.23	0.29	0.24	0.25	0.26	0.23	0.21	0.24	0.31	0.30
τ_2 (ps)	2.9	4.4	3.0	2.8	2.3	2.5	5.0	2.2	3.3	5.3	5.6	7.2	6.1	7.4	5.7	7.3
a_2	0.25	0.13	0.25	0.24	0.27	0.23	0.15	0.24	0.44	0.41	0.37	0.36	0.43	0.42	0.43	0.38
τ_3 (ps)	0.72	1.0	1.1	1.0	0.59	0.69	0.74	0.69	0.34	0.78	0.98	1.2	0.52	0.72	0.81	0.86
a_3	0.61	0.66	0.51	0.48	0.57	0.52	0.62	0.48	0.31	0.34	0.37	0.41	0.36	0.34	0.26	0.32
$<\tau>$ (ps)	12.7	19.9	20.7	24.1	5.1	7.8	7.5	9.6	12.0	17.6	20.0	19.3	16.9	19.7	22.9	24.8

Table 7.3. Fitting parameters for the time-resolved fluorescence of HBP2I.The errors are less

than 11%.

	HBP3I														
	MeCN				MeOH				OcOH				EG			
	Emission Wavelength (nm)															
	480	496	530	556	496	530	556	580	496	530	556	580	496	530	556	580
τ_1 (ps)	80	60	59	76	37	45	46	56	43	57	76	80	68	84	62	66
a_1	0.06	0.10	0.17	0.26	0.16	0.23	0.43	0.16	0.22	0.27	0.34	0.27	0.13	0.23	0.31	0.38
τ_2 (ps)	3.4	2.3	2.3	12.8	2.2	4.9	7.1	7.1	4.4	5.4	6.6	6.7	9.9	9.1	9.9	6.6
a_2	0.29	0.44	0.41	0.20	0.45	0.25	0.11	0.19	0.39	0.44	0.29	0.34	0.32	0.29	0.32	0.38
τ_3 (ps)	0.37	0.32	0.72	2.7	0.22	0.82	1.5	0.79	0.36	0.50	1.4	1.1	1.9	4.4	1.3	1.1
a_3	0.66	0.46	0.41	0.40	0.39	0.52	0.46	0.65	0.39	0.28	0.37	0.39	0.23	0.23	0.37	0.25
τ_4 (ps)				0.23									0.28	0.55		
a_4				0.15									0.32	0.25		
$\langle\tau\rangle$ (ps)	5.7	7.1	11.5	23.1	6.8	11.9	21.4	10.5	11.3	18.1	28.3	24.4	12.4	23.3	22.8	27.6

Table 7.4. Fitting parameters for the time-resolved fluorescence of HBP3I. The errors are

less than 12%.

	HBP4I															
	MeCN				MeOH				OcOH				EG			
	Emission Wavelength (nm)															
	496	530	556	580	496	530	556	580	496	530	556	580	496	530	556	580
τ_1 (ps)	10	15	86	89	30	33	32	33	53	52	70	57	3.9	17.5	28	33
a_1	0.12	0.13	0.14	0.28	0.14	0.20	0.19	0.14	0.19	0.28	0.25	0.29	0.24	0.13	0.23	0.24
τ_2 (ps)	0.29	0.39	0.79	1.9	2.2	3.4	2.6	3.0	4.5	4.6	7.3	9.3	0.32	2.0	4.5	5.0
a_2	0.88	0.87	0.86	0.72	0.34	0.25	0.24	0.29	0.35	0.33	0.32	0.23	0.76	0.42	0.45	0.37
τ_3 (ps)	-	-	-	-	0.39	0.65	0.53	0.60	0.44	0.69	0.89	1.4	-	0.20	0.61	0.73
a_3	-	-	-	-	0.52	0.55	0.57	0.57	0.46	0.38	0.43	0.49	-	0.45	0.31	0.39
$\langle\tau\rangle$ (ps)	1.5	2.4	12.8	26.2	5.0	7.8	7.0	5.8	12.2	16.5	20.1	19.0	1.2	3.3	8.9	10.2

Table 7.5. Fitting parameters for the time-resolved fluorescence of HBP4I. The errors are

less than 13%.

Figure 7.13 shows the variation of the average lifetime of each chromophore at the peak

emission wavelength against viscosity. In all cases, HBP4I has the shortest fluorescence

lifetime. HBP2I and HBP3I exhibit a viscosity dependence in the alcohols, with the lifetime

increasing approximately 2 times from methanol to ethylene glycol in HBP2I and HBP3I. This

is not the case for HBP4I however, where the lifetime in EG is half of that in methanol. For

HBP3I and HBP4I the lifetimes are relatively low in MeCN. However in HBP2I, the lifetime is

significantly extended.
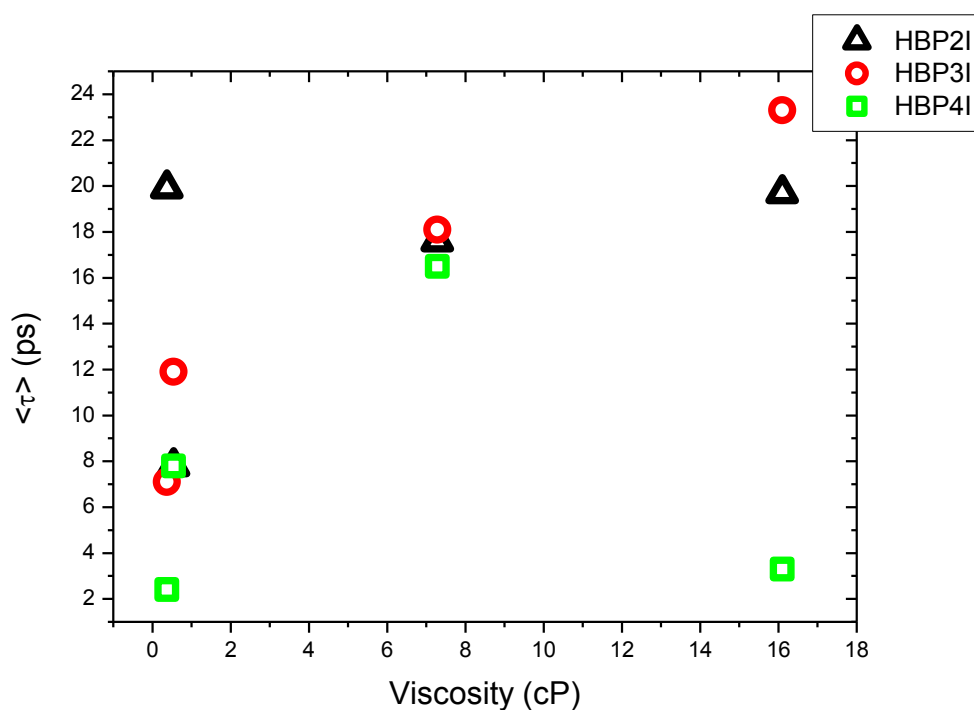
Figure 7.13. The average lifetime of the time-resolved fluorescence of HBP2I (black), HBP3I

(red) and HBP4I (green) as a function of solvent viscosity.

Analysis of the time-resolved fluorescence is further complicated when considering the wavelength dependence in addition to the solvent dependence. Figure 7.14 illustrates that these chromophores show a strong wavelength dependence which differs with the solvent and pyridine nitrogen position. Looking firstly at the behaviour of the chromophores in particular solvents, in ethylene glycol the average lifetime increases with wavelength for all chromophores. The same behaviour is observed in acetonitrile, with a large increase in $<\tau>$ for HBP4I at the red edge. In methanol, HBP2I and HBP4I show little variation while HBP3I increases up to the maximum then decreases on the red edge. This behaviour is also observed in octanol for all chromophores.
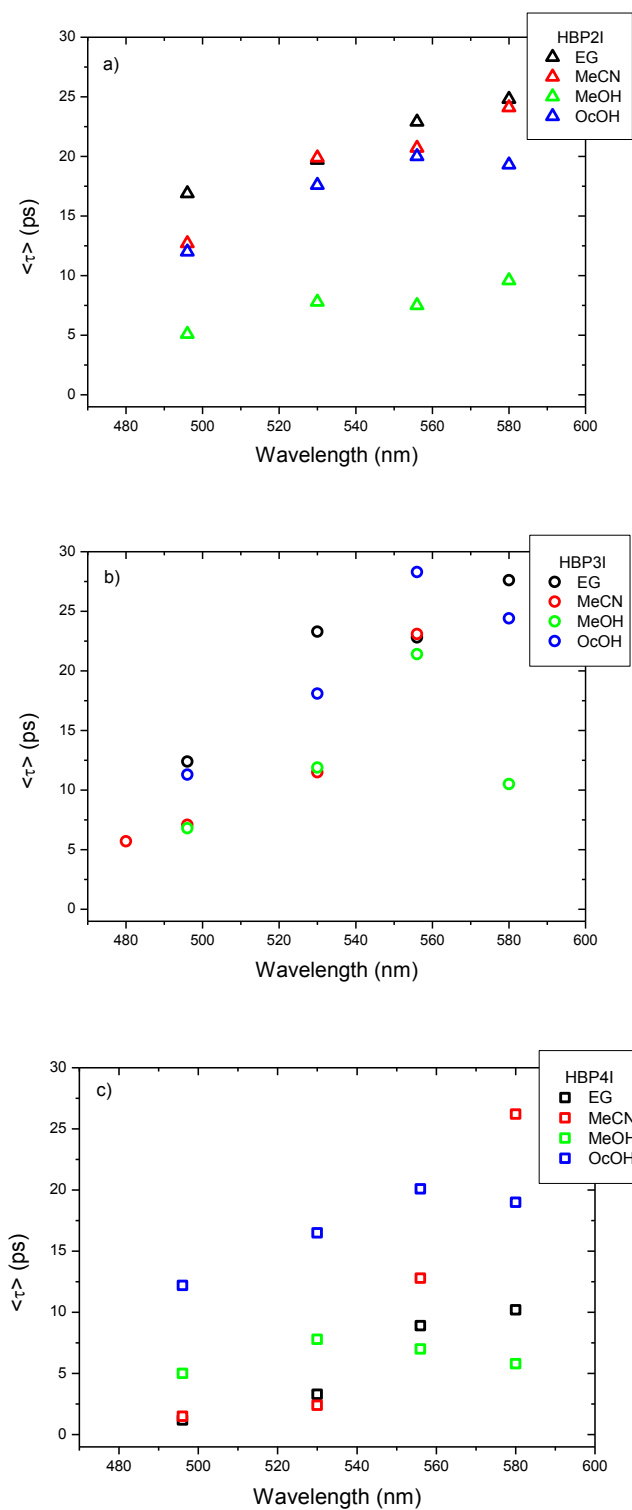
Figure 7.14. The wavelength dependence of the average lifetime of the time-resolved

fluorescence of HBP2I (a), HBP3I (b) and HBP4I (c) in EG (black), MeCN (red), MeOH (green)

and OcOH (blue).

224

Comparing the individual chromophore behaviour of the average lifetime across the wavelength range in each solvent, in ethylene glycol HBP4I is significantly lower compared to HBP2I and HBP3I, it is also considerably shorter in MeCN at blue wavelengths. Whilst in MeOH and octanol, there is not a significant difference. This highlights the complex solvent dependence of the chromophores.

7.3.2. Temperature Dependence of the Fluorescence Decay of HBP3I

The temperature dependence of the time-resolved fluorescence of HBP3I in ethylene glycol was measured as described in Section 4.4.4. The sample was measured at 278 K, 293 K, 303 K and 353 K. Figure 7.15 shows that as the temperature is increased, the fluorescence decay becomes faster. This behaviour is more pronounced than was observed for Kaede. The fitting parameters are given in Table 7.6.
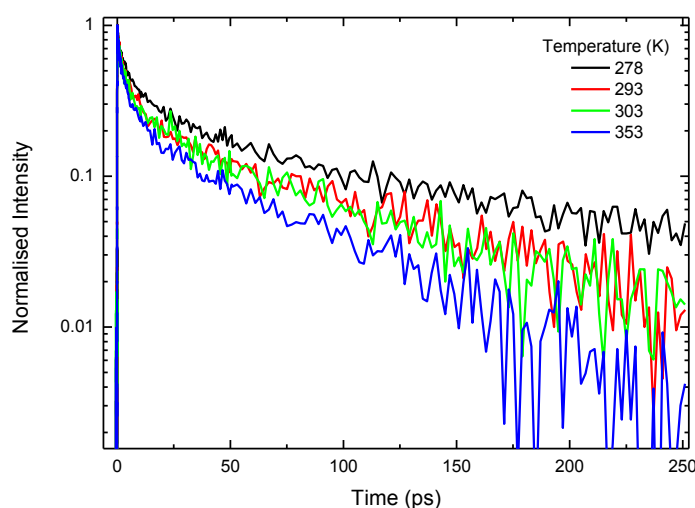
Figure 7.15. Time-resolved fluorescence of HBP3I in ethylene glycol at 278 K (black), 293 K (red), 303 K (green) and 353 K (blue).

T (K)	278	293	303	353
η (cP)	46	21	14	3.5
τ_1 (ps)	65	67	55	54
a_1	0.31	0.26	0.29	0.23
τ_2 (ps)	5.7	6.2	3.8	4.9
a_2	0.42	0.43	0.48	0.42
τ_3 (ps)	0.49	0.82	0.46	0.7
a_3	0.27	0.31	0.23	0.35
$<\tau>$ (ps)	22.6	20.1	18.0	14.9

Table 7.6. Fitting parameters for the time-resolved fluorescence of HBP3I at 278, 293, 303 and 353 K. The errors are less than 11%.

As described in Chapter 4, the average lifetime determined for each temperature was used to estimate the radiationless decay rate (k_{nr}). The relation between this rate and the solvent viscosity is given by,

$$\kappa_{nr} = \frac{C}{\eta^\alpha},$$
(7.2)

where C is a constant of proportionality. A plot of *In* k_{nr} against viscosity was then produced (Figure 7.16) where analysis yields the exponent α. A very small value of 0.009 ± 0.002 was obtained for α, which is higher but within the errors of that found for Kaede (Chapter 4). This indicates that nonradiative decay is weakly dependent upon viscosity.
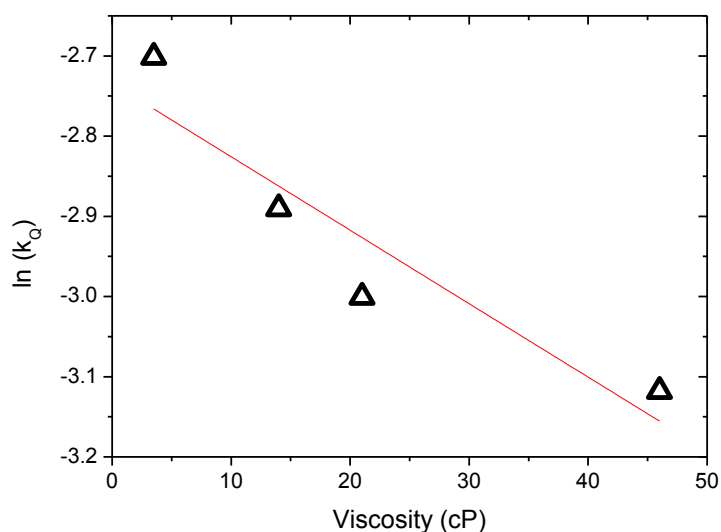
Figure 7.16. The rate of nonradiative decay exhibits a weak dependence on viscosity. The red line is the fit, giving a gradient of 0.009 ± 0.002.

7.4. Conclusions

The steady-state absorption spectra (Figure 7.2) show that the absorption of the HBPXIs is shifted by a few nm compared to that of Kaede (Chapter 4) and roughly 65 nm compared to HBDI. The magnitude of this shift depends on both the pyridine nitrogen position and the solvent. The absorption is also blue shifted in MeCN and THF for all chromophores and in water for HBP4I. The intensity of the steady-state fluorescence of the pyridines (Figure 7.5) is comparable to that of Kaede. However the emission spectra are red-shifted by 30 – 40 nm, suggesting a greater change in the excited state than the ground-state upon substitution of the imidazole of Kaede for a pyridine ring. Structure is also observed in the spectra indicating that like Kaede, these chromophores also aggregate at relatively low concentrations. The steady-state emission exhibits a strong solvent dependence, where the

fluorescence is enhanced in MeCN and THF and suppressed in water. Thus, indicating the importance of the hydrogen bonding nature of the solvent on the excited state, as was found for Kaede in Chapter 4.

The time-resolved fluorescence shows both a solvent and wavelength dependence, as well as being strongly affected by the pyridine nitrogen position. (Section 7.3). Similarly to Kaede, the decays are non monoexpoential and this is likely to be in part due to the formation of aggregates. The decays exhibit a dependence on viscosity at early times, becoming dominated by the solvent polarity and hydrogen bonding nature at long times. The position of the pyridine also influences the excited state dynamics, where in HBP4I nonradiative decay is strongly enhanced in EG and in MeCN at blue edge of the spectrum. Although upon moving to the red edge of the spectrum of HBP4I in MeCN, the average lifetime increases significantly. However, little difference is observed in the fluorescence decays in MeOH and octanol upon moving the nitrogen. Comparing to Kaede (Chapter 4), in methanol the average lifetime is in agreement for HBP2I and HBP4I but slightly longer in HBP3I. Whilst in ethylene glycol, HBP2I is again in agreement and HBP3I slightly longer but the fluorescence is strongly suppressed in HBP4I.

The results presented in this chapter highlight the complexity of chromophore photophysics. Further investigation of these chromophores is needed to obtain a complete picture of their photophysics. TD-DFT calculations are required to investigate the dipole moment of the first excited states of these chromophores. These results may clarify the solvent sensitivity observed in the steady-state spectra (Section 7.2). The sample concentration and excitation wavelength dependence of the steady-state fluorescence should also be examined to study the effects of aggregation of the chromophores, for Kaede

it was shown that aggregation enhanced the fluorescence quantum yield (Chapter 4). To

reveal the nature of the coordinate promoting nonradiative decay, transient absorption

measurements such as those described for Kaede in Chapter 4 could be performed. An

isoviscosity study would also allow determination of the intrinsic barrier to nonradiative

decay.

7.5. References

(1)Dong, J.; Solntsev, K. M.; Poizat, O.; Tolbert, L. M. *J. Am. Chem. Soc.* **2007**, *129*, 10084.
(2)Hsieh, C.-C.; Chou, P.-T.; Shih, C.-W.; Chuang, W.-T.; Chung, M.-W.; Lee, J.; Joo, T. *J. Am. Chem. Soc.* **2011**, *133*, 2932.
(3)Kang, J.; Zhao, G.; Xu, J.; Yang, W. *Chem. Commun.* **2010**, *46*, 2868.
(4)Chen, K.-Y.; Cheng, Y.-M.; Lai, C.-H.; Hsu, C.-C.; Ho, M.-L.; Lee, G.-H.; Chou, P.-T. *J. Am. Chem. Soc.* **2007**, *129*, 4534.
(5)Vengris, M.; van der Horst, M. A.; Zgrabli, G.; van Stokkum, I. H. M.; Haacke, S.; Chergui, M.; Hellingwerf, K. J.; van Grondelle, R.; Larsen, D. S. *Biophys. J.* **2004**, *87*, 1848.
(6)Chen, Y.-H.; Lo, W.-J.; Sung, K. *The Journal of Organic Chemistry* **2012**, *78*, 301.
(7)Conyard, J.; Kondo, M.; Heisler, I. A.; Jones, G.; Baldridge, A.; Tolbert, L. M.; Solntsev, K. M.; Meech, S. R. *The Journal of Physical Chemistry B* **2011**, *115*, 1571.
(8)Baranov, M. S.; Lukyanov, K. A.; Borissova, A. O.; Shamir, J.; Kosenkov, D.; Slipchenko, L. V.; Tolbert, L. M.; Yampolsky, I. V.; Solntsev, K. M. *J. Am. Chem. Soc.* **2012**, *134*, 6025.
(9)Huang, G.-J.; Ho, J.-H.; Prabhakar, C.; Liu, Y.-H.; Peng, S.-M.; Yang, J.-S. *Org. Lett.* **2012**, *14*, 5034.
(10)Tou, S.-L.; Huang, G.-J.; Chen, P.-C.; Chang, H.-T.; Tsai, J.-Y.; Yang, J.-S. *Chem. Commun.* **2014**, *50*, 620.
(11)Yang, J.-S.; Huang, G.-J.; Liu, Y.-H.; Peng, S.-M. *Chem. Commun.* **2008**, 1344.
(12)Addison, K.; Heisler, I. A.; Conyard, J.; Dixon, T.; Bulman Page, P. C.; Meech, S. R. *Faraday Discuss.* **2013**.
(13)Paul, A.; Mandal, P. K.; Samanta, A. *Chem. Phys. Lett.* **2005**, *402*, 375.
(14)Paul, A.; Mandal, P. K.; Samanta, A. *The Journal of Physical Chemistry B* **2005**, *109*, 9148.
(15)Strickler, S.; Berg, R. A. *The Journal of Chemical Physics* **1962**, *37*, 814.
(16)Litvinenko, K. L.; Webber, N. M.; Meech, S. R. *The Journal of Physical Chemistry A* **2003**, *107*, 2616.
(17)Voliani, V.; Bizzarri, R.; Nifosì, R.; Abbruzzetti, S.; Grandi, E.; Viappiani, C.; Beltram, F. *The Journal of Physical Chemistry B* **2008**, *112*, 10714.
(18)Addison, K.; Conyard, J.; Dixon, T.; Bulman Page, P. C.; Solntsev, K. M.; Meech, S. R. *The Journal of Physical Chemistry Letters* **2012**, *3*, 2298.

Chapter 8 – Summary

In this thesis the photophysics of the green fluorescent protein chromophore (HBDI), the KaedeFP chromophore, and some related analogues have been studied using ultrafast methods.

The importance of protein-chromophore interactions in controlling the behaviour of photoswitchable fluorescent proteins was highlighted through the study of HBDI and the FHBMI chromophore. HBDI is found both in the green fluorescent protein and the photoswitchable fluorescent protein Dronpa (as well as many others), while a chromophore closely related to FHBMI is the fluorophore of the kindling fluorescent protein. The *cis* and *trans* states of HBDI were investigated in order to establish the importance of chromophore isomerisation in the photophysics of Dronpa. Whilst it is known that the chromophore is *cis* in the bright state and *trans* in the dark state, the time-resolved fluorescence decays of the different isomeric forms of the isolated chromophore were indistinguishable. Furthermore, in Chapter 6 it was shown that whilst the optical properties of green fluorescent protein and kindling fluorescent protein are very different, the photophysical behaviour of HBDI and FHBMI is surprisingly similar.

The chromophore of the green-to-red photoswitchable fluorescent protein KaedeFP (Kaede) was investigated in detail. It was shown that this chromophore undergoes aggregation-induced fluorescence at relatively low concentrations, where the HBDI chromophore remains monomeric. The preliminary studies of the Kaede analogues suggest that this is a general feature of Kaede like chromophores.

For chromophores in solution, the importance of the hydrogen bonding nature of the solvent is a consistent feature throughout this work. For Kaede it was shown that radiationless decay is enhanced in strongly hydrogen bonding solvents, whereas the fluorescence lifetime was extended in highly polar aprotic solvents. For the HBDI analogues studied in Chapter 5, the addition of a para amino group was found to hinder internal conversion, extending the fluorescence lifetime by 4-5 times compared to that of HBDI. Whilst the addition an ortho hydroxyl group in combination with the para amino group, extends the lifetime by up to 60 times due to the formation of an intramolecular hydrogen bond which restricts the torsional motions of the chromophore. For this molecule the average fluorescence lifetime was shortened in hydrogen bond donating solvents, indicating disruption of the intramolecular hydrogen bond.

The theoretical model described in Chapter 6 successfully reproduced the excited state decay of anionic HBDI in a fluid solvent. The fitting parameters recovered are consistent with the proposal that complete rotations of the bridging bonds are not required for deactivation of the excited state. The weak fluorescence of the isolated chromophore is strongly enhanced in the protein and it has been shown that there is sufficient space within the protein cavity to allow significant rotation around the bridging bonds. Therefore it is unlikely that chromophore isomerisation within the protein would be sufficiently hindered by steric crowding alone. However, it is possible that the chromophore-protein hydrogen bonds in the cavity could suppress the radiationless decay mechanism of the isolated chromophore. The simulations failed for neutral HBDI and this was attributed to the lack of data for the neutral potential energy surfaces. More detailed calculations on the neutral

chromophore are desirable as this state is of particular importance for photoswitchable fluorescent proteins.

Preliminary studies of a series of Kaede like chromophores were presented in Chapter 7. The steady-state emission spectra appear to indicate aggregation of the molecules, as was observed for Kaede. This could be confirmed by investigation of the effects of sample concentration and excitation wavelength. The steady-state spectra also indicate sensitivity to solvent polarity. The origin of this effect could be revealed through TD-DFT calculations. Additional suggestions for future work include an isoviscosity analysis to determine the intrinsic barrier to radiationless decay and transient absorption measurements to reveal the nature of the coordinate promoting this nonradiative decay.